Westfälische Wilhelms-Universität Münster

› **Setup and calibration of a position sensitive microchannel plate detector and analysis of a test run optimizing the WITCH experiment**

› Peter Friedag, Dissertation 2013

wissen.leben
WWU Münster

Experimentelle Physik

Dissertationsthema:
Setup and calibration of a
position sensitive microchannel plate detector
and
analysis of a test run
optimizing the WITCH experiment

Inaugural-Dissertation
zur Erlangung des Doktorgrads der Naturwissenschaften
im Fachbereich Physik
der Mathematisch-Naturwissenschaftlichen Fakultät
der Westfälischen Wilhelms-Universität Münster

vorgelegt
von
Peter Friedag
aus
Nordhorn

- 2013 -

Zusammenfassung

Die Natur der schwachen Wechselwirkung ist bislang nicht vollständig geklärt. Das Standardmodell der Teilchenphysik umfasst im Rahmen der V–A-Theorie nur vektorielle und axial-vektorielle Beiträge. Basierend auf Symmetrieüberlegungen sind weitere, exotische Wechselwirkungsarten möglich, welche experimentell bislang nur auf einem Prozent-Level ausgeschlossen wurden. Der sogenannte $\beta-\nu$-Winkelkorellationskoeffizient a ist ein Parameter, welcher stark abhänging von den zugrundeliegenden Wechselwirkungsarten ist. Eine indirekte Methode zur Bestimmung von a stellt die Messung eines Rückstoß-Energiespektrums der Tochterkerne nach dem β-Zerfall dar. Die Form des Spektrums wird bestimmt durch den Wert von a. Die WITCH-Kollaboration strebt die Bestimmung von a mit einer Genauigkeit von $\frac{\Delta a}{a} \leq 0.005$ über eine Messungen des ^{35}Ar-Rückstoß-Energiespektrums an. Hierzu werden ^{35}Ar-Ionen in einer Penningfalle gespeichert und die Rückstoßenergie der Tochterkerne mit Hilfe eines Retardierungsspektrometers mit magnetisch-adiabatischer Kollimation (MAC-E-Filter) bestimmt. Für den Nachweis der Rückstoßionen wird ein positionsempfindlicher Mikrokanalplattendetektor (MCP-Detektor) verwendet.

Im Rahmen dieser Arbeit wurde ein neuer MCP-Detektor mit größerer aktiver Oberfläche aufgebaut und in Betrieb genommen. Durch eine detaillierte Analyse der Schwachstellend des alten Detektorsystems konnte die Signalqualität verbessert, eine homogene Nachweiseffizienz erzielt, der Detektor kalibriert und eine zuverlässige Funktionsweise sichergestellt werden. Im zweiten Teil dieser Arbeit wurden anhand von Messdaten aus einer Teststrahlzeit im Okt. 2011 eine Analyseroutine entwickelt und nach experimentellen Schwachstellen gesucht. Mit Hilfe dieser Analyse wurde eine unbeabsichtigte Penningfalle im Spektromter gefunden, die Untauglichkeit sehr kleiner Retarderungsspannungen nahe einem Wert von $U_{ret} = 0$ gezeigt, ein Synchronisierungsproblem zwischen der Datenaufnahme und der Retardierungsspannungsversorgung entdeckt und zwei Datenaufnahmen, welche inkonsistente Daten produzieren, identifiziert. Dies führte zu einem optimierten Messzyklus welcher in einer späteren Messung im Nov. 2012 eingesetzt wurde. Zudem wurden zwei wichtige systematische Effekte abgeschätzt, welche sich als kritisch für eine Präzisionsmessung von a herausstellten. Als Ergebnis dieser Analyse wurde ein Wert von $a = 0.45^{+0.48}_{-0.39}{}_{\,stat} \pm 0.29_{syst}$ bestimmt.

Abstract

The standard model of particle physics only implies vectorial and axial-vectorial currents. Symmetry considerations allow for additional, exotic currents, too. Experimentally these are ruled out only to a percent level. The so-called $\beta-\nu$ angular correlation coefficient a is a parameter who's value strongly depends on the underlying interaction types. An indirect method for its determination is the measurement of the recoil energy spectrum of the daughter nuclei after beta decay. The shape of the spectrum is dependent on the value of a. The WITCH collaboration aims to determine a with a precision of $\frac{\Delta a}{a} \leq 0.005$ from a measurement of the recoil energy spectrum of the ^{35}Ar decay. For this purpose ^{35}Ar$^+$ ions are stored in a Penning trap and the recoil energy of the daughter nuclei will be determined by means of a retardation spectrometer with magnetic adiabatic collimation (MAC-E filter). To detect the recoil ions a position sensitive microchannel plate detector (MCP detector) is used.

In this thesis a new MCP detector with larger active surface has been set up and commissioned. A detailed weak point analysis of the old detector design lead to enhanced signal quality, a homogeneous detection efficiency and a stable mode of operation of the detector system. Additionally a method to measure the relative detection efficiency and determine the position resolution of the detector has been developed. In the second part of this thesis, the data from a commissioning run in Oct. 2011 was used to establish an analysis routine to extract a and look for experimental deficiencies. By means of this analysis we could locate an unintentional Penning trap in the spectrometer, showed that measurements at very low retardation potentials are unsuited, discovered a synchronization problem between the data acquisition and the retardation voltage supply and found that two independent data acquisition branches produced inconsistent data. Altogether this lead to s an optimized measurement cycle and improved data taking applied in a later measurement in Nov. 2012. Additionally on the basis of this analysis we were able to rate two important systematic effects with are of concern for a precision measurement of a. As result of this analysis a value of $a = 0.45^{+0.48}_{-0.39}{}_{\,stat} \pm 0.29_{syst}$ was determined.

Contents

INTRODUCTION

Today the Standard Model of particle physics is the most outright theory in the description of physical phenomena. Although its predictions are well confirmed by experiments – for instance all elementary particles of the standard model have been found experimentally – there are already observations – like the non-zero rest mass of the neutrino or the fact that the Standard Model does not include gravitational interaction – which indicate the existence of physics beyond the Standard Model.

Besides others, one open question is the nature of the weak interaction. In the Standard Model formulation of the weak interaction, only vectorial and axial vectorial interaction are considered, which is summarized as the V–A theory (see sec. 1.1.2). But other interaction types are in principle possible as well, which have been experimentally excluded just on a level of several percents (see sec 1.1.3).

Hence, this situation is unsatisfactory for a precision theory like the Standard Model. Most of the relevant results originate from correlation experiments which go back several decades in time (see sec. 1.2) and technology and techniques have advanced tremendously over the last years. Altogether this calls for new experiments in this field to push the limits further.

One variable which has already been addressed in numerous experiments is the so-called $\beta - \nu$ annular correlation coefficient a. The WITCH experiment uses an indirect method for its determination by measuring the recoil energy spectrum of the daughter nuclei after beta decay. The shape of this spectrum strongly spends on the value of a (see sec. 3.2.2). For a given decay, the value of a depends on the participating interaction types (see sec. 1.1.5). So by deducing the value of a from the shape of a measured recoil spectrum it is possible to determine the underlying types of interaction.

In the first place the WITCH experiment aims to determine a from the measurement of the recoil spectrum of the ^{35}Ar decay with a precision of $\frac{\Delta a}{a} < 0.005$. The particularly versatile layout of the experimental setup and the availability of several hundreds of isotopes from over 60 different elements at the ISOLDE isotope separator calls for many other measurements once the initial goal has been reached.

The WITCH experiment uses state-of-the-art technologies to measure a recoil energy spectrum of the daughter ions from the ^{35}Ar decay (see sec. 1.3). Therefore ^{35}Ar ions are prepared and stored in a double Penning system which provides a scattering-free source. Due to its high angular acceptance and good energy resolution, a MAC-E filter spectrometer is used to measure the kinetic recoil energy of the daughter ions. To detect the recoil ions, a position sensitive microchannel plate detector with delay line anode is used in combination with a post-acceleration section. such a system has a high detection efficiency for recoil ions.

In the following section we first give a historical overview of the theory of the beta decay and discuss successively the developments in this file of research and lay down the motivation for the experiment. We close that section with a discussion of the state of the art in the research of exotic interaction.

In sec. 1.3 we explain the setup of the WITCH experiment. The individual parts of the setup will be discussed in more detail each in a separate subsection. Details about the MCP detector system, along with calibration measurements are given in more detail in part I of this thesis. Part II deals with the development of a new data analysis routine using data from a test run in 2011, a weak point analysis with this data to optimize the WITCH experiment and a discussion two important systematic effects.

1.1. Theoretical motivation

In 1896 the famous serendipity of Henri Becquerel lead to the discovery of radioactivity. This was first observed in the reaction of uranium salts with photographic plates [Bec96, Bec96a]. Further research by Henri Becquerel and his student Marie Curie, together with her husband Pierre Curie, lead to the discovery of additional radioactive elements such as Polonium and Radium. In 1903 Henri Becquerel shared the Nobel Prize in Physics with Marie and Pierre Curie.

In 1899 Ernest Rutherford separated three different types of radiation emitted from radioactive substances – alpha, beta (β^-) and gamma radiation – by their deflection in a magnetic field. In 1908 he was honored with the Nobel Prize in Chemistry. Otto van Baeyer, Lise Meitner and Otto Hahn showed in 1911 that electrons originating from the beta decay of Radium show a continuos distribution. Since in a two-body decay this would violate the conservation of energy, momentum and orbital momentum Wolfgang Pauli proposed the participation of a third particle, which he called neutron, in this process [Pau30]. Later in 1931 the name of this particle was changed by Enrico Fermi into neutrino, meaning small neutron. The first experimental evidence was provided by Clyde Lorrain Cowan and Frederik Reines in 1956 [Rei56]. The β^+ decay was discovered in 1934 in the decay of ^{30}P by Frédéric and Irène Joliot-Curie [Jol34]. The electron capture was first observed by Luis Alvarez in the decay of ^{48}V in 1937 [Alv37].

In beta decay either a neutron is converted into a proton under emission of an electron and an electron anti-neutrino or a proton converts into a neutron where a positron and an electron neutrino are emitted. The first of these processes is called β^- and the latter β^+ decay, named after the charge of the first fermion. For the free particles – neutron or proton – only the first process can be observed due to energy conservation, with a neutron lifetime of $\tau_n = (881.5 \pm 1.5)$ s [Nak10]. In the nucleus both processes can occur. Besides the β^+ decay, the electron capture occurs, where an electron from an inner shell of the atom and a proton from the nucleus transforms into a neutron while an electron neutrino is emitted.

For a mother nucleus $^A_Z X$ with Z protons and A nucleons and a daughter nucleus Y these processes can be written as:

$$\beta^- \text{ decay:} \quad {}^A_Z X \longrightarrow {}^A_{Z+1} Y + e^- + \bar{\nu}_e$$
$$\beta^+ \text{ decay:} \quad {}^A_Z X \longrightarrow {}^A_{Z-1} Y + e^+ + \nu_e$$
$$\text{Electron capture:} \quad {}^A_Z X + e^- \longrightarrow {}^A_{Z-1} Y + \nu_e$$
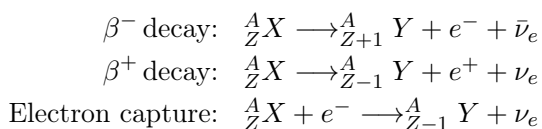
In these formulae e^+ and e^- denote a positron and an electron while ν_e and $\bar{\nu}_e$ denote a neutrino and an anti-neutrino.

1.1.1. Fermi's theory of the beta decay

The first quantitative theoretical description of the beta decay was presented in 1934 by Enrico Fermi [Fer34]. In analogy to the classical electromagnetic interaction Hamiltonian he formulated a beta decay Hamiltonian. He chose a current-current coupling as ansatz for the beta decay hamiltonian:

$$
\begin{aligned}
H_\beta &= \frac{G_F}{\sqrt{2}} \quad \underbrace{J_h^\mu(x)}_{\text{charged hadronic current}} \qquad \cdot \qquad \underbrace{j_{e\mu}(x)}_{\text{charged leptonic current}} \\
&= \frac{G_F}{\sqrt{2}} \quad \left(\psi_p^\dagger(\vec{r})\gamma^\mu\psi_n(\vec{r}) \quad \cdot \quad \psi_{e^-}^\dagger(\vec{r})\gamma_\mu\psi_{\bar{\nu}}(\vec{r}) \right)
\end{aligned}
\tag{1.1.1}
$$

where G_F is the Fermi coupling constant for the weak interaction, the charged leptonic current $j_{e\mu}(x) = \psi_{e^-}^\dagger(\vec{r})\gamma_\mu\psi_{\bar{\nu}}(\vec{r})$ describes the conversion of an anti-neutrino into an electron and the hadronic current $J_h^\mu(x) = \psi_p^\dagger(\vec{r})\gamma^\mu\psi_n(\vec{r})$ describes the conversion of neutron into a proton. $\psi_p^\dagger(\vec{r})$ and $\psi_{e^-}^\dagger(\vec{r})$ are the adjoint wave functions of the proton and the electron, $\psi_n(\vec{r})$ and $\psi_{\bar{\nu}}(\vec{r})$ are the wave functions of the neutron and the anti-neutrino.

In 1933 Wolfgang Pauli had already shown that such a Hamiltonian could have five possible forms to be relativistically invariant. These are the scalar, **S**, the pseudo-scalar, **P**, the vector, **V**, the axial vector, **A** and the tensor, **T**, interaction – named after their transformation [Pau33, Pau33a]. Despite the fact Enrico Fermi was aware of this, he only considered a vector type interaction in his theory.

1.1.2. The V–A theory

In 1936 George Gamow and Edward Teller extended this approach to all possible Lorentz invariant current-current interactions (scalar, pseudo-scalar, vector, axial vector and tensor interaction) [Gam36].

Table 1.1.: Selection rules for Fermi and Gamow-Teller decays. ΔI is the difference between nuclear spins of the mother and the daughter nucleus, ΔT is the difference between isospins of the mother and the daughter nucleus and $\Delta\pi$ is the difference in parity between the mother and the daughter nucleus. A pure Fermi decay allows scalar and vector interaction, a pure Gamow-Teller decay allows tensor and axial vector interaction.

	Selection rule	Interaction types
Fermi	$\Delta I = 0$ $\Delta T = 0$ $\Delta\pi = 0$	Scalar & Vector
Gamow-Teller	$\Delta I = 0, \pm 1 \, (0 \nrightarrow 0)$ $\Delta T = 0, \pm 1 \, (0 \nrightarrow 0)$ $\Delta\pi = 0$	Tensor & Axial vector

In Fermis approach in a beta transition no difference between nuclear spin ($\Delta I = 0$), isospin ($\Delta T = 0$) and the parity ($\Delta\pi = 0$) of the mother and daughter ion is allowed. George Gamow and Edward Teller considered the nuclear spin and obtained selection rules.

The selection rules for pure Fermi and Gamow-Teller transitions are listed in tab. 1.1. Decays that are covered either by the Fermi or the Gamow-Teller selection rules are called allowed decays. Other decays (e. g. $\Delta I > 1$) also occur but are suppressed by multiple orders of magnitude. Therefore they are called forbidden transitions. At present first order forbidden transitions are of no importance for precision weak interaction studies due to their complicated theoretical description.

The Gamow-Teller transition requires either an axial vector or a tensor form of the interaction, while the Fermi transition requires a vector or scalar interaction.

In 1937 Markus Eduard Fierz showed that if both, scalar and vector, or both, axial vector and tensor interactions, are present in beta decay, there would be an interference term in the beta decay spectrum. Its size depends on the electron energy [Fir37]. In 1949 L. M. Langer and H. C. Price have shown the presence of either axial vector or tensor interaction in the measurement of beta spectra of unique forbidden transitions of various nuclei [Lan149].

In 1957 George Sudershan and Robert Marshak undertook an analysis of the data on beta decay, μ-decay, μ-capture and π-decay, arriving at the conclusion that a universal weak interaction of the form $H_w \propto J^{\dagger}J$, with J as the weak current, is only possible if the space time structure of the current J is V–A [Sud57, Sud58]. Their result was presented in 1957 on the Padua-Vernice conference. Richard Feynman and Murray Gell-Mann independently published a similar approach [Fey58]. At the time of the publication their proposal was already in conflict with published data on the beta decay of ^{6}He [Rus53, Rus55] and the decay of the positive pion [And57].

A correlation measurement between the electron and the recoil nucleus in the decay of ^{6}He B. M. Rustad and L. M. Ruby showed $a = +0.34 \pm 0.09$ which is consistent with pure tensor coupling (see sec. 1.1.4 and sec. 1.1.5 for details about a). In 1958 at an APS meeting, C. S. Wu presented critique of that measurement. They pointed out that the detection efficiency had a strong angular dependence, the ^{6}He gas pressure gradient had to be known to great accuracy, and there were back-scattering effects. Taking into account all these systematic effects they concluded that the errors were large enough so that a could be just as consistent with $a = -1/3$ (pure axial vector coupling) as with $a = +1/3$ (pure tensor coupling). B. M. Rustad and L. M. Ruby themselves presented a similar critique at the same meeting. A measurement of the recoil energy spectrum of the daughter nucleus of ^{6}He decay showed $a = -(0.39 \pm 0.02)$ [Ham58]. Although the value differs more than one standard deviation from the expected value of $a = -0.33$ it indicated that axial vector interaction is dominant. According to ref. [Pak09] their value was later changed to $a = -(0.33 \pm 0.03)$, ruling out the tensor interaction.

The ratio $R = \Gamma(\pi \to e\nu)/\Gamma(\pi \to \mu\nu)$ strongly depends on the space-time structure of the decay interaction. In ref. [And57] the authors H. L. Anderson and L. Lattes reported a value of $R < 10^{-5}$ which is in disagreement with vector and axial vector coupling and prefers tensor coupling. A new measurement done by G. Impeduglia et al. found a value of $R = (9.2 \pm 3.7) \cdot 10^{-5}$ which is in good agreement with a vector and axial vector coupling [Imp58].

The very elegant and famous measurement of the helicity of neutrinos carried out by Maurice Goldhaber et al., showing that neutrinos are left-handed, is an additional confirmation of the V–A structure of the weak current [Gol57].

In 1956 Tsung-Dao Lee and Chen Ning Yang proposed a measurement to test parity violation in the weak interaction [Lee56]. One year later this measurement of the correlation between the emission direction of the beta particle and the spin of the nucleus was carried out by Chien-Shiung Wu which lead to the discovery of maximum parity violation in the weak interaction. For this only T. D. Lee and C. N. Young received the Nobel Price in Physics 1957 while C. S. Wu went away empty-handed. The negative sign in V–A (V *minus* A) can be determined from the direction of the observed asymmetry in the Wu experiment.

The above mentioned development show that correlation experiments in beta decay play a decisive role in the determination of the properties of the weak interaction.

In the mid-seventies left-right symmetric models (L-R models) have been developed [Beg77, Moh75, Moh75a]. In the Standard Model, parity violation in the weak interaction is embedded, by establishing left-handed fermions to transform like $SU_L(2)$ doublets and right-handed fermions transform as singlets [Her01]. In the simplest left-right symmetric models the $SU(2)_L \times SU(2)_R \times U(1)$ gauge group is introduced. Additionally to the transformation under $SU(2)_L$ above, the right-handed fermions transform under $SU(2)_R$ as doublets, whereas the left-handed transform as

singlets. Through the gauge symmetry of these models additional bosons are introduced. Besides the known W and Z bosons (in L-R models they are usually called W_1 and Z_1), a second charged boson (W_2) and a second neutral gauge boson (Z_1) are introduced. In analogy to quark or neutrino mixing the weak eigenstates of W_L and W_R are linear combinations of the mass eigenstates W_1 and W_2 with a mixing angel ζ and CP-violating phase ω [Her01].

In these models, parity violation originates from the difference of the masses of the left-handed and right-handed bosons. For instance, the predominantly left-handed W_1 boson is associated with a gauge field with predominantly V–A couplings, while the predominantly right-handed W_2 boson is associated with a gauge field with predominantly V+A couplings. According to ref. [Beg77], weak interactions at low energies in the charged-current sector are predominantly V–A, and V+A interactions can be present at a level up to 13% in the amplitudes. The gauge field with predominantly V+A couplings is suppressed because of the larger mass of the predominantly right-handed W_2 boson. In ref. [Her01] the mass limits for the W_2 boson are given as $800\,\mathrm{GeV} \gtrsim m_2 < 1.8\,\mathrm{TeV}$, which is at least 10 times the mass of the W_1 boson, which is $W_1 = 80.385 \pm 0.015\,\mathrm{GeV}$ [Ber12].

1.1.3. The Standard Model for the beta decay & current experimental limits

The most general beta decay hamiltonian can be written as [Lee56]:

$$
\begin{aligned}
\mathcal{H}_\beta &= (\psi_p^\dagger \gamma_4 \psi_n)(C_S \psi_e^\dagger \gamma_4 \psi_\nu + C_S' \psi_e^\dagger \gamma_4 \gamma_5 \psi_n u) \\
&+ (\psi_p^\dagger \gamma_4 \gamma_\mu \psi_n)(C_V \psi_e^\dagger \gamma_4 \gamma_\mu \psi_\nu + C_V' \psi_e^\dagger \gamma_4 \gamma_\mu \gamma_5 \psi_n u) \\
&+ \frac{1}{2}(\psi_p^\dagger \gamma_4 \sigma_{\lambda\mu} \psi_n)(C_T \psi_e^\dagger \gamma_4 \sigma_{\lambda\mu} \psi_\nu + C_T' \psi_e^\dagger \gamma_4 \sigma_{\lambda\mu} \gamma_5 \psi_n u) \\
&+ (\psi_p^\dagger \gamma_4 \gamma_\mu \gamma_5 \psi_n)(-C_A \psi_e^\dagger \gamma_4 \gamma_\mu \gamma_5 \psi_\nu - C_A' \psi_e^\dagger \gamma_4 \gamma_\mu \psi_n u) \\
&+ (\psi_p^\dagger \gamma_4 \gamma_5 \psi_n)(C_P \psi_e^\dagger \gamma_4 \gamma_5 \psi_\nu + C_P' \psi_e^\dagger \gamma_4 \psi_n u) \\
&+ h.c. \tag{1.1.2}
\end{aligned}
$$

with $\gamma_i, \quad i \in [1,5]$ the γ matrices defined according to refs. [Lee56, Ros55]. In other common notations $\gamma_4 = \gamma_0$ and $\bar{\psi} = \psi^\dagger \gamma_0$. *h.c.* is the hermitian conjugate and the tensor operator is

$$
\sigma_{\lambda\mu} = -\frac{1}{2} i (\gamma_\lambda \gamma_\mu - \gamma_\mu \gamma_\lambda). \tag{1.1.3}
$$

Each line in eq. 1.1.2 describes one of the interaction types S, V, T, A or P. The complex coupling constants fully describe the interaction and its symmetries. In total they consist of 20 numbers (a real and an imaginary part each for C_i and C_i') which have to be determined experimentally.

In the SM the following values for the coupling constants are assumed (all are real):

$$
\begin{aligned}
C_V = C_V' &= 1 \\
C_A = C_A' &\approx -1.27 \\
C_S = C_S' &= 0 \\
C_T = C_T' &= 0 \\
C_P = C_P' &= 0 \tag{1.1.4}
\end{aligned}
$$

Maximum parity violation corresponds to $C_i = C_i'$. The fact that $C_A \neq -1$ is a sign of the inner structure of the proton and the neutron. The exact value of $C_A = C_A'$ has to be determined from the neutron decay [Sev06]. Without making any further assumptions except that the coupling constants are real ($C_i, C_i' \in \mathbb{R}$), which corresponds to time reversal invariance, it is possible to deduce experimental limits on the scalar and tensor coupling constants and for the ratio of C_A/C_V.

However, the experimental precision of the C_i still allows for significant deviations from the SM values, i. e. for physics beyond the SM. A least square fit to experimental data from nuclear beta and neutron decays results in (90% C.L.) [Sev06]:

$$-1.40 < \quad \frac{C_A}{C_V} \quad < -1.17$$
$$-0.065 < \quad \frac{C_S}{C_V} \quad < 0.070$$
$$-0.076 < \quad \frac{C_T}{C_A} \quad < 0.090 \tag{1.1.5}$$

In a recent survey of superallowed $0^+ \rightarrow 0^+$ nuclear β decays, a new limit on the scalar interaction, under the assumption of time reversal invariance, is given as [Har09]:

$$\left| \frac{C_S}{C_V} \right| \leq 0.065 \tag{1.1.6}$$

Under the assumptions of time reversal invariance *and* maximum parity violation, in the same reference the authors also present a more stringent limit on scalar interaction is given [Har09]:

$$\frac{C_S}{C_V} = (0.0011 \pm 0.0013) \tag{1.1.7}$$

Assuming only time reversal invariance, the current experimental limits on scalar and tensor interactions, are in the range of several percents and still leave room for improvements. The limit for $\frac{C_A}{C_V}$ is compatible with the SM prediction, again with a precision of several percents. According to ref. [Sev06], in the non-relativistic treatment of the nucleus it is easy to show that the pseudo-scalar hadronic current $\psi_p \gamma_5 \psi_n^\dagger$ vanishes, therefore the pseudo-scalar term in eq. 1.1.2 can be neglected in the calculation of the experimental observables.

Deviations from the SM values for the coupling constants have direct consequences for the transformation properties of the hamiltonian density given in eq. 1.1.2. If either $C_i = 0$ or $C_i' = 0$, parity would be conserved. If the coefficients $C_i \neq C_i'$ parity violation would not be maximal. The presence of an imaginary part in the coefficient C_i and C_i' would be a sign of time reversal violation. The vanishing of either C_i or C_i' would correspond to charge conjugative variance. This is summarized in tab. 1.2.

Table 1.2.: Consequences for the coupling constants due to the violation of the discrete symmetries and the conditions as they are present in the SM formulation. Partially taken from ref. [Sev06].

Symmetry	Condition for violation	Standard model
C	($\Re(C_i) \neq 0$ and $\Re(C_i') \neq 0$) or ($\Im(C_i) \neq 0$ and $\Im(C_i)' \neq 0$)	$\Re(C_i) \neq 0$ and $\Re(C_i') \neq 0$
P	$C_i \neq 0$ and $C_i' \neq 0$	$C_i \neq 0$ and $C_i' \neq 0$
T	$\Im(C_i/C_j) \neq 0$ or $\Im(C_i'/C_J) \neq 0$	$C_i, C_i' \in \mathbb{R} \Rightarrow$ $\Im(C_i/C_j) = 0$ and $\Im(C_i'/C_J) = 0$, $\forall\, i,j \in [S,V,A,T,R]$

However, most of the results on which the SM is based on, reach back several decades in time. New technologies allow for significantly improved correlation studies and to search for physics beyond the SM with precision beta decay experiments.

1.1.4. The β energy spectrum and angular correlation

In 1957 J. Jackson, S. Treiman and H. Wylde calculated rate formula including Coulomb corrections from the Hamiltonian density. For the distribution in electron and neutrino directions and electron energy they found [Jac57]:

$$\omega(\vec{\sigma}|E_\beta, \Omega_\beta, \Omega_\nu)\, dE_\beta\, d\Omega_\beta\, d\Omega_\nu = \frac{F(\pm z, E_\beta)}{(2\pi)^5}\, p_\beta\, E_\beta\, (E_0 - E_\beta)^2 dE_\beta\, d\Omega_\beta\, d\Omega_\nu$$

$$\cdot \frac{\xi}{2}\left[1 + a\frac{\vec{p}_\beta \cdot \vec{p}_\nu}{E_\beta\, E_\nu} + b\frac{m_e}{E_\beta} + A\frac{\langle\vec{J}\rangle}{J}\cdot\frac{\vec{p}_\beta}{E_\beta} + \vec{\sigma}\cdot\left[G\frac{\vec{p}_\beta}{E_\beta} + H\frac{\vec{p}_\nu}{E_\nu} + K\frac{\vec{p}_e}{E_e + m_e}\left(\frac{\vec{p}_\beta \cdot \vec{p}_\nu}{E_\beta E_\nu}\right) + L\frac{\vec{p}_\beta \times \vec{p}_\nu}{E_\beta E_\nu}\right]\right].$$

$$(1.1.8)$$

Here the common convention $\hbar = c = 1$ is used. $F(\pm z, E_\beta)$ is the the Fermi function for electrons (upper sign) and positron (lower sign) respectively (see e. g. [Bla52]), z is the charge of the daughter nucleus, E_β and $E_\nu = E_0 - E_\beta$ refer to the energies of the beta particle and the neutrino, p_β and p_ν to the momenta of the beta particle and the neutrino, Ω_β and Ω_ν the solid-angle elements of the beta particle and the neutrino, m_β the mass of the beta particle, $\vec{\sigma}$ the polarization vector of the beta particle and the degree of nuclear polarization is given by $\frac{\langle J\rangle}{J}$. The mass of the neutrino is assumed to be zero $m_\nu = 0$ and the recoil energy of the daughter nucleus which is typically about 4–5 orders of magnitude smaller than the beta energy was neglected. The common normalization factor ξ contains the coupling constants in the following way [Jac57]:

$$\begin{aligned}\xi &= |M_F|^2(|C_S|^2 + |C_S'|^2 + |C_V|^2 + |C_V'|^2)\\ &+ |M_{GT}|^2(|C_A|^2 + |C_A'|^2 + |C_T|^2 + |C_T'|^2)\end{aligned}$$

$$(1.1.9)$$

where M_F and M_{GT} are the Fermi and Gamow-Teller matrix elements. The various correlation constants a, b, A, G, H, K and L are listed including all Coulomb correction in the appendix of ref. [Jac57]. The correlation coefficients also contain coupling constants and therefore depend on the different combinations of these.

1.1.5. The $\beta - \nu$ angular correlation coefficient a

In case the angle θ between the momentum of the neutrino and the momentum of the beta particle is measured, the so-called β–ν angular correlation coefficient a can be determined [Jac57].

$$\begin{aligned}a\xi &= |M_F|^2\left[|C_V|^2 + |C_V'|^2 - |C_S|^2 - |C_S'|^2 \mp \frac{\alpha z m_e}{p_\beta}\cdot 2\cdot\Im(C_S C_V^* + C_S' C_V'^*)\right]\\ &+ \frac{|M_{GT}|^2}{3}\left[|C_T|^2 + |C_T'|^2 - |C_A|^2 - |C_A'|^2 \mp \frac{\alpha z m_e}{p_\beta}\cdot 2\cdot\Im(C_T C_A^* + C_T' C_A'^*)\right]\end{aligned}$$

$$(1.1.10)$$

where the upper sign denotes a β^- decay and the lower sign a β^+ decay. If the coupling constants have an imaginary part ξa shows a dependency on the impulse of the beta particle. From eq. 1.1.10 we see that $a\xi$ depends quadratically on the coupling constants for exotic currents. In practice the Fierz interference term $b\frac{m_e}{E_\beta}$ will be measured as well, why the experimental variable will be in fact [Kon10]:

$$\tilde{a} = \frac{a}{1 + b\frac{m_e}{E_\beta}}$$

$$(1.1.11)$$

with [Jac57]

$$b\xi = \pm 2\Gamma\Re\left[|M_F|^2(C_S C_V^* + C_S' C_V'^*) + |M_{GT}^2(C_T C_A^* + C_T' C_A'^*)|\right]$$

$$(1.1.12)$$

with ξ defined by eq. 1.1.9 and $\Gamma = \sqrt{1 - \alpha^2 Z^2}$. In case of the Standard Model where the Fierz interference coefficients equals zero $b = 0$, the observable in eq. 1.1.11 becomes equal to a.

The Gamow-Teller-to-Fermi mixing ratio ρ is defined as [Sev06]:

$$\rho = \frac{C_A M_{GT}}{C_V M_F} \tag{1.1.13}$$

For a pure Fermi decay $\rho = 0$. For a pure Gamow-Teller decay one has to calculate the limit $\rho \to \infty$. In the Standard Model a can be expressed as function of the Gamow-Teller-to-Fermi mixing ratio ρ [Sev06]:

$$a_{SM} = \frac{1 - \rho^2/3}{1 + \rho^2} \tag{1.1.14}$$

Under the assumptions of maximal parity violation and no time reversal violation, this equation can be extended for possible non-Standard Model terms as [Sev06]:

$$a \approx a_{SM} - \frac{1}{(1 - \rho^2)^2} \left[\left(1 + \frac{1}{3}\rho^2 \right) \frac{|C_S|^2 + |C_S'|^2}{|C_V|^2} + \frac{1}{3}\rho^2 (1 - \rho^2) \frac{|C_T|^2 + |C_T'|^2}{|C_A|^2} \right] \tag{1.1.15}$$

Under this assumption a is not dependent on the beta impulse p_β anymore. For a pure Fermi decay respectively a pure Gamow-Teller decay this expression reduces to:

$$a_F \approx 1 - \frac{|C_S|^2 + |C_S'|^2}{|C_V|^2} \tag{1.1.16}$$

$$a_{GT} \approx -\frac{1}{3}\left(1 - \frac{|C_T|^2 + |C_T'|^2}{|C_A|^2} \right) \tag{1.1.17}$$

In the Standard Model for a pure Fermi decay $a = 1$ and for a pure Gamow-Teller decay $a = -1/3$.

1.1.6. The recoil energy spectrum

Since for a direct measurement of a, the neutrino momentum has to be measured, a needs to be determined by alternative methods. One is to measure the recoil energy spectrum of the daughter ions after beta decay – like in the WITCH experiment. By varying a retardation potential, an integrated recoil energy spectrum will be measured. So for a given potential only ions with a kinetic energy above a certain threshold will be detected.

The recoil energy spectrum for a given decay cannot be calculated analytically, although it is possible to calculate it numerically. According to ref. [Glu98] the zeroth order recoil energy spectrum can be written as:

$$R_0(E_{rec}) = \int_{E_{\beta,\,min}}^{E_{\beta,\,max}} dE_\beta W_0(E_\beta, E_{rec}). \tag{1.1.18}$$

The upper and lower limit of integration are given by [Glu98]:

$$E_{\beta,\,min/max} = \frac{(\Delta - E_{rec} \mp p)^2 + m_e^2}{2(\Delta - E_{rec} \mp p)} \tag{1.1.19}$$

where

$$p = \sqrt{2m_f E_{rec} + E_{rec}^2} \tag{1.1.20}$$

$$\Delta = m_i - m_f \tag{1.1.21}$$

with m_i and m_f the initial atomic and final ion mass of the decaying nucleus. $W_0(E_\beta, E_{rec})$ is the zeroth order Dalitz distribution of the beta energy E_β and the recoil energy E_{rec} which can be calculated via [Glu98]:

$$W_0(E_\beta, E_{rec}) = W_0^{e\nu}(E_\beta, c_{e\nu}) \frac{dc_{e\nu}}{dE_{rec}} \tag{1.1.22}$$

with

$$\frac{dc_{e\nu}}{dE_{rec}} = \frac{m_i(E_{\beta m} - E_\beta)}{\beta E_\beta E_\nu} \tag{1.1.23}$$

$$E_{\beta m} = \Delta - E_{rec,m} \tag{1.1.24}$$

$$E_{rec,m} = \frac{\Delta^2 - m_e^2}{2m_i} \tag{1.1.25}$$

$$\beta = \sqrt{1 - \frac{m_e^2}{E_\beta^2}}. \tag{1.1.26}$$

From energy conservation follows:

$$E_\nu = \Delta - E_\beta - E_{rec}. \tag{1.1.27}$$

The Dalitz distribution of the cosine of the angle θ between the momenta of the beta particle and the neutrino [Glu98]

$$c_{e\nu} := \cos\theta = \frac{m_i(E_{\beta max} - E_\beta) - E_\nu(m_i - E_\beta)}{\beta E_\nu E_\beta} \tag{1.1.28}$$

can be written as [Jac57]:

$$W_0(E_\beta, c_{e\nu}) = F(A, Z) p_\beta E_\beta E_\nu^2 \cdot (1 + a\frac{p_\beta}{E_\beta} c_{e\nu} + b\frac{m_e}{E_\beta} + h.o.) \tag{1.1.29}$$

where *h.o.* denotes higher order terms, with will be neglected in the following. In this formula a is the beta neutrino angular correlation coefficient and b is the Fierz interference coefficient. In the SM the Fierz interference coefficient is assumed to be $b = 0$. $F(\pm Z, E_\beta)$ is the Fermi function for electrons (upper sign) respectively positrons (lower sign) (see e. g. [Bla52]). Combining the above formulae 1.1.18, 1.1.22, 1.1.23 and 1.1.29 we find the following expression for the recoil energy spectrum:

$$R_0(E_{rec}) = \int_{E_{\beta,min}}^{E_{\beta,max}} dE_\beta \cdot F(A, Z) p_\beta E_\beta E_\nu^2 \cdot \left(1 + a\frac{p_\beta}{E_\beta} c_{e\nu} + b\frac{m_e}{E_\beta}\right) \cdot \frac{m_i(E_{\beta m} - E_\beta)}{\beta E_\nu E_\beta} \tag{1.1.30}$$

On the basis of this formula we generated recoil energy spectra for the β^+ decay of ^{35}Ar to ground state ^{35}Cl for two different values of $a = 0$ and $a = 1$. These we compared with two corresponding spectra we received from the author of refs. [Glu93, Glu98], to ensure the correct operation of the calculation routine. These are shown in fig. 1.1. The solid blue and red lines are spectra from

the author of refs. [Glu93, Glu98], the black data points have been calculated by ourselves. Both methods are in agreement. The author of of refs. [Glu93, Glu98] made a comparison between his simulated recoil energy spectra and measured data from ref. [Joh63] (see also sec. 1.2) where he found agreement up to a level where radiative corrections plays a role.
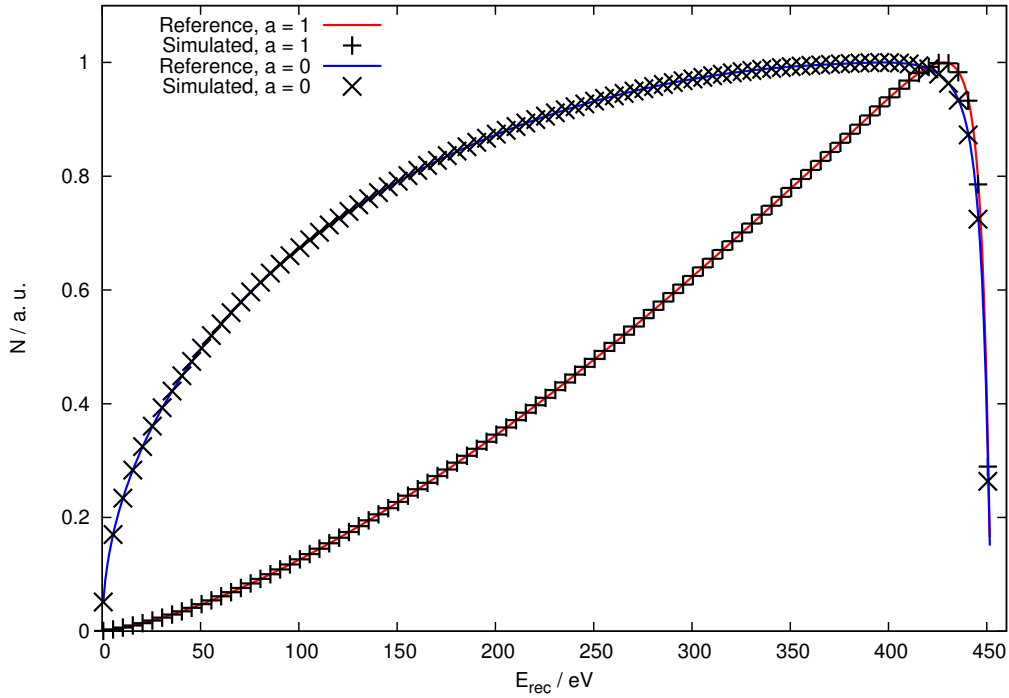
Figure 1.1.: Generated recoil energy spectra for the beta decay of ^{35}Ar to the ground state of ^{35}Cl for two different values of $a = 1$ (red line and + like data points) and $a = 0$ (blue line and x like data points). The blue and the red lines have been simulated by the author of refs. [Glu93, Glu98]. The black points have been simulated by our own routine. We can see a very good agreement between both.

Our generated spectra will be used for the data analysis in part. II of this thesis as input for tracking simulations. A fit function will be comprised out of the simulation results, which will be fit to experimental data to extract a value for a.

1.2. State of the art

The beta neutrino angular correlation has been addressed already by various experiments and there is still a high interest in such measurements to date. A handful of experiments are now in the data taking phase. Modern experiments almost all use ion traps (Paul or Penning traps), atom traps (Magneto Optical Trap (MOT)) or cold or ultra cold neutron beams. Probably the most outstanding experiment on this field is the measurement of C. S. Johnston from back in 1963 which still provides the best limit on the tensor interaction today. In the following section we will give an historical overview and discuss the state of art in this field of research.

1.2.1. Bygone experiments

In 1963 C. S. Johnson et al. measured the recoil energy spectrum from the pure Gamow-Teller decay of ^{6}He. The ^{6}He ions were produced by a reactor in the reaction ^{9}Be(n,α)^{6}He. Using an electromagnetic $\frac{m}{q}$-analyzer. They were able to extract a in that decay with a relative precision of about 1%: $a = (-0.3343 \pm 0.0030)$. Their result remains until today as the most stringent limit on the tensor coupling constant: $\frac{|C_T|^2 + |C_T'|^2}{|C_A|^2 + |C_A'|^2} \leq 0.4\%$ [Joh63].

By analyzing the effect of lepton recoil on the shape of the narrow proton group following the superallowed $0^+ \longrightarrow 0^+$ decay of ^{32}Ar, a group at the ISOLDE was able to determine a in this decay with a relative precision of about 1%: $a = 0.9989 \pm 0.0052 \pm 0.0036$ [Ade99]. Following an improvement in the measurement of the Q-value for the ^{32}Ar decay the value was later changed to $a = 1.0050(52)$ [Bla03].

1.2.2. Present experiments

The best limit on scalar interaction to date comes from a measurement on ^{38m}K with the TRINAT MOT trap at TRIUMF, with $a = 0.9981(30)(32)$ [Gor05]. Here the recoil ions were detected in coincidence with the beta particle and the time-of-flight (TOF) of the recoil ions was measured.

A similar coincidence measurement is used by the LPC trap experiment at GANIL, Caen [Rod06]. Instead of a MOT a Paul trap is used as a scattering-free source. Their analysis of a first measurement of the recoil energy spectrum from the decay of ^{6}He from 2006 was published in 2011 [Fle11], yielding $a = -0.3335(73)(74)$, which is just below the Johnston et al. result from 1963 [Joh63]. In 2008 the measurement was repeated to collect enough statistics (about 20 times more) to decrease the statistical error bars below the value of Johnston et al. [Lie11]. The data analysis for this is still ongoing.

In a collaboration with the WITCH experiment in 2011 a measurement of the recoil energy spectrum of the decay of ^{35}Ar by the LPC trap was performed. Moreover this measurement yields the relative charge state distribution of the daughter nucleus and the shake-off probability [Gor12]. This result will be used in the data analysis described in part II of this thesis, for the least square fit of the recoil energy spectrum.

Currently a new setup, called **W**eizmann **I**nstitute **R**adioactive **E**lectrostatic **D**evice (WIRED), is being installed at the Weizmann Institute of Science in Rehovot, Israel, to perform a precision measurement of the β–ν correlation from ^{6}He. The ^{6}He$^+$ radioisotopes are produced by neutron induced reactions and an electron ion beam trap (EBIT) for ionization.The ^{6}He$^+$ radioisotopes will be stored in a second electrostatic ion beam trap (EIBT). The position and time-of-flight of the recoil ^{6}Li^{++} are measured on a position sensitive microchannel plate (MCP) detector [Avi12]. In the aSPECT experiment cold neutrons, produced at the ILL in Grenoble, are used to measure the beta neutrino angular correlation coefficient a in the decay of the free neutron. Like in the WITCH experiment, a MAC-E filter retardation spectrometer is used to probe the kinetic energy of the protons after the neutron decay. A first published result is $a = -0.1151(40)$ [Bae08], with purely

statistical uncertainties. Systematic effects of the experiment are currently under investigation. Probably the largest contribution is due to the neutron half-life. For 2013 a new beam time was commissioned recently to aim for a relative precision of $1 - 2\%$ [Bec12].

Another experiment that aims for a precise determination of a ($< 1\%$ relative uncertainty) in the neutron beta decay by a different method proposed 1996 by Yerozolimsky and Mostovoy [Yer04], is the aCORN experiment. Electrons and recoil protons from neutron decay in a cold beam are detected in coincidence. The momenta of the particles are selected so that the protons form two kinematically distinct time-of-flight groups as a function of electron energy. The count rate asymmetry in these two groups is proportional to a. Precision spectroscopy of the protons is not required [Wit09]. It is currently integrated and tested at the Indiana University Cyclotron Facility (IUCF) and then will be moved to the NIST Center for Neutron Research for the initial physics run. The beginning of the data taking is planned for 2013 [Bec12].

The Berkley MOT trap experiment, published their first result for a of the decay of ^{21}Na, $a = 0.5243(91)$ [Sci04], with is almost four standard deviations off the SM value $a = 0.5587(27)$ [Sev08]. The reason for this turned out to be the formation of molecular sodium which influences the recoil energy distribution. An investigation of this effect followed by a new measurement, produced a value of $a = 0.5502(60)$ [Vet11] which is in good agreement with the SM prediction.

The β-decay Paul trap at the Argonne National Laboratory in Illinois, USA, is recently under commissioning. In a first approach the experiment aims to measure the the $\beta - \nu$ angular correlation in the beta decay of ^{8}Li by inferring the momentum of the neutrino from the kinematic shifts impart to the breakup α particles. The trap electrodes are designed in such a way that they allow a variety of detector systems to be installed at the same time which surround the stored ion cloud. The layout of the experiment allows many other β decay studies [Sci12].

1.3. The setup of the WITCH experiment

The WITCH experiment is set up in the experimental hall of the **I**sotope **S**eparator **ONL**ine **DE**vise (ISOLDE) which is located at the European Organization for Nuclear Research (in french: Organisation européenne pour la recherche nucléaire, formerly named **C**onseil **E**uropéen pour la **R**echerche **N**ucléaire (CERN)). In a first approach the experiment wants to measure the recoil energy spectrum of the daughter nuclei after the β^+ decay of ^{35}Ar. The measured spectrum will be used to extract a value of a. In the letter of intent a precision of $\frac{\Delta a}{a} \leq 0.5\%$ is mentioned as goal [Bec03].

Once the initial goal has been reached, the design of the experiment and the location allow to proceed with further studies, particularly owning this to its versatile layout. The following key features are characteristic for the experimental setup of WITCH and the ISOLDE isotope separator where it is located:

- The ISOLDE facility can deliver approx. 600 different isotopes from over 60 different elements.

- The application of two Penning traps allows practically any type of ion to be stored in while providing a scattering-free source.

- The MAC-E filter spectrometer can probe the full range of recoil energies, with a low background rate, good energy resolution and high angular acceptance.

- In combination with the post-acceleration and focussing devices of the spectrometer, the position sensitive microchannel plate detector with delay line anode is applicative for the detection of any type of recoil ions with high efficiency.

In this section we discuss the experimental setup of the WITCH experiment. We start with a brief overview of the CERN research facility and concentrate on the infrastructure associated with our experiment. After giving an overview of the ISOLDE online facility we discuss the individual stations of the WITCH setup.

The setup of the WITCH experiment is located in the experimental hall of the ISOLDE facility. The ISOLDE online isotope separator and its experimental hall resides on the main area of the CERN. The ISOLDE separator uses 1.4 GeV protons to create a large variety of isotopes through spallation, fragmentation and fission by shooting them on different types of target materials. These protons are first accelerated in the **LIN**ear **AC**celerator (LINAC) with an initial energy of 50 MeV and afterwards transferred to the **P**roton **S**ynchrotron **B**ooster accelerator (PSB) which increases the energy of the protons to 1.4 GeV before they are transferred to the ISOLDE experimental hall respectively the **P**roton **S**ynchrotron (PS) which increases the energy of the proton further to be used by other experiments.

1.3.1. The ISOLDE facility

The ISOLDE (**I**sotope **S**eparator **O**n**L**ine **D**evice) is an online isotope separator. Proton bunches with a time separation of 1.2 s, an energy of 1.4 GeV and an average intensity of about 2 μA coming from the PSB are shot onto a target. From spallation, fragmentation or fission reactions, a variety of elements is created. By means of surface ionization, electron impact in a plasma or laser resonant ionization of the atoms a radioactive beam is extracted from the mixture. Through inventing many different target-ion-source combinations it is possible to chose from more than 600 different isotopes from over 60 different elements with masses ranging from $^{6}_{2}$He to $^{232}_{88}$Ra. Accessible intensities reach from 1 up to 10^{11} atoms per proton bunch [Kug00].

Two mass separators are available to extract the designated nucleus from the mixed ion beam: The GPS (**G**eneral **P**urpose **S**eparator) and the HRS (**H**igh **R**esolution **S**eparator). The GPS has
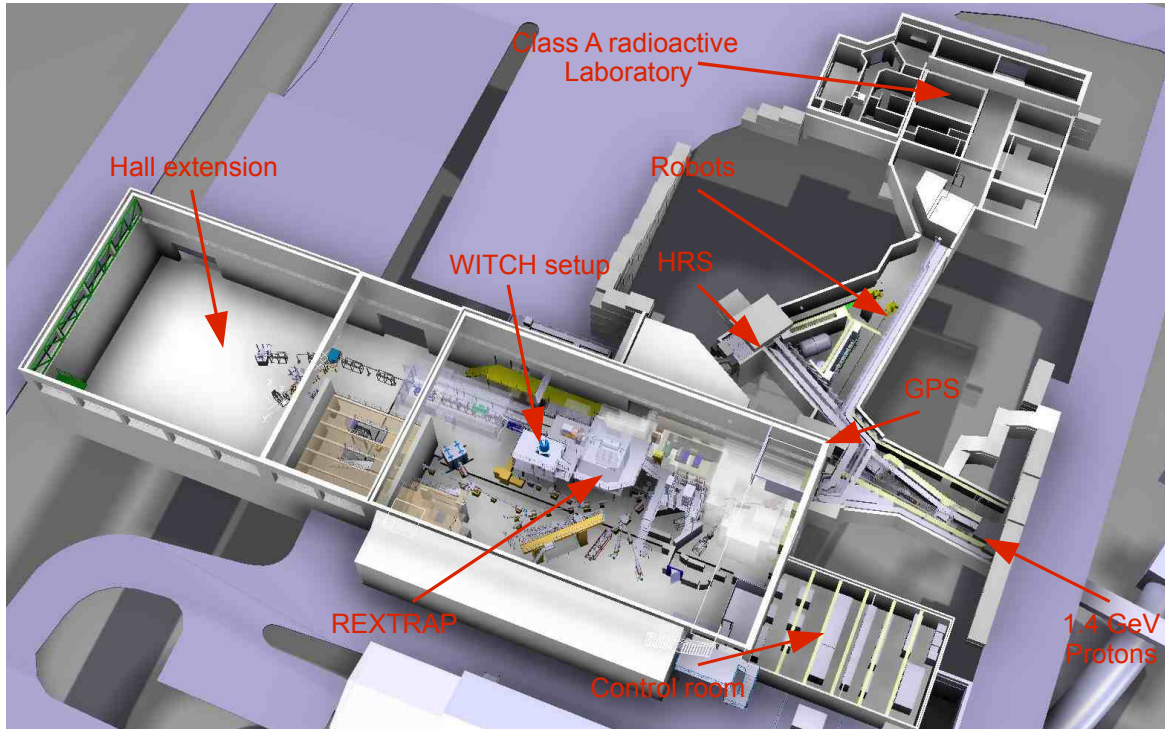
Figure 1.2.: Overview of the ISOLDE online isotope separator facility. The main features of the separator facility are highlighted with red arrows. The positions of he WITCH setup and REXTRAP are shown as well. The 1.4 GeV protons are coming from the bottom right corner. The CAD drawing was taken from ref. [Iso12].

a mass resolving power of $\frac{\Delta m}{m} \approx \frac{1}{1000}$ and is able to serve up to three experiments at a time. The HRS with a mass resolution of $\frac{\Delta m}{m} \approx \frac{1}{5000}$ can deliver beam to only one user at a time.

The prime physics candidate for the WITCH experiment is ^{35}Ar, a noble gas. It has a high electron affinity.[1] Finally the continuous ion beam is emitted with an energy of 30 keV. Preposed to the WITCH experiment is REXTRAP, a cooler and buncher Penning trap, used to transform the continuous ISOLDE beam into bunches.

1.3.2. REXTRAP

REXTRAP is a long Penning trap, which is used to manipulate the continuos radioactive ion beam and the first element for the beam preparation for WITCH. It consists of a 1.3 m long trap electrode system hosted inside a 3 T superconducting magnet. Before and after the actual Penning trap are a deceleration and an acceleration part. They both consist of several lenses and steerer electrodes to optimize the injection and ejection of the ion beam. The Penning trap itself consists of about 30 electrodes with inner diameters of 40 mm. The inner ring electrode is segmented into eight parts which allows to apply different excitations. The whole electrode structure is mirror symmetric with respect to the trap center. The whole Penning trap is on 30 kV[2] with respect to ground potential and is hosted inside a HV cage [Ame05].

---

[1]The singly charged ^{35}Ar$^+$ ions are sensitive to charge exchange whereby, if the vacuum in the Penning traps and beam line system is not good enough, the ions become neutralized an get lost.

[2]The ISOLDE separator is on 30.2 keV with respect to ground potential. When the ions are injected into REXTRAP about 200 eV kinetic energy are lost in collisions with the buffer gas. The ions which are ejected from REXTRAP into the WITCH beam line system (which is on ground potential) with 30 keV.

The ions injected into the Penning trap first interact with the buffer gas in a high pressure region. Through the high buffer gas pressure of 10^{-3} mbar the ions loose enough energy to be trapped in the potential minimum in the trapping region. Here the buffer gas pressure is about an order of magnitude lower and rotating wall and sideband excitations can be applied [Ame05]. Afterwards the cooled ion bunches are emitted to the WITCH beam line system with a time separation of 0.3 s.

For offline tests a surface ion source is installed in front of REXTRAP that can deliver ^{39}K, ^{41}K, ^{85}Rb, ^{87}Rb or ^{133}Cs ions. In ref. [Gor12] a more detailed description along with potential settings used in two radioactive WITCH runs in 2011 can be found.

1.3.3. The WITCH beam line

The bunched ion beam coming from REXTRAP is guided via the **H**orizontal **B**eam **L**ine (HBL) of WITCH. Fig. 1.3 shows an overview of the electrodes and diagnostics of the HBL. The naming conventions of the individual divides are explained in the figure caption.
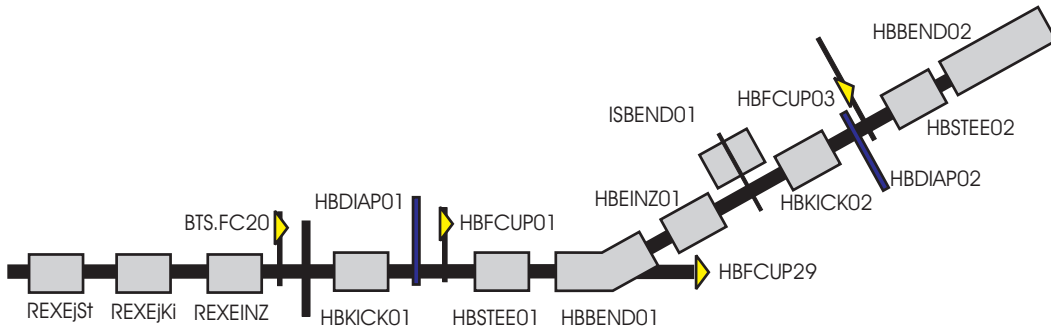

Figure 1.3.: Schematic overview of the electrodes and diagnostics of the HBL, taken from ref. [Coe07b]. The REXTRAP ejection steerer and kicker electrodes REXEjSt and REXEjKi, the einzel lens REXEINZ and the last Faraday cup (BST.FC20) are shown as well. The further naming conventions are as follows: HB means *horizontal beam line*, IS means *ion source* and REX *REXTRAP*. BEND stands for *bender electrode*, KICK for *kicker electrode*, STEE for *steerer electrode*, FCUP for *Faraday cup* and DIAP means *diaphragm*. The numbers increase subsequently in direction of the ion beam. The kicker electrode HBKICK01 serves as a beam gate for the WITCH setup. The whole HBL is a single vacuum section, typically at a pressure of $2 \cdot 10^{-2}$ mbar [Gor12].

A surface ion source, combined with a small radio frequency quadrupole (RFQ), serves as an offline ions source [Tra11], which enables a self-sufficient operation of the WITCH setup for tuning and test purposes. The 90°-bender ISBEND01 is used to insert the ions from the RFQ. The last bender electrode injects the ion beam into the VBL. A set of voltage settings for the HBL electrodes used in two radioactive runs in 2011 can be found in ref. [Gor12].

Fig. 1.4 shows an overview of the electrodes and diagnostics of the **V**ertical **B**eam **L**ine (VBL). The naming conventions are given in the figure caption. The VBL consists of a pulsed drift tube (PDT) followed by a set of steerer and focussing electrodes that are used to inject the ion bunches into the strong magnetic field of the trap magnet. The PDT lowers the total energy of the ion bunches from 30 keV to below 200 eV, which allows to capture the ions in the cooler Penning trap. While the ion bunch is passing through the PDT, which has a length of 693 mm and a typical time acceptance of 2.8 μs, the electrode is switched from 21 kV to -9 kV, which leaves the ions
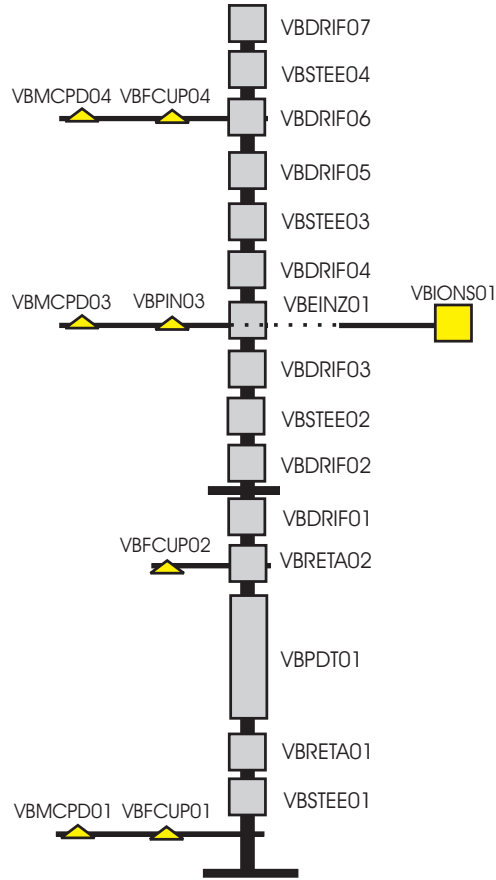
Figure 1.4.: Schematic view of the electrodes and diagnostics of the VBL taken from ref. [Coe07b]. The naming conventions are as follows: VB means *vertical beam line*, BEND stands for *bender electrode*, KICK for *kicker electrode*, STEE for *steerer electrode*, DRIF for *drift electrode*, RETA for *retardation electrode*, for *ion source*, MCPD for *microchannel plate detector* and FCUP for *Faraday cup* and DIAP means *diaphragm*. VBIONS01 is a cross beam ions source for $^{40}Ar^+$ ions (see ref. [Bak11] for details). The numbers increase subsequently in direction of the ion beam.

with about 9 keV kinetic energy [Coe07]. By means of a subsequently increasing potential the ions kinetic energy is further reduced allowing them the enter the cooler trap with about 200 eV kinetic energy. A detailed description of the working principle of the PDT can be found in ref. [Coe07]. Improvements of the PDT resistances allowed to operate the PDT with frequencies up to 10 Hz [Tan11]. At the position VBIONS01 (see fig. 1.4) a cross beam ions source for $^{40}Ar^+$ ions is installed. A detailed description and characterization of this device can be found in ref. [Bak11]. A set of voltage settings for the VBL electrodes used in two radioactive runs in 2011 can be found in ref. [Gor12].

1.3.4. The double Penning trap system

The WITCH experiment uses a double Penning trap system for preparation and storage of the radioactive ions. These two cylindrical Penning traps are almost identical in construction. Each one consists of three upper and three lower end cap electrodes, four correction electrodes and a

central ring electrode. The central ring electrodes are each divided into eight segments, giving the possibility to apply excitations to the stored ion cloud. The lower trap, the cooler trap, disposes a gas inlet system to cool the trapped ions by means of collisions with the buffer gas atoms. The upper trap, called the decay trap, misses the most upper end cap electrode compared to the cooler trap conditional upon construction issues [Bec12]. The two traps are interconnected by a differential pumping diaphragm.

All trap electrodes have an inner diameter of 40 mm and an outer diameter of 44 mm and are interconnected by PEEK insulators (Polyetheretherketon, specific contact resistance at 23°C: $\rho_{23} > 10^{14}\,\Omega$ cm, specific surface resistance at 23°C: $\rho_{s\,23} > 10^{13}\,\Omega$/sq, taken from ref. [Qua13]). The pumping diaphragm has an inner diameter of 2.5 mm. The cooler trap has a total length of 190 mm, the pumping diaphragm has a length of 54 mm and the decay trap has a length of 184 mm. The whole construction is held together by a mounting structure made from titanium. The total length of this construction is 529 mm.
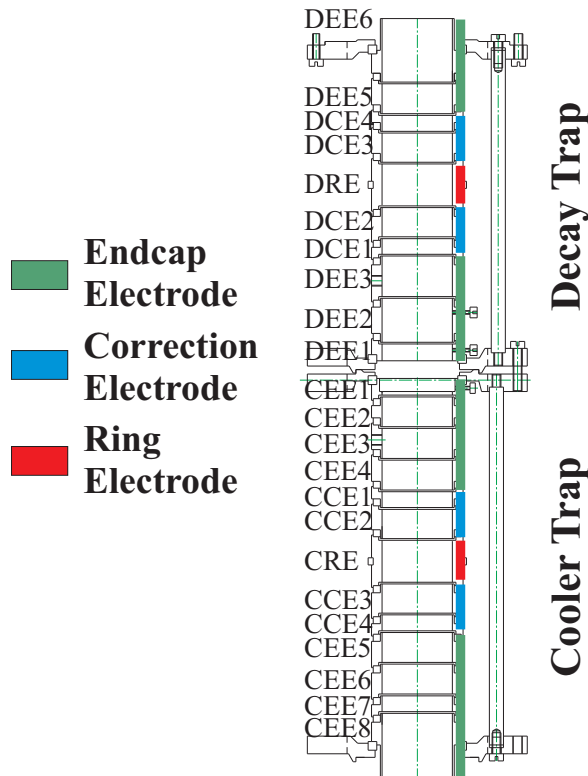
Figure 1.5.: Schematic drawing of the double Penning trap system, along with the correct labeling of the electrode names. Naming conventions are as follows: C means *cooler trap*, D *decay trap*, EE stands for *end cap electrode*, CE for *correction electrode* and RE for *ring electrode*. For some reason the differential Pumping diaphragm between the two traps is not shown in this figure. Taken from ref. [Tan11a].

Fig. 1.5 shows a schematic drawing of the double Penning trap system (taken from ref. [Tan11a]), along with the correct labeling of the electrode names. Naming conventions are described in the caption of fig. 1.5. The differential pumping diaphragm was omitted in this figure. For some reason

it was decided to decrease the numbering of the electrodes of the cooler trap in beam direction and increase it for the decay trap [Bec12].

The applied potentials and timings are set by a FPGA card (**F**ield **P**rogrammable **G**ate **A**rray) and two power supplies which are integrated in the WITCH control system [Tan11]. A more detailed description of the mechanical design, the electronic layout, the buffer gas system and the general trapping can be found in ref. [Gor12]. This reference also provides information about Penning trap simulations especially made for this system. A description of the trapping cycle used in the October beam time in 2011 will be given in Part II.

1.3.5. The MAC-E filter spectrometer

Fig. 1.6 shows an overview of the MAC-E filter spectrometer along with the double Penning trap system and the post-acceleration and detection section. Explanations are given in the caption for fig. 1.6.

To probe the kinetic energy of the recoil ions a so-called MAC-E filter [Lob85, Pic92] spectrometer is used. The decay volume (in our case it is the ion cloud in the decay trap) is hosted in a strong magnetic field (normally the trap magnet is operated at $B_{trap} = 6$ T but can in principle provide field strengths up to 9 T). The recoil ions after decay which are emitted into the upper 2π escape into the spectrometer where the magnetic field strength is reduced successively to a value of $B_{spec} = 0.1$ T. Since the change in the magnetic field strength is slow, the momentum vector transforms adiabatically and the magnetic momentum is constant:

$$\mu = \frac{E_\perp}{B} = const. \qquad \Rightarrow \qquad \frac{E_{\perp,\,ini}}{E_{\perp,\,fin}} = \frac{B_{trap}}{B_{spec}} \tag{1.3.1}$$

where B_{trap} and B_{spec} are the magnetic fields at the position of the decay volume and in the spectrometer, $E_{\perp,\,ini\,/\,fin} = \frac{\vec{p}_{\perp,\,ini\,/\,fin}^2}{2 \cdot m}$ where $\vec{p}_{\perp,\,ini}$ is the transversal momentum of the recoil ion with respect to the magnetic field line vector at the position of the source (indexed ini) respectively in the spectrometer (indexed fin) and m is the mass of the recoil ion. By applying a retardation potential U_{ret} in the spectrometer it is possible to probe the longitudinal kinetic energy:

$$E_{rec\,||} = \frac{\vec{p}_{||}^2}{2m} = E_{rec,\,tot} - E_{rec,\perp,\,fin} = E_{rec,\,tot} - \frac{B_{spec}}{B_{trap}} E_{rec,\perp,\,ini} > q \cdot U_{ret} \tag{1.3.2}$$

so that ions which fulfill this condition can pass the retardation potential maximum and are focused onto the detector. This leads to a step-like integral transmission function for a MAC-E filter spectrometer with $0\% - 100\%$ rise ΔE (see below for definition of ΔE) [Pic92]:

$$T_{MAC-E}(E_{rec}, U_{ret}) = \begin{cases} 0 & \text{for} \quad E_{rec} < q \cdot U_{ret} \\ \left(1 - \sqrt{1 - \left(1 - \frac{qU_{ret}}{E_{rec}}\right)\frac{B_{trap}}{B_{spec}}}\right) & \text{for} \quad qU_{ret} < E_{rec} < \frac{qU_{ret}}{\left(1 - \frac{B_{spec}}{B_{trap}}\right)} \\ 1 & \text{for} \quad E_{rec} \geq \frac{qU_{ret}}{\left(1 - \frac{B_{spec}}{B_{trap}}\right)} \end{cases} \tag{1.3.3}$$

From the extreme case, when the recoil ion in the decay volume is emitted perpendicular to the magnetic field lines, $E_{\perp,\,ini} = E_{rec}$, one can deduce the energy resolution of the MAC-E filter spectrometer:

$$\frac{\Delta E_{rec}}{E_{rec}} = \frac{B_{spec}}{B_{trap}} = \frac{0.1\,\text{T}}{6\,\text{T}} \approx 1.6\% \tag{1.3.4}$$

From the decay trap towards the spectrometer the retardation potential is increased stepwise

Figure 1.6.: Schematic cross section of the electrode and magnet geometry of the WITCH Spectrometer including the traps as it is implemented in the tracking simulations and field calculations. The whole geometry except of the anti-ionization wire is cylinder symmetrical with respect to the x-axis. The spectrometer electrodes, the magnets and the MCP detector are labeled with the names. SPDRIF01 is a segmented electrode consisting of several ring elements. Concerning the labeling of the trap electrodes please refer to fig. 1.5. Retardation electrodes are colored in orange, drift and acceleration electrodes are colored in blue, the einzel lens electrode in purple and the trap electrodes and the cryostat are colored in black. The magnets and the MCP detector are indicated in red. The individual retardation electrodes and trap segments cannot be distinguished in this figure. The anti-ionization wire is drawn in the plot as well.

by seven retardation electrodes. To the sixth and the seventh retardation electrodes the maximum retardation potential is applied. An anti-ionization wire has been installed right behind the analysis plane – the position in the plateau region of the spectrometer with $B_{spec} = 0.1$ T, where the retardation potential reaches its maximum. Due to this local potential maximum and the residual magnetic field this section acts like a Penning trap for electrons. The anti-ionization wire absorbs stored electrons which pass the volume of the wire due to the magnetron drift. The primary design of such a wire for use in the KATRIN experiment, which can be moved transfers to the beam direction, is describe in ref. [Bec10].
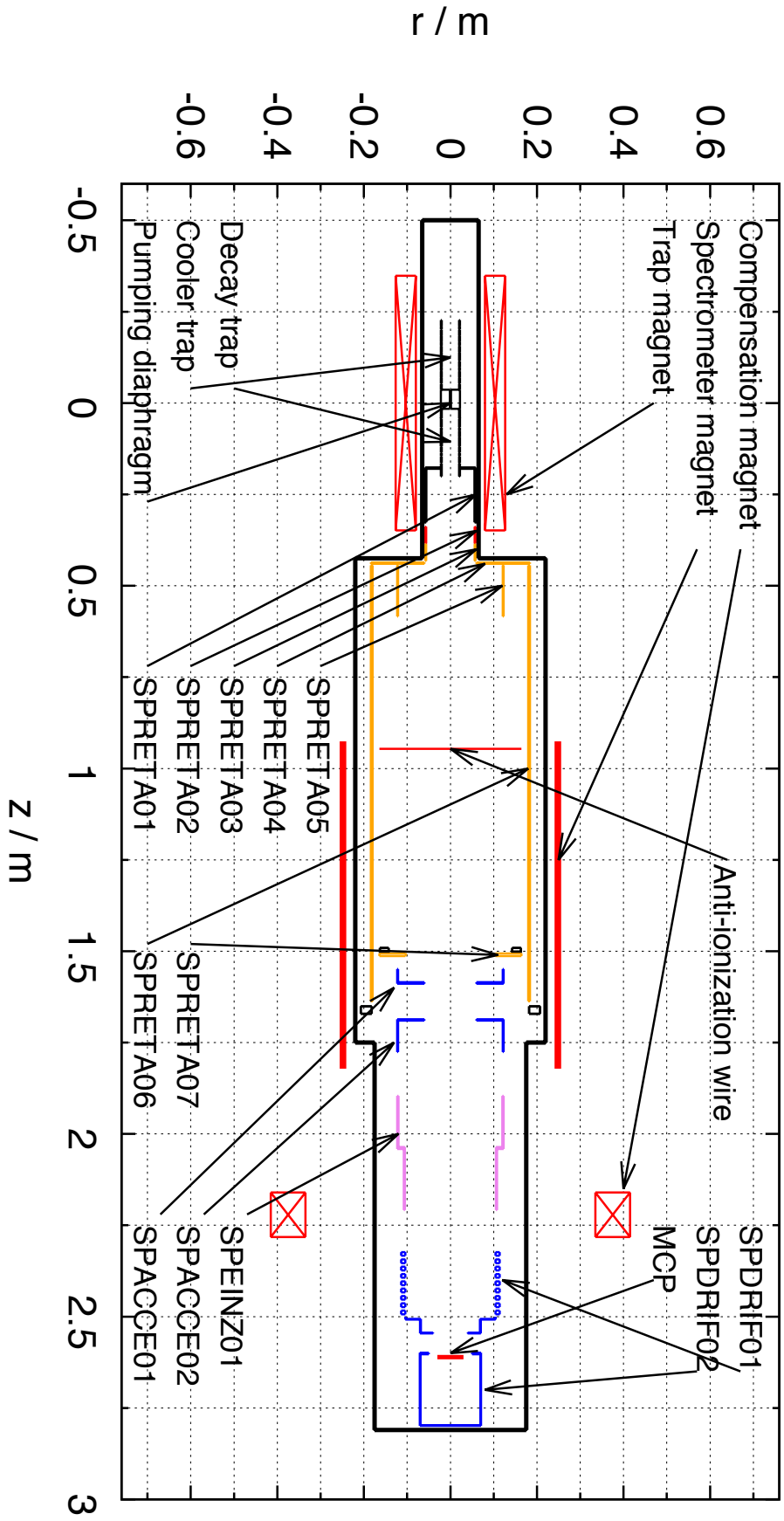
In fig. 1.6 a schematic cross section of the electrode and magnet geometry of the WITCH Spectrometer including the traps as it is implemented in the tracking simulations and field calculations is shown (see sec. 3.3). Please notice that the whole geometry is cylinder symmetrical with respect to the z-axis. The spectrometer electrodes, the magnets and the MCP detector are labeled with the names. Naming conventions are according to ref. [Del05]: *SP* is for *spectrometer*, *RETA* is for *retardation electrode*, *ACCE* stands for *post-acceleration electrode*, *EINZ* for *einzel lens electrode* and *DRIF* for *drift electrode*. The enumeration increases in the direction in which the ions fly.

1.3.6. The post-acceleration section and the position sensitive microchannel plate detector

Ions whose longitudinal energy at the position of the retardation potential maximum is large enough to overcome it, are afterwards re-accelerated to several keV which is necessary for detection with a microchannel plate detector. Furthermore an electrostatic einzel lens is used to focus the ions on the detector.

The WITCH experiment uses a position sensitive microchannel plate detector with delay line anode readout. The active diameter of this detector system is about 80 mm. The manufacturer of the detector hardware is Roentdek (model *DLD80*) and the microchannel plates used in this setup are manufactured by the company Photonis (*Longlife* Series). More details of the position sensitive microchannel plate detector and data acquisition system of the WITCH experiment will be given in part I of this thesis, along with information on the calibration measurement.

Part I.

Setup and calibration of a new position sensitive microchannel plate detector

Setup and calibration of a new position sensitive microchannel plate detector

In the WITCH experiment a position sensitive detector is needed to detect recoil ions with energies of about 100 eV to 1 keV, masses of 10 u to 150 u and charge states of +1 e up to +5 e. For such a purpose the options are limited. Semiconductor detectors have a dead layer of about 0.2 μm [Egg05], which is sufficient to stop almost all recoil ions which will then not be detected. The disadvantage of a scintillator detector is that it doesn't provide position information. The best option seems to be a microchannel plate detector with delay line anode read-out.

Microchannel plates (MCPs) are known for their high efficiency in the detection of ions with energies of several keV. The application of a delay line anode allows to record the position information with a resolution typically in the order of 0.1 mm [Roe11, Lie05]. Recoil ions at the WITCH experiment usually have energies of several 100 eV. A post-acceleration potential -3.2 kV applied to the front MCP surfaces accelerates the recoil ions to an energy of $q \cdot 3.2$ keV, where q is the electric charge of the ion. A disadvantage is that MCPs can have inhomogeneous gain factors. In combination with a certain discriminator threshold this can result in an inhomogeneous detection efficiency. Therefore it is necessary to calibrate the position dependent detection efficiency of our detector.

To record the position of a detected event, a delay line anode is used in our detector setup. A delay line creates a time delay as function of the position but only in one dimension. Using a second delay line perpendicular to the first one can create a two-dimensional image. Delay lines are know for their good spatial resolution.

In 2010 the old position sensitive MCP detector was replaced by a new one with a larger diameter. The old detector, with an active diameter of 40 mm, could not detect all ions from a measurement of an ^{35}Ar recoil spectrum as tracking simulations had shown. Its MCP had reduced efficiency in the center such that it was almost blind in that region. Apart from this the old detector was a loan from the LPC-Trap experiment at CAEN which had to be returned.

Initially the signal processing was done like for the old detector, where the delay line signals have been decoupled by capacitors in the vacuum and processed by the use of pulse transformers. The signals were afterwards lead via 50 Ω coax cables to a BNC (Bayonet Neill-Concelman) feedthrough. These coax cables have been identified as a serious source for problems. They were insulated with a mesh of tiny copper wires, where easily small pieces could fall off and turns into conductive dust particles. This dust could shortcut the delay line anode and disable the position read-out (see 2.2.2).

This problem was solved by replacing the signal decoupling with the standard solution provided

by the manufacturer and paying particular attention to a clean working environment. This also improved the signal quality. Incidents with shortcut delay line anodes have become rare since then and a stable mode of operation has been shown over time periods of severals weeks and even months.

In this chapter we describe the setup and handling of the new position sensitive MCP detector along with its components. We discuss the calibration procedure and results: In particular a test of the relative detection efficiency as function of the position, estimation of the absolute detection efficiency and an investigation of the position resolution of our detector.
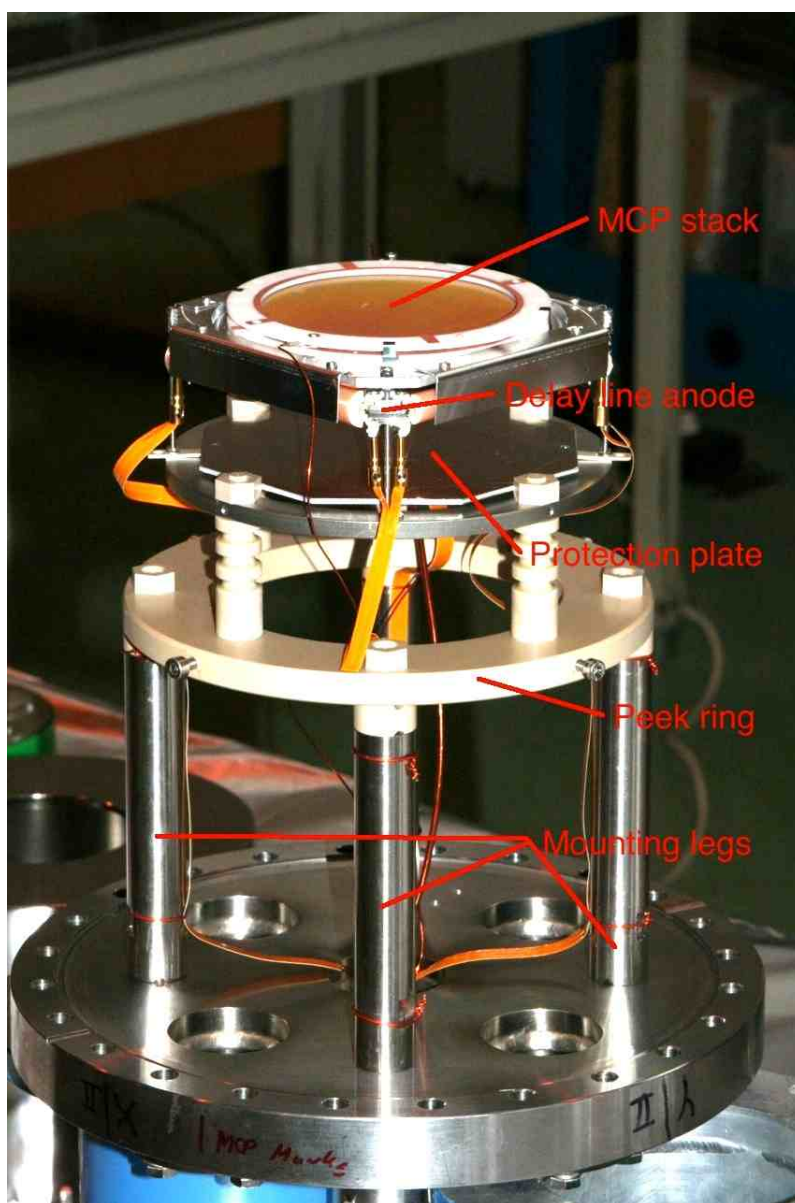
Figure 2.1.: Setup of the MCP detector shown upside down compared to when it is installed hanging from the top of the spectrometer. The surrounding electrode SPDRIF02 has been removed. On top are the MCPs arranged in a Chevron stack. Below the MCPs, the delay line anode is mounted. The backside of the delay line is protected by a metal plate. This part of the detector is mounted on a Peek ring, which is attached with four legs to the detector flange. Connections for voltage supply and signals are led to a 12 pin feedthrough on the bottom.

2.1. Introduction

The WITCH MCP detector is installed on top of the retardation spectrometer. It is oriented upside down such that the surface normal of the front MCP points inside the spectrometer. Behind the stack of two MCPs a delay line electrode is located that provides the position information. An aluminum plate protects the backside of the delay line anode. To insulate the detector from the mounting legs attached to the flange it is placed on four legs attached to a ring that is made from Peek. The detector is surrounded by an electrode called SPDRIF02 (see figs 1.6 and 2.18 for an illustration and a picture of that electrode), that is attached with four screws to the Peek ring. A hole inside that ring allows to lead the signal and voltage supply cables to a CF-40 12 pin feedthrough mounted in the center of the CF-200 detector flange. A second CF-40 feedthrough holds the SHV-10 connector for the voltage supply of the SPDRIF02 electrode. Fig. 2.1 shows a picture of the detector flange with the MCP detector but without the electrode SPDRIF02.

A **M**icro **C**hannel **P**late (MCP) consists of between a several hundred thousand up to a few million channels. Each channel acts as a separate electron multiplier. An incoming ion hitting the wall of a microchannel can create secondary electrons. By applying a potential difference in the order of 1 kV, the electrons are accelerated towards the channel's end and collide several times with the channel wall. In each collision further secondary electrons are created. This results in an electron avalanche, like in a photomultiplier tube or in a channeltron, like it is illustrated in fig. 2.2.
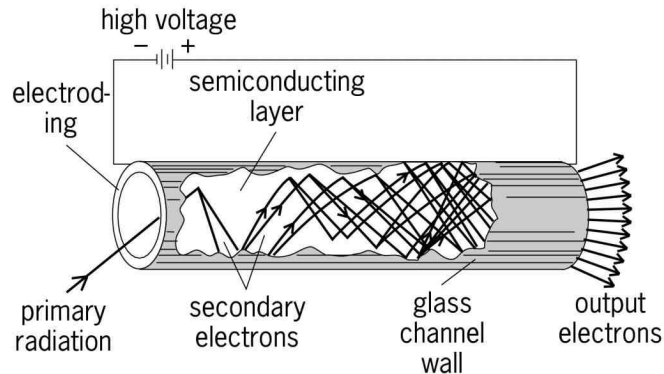
Figure 2.2.: The principle of the microchannel plate taken from ref. [Wiz09]. An incoming particle hitting the channel wall creates a secondary electron. By applying a voltage difference of approx. 1 kV between the front and end of the channel, the electron is accelerated towards the end. In further collisions additional secondary electrons are created and so the signal from the initial particle will be amplified.

The **D**elay **L**ine **A**node (DLA) converts a position information into a difference in the propagation time of a signal in a wire to its ends. The DLA is placed below the MCP. It consists of a wire convoluted to a coil. The electron cloud leaving the MCP channel hits the coil at a certain position. This creates a signal that travels to both ends of the coil. From the relative time difference of the arrival times one can calculate the position on the coil in one dimension. This is illustrated in fig. 2.3. Using a second coil perpendicular to the first one, a two-dimensional position can be reconstructed.

RoentDek
Handels GmbH

Figure 2.3.: The principle of the delay line taken from ref. [Roe11]. The electron cloud from the amplification process in the MCP arrives on a wire underneath the MCP stack and cre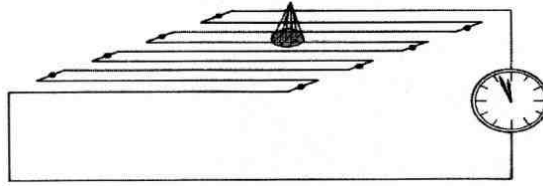ates a signal. This travels to both ends of the delay line. From the relative time difference of the signals one can calculate the position on the wire.

2.2. The MCP detector setup

The MCP detector consists essentially of a stack of MCPs, the delay line anode and electronics for the signal processing. The software used for the data acquisition is integrated in the so-called WITCH CS and will not be discussed here[1]. More information on this can be found in [Tan11]. An electrode which surrounds the detector has been re-machined and electropolished to minimize the risk of discharges in the spectrometer. The high voltage for the detector is supplied via a voltage divider.

2.2.1. The microchannel plates

A MCP is manufactured from a cluster of fibers made out of lead glass to obtain some conductance that are stretched and such shrinked in diameter. These fibers are embedded in a glass substrate which holds them together. By cutting slices from this, thin plates with multiple small channels are created. A protective edge of glass allows better handling of the plate and adds stability.

The MCPs of our detector are from the *Long Life Series* of *Photonis*. The surfaces of the MCPs are coated with multiple layers. A 1 nm thin emissive layer of doped SiO_2 is placed on a 20 nm substrate of SiO_2 with a 200 nm conductive layer of NiCr underneath (see fig. 2.4). The detailed composition of the emissive layer is kept secret by the manufacturer. Fig. 2.4 illustrates the coating of the MCPs [Roe12]. The channel walls are chemically formed but details about this process are secret as well. The geometric properties of our MCPs are listed in tab. 2.1.

The coating of microchannel plates is extremely sensitive. *Thus the MCPs can only be touched on the edges that are protected by a glass rim. Any kind of mechanical contact (e. g. touching with gloves) on the active surface can destroy or damage the MCP.* Cleaning of the MCPs is only possible by using a faint stream of pressurized air or better (because it is cleaner) Helium[2].

The two MCPs of this detector are arranged in a Chevron assembly (see fig. 2.5). This means the channel axises of the are two MCPs are tilted against each other with the intention to avoid ion feedback. If the channels are arranged in parallel, electrons leaving the channel at the end of the amplification process can create positively charged ions which travel back in the MCP channels and create another event when they collide with the channels wall. The result would be distorted signals. A similar phenomena appears when the MCPs are oriented correctly but operated in bad vacuum and rest gas atoms are present in the microchannels. The Chevron stack can provide gain factors up to 10^7, up to 1000 times higher then for a single MCP with comparable potential difference per plate [Wiz09].

---

[1] In summer 2012 a new DAQ system has been installed, see sec. 4.

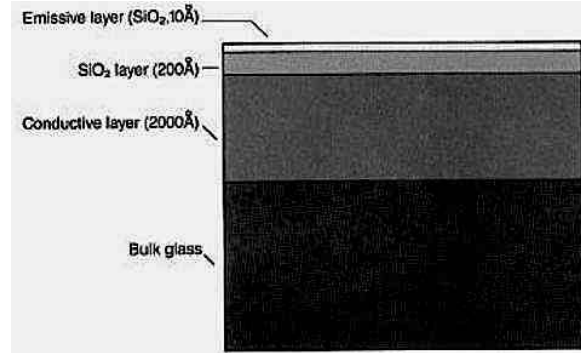[2] Be careful, spray cans with pressurized air can contain traces of oil!

Figure 2.4.: Schematic illustration of the coating of our MCPs taken from ref. [Roe12]. A conductive layer of about 2000 Å is coated on a glass substrate. The conductive layer is covered with a 200 Å thin SiO$_2$ layer. On top of it the actual emissive layer is applied.

Table 2.1.: Geometrical properties of the MCPs [Roe11]. Listed are the outer and the active diameter of the MCP and its thickness, diameter, center-to-center spacing, aspect ratio (ratio of length to diameter of the channels) and bias angle of the pores along with the open area ratio (see eq. 2.2.3) and the number of channels in the active area (see eq. 2.2.4).

Outer diameter	86.6 mm
Active diameter	83 mm
Thickness	1.5 mm
Pore size (diameter)	25 μm
Center-to-center spacing	32 μm
Aspect ratio α (length of channel / diameter of channel)	60
Bias angle	$8 \pm 1°$
Open area ratio	$(50 \pm 5)\,\%$
Number of channels in active area	$(5.5 \pm 0.6) \cdot 10^6$
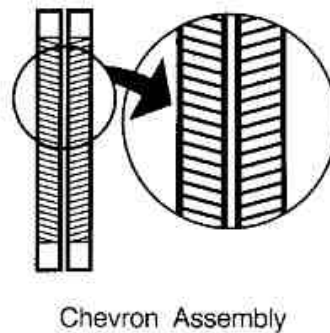
Chevron Assembly

Figure 2.5.: Illustration of the chevron assembly and the orientation of the microchannels. The channel axises are tilted agains each other to prevent electrode feedback. The use of two MCPs instead of one can increase the relative gain factor by about 1000 compared to a single MCP. Taken from ref. [Bar12].

To achieve a correct orientation of the channels the MCPs are marked on one side (see fig. 2.6). These marks have to be placed face to face when assembling the MCP stack. According to the manufacturer it is only possible to say that for a matched pair of MCPs the orientation of the channels of the MCPs in relation to the marks is identical [Roe12][3].

If the detector is not in use, the MCPs should be stored in pre-vacuum. On atmosphere they can soak humidity from the air and their surfaces have to be protected from dust and dirt. If new MCPs are used for the first time they have to be conditioned. This means that the voltage between the front and the back of the MCPs must be raised in 100 V steps with a waiting time of 15 min between each step. Through this process small inhomogeneities on the surface, that might originate from the manufacturing process will be smoothened [Roe12]. A detailed description on the handling of the MCPs and a small animation of the assembling process can be found in [Roe11a, Roe11b] .

Figure 2.6.: The mark of the front microchannel plate is highlighted with the red circle.

The open area ratio is the ratio of the area of the open pores of to the active area of the MCP. The MCP channels are arranged in an hexagonal order with a center to center spacing of $p = 32\,\mu$m and a channel diameter of $d = 25\,\mu$m. Assuming that these properties are constant over the entire MCP surface we can give an upper limit for the open area ratio $R_{\mathrm{OA,up}}$, which we calculate in the following. Nevertheless the manufacturer gives only a lower limit for the open area ration which is due to imperfections in the production process – e. g. the draw of the fibers or the evaporation of the electrode material. This lower limit is:

$$R_{OA,low} = 0.45 \tag{2.2.1}$$

---

[3]Checking by eye with the help of a light source it seems that the channels are oriented towards the mark

The holes of the MCP are arranged in an hexagonal order. Such a hexagon can be divided into six triangles with equal sides p and area A_{tri}:

$$A_{tri} = \frac{1}{2} \cdot p \cdot p \cdot \sin 60^\circ = \frac{\sqrt{3}}{4} p^2$$

where p is equal to the center to center spacing. The holes of the MCP channels have the area A_{hole}:

$$A_{hole} = \frac{\pi d^2}{4}$$

Each triangle includes half of such a hole with diameter d. The upper limit of the open area ratio can be calculated to:

$$R_{OA,up} = \frac{A_{hole}}{2 \cdot A_{tri}} = \frac{\pi}{2 \cdot \sqrt{3}} \left(\frac{d}{p}\right)^2$$

For our MCPs we find:

$$R_{OA,up} = \frac{\pi}{2 \cdot \sqrt{3}} \left(\frac{d}{p}\right)^2 = 0.55 \tag{2.2.2}$$

Finally we give the open area ratio of our detector as the average of eq. 2.2.1 and 2.2.2:

$$R_{OA} = \frac{\pi}{2 \cdot \sqrt{3}} \left(\frac{d}{p}\right)^2 = 0.50 \pm 0.05 \tag{2.2.3}$$

The open area ratio is in principle the upper limit for the absolute detection efficiency of such a MCP detector. During the amplification process in a microchannel a charge load of typically 10^6 to 10^7 electrons is created.

The number of channels of one of our MCPs is:

$$N_{channels} = \frac{A_{active} \cdot R_{OA}}{A_{hole}} = (5.5 \pm 0.6) \cdot 10^6 \tag{2.2.4}$$

where $A_{active} = \frac{\pi \cdot (83\,\text{mm})^2}{4} = 54.1\,\text{cm}^2$ is the active area of the MCP and $A_{hole} = \frac{\pi \cdot (25\,\mu\text{m})^2}{4} = 491\,\mu\text{m}^2$ is the area of one channel. The uncertainty of this value is due to the uncertainty of the open area ratio.

The MCPs used in this detector are matched in resistance, which means that the resistances of both microchannel plates deviate less then 10%. This is important to ensure a comparable potential difference between the top and bottom of each plate when they are stacked and simply shortcut at their connection. Tab. 2.2 shows the resistances and capacities of each MCP and in combination measured with a multimeter. Pictures from both sides of the front MCP are shown in fig. 2.7 and from both sides of the back MCP are shown in fig. 2.8.

Figure 2.7.: Pictures of the front MCP laying in the transport box from the front side (top) and the back side (bottom). The top side of the MCP has been longer exposed to atmosphere, why it is more contaminated with dust.

Figure 2.8.: Pictures of the back MCP laying in the transport box from the front side (top) and the back side (bottom).

Table 2.2.: Resistances of the MCPs measured with a multimeter. For the measurement the front and back side of the MCPs have been contacted using the ceramic rings shown in fig. 2.9.

Microchannel Plate	Resistance
Front plate	15.0 MΩ
Back plate	15.8 MΩ
Stack	30.8 MΩ

The stack is held together between two ceramic rings. The ring in contact with the back plate is coated with a copper electrode on one side, the ring in contact with the front plate has copper contacts on both sides. This allows to place a post-acceleration grid in front of the MCPs. Such a grid is not used for this detector. The geometrical properties of the ceramic rings are listed in tab. 2.3. Pictures of the sides of the ceramics that are in contact with the MCPs are shown in fig. 2.9. The ceramics are screwed together with four Nylon screws. To avoid damaging of the MCPs and sparking, metal screws must not be used for this purpose.

Table 2.3.: Geometrical properties of the ceramic rings measured with a caliper rule.

Material	Height	Inner diameter	Outer diameter	Outer diameter of the front ring electrode	Outer diameter of the back ring electrode
Marcor & copper	2 mm	83 mm	105 mm	86.6 mm	93 mm

Generally speaking, the lifetime of a MCP is limited by the amount of charge it can produce. Each MCP has a certain amount of charge it can produce until it is 'empty'. Thus the back MCP ages faster then the front MCP since the already amplified charge load coming from the front plate creates more secondary electrons in the back plate. Hence flipping over the MCP stack is a possibility to enhance the lifetime of the stack.

The efficiency for different types of radiation varies for different types of microchannel plates. In ref. [Sch74] we find a range of the efficiency for different types of radiation. For better comparison with our MCPs we multiplied these values with the open area ratio R_{OA} which is given in tab. 2.4. We find the largest efficiencies (27.5 - 46.8 %) for electrons with energies between 0.2 - 2 keV and for positively charged ions with energies between 2 - 50 keV. For ultra violet light or soft X-rays the efficiency ranges between 2.8 - 9.9 %.

The gain G per incoming particle is a function of the bias voltage V. Although it depends on multiple other factors like the type of the initial particle, their energy, charge state and the rate of the incoming particles the shape of the curve is always similar. The largest contribution to the gain function comes from the aspect ratio α, which is the ratio of channel length to channel diameter [Roe12]. Typical aspect ratios range from 40 up to 120, while for our MCPs it is $\alpha = 60$. The larger the aspect ratio the lower is the gain factor at a given voltage. Moreover it is possible that within one production charge that the gain factors differs by up to a factor 5, which is why the manufacturer does not provide a gain versus bias voltage curve with the MCP [Roe12]. Nevertheless in the specifications of our MCPs, a lower limit for the gain factor at two different bias voltages (taken from the MCP specifications sheet, see fig. A.13 in the appendix), is given.

Fig. 2.10 shows typical gain curves for MCPs with an aspect ratios $\alpha = 40$ (X-type data points) and $\alpha = 60$ (O-type data points) in a double logarithmic scale taken from [Ebe79]. The continuous lines in that graph are drawn for a theoretical model that treats the MCP as a multi-dynode amplification process. In that reference it is shown that in first order approximation the relation
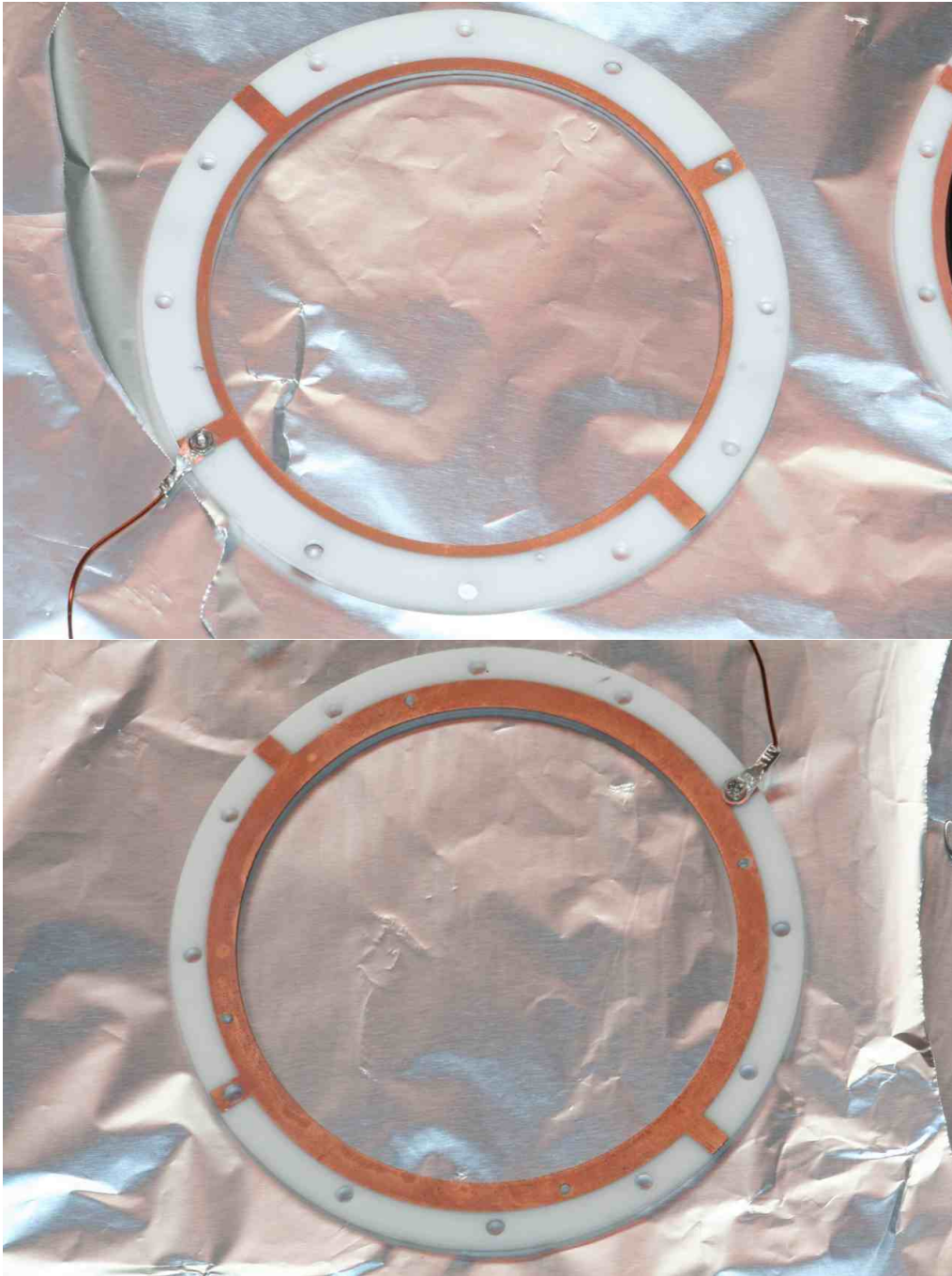
Figure 2.9.: Pictures of the ceramic rings used to assemble the MCP stack. Top: The side of the front ceramic ring in contact with the front MCP. Bottom: The side of the bottom ceramic ring in contact with the back MCP.

Table 2.4.: Range of the detection efficiency of channel multipliers for different types of radiation multiplied by the geometrical factor R_{OA} of our MCP (from ref. [Sch74]).

Type of radiation	Energy range or wave length	Detection efficiency / %
Electrons	0.2 - 2 keV	27 - 47
	2 - 50 keV	5 - 33
Positive ions (H^+, He^+, A^+)	0.5 - 2 keV	3 - 47
	2 - 50 keV	33 - 47
	50 - 200 keV	2 - 33
U. V. radiation	300 - 1100 Å	3 - 10
	1100 - 1500 Å	1 - 5
Soft X-rays	2 - 50 Å	3 - 10
Diagnostic X-rays	0.12 - 0.2 Å	≈ 1

Table 2.5.: Lower limits for the gain factor for two different bias voltages for a single MCP of the type we're using. Taken from the MCP specifications sheet, see fig. A.13 in the appendix.

MCP bias voltage / V	Minimum gain factor
900	400
1200	10000

between $\log G$ and $\log(\frac{V}{n \cdot V_c})$ is linear, where V_c is the so-called first crossover potential which is the minimum potential for unity secondary emission ratio (see [Ebe79] for details) and $n = \frac{\alpha}{\beta}$ with α the aspect ratio and β a dimensionless proportionality constant (see ref. [Ebe79] for details).
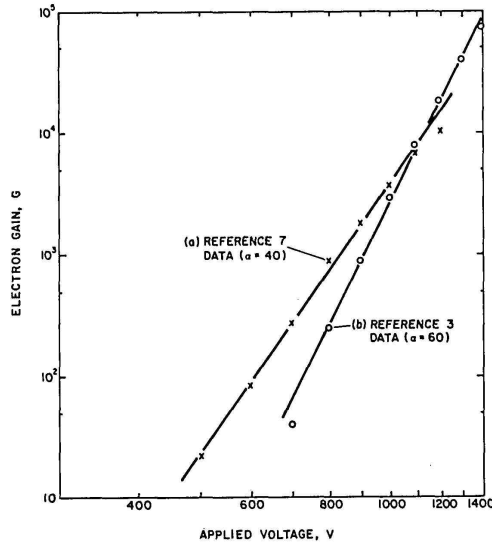

Figure 2.10.: Typical gain curves for for MCPs with an aspect ratios $\alpha = 40$ (X-type data points) and $\alpha = 60$ (O-type data points) in a double logarithmic scale taken from [Ebe79].

The MCPs are delivered in spacial boxes. For our MCPs these boxes are made of hard plastic. Inside on one side a deepening that fit exactly with the outer diameter and and thickness of the MCP is milled. Another deepening, milled on both sides, with the active diameter ensure that the case does not get in contact with the active surface of the MCP. The two sides are screwed together with four M2 screws for Allen keys. Fig. 2.11 shows the outside one of the boxes from both sides.

Figure 2.11.: One of the boxes in which the MCPs were delivered shown from the two outer sides (top) and the insides (bottom).

2.2.2. The delay line anode

The **D**elay **L**ine **A**node (DLA) consists of a *Holder* and two coils: One coil for the X and one for the Y direction. The *Holder* has a metal core with four checkered ceramic insulators at the edges. Around these insulators the delay lines are convoluted, the first one in one direction with a smaller circumferences (X), the second in direction perpendicular to the first one with a larger circumference (Y). Each coil has two wires that are convoluted in parallel with a pitch of 0.5 mm around the holder, the *Reference* and the *Signal* line. *Reference* is on a more negative potential than *Signal* (-37.5 V). Thus *Signal* is more attractive to the electrons coming from the back plate and produces a larger signal then *Reference*.
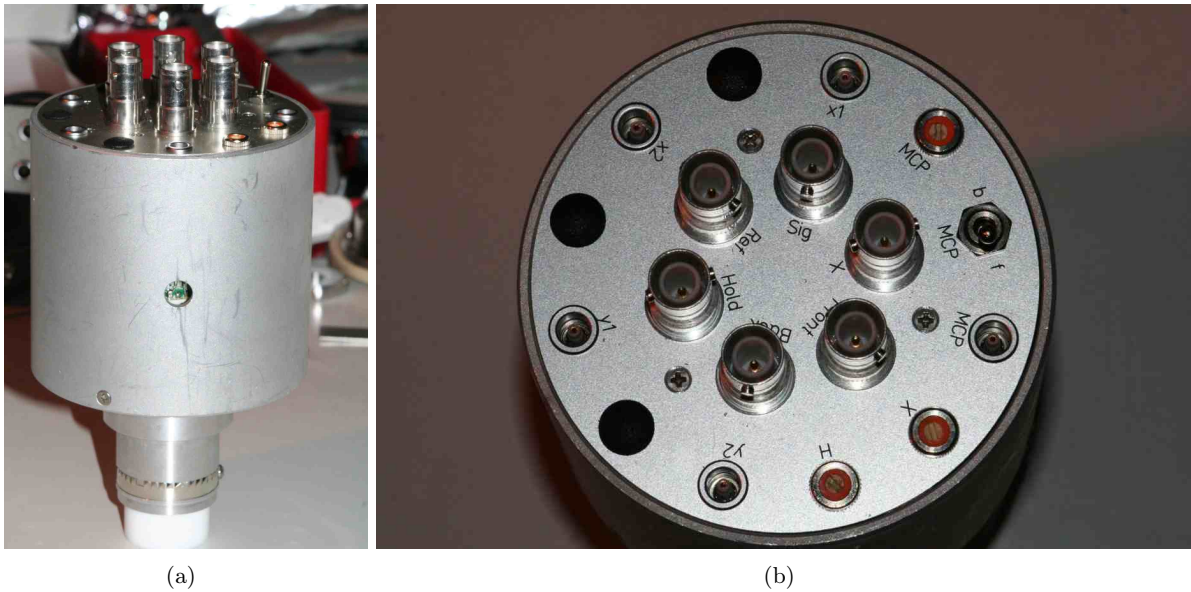

(a)　　　　　　　　　　　　　　　　　　　　(b)

Figure 2.12.: The Roentdek FT12TP for the voltage supply and the decoupling of the *Front*, the *Back* and the delay line signals. (a) Side view of that device. At the bottom there is an teflon insulated plug to connect it to the 12-pin feedthrough. In the center of the picture one can see the cut-out to excess the sidewise potentiometer. (b) View from the top. In the center one can see the six high voltage connectors. More to the edge the five Lemo connectors for the main and the delay line signals can be found as well as three potentiometers labeled *MCP*, *H* (for the termination of the signal created from the *Holder*) and *X* (foreseen for the signal from the post-acceleration grid but not used at the moment.

The signal decoupling happens in the so-called FT12TP [Roe11]. First all eight signals from *Reference* and *Signal* from each delay line end (X1, X2, Y1 and Y2) are decoupled from the high voltage, by four 1 nF capacitors [Roe12]. For noise reduction, afterwards at each end of the delay lines the signal from *Reference* is subtracted from the corresponding signal of the *Signal* line. The results for X1, X2, Y1 and Y2 are lead to one Lemo socket each that is positioned on the top of the FT12TP (see fig. 2.12).

Although the details of the signal processing inside the FT12TP are not provided by the manufacturer we can give a schematic circuit for the decoupling of the delay line signals. This is shown in fig. 2.13 for one end of the delay line, e. g. X1. The high voltage for *Signal* and *Reference* is supplied via a 1.2 MΩ resistance each, which eliminates the noise picked up from the high voltage cables and protects the delay line from voltage swings. The signals from *Signal* and *Reference* are each decoupled by a 1 nF capacitor. This is then lead to the input of a pulse transformer (e. g. model TP-104). This consists on the input side of two coils that are connected in opposite direc-

tion. The input currents from *Reference* and *Signal* create magnetic fields with opposite sings. The resulting magnetic field is picked up by a third coil on the output side of the transformer. So the input signal from *Reference* is subtracted from the one from *Signal*.
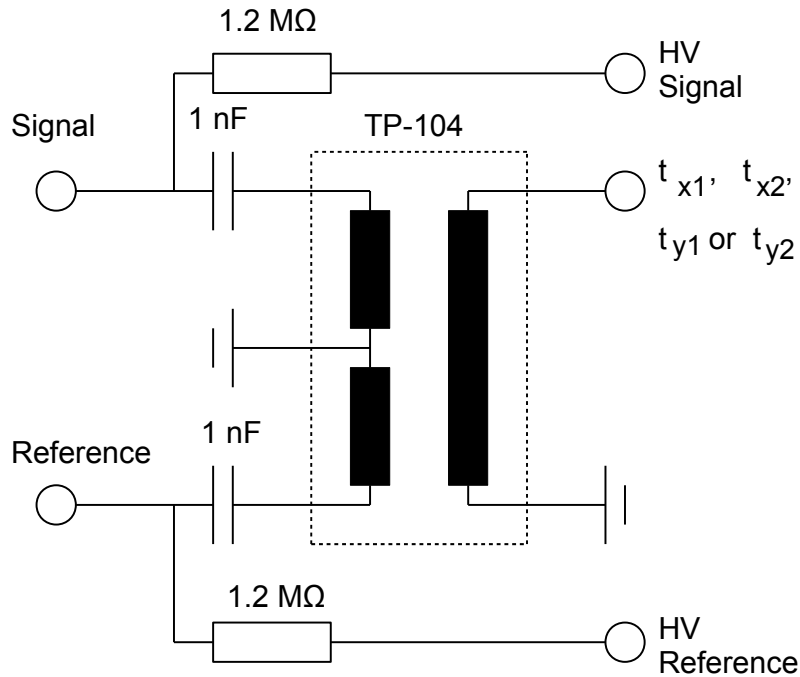

Figure 2.13.: A basic circuit for the decoupling of the delay line signal at one end, e. g. X1. The high voltage for *Signal* and *Reference* is supplied via a 1.2 MΩ resistance each, which eliminates the noise picked up from the high voltage cables and protects the delay line from voltage swings. The signals from *Signal* and *Reference* are each decoupled by a 1 nF capacitor. This is then lead to the input of a pulse transformer (e. g, model TP-104). The input currents from *Reference* and *Signal* thus create magnetic fields with opposite sings. The resulting magnetic field is picked up by a third coil on the output side of the transformer.

Fig. 2.14 shows a picture of the delay line anode. To protect the backside of the anode an aluminum plate is placed right underneath. The *Holder* is mounted via four M2 threaded rods to a metal ring. This ring is screwed to a mounting structure made from Peek that insulates the *Holder* from the flange. The electrical connection for the holder is attached with nuts to the threaded rods and lead to the 12 pin feedthrough.

Over the delay line, a plate to mount the MCP stack is placed (see fig. 2.15). The lower ceramic ring fits into the ring-shaped notch, whereby the stack is centered. The two angulated sheets to the right and to the left are used to attach the MCP stack by pressing the bottom ceramics on the mount and tighten them with four screws. This plate is attached to the *Holder* via the same four threaded rods that are used to mount the *Holder* to the metal ring. A picture of the MCP mounting plate mounted on top of the DLA is shown in fig. 2.16.

The ends of the *Reference* and *Signal* wires of the delay line are attached to separate threaded rods each. Two of them are located at each corner of the *Holder*, eight in total. These rods are electrically insulated from the *Holder*. Each line has a length of 90 ns and a resistance of approx. 13 Ω (see tab. 2.6). The inner coil is used to determine the x-coordinate, the outer one for the y-coordinate. Each pair of *Reference* and *Signal* is connected via Kapton insulated ribbon cables to the 12-pin feedthrough. These cables are attached with special plugs to the threaded rods, as it
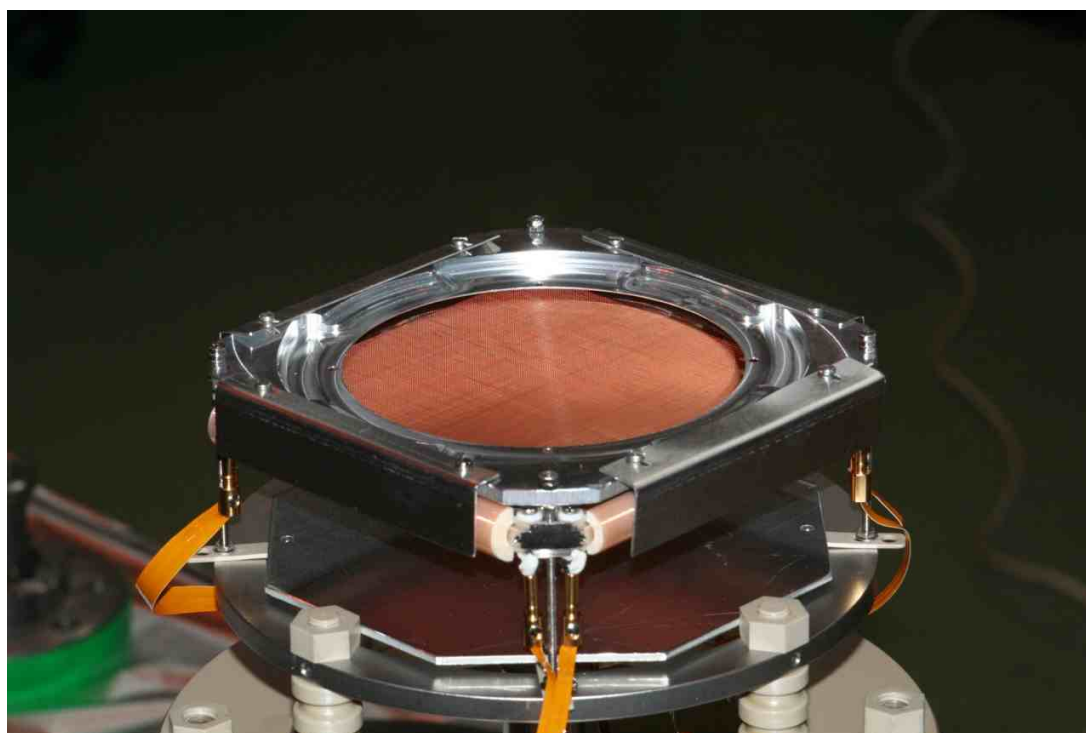
Figure 2.14.: Picture of the delay line anode with the mounting plate for the MCP stack on top. To protect the backside of the anode an aluminum plate is placed underneath. The *Holder* is mounted on a metal ring that is attached to a structure made of Peek.

is shown in fig. 2.17 left. The connection on the flange is shown in fig. 2.17 right.

The connections on the 12-pin feedthrough have to be placed in a certain order to work correctly with the FT12TP which will be plugged onto the 12-pin feedthrough. This is explained in detail in [Roe11]. The orientation of each end of the delay lines is marked on that sides of the flange. This is important when processing the recorded position information (see sec. 2.3.7).

Table 2.6.: Electrical resistance and approx. signal traveling length of the delay line anode.

Coordinate	Position	R / Ω	Approx. length / ns
X	Inner delay line	13.0	90
Y	Outer delay line	13.3	90

Figure 2.15.: Pictures of the mounting plate placed from the top and back side. On each of the four sides L-shaped metal plates are installed to protect the delay line anode from the sides. Two of them can be slid to side to bear the notch with can hold the ceramic ring of the back MCP. By sliding back the L-shaped plate and attaching it with each two screws the ceramic ring becomes attached to the mounting plate.
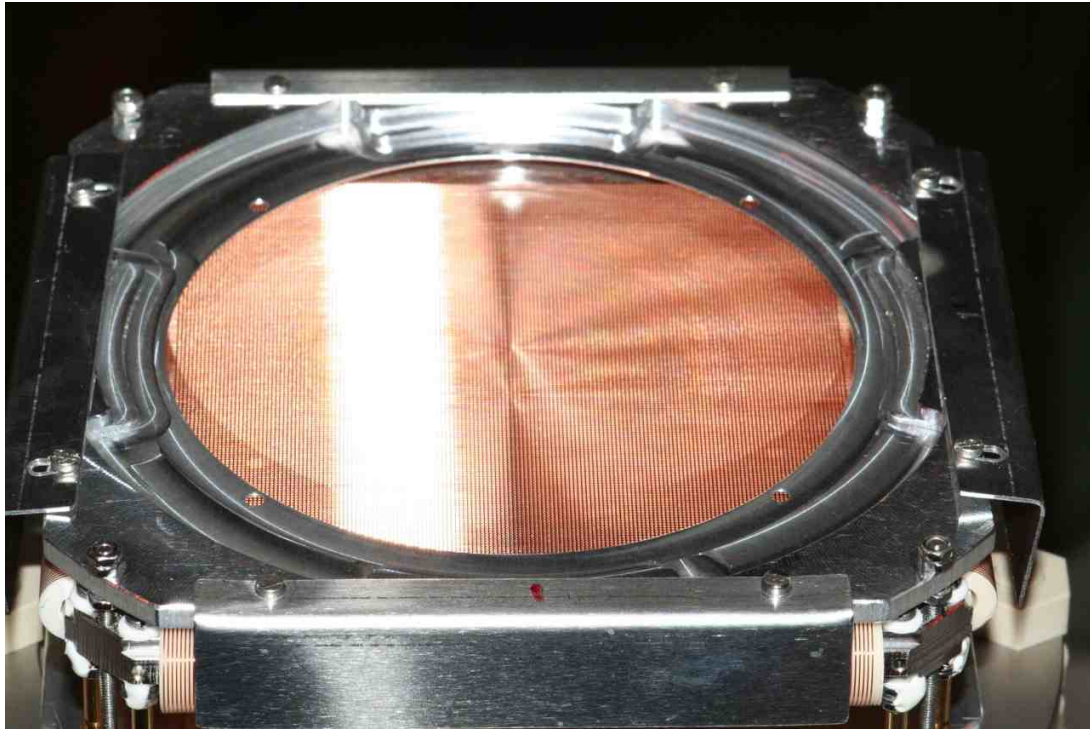
Figure 2.16.: Picture of the mounting plate placed on top of the delay line anode. Below the delay line anode wires are visible. The two L-shaped metal plats to the left and to the right can be slid to side to bear the notch with can hold the ceramic ring of the back MCP.

(a)   (b)

Figure 2.17.: (a) Picture of the gold plated plugs to connect the ribbon cables to the threaded rods at the ends of the delay lines. (b) Connections of the ribbon cables at the 12-pin feedthrough. The ends of the ribbon cables are plugged with small thin plugs to the metal pins of the feed trough.

The delay line anode is very sensitive to dust and impurities, because it can easily cause a shortcut between *Reference* and *Signal* and spoil the position information. 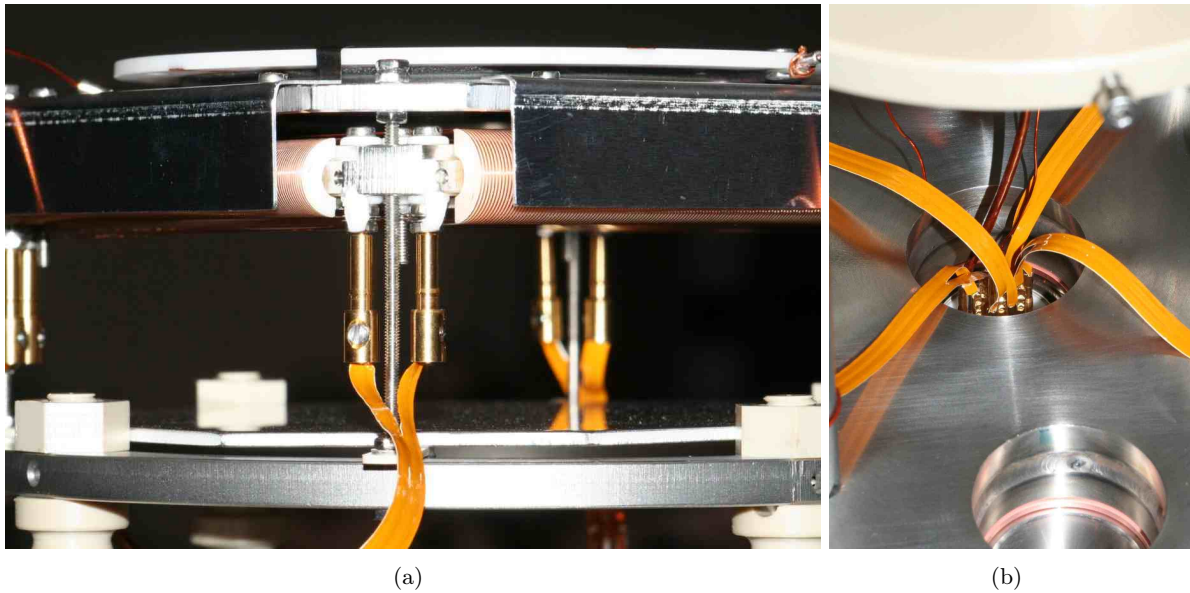*Thus it is important to work in a clean and dust-free environment and to clean the detector with pressurized air (or Helium) before its installation.* Conductive dust could shortcut the *Reference* and *Signal* of one or both coils, which disables the position information in these dimensions. To diagnose a shortcut, one has to measure the resistance between *Signal* and *Reference* with a multimeter. This could either be done directly on the delay line, when the detector is not installed or – if the detector is already installed – at the 12-pin feedthrough or HV connections for *Signal* and *Reference* at the FT12TP (see section 2.2.4). When measuring at the connection for *Reference* and *Signal* on the FT12TP you have to take into account the 1 MΩ protective resistances inside, so a shortcut would result in a measurement of approx. 2 MΩ. A high-ohmic connection between *Reference* and *Signal* can e. g. stem from humidity condensed on the delay line anode and does not affect its functionality. Usually it disappears when the detector is under vacuum again.If a shortcut appears outside the vacuum cleaning the delay line with pressurized air (or helium) might help to remove the shortcut. If this does not work, measuring the resistance at both ends of the delay line can help to locate it. Using a fine paint brush may help to remove it. It can happen the a shortcut appears right after the voltage has been applied. In that case one can try to switch on and off the voltage, which might move the dust particle that is causing the shortcut. If this does not help it is recommended to take out the detector and remove the shortcut outside of the vacuum.

2.2.3. The SPDRIF02 electrode

The detector is housed in a cylindrical electrode, which is named SPDRIF02 because it is the second drift electrode behind the einzel lens electrode SPEINZ01 in the spectrometer (see fig. 1.6 for details). On top the electrode has an 80 mm diameter hole right in front of the MCP. This electrode is attached with four screws to the Peek ring on which the mounting structure for the delay line is attached. The electrical connection is lead to a SHV-10 feedthrough on the detector flange. The surface of the SPDRIF02 electrode has been electropolished. Fig. 2.18 shows the detector surrounded by the SPDRIF02 electrode.
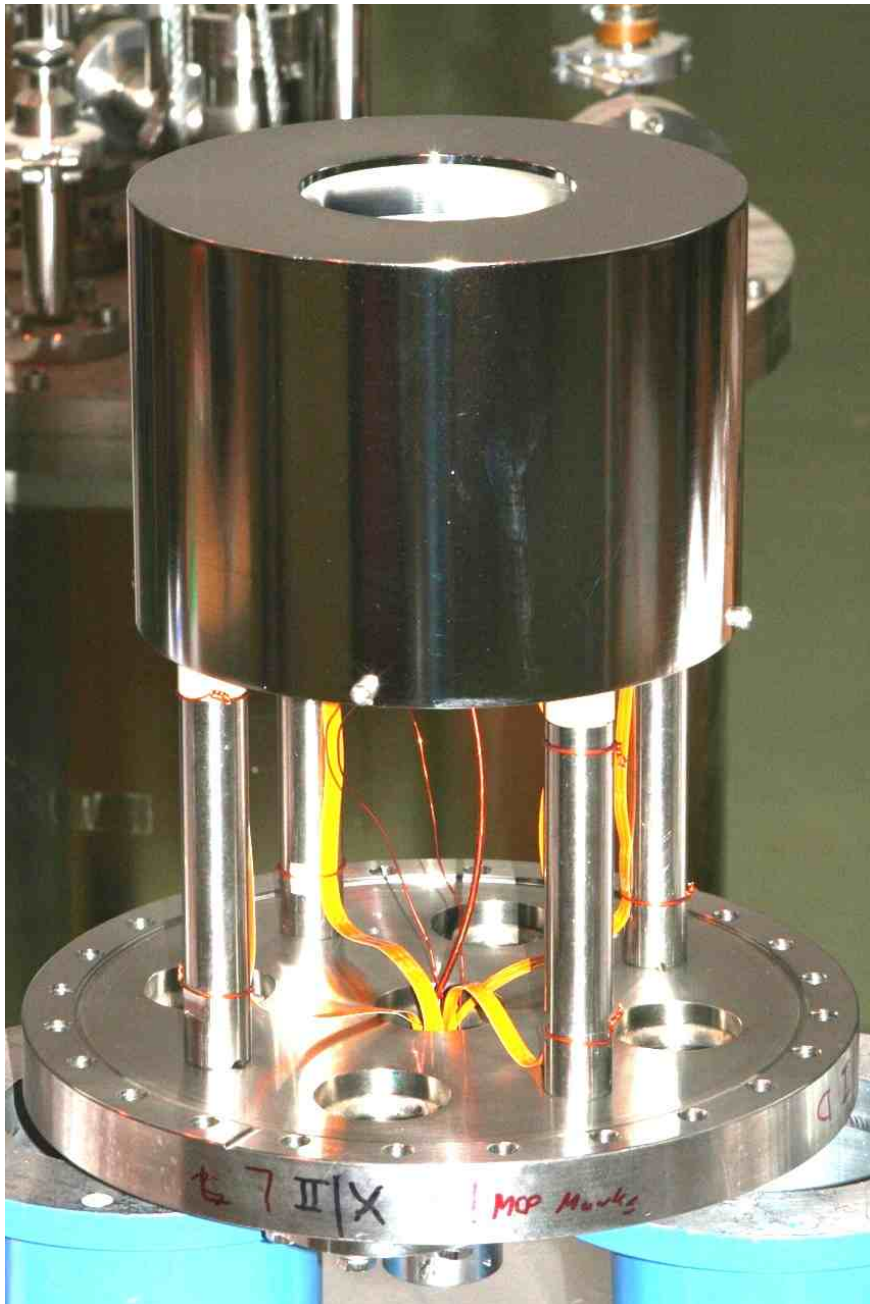

Figure 2.18.: The detector with the surrounding SPDRIF02 electrode.

2.2.4. The high voltage supply

The detector can be divided into five sections that have to be on different potentials. These are the front of the MCP stack (*Front*), the back of the MCP stack (*Back*), the holder of the delay lines (*Holder*), the reference wires (*Reference*) and the signal wires of both delay lines (*Signal*). As voltage supply a CAEN 570N is used in combination with a voltage divider. A picture of the CAEN 570N module is shown in fig. 2.19.

Figure 2.19.: The CAEN 570N power supply used for the voltage supply of the detector.

All voltage connections go to the FT2TP. Inside the FT12TP are 1 MΩ protective resistances after each connector except for the connection of MCP front, which has a 10 kΩ resistance. Fig. 2.12 shows two pictures of the FT12TP taken from the top and from the side. The FT12TP has 6 SHV-5 sockets labeled *X, Front, Back, Holder, Reference* and *Signal*. The *X* is foreseen to connect a post-acceleration grid mounted in front of the MCP stack. This option is not used for our detector.

The requirements for the high voltage supply are the following [Roe11]:

- A potential difference between -2100 V and -2600 V between *Front* and *Back*

- A potential difference between -0 V and -250 V between *Back* and *Holder*

- A potential difference between -550 V and -300 V between *Back* and *Reference*

- A stable potential difference between -20 V and -50 V between *Reference* and *Signl*

This is managed by a voltage divider. The voltage offset between *Reference* and *Signal* is applied by a battery box, called Roentdek BAT3 with one SHV-5 input and two SHV-5 outputs. Four 9 V batteries inside provide a voltage offset of 37.5 V between both outputs. The advantage of this solution is that the voltage offset provided by a battery is very constant. A picture of the voltage divider box is shown in fig. 2.21(a) and the battery pack is shown in fig. 2.21(b).

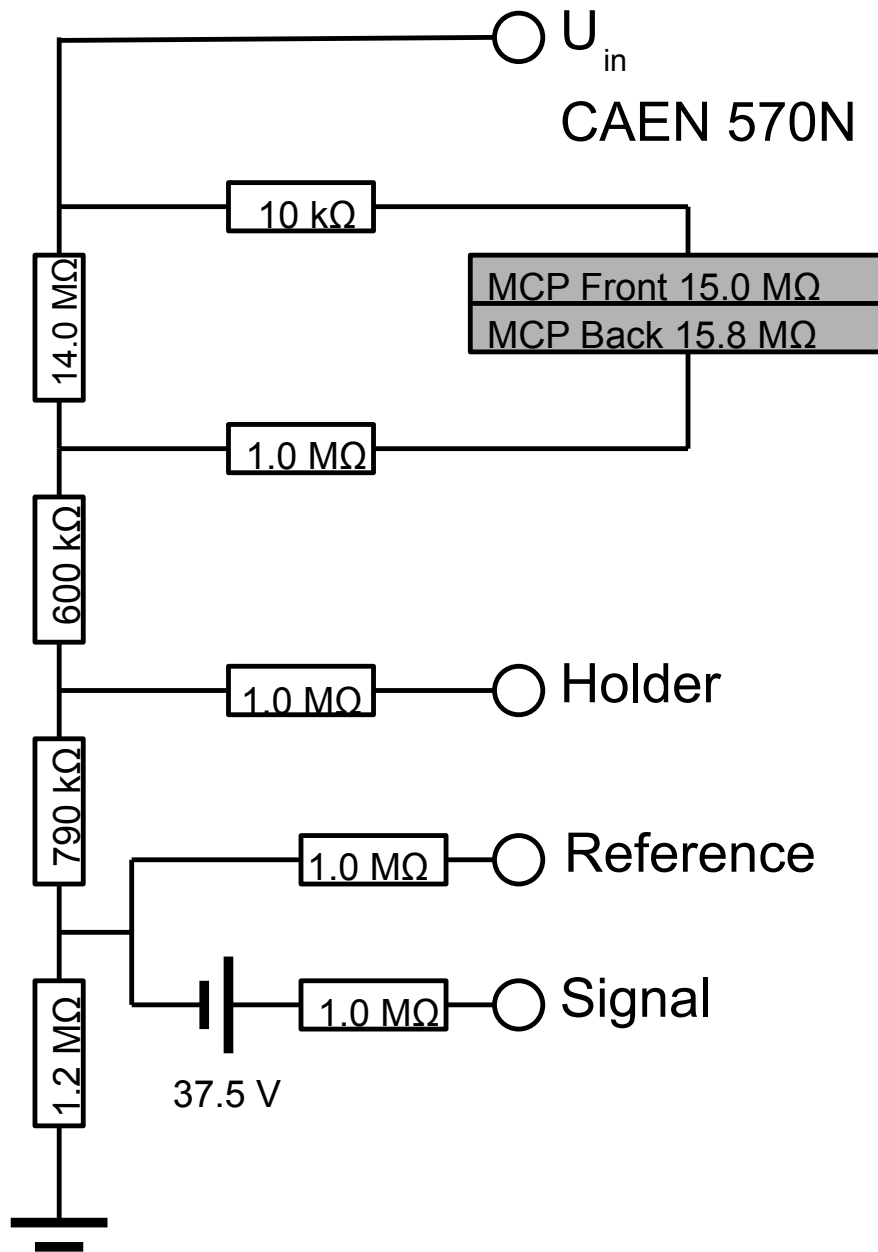**Figure 2.20.:** Scheme of the voltage supply of the detector. Before each connection protection resistances of about 1 MΩ (exempt MCP *Front*) are inserted. The constant voltage offset between *Signal* and *Reference* is applied by a battery package of four 9V battery in series.
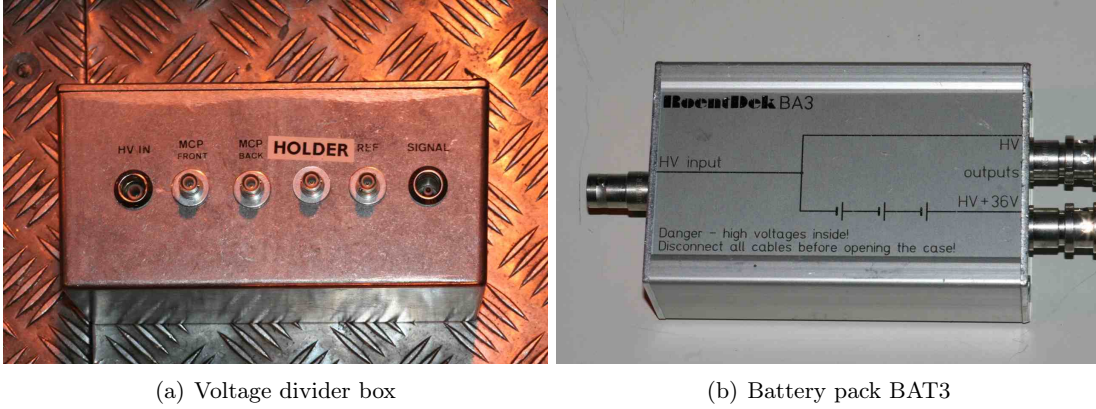
(a) Voltage divider box   (b) Battery pack BAT3

Figure 2.21.: Picture of the voltage divider box and the battery pack BAT3 for the voltage offset between *Reference* and *Signal*. All connections are connected via SHV-5 pugs except for the HV input to the voltage divider box with has a female HV Lemo socket.

A scheme that describes the voltage supply of the detector is shown fig. 2.20. While increasing the high voltage of the detector it is important to monitor two values:

- The potential difference between *Front* and *Back*[4]:

$$U_{FB} = U_{in} \cdot \frac{9.7\,\mathrm{M\Omega}}{12.3\,\mathrm{M\Omega}} \cdot \frac{30.8\,\mathrm{M\Omega}}{31.8\,\mathrm{M\Omega}} \qquad (2.2.5)$$

- The current, monitored at the power supply:

$$I_{in} = \frac{U_{in}}{R_0} = \frac{U_{in}}{12.3\,\mathrm{M\Omega}}$$

  where $R_0 = 12.3\,\mathrm{M\Omega}$ is the resistance between the output of the power supply and the ground potential.

If for instance, a potential of 3.23 kV is applied between U_{in} and the ground potential, the potential between *Front* and *Back* is $U_{FB} = 2.47$ kV and $I_{in} = 2.62\,\mu\mathrm{A}$. In principle it is possible to put the whole detector on a higher potential by replacing the 1.2 MΩ resistance by a larger one. Here, the limiting factor is the 12-pin feedthrough, which is rated to 4.5 kV.

---

[4]The 9.7 MΩ is the resistance between U_{in} and contact between the 600 kΩ and the 14.0 MΩ resistance can be calculated as $\left(\frac{1}{14.0\,\mathrm{M\Omega}} + \frac{1}{31.8\,\mathrm{M\Omega}}\right)^{-1} = 9.7\,\mathrm{M\Omega}$. The 12.3 MΩ is the resistance between U_{in} and ground, calculated as $\left(\frac{1}{14.0\,\mathrm{M\Omega}} + \frac{1}{31.8\,\mathrm{M\Omega}}\right)^{-1} + 600\,\mathrm{k\Omega} + 790\,\mathrm{k\Omega} + 1.2\mathrm{M\Omega} = 12.3\,\mathrm{M\Omega}$

2.2.5. The processing of the signals

Fig. 2.22 shows a pictures taken with the oscilloscope. The yellow trace is the main MCP signal, the blue one the trigger pulse of the main MCP signal, the red trace the X1 delay line signal taken with the oscilloscope. The rise time of the main MCP and the delay line signals is appox. 3 to 4 ns.
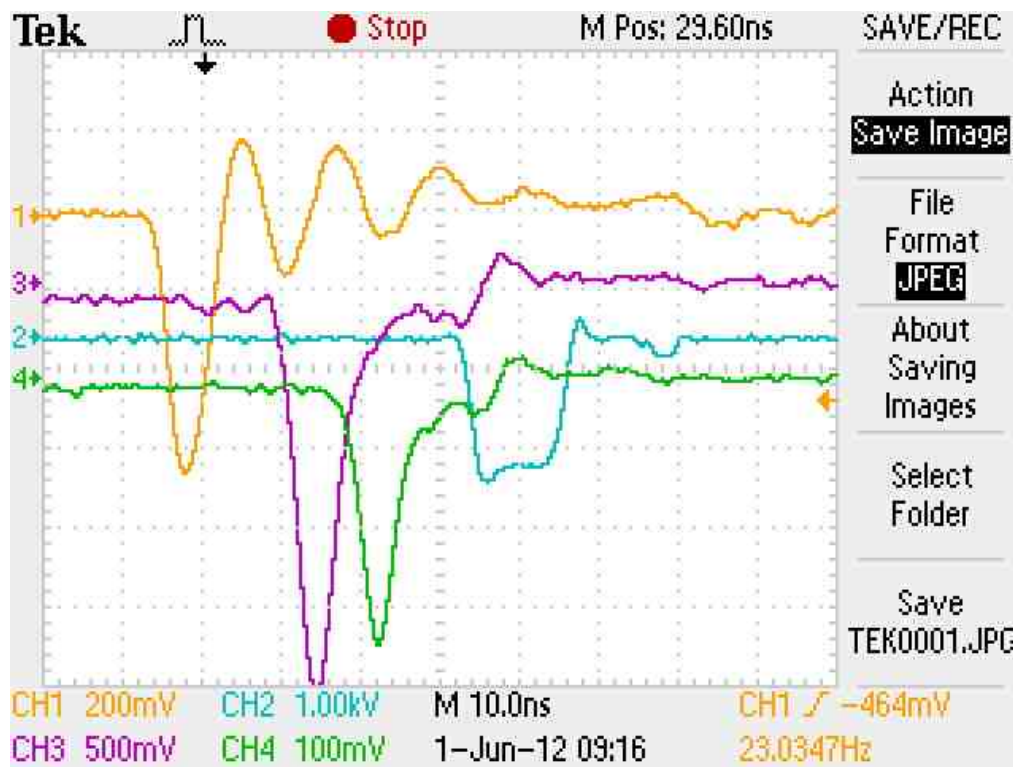

Figure 2.22.: Picture of the main MCP signal (yellow trace), the trigger of the main MCP signal (blue trace), the X1 delay line signal (purple trace) and the Y2 delay line signal (green trace), taken with the oscilloscope.

All analogue NIM modules used for the signal processing are placed in a separate crate. The power connectors of all analogue modules used for the analogue data processing, namely the NIM crate with the LeCroy 612A amplifier and the LeCroy 821 discriminator, the amplifier FAMP1+ and the discriminator CFD1x are equipped with line filters.

An important part of the signal processing happens in the FT12TP. The inside of this box is hidden behind a metal cylinder and its inside is cast in an epoxy. The manufacturer doesn't provide a scheme of the circuit. From the old detector a similar way to process the signals is known. A scheme of the electric circuit is shown in fig. A.14. More details will be discussed in the coming two sections separately for the main MCP signal and the delay line signals. A schematic explaining the principle of the whole signal processing is shown in fig. 2.23. The cable lengths (given in ns) used are written next to the lines. The details will be discussed in the following two sections.
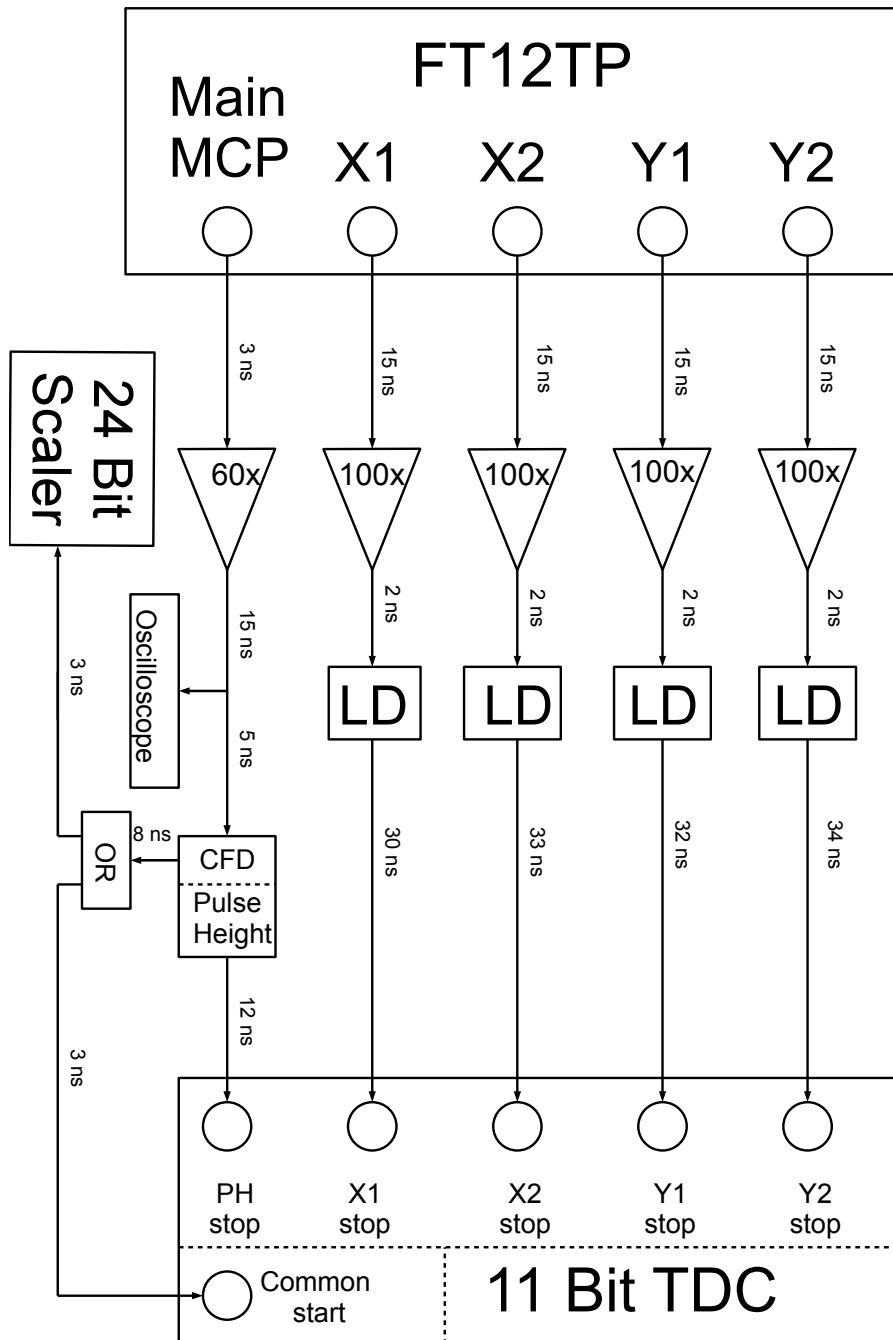
Figure 2.23.: Principle of the signal processing. Signals decoupled in the FT12TP are amplified and discriminated. The Main MCP signal could be either picked up at the front or the back MCP. It is counted by a 24 bit scaler and used as a common start trigger for the TDC. The pulse height of the main signal is encoded in a time delay which is used as stop signal for the first TDC channel. The four delay line signals are used as stop triggers for the channel two to five of the TDC. The time delay due to the progression of the signals in the cables are written next to each line.

2.2.5.1. The main MCP signal

The main *MCP* signal could be either picked up at the front or the back MCP. A switch on top of the FT12TP can be used select one of these two sources. In the FT12TP the signal of choice is first decoupled from the high voltage with 1 nF capacitors [Roe12] and then lead to the output labeled *MCP*. Two potentiometers, one on top of the FT12, labeled MCP and one at the side without a label (see fig. 2.12 left side, the cut out in the cylindrical aluminum housing) can be used to match the impedance of this signal and thus improve its quality. All of this is shown in fig 2.12. A third potentiometer named *Holder* is used to reduce the crosstalk from the holder of the delay lines.

The main MCP signal is first amplified by a factor of 60 with the Roentdek FAMP1+ (for a manual see ref. [Roe11c]). Afterwards the signal is lead to a **C**onstant **F**raction **D**iscriminator (CFD), the CFD1x from Roentdek (for a manual see ref. [Roe11d]), which has the ability to encode the pulse height in a time delay which can then be used to record the pulse height with a time-to-digital converter (TDC).

A CFD works in principle like this: When a signal above the threshold that is set arrives, it creates tow signals: a delayed signal and an inverted and an attenuated signal. In a second step it adds both signals and gives a trigger at the time of the zero crossing. It can be shown that the zero crossing appears always at the same time independently of its amplitude, when the delay t_{delay} and the fraction f are chosen via this equation:

$$t_{delay} = t_{rise}(1 - f) \qquad (2.2.6)$$

where t_{rise} is the rise time of the signal, t_{delay} the delay time of the delayed signal and f the attenuation factor. The rise time is defined as the time, a signal needs to get from 10% to 90% of is maximal value A typical rise time for an MCP signal is 5 ns while it is a bit longer, 10 ns, for a delay line signal. Fig. 2.24 illustrates the principle of a CFD.
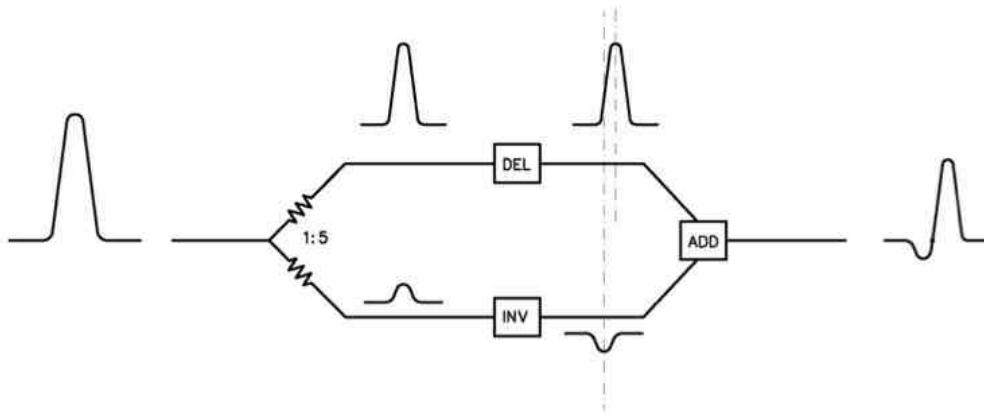
Figure 2.24.: Illustration of the working principle of a constant fraction discriminator, taken from ref. [Roe11d].

This CFD has the ability to encode the height of the incoming signal either in a delayed pulse or in the signal width of the discriminator. Therefore it inverts the incoming signal and attenuates maximum with a constant rate of 2.5 V per 15 ns. For proper operation it is important to set the start of the ramp and the maximum of the inverted signal at the same time. This can be achieved by choosing a suitable delay cable between A_{in} and A_{out} of the CFD1x. The slope of $0.1\bar{6}$ V/ns is fixed. When it reaches 0 the CFD1x returns a pulse at the *Stop* output. The FAMP1+ is shown in fig. 2.25(a) and the CFD1x is shown in fig. 2.25(b).

With a multimeter one can read out the threshold setting of the CFD between the two connections labeled *Threshold* and *GND*. To adjust the threshold value the Screw labeled *Threshold* can be used. The delay time can be set by choosing the right cable length between both sockets labeled *Delay*. If the CFD triggers a signal the red LED in the top left corner blinks. The screw labeled *W* can be used to set the width of the trigger signal. Typical settings for the CFD1x and the FAMP1+ are listed in tab. 2.7.

Table 2.7.: Typical set of settings of the CFD1x and FAMP1+.

Amplification	Threshold / mV	Delay / ns $(Delay \rightarrow Delay)$	Delay / ns $(A_{in} \rightarrow A_{out})$	Fraction
60	200	2	2	0.35

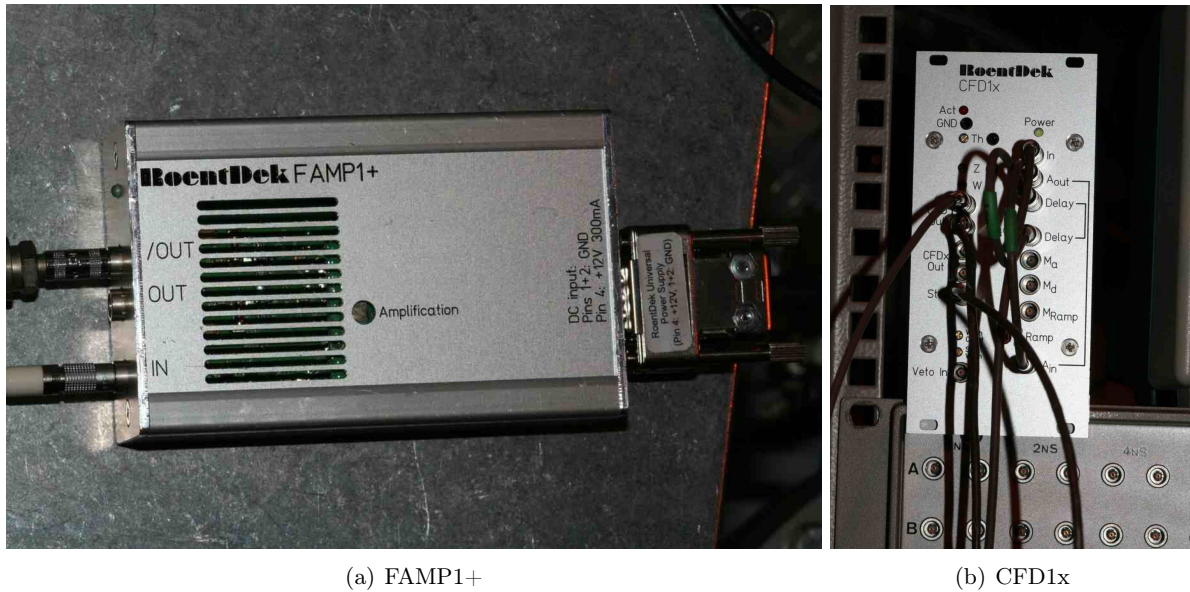(a) FAMP1+   (b) CFD1x

Figure 2.25.: The fast amplifier FAMP1+ (a) and the constant fraction discriminator CFD1x (b) for the signal processing of the main MCP signal (*Front* or *Back*). The amplification factor of the FAMP1+ can be adjusted with the screw on the side of the housing. For details about the CFD1x see the text.

A 24 bit scaler module counts the triggers from the main MCP signal (either front or back), which can be used for dead time correction. This trigger serves also as a common start signal for an 8 channel TDC with 11 bit resolution. The pulse height stop signal from the CFD1x serves as stop signal for channel 4 of the TDC (see fig. 2.26(b)). The delay between the Stop signal and the TDC can be adjusted by a delay box (see fig. 2.27(d)).

2.2.5.2. The delay line signals

In the FT12TP for each end of the delay line the signal from the *Reference* line is subtracted from the *Signal* line after they were decoupled from the high voltage by the use of 1 nF capacitors [Roe12]. Afterwards they can be picked up at the outputs labeled $X1$, $X2$, $Y1$ and $Y2$. A detailed circuit of the FT12TP is not provided by the manufacturer and the electronics are hidden in an epoxy.

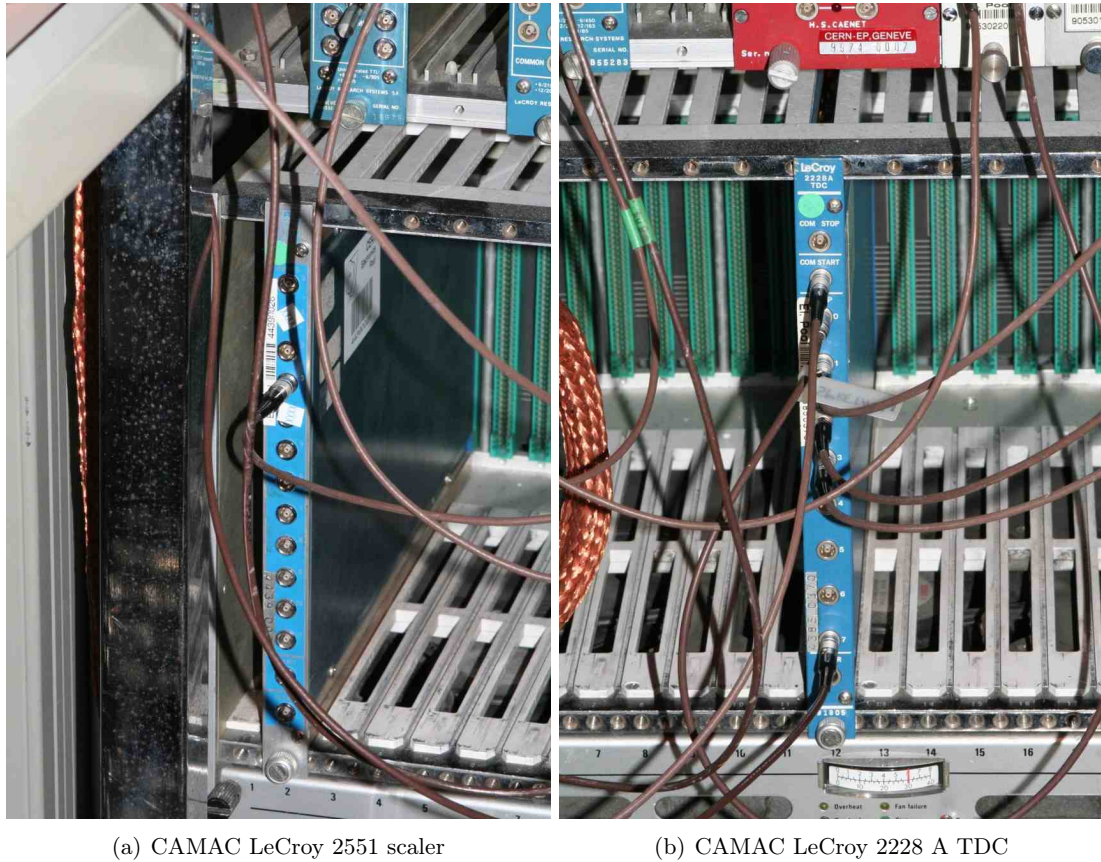(a) CAMAC LeCroy 2551 scaler   (b) CAMAC LeCroy 2228 A TDC

Figure 2.26.: The CAMAC scaler (a) and the TDC (b) of the data acquisition. The scaler is a LeCroy 2551 12 channel 200 MHz scaler and the TDC is a LeCroy 2228 A high precision time-to-digital converter.

Pictures of the FT12TP can be found in fig. 2.12. Since the details of the inside of the FT12TP are unknown we show in fig. A.14 (see Appendix A) the circuit of the signal processing like it was done for the old detector. The 1 nF capacitors and the the 1.2 MΩ resistors from the HV supply form a high pass filter with a time constant $\tau = \frac{1}{R \cdot C} = 833$ Hz. After the FT12TP, the delay line signals are first amplified by a factor of 100 in a LeCroy 612 A 12 Channel Amplifier. Thereafter they're sent to a leading edge discriminator, LeCroy 821 (CS) (see fig. 2.27). Although this model has four channels, two of them are in use since the on each module one channel is broken. The LeCroy 821 CS is used to discriminate the signals from X1, X2 and Y2 on the channels 1, 2 and 4. The LeCroy 821 is used to discriminate Y1 on channel 4. Both models have identical specifications, except that the CS has 2 instead of 1 inverted outputs on the front.

A Leading edge Discriminator (LD), returns a trigger when the incoming signal passes a certain threshold. Compared to the CFD, the LD has the disadvantage, that when the height of the signal is changing the trigger is coming to different times and thus the timing information is less precise. To set the threshold on the LeCroy 821 each of the four channels has two sunk-in M2 screws (*threshold* and *width*) and a connection at the top left corner. Between the connector and the ground potential one can read out the threshold value of each channel with a multimeter. *The monitored threshold value is enlarged by a factor of 10!* The screw labeled *threshold* can be used to raise and lower the threshold, the one labeled *width* can be used to adjust the width of the trigger pulse. When an incoming signal is triggered, the red LED in the top left corner blinks.
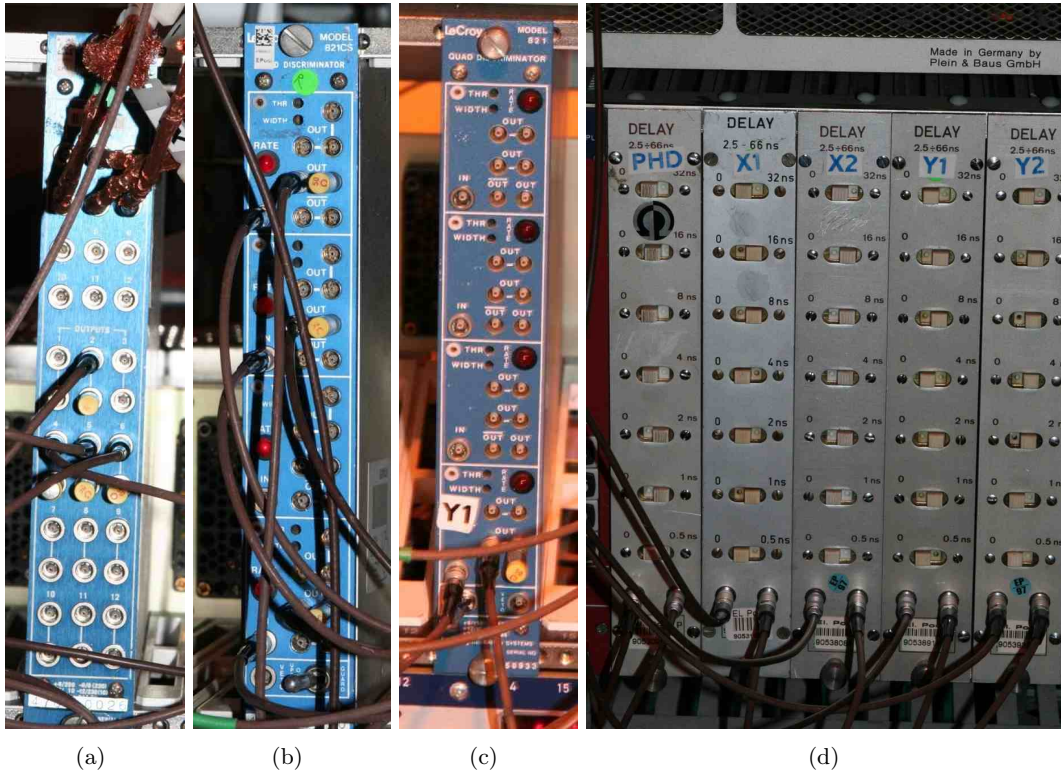
(a)   (b)   (c)   (d)

Figure 2.27.: From left to right: The LeCroy 612A amplifier (a), the leading edge discriminators LeCroy 821 (CS) (b & c) which is used to process X1, X2, and Y2, the leading edge discriminator used to process Y1 and the cable delay boxes (d) used to adjust the delays for the form delay line signals X1, X2, Y1 end Y2 and the pulse height information (PHD). All of these modules are hosted in one NIM crate.

The four delay line triggers serve as stop signals for the first four channels TDC (channel 0–3) one for each channel, to record the position information. The delay between the LD and the TDC can be adjusted with a delay box (see fig. 2.27). In tab. 2.8 a list of typical thresholds, delays between the discriminators and TDC and amplification factors are listed.

Table 2.8.: Typical settings of thresholds, delays and amplification factors for the delay lines.

Channel	Amplification factor	Delay / ns	Threshold / mV
X1	10	30	-45
X2	10	33	-60
Y1	10	32	-70
Y2	10	34	-83

2.3. Detector calibration in 2011

For the calibration a series of measurements in a separate chamber with a collimated alpha source, a longtime measurement with an uncollimated alpha source and a longtime background measurement have been performed. Afterwards the detector was installed on top of the spectrometer.

2.3.1. The calibration setup

For the calibration measurements we used an ^{241}Am alpha source. During the measurement the detector was installed in the detector test chamber. For the measurements with the collimated source the source was placed in a source holder that was attached to a manipulator feedthrough with allowed to move the source forth and back and sideways.

2.3.1.1. The ^{241}Am alpha source

For the calibration a 40 kBq ^{241}Am source was used. In that source americium oxide is fixed in a Silver foil of 200 μm thickness and covered with a layer of 1.8 μm Palladium. This foil is pressed by a steel O-ring into a stainless steel holder. It has been manufactured in 2007 by Eckert & Ziegler. The number of the source is 4263RP. The activity of the source has been measured by the CERN Radiation Protection Sources Groupon 03/08/2011:
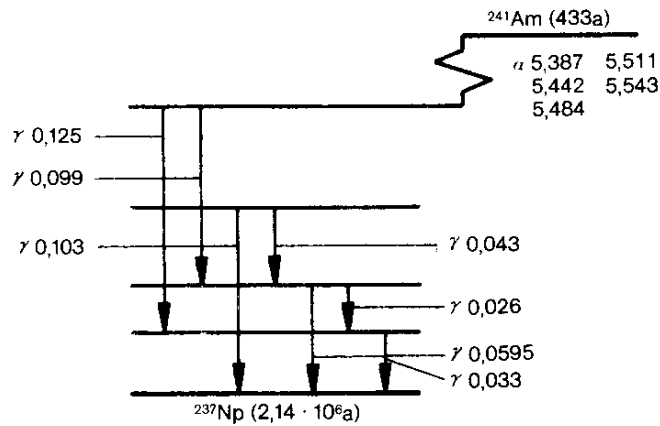
$$A_S = 40.0(4.0)\,\text{kBq} \tag{2.3.1}$$

Figure 2.28.: Simplified decay scheme of ^{241}Am taken from [Nor11]. ^{241}Am undergoes with nearly 100% probability alpha decay to various excited states of 237Np and has a half-life of about 433 a. For more details see the text.

A simplified decay scheme of ^{241}Am is shown in fig. 2.28 (the complete decay scheme can be found in fig. A.15 in the Appendix). ^{241}Am undergoes with nearly 100% probability alpha decay to various excited states of ^{237}Np and has a half-life of 432.6 a. The majority of the alphas have energies of 5484 keV (84.8%) or 5442 keV (13.1%). The excited states of ^{237}Np decay via gamma decay or emission of conversion electrons. The branching ratio for the gamma decay is about

$$R_{B,\gamma} \approx 75\%. \tag{2.3.2}$$

So we can expect about three gammas for every four alphas that are created in the source. The gammas from the decay of the excited ^{237}Np states have mostly energies in the diagnostic X-ray region: 59.5 keV (35.9%), 13.9 keV (37%) or 26.3 keV (2.3%) [Bas06]. There are various other energies which contribute with about 0.1% or less, that will be neglected. We can estimate the relative intensity of gammas that pass the Pd sealing via [Ndt12]:

$$\frac{I(x)}{I_0} = e^{-\mu \cdot x} \tag{2.3.3}$$

where I_0 is the initial intensity, $I(x)$ the intensity after they have passed the Pd cover, μ the linear attenuation coefficient and $x = 1.8\,\mu$m the thickness of the Pd foil. Pd has a density of $\rho = 12\,\frac{\text{g}}{\text{cm}^3}$ [Nis12], for 60 keV gamma photons we find $\frac{\mu}{\rho} = 5.4\,\frac{\text{cm2}}{\text{g}}$ and for 15 keV gamma photons we find $\frac{\mu}{\rho} = 37\,\frac{\text{cm2}}{\text{g}}$ [Nis12a]. From this we can estimate the rate of gammas that can pass the Pd foil as $\frac{I(x)}{I_0} = 99\%$ for the 60 keV gamma photons and $\frac{I(x)}{I_0} = 92\%$ for the 15 keV gamma photons. The typical detection efficiency for diagnostic X-rays in this energy regime is about 1% (see tab. 2.4). Since gammas create predominantly small pulse heights [Roe12] in combination with a certain threshold setting the efficiency of our detector for gammas may also be less. We assume that the detector has an efficiency for these gammas of

$$\epsilon_\gamma = (0.01 \pm 0.01). \tag{2.3.4}$$
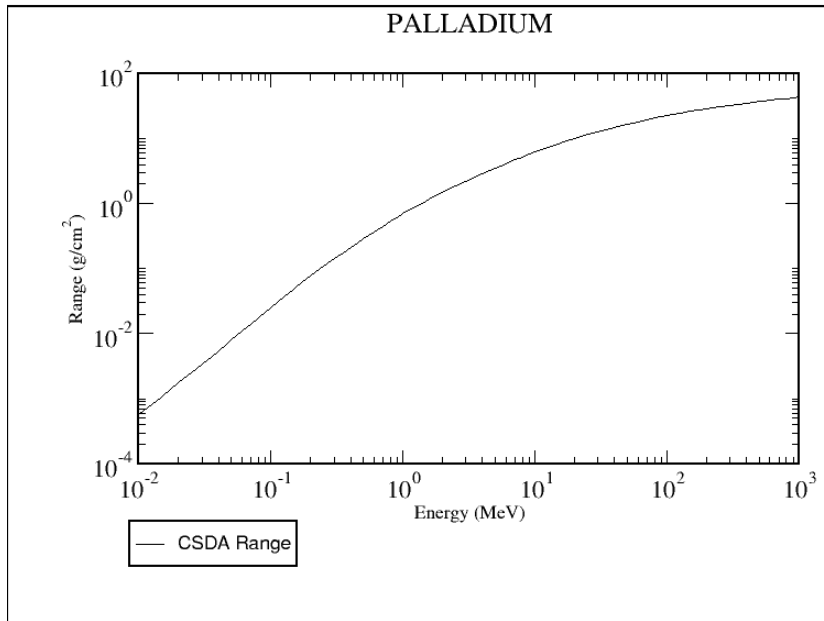
Figure 2.29.: CSDA range of electrons in Pd as function of their energy calculated with ESTAR [Est11].

Moreover conversion electrons and Auger electrons of various energies are created in the source. About 35% have an energy 10.1 keV, 30% have 37.1 keV, 17% have 10.8 keV, 14% have 3.9 keV, 9.1% have 21.0 keV, 4.4% have 27.9 keV, 3.6% have 20.6 keV, 3.0% have 37.1 keV and 2.4% have 37.7 keV. Other energies contribute with less then 1% each. To estimate how many electrons we can expect from the source we use the software ESTAR [Est11] to calculate the continuous slowing down

approximation range (CSDA range) of electrons in Pd as function of their energy, which is shown in fig. 2.29. The Pd cover of our source has a thickness times density of $dx \cdot \rho = 1.8\,\mu\mathrm{m} \cdot 12\,\frac{\mathrm{g}}{\mathrm{cm^3}} = 2.16 \cdot 10^{-3}\,\frac{\mathrm{g}}{\mathrm{cm^2}}$. The calculated CSDA range of 10 keV electrons is $5.6 \cdot 10^{-4}\,\frac{\mathrm{g}}{\mathrm{cm^2}}$, of 20 keV electrons it is $1.7 \cdot 10^{-3}\,\frac{\mathrm{g}}{\mathrm{cm^2}}$, for 25 keV electrons it is $2.5 \cdot 10^{-3}\,\frac{\mathrm{g}}{\mathrm{cm^2}}$ and higher for larger energies. This means predominantly electrons with energies of about 25 keV or higher are leaving the source. If we sum up the branching ratios of these electrons we find

$$R_{B,\beta} \approx 0.4. \tag{2.3.5}$$

Here we should mention that especially the low energetic electrons are deflected by the MCP surface which is on an approx. -3 kV more negative potential than the source. Furthermore the opening angle of the detector effects the path length of the electrons in the Pd foil. Some electrons, predominantly arriving at the detector on outer radii, will experience a longer travel distance in the Palladium. For the efficiency of betas we find in tab. 2.4 a wide range of about 10 to 66%. Thus we assume an average value with large uncertainties.

$$\epsilon_\beta = (0.35 \pm 0.35). \tag{2.3.6}$$

We should again notice that the value given in tab. 2.4 has been multiplied with the geometrical factor R_{OA}.

In consideration of the gamma activity and the conversion electrons of the ^{241}Am source we define a modified source activity

$$\tilde{A}_S = A_S \cdot \left(1 + R_{B,\beta} \cdot \frac{\epsilon_\beta}{R_{OA}} + R_{B,\gamma} \cdot \frac{\epsilon_\gamma}{R_{OA}}\right) = 54(15)\,\mathrm{kBq}. \tag{2.3.7}$$

In a first series the source was placed in the source holder. Two apertures in 7 mm and 29 mm away from the surface of the source were mounted. The source holder was attached to a linear feedthrough which was mounted in a horizontal tilter, which both together will be called manipulator flange. This manipulator flange was used to move the source in the x-y-plane. In a second measurement, the two apertures have been removed for a measurement with the uncollimated source. Fig. 2.30 shows a picture of the alpha source placed in the source holder without the two apertures. The source holder was on ground potential.

About the actual features of the source we only know little. In the info sheet of the source that was provided by the CERN Radiation Protection Sources Group, it is written that the americium oxide is fixed in the silver foil. The method is not described further and it is not said in what depth the ions are fixed or how the activity is distributed over its surface. To secure the handling of the source it has a protective sealing of 1.8 μm of Pd. Due to that Pd sealing the alphas will suffer energy loss when they leave the source. The energy distribution of the alphas leaving the source has been measured for another source (4257RP) that is identical in specifications to the one we're using in this calibration (4263RP). A plot of that spectrum was provided by the CERN Radiation Protection Sources Group. This is shown in fig. 2.31. We see that the energy of the ions is distributed around a mean value of about 4.8 MeV.

Alpha particles (with energies of approx. 5.5 MeV) that pass this layer have a small probability to interact with the ions in that layer and can create secondary ions. To investigate this simulations with the software called SRIM/TRIM (SRIM stands for *The Stopping and Range of Ione in Matter*), were performed. For this simulation we assumed 10000 He^{2+} ions with an energy of 5485 keV shot through a 1.8 μm Pd foil. The He^{2+} ions were tracked from one side of the foil to the other. First we draw the energy spectrum of the ions that reached the other end of the foil. This is shown in fig. 2.32 [Zbo12]. The energy distribution looks similar to the one shown in fig. 2.31 also with a

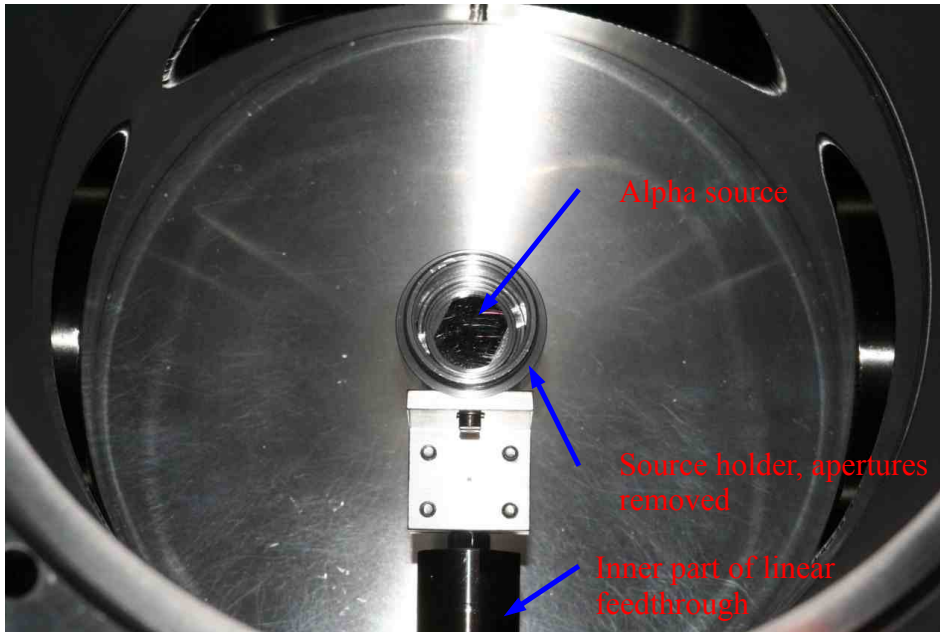**Figure 2.30.:** Picture of the ^{241}Am source that is placed in the source holder, attached to a linear feedthrough to move the source in one dimension.
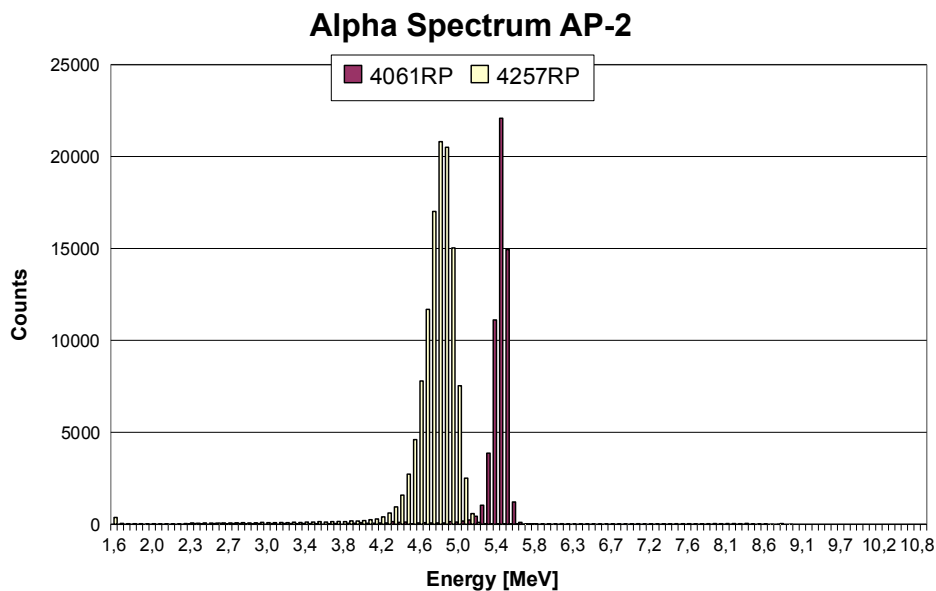

Figure 2.31.: Measured spectrum of sources 4257RP and 4061RP as provided by the CERN Radiation Protection Sources Group. This source 4257RP is identical in its specifications to the one used for this calibration (4263RP). Taken from ref. [Cer12].

mean value of about 4.8 MeV but more narrow. This is understandable if we consider that we did not simulate the whole ^{241}Am spectrum but only the major energy contribution with about 85%. From this we conclude that the assumption that the ^{241}Am atoms are fixed on the surface of the silver foil is valid.
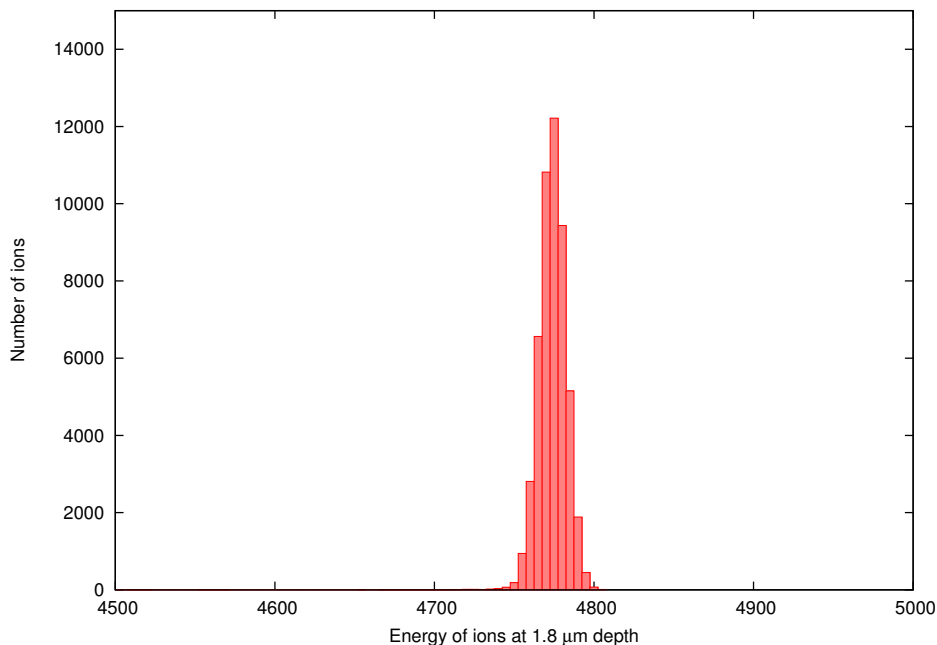
Figure 2.32.: Kinetic energy spectrum of 10000 He^{2+} ions with an energy of 5485 keV shot through a 1.8 µm Pd foil after leaving the foil on the other side [Zbo12].

The SRIM program calculates the probability that a Pd ion is sputtered with about 2‰. These ions leave the Pd foil with identical probabilities in both directions [Zbo12]. This means for about every 1000 alphas one Pd ion is created that is emitted towards the detector. So we can estimate the rate of these Pd ions as

$$R_{Pd} = 0.001 \cdot A_S = 20 \, \text{Hz}. \tag{2.3.8}$$

2.3.1.2. The detector test chamber

For the calibrations the detector was placed in the detector test chamber, located on the upper WITCH platform next to the cryostat. This chamber is identical in construction to the detector chamber on top of the cryostat but has additionally a 251 mm elongation on top in which the detector is placed. On the side of the chamber a penning gauge is installed. During the measurements the gauge was switched off. The pressure was determined to be below $1 \cdot 10^{-6}$ mbar before and after each series of measurements.

The ^{241}Am alpha source was placed in a source holder. The surface of the source is 70 mm away from the MCP. For the measurements with a collimated source two apertures with 4 mm diameter holes were used. The distance from the source to the first aperture is 7 mm and from the source to the second aperture it is 29 mm. The source holder was attached to a manipulator flange. It consists of a linear feedthrough, which was build in on a horizontal tilter. This allows to move the source in a plane that is parallel to the MCP surface. The motion was controlled by two step motors, that were addressed by a LabView based software. The motion of the manipulator flange was calibrated in Münster with the help of the KATRIN 3D measuring machine for the assurance of the wire combs of the KARTIN main spectrometer. A picture of the manipulator flange at the calibration measurement of the linear and the angular motion of the manipulator in the clean room in Münster is shown in fig. 2.33.
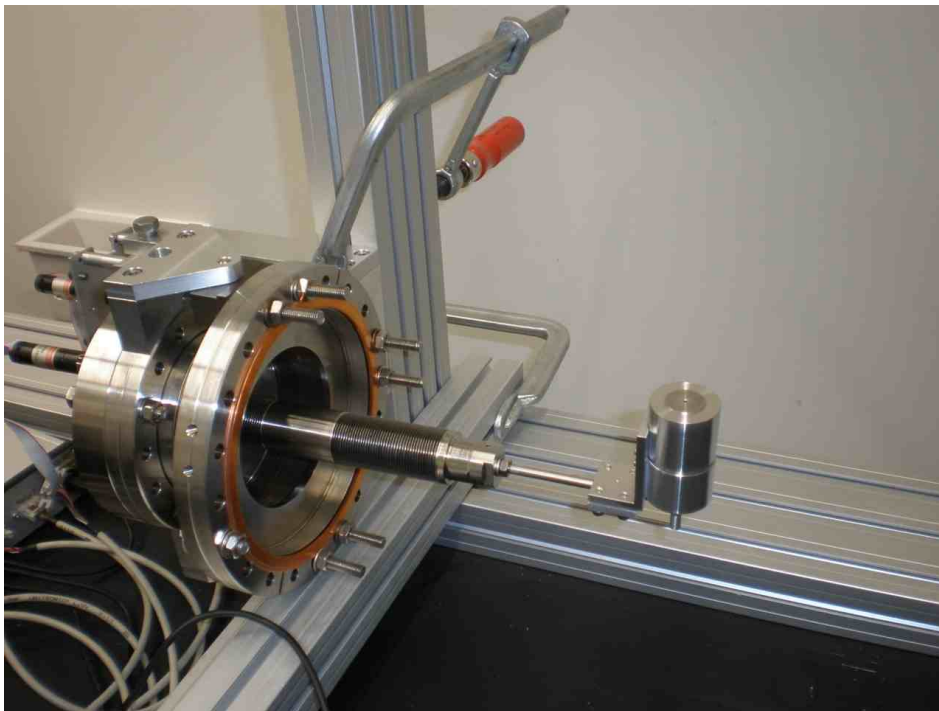
Figure 2.33.: Picture of the manipulator flange in the KATRIN 3D measuring machine for the quality assurance of the wire combs of the KARTIN main spectrometer in the clean room in Münster.

Unfortunately it turned out that the position of the source was not precisely reproducible under vacuum. We observed a jitter of approx. 2 mm of the spot in the position of the source on the MCP when it was send to identical positions. Fig. 2.34 shows two measurements, where the source was sent to identical coordinates. Comparing the right image with the left one, the position of the spot jitters about 2 mm to the bottom left corner. A similar behavior was observed independently of in which direction the source has been moved. Consulting an engineer we found that both, the

linear feedthrough and the tilter have play. This has not been observed during the calibration in Münster on atmosphere. Probably an incident during the transport or the installation caused this malfunction or the forces on the bellows under vacuum. Anyway, this means that the position information of the measurement with the collimated source is not trustworthy. But to calibrate the efficiency in that spot the measurements are still suitable. For a dedicated test of the spatial resolution the data is not good enough as we observe fluctuations in the spot size and the statistic is too low.
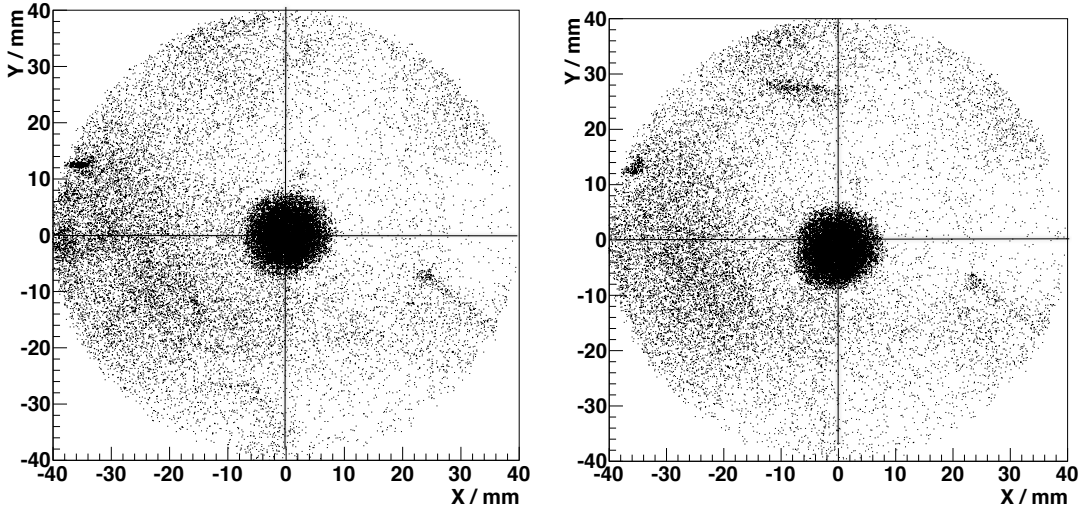

Figure 2.34.: Position distributions of two measurements with the collimated source placed in the source holder, attached to a linear feedthrough to move the source in one dimension. The right measurements was performed a few hour after left one. In the right image the spot from the source is shifted to the bottom left corner by about 2 mm. The lines at X = 0 and Y = 0 are there to guide the eye.

2.3.2. Detector settings

During the calibration the voltage at the MCP front was set to $U_{in} = -3250$ V with respect to ground potential. Thus, according to the voltage divider shown in fig. 2.21, the potential difference between the front and the back of the MCP stack was $U_{FB} = -2480$ V. The MCP back signal is used as the main MCP signal. The signal was amplified by a factor of 60 using the amplifier FAMP1+. As discriminator for the main signal the CFD1x was used, which also provides the pulse height information.

The distribution of the pulse heights of the main signal, the so-called Pulse Height Distribution (PHD) can be an indication for the type of radiation that was detected with the MCP. Alphas and ions (with energies over 3 keV) create predominantly large pulses. Thus the PHD is moved towards larger energies and has a Gaussian-like shape [Lie05]. The reason for this is that these particles interact early at the beginning of the channel, while betas and gammas have a higher probability to penetrate through the channel walls and interact further in the next channel. Thus their PHD is moved to lower energies and has a more narrow shape with a maximum at lower amplitudes and a long tail towards higher amplitudes.

The delay line signals were amplified two times by a factor of 10 in the LeCroy 612 A module by using two channels in series for each signal. The output of the first channel was connected with a 1 ns cable to the input of the second channel. Thus we achieved an amplification factor of 100 in total. The actual delay and fraction settings of the CFD1x are already described in section 2.2.5.1.

The amplification factors and threshold settings along with the used modules for each channel are listed in tab. 2.9. As we would expect the outer delay line (Y) shows a larger signal then the inner one (X), since it is closer to the MCP and the inner delay line is shielded by the outer one. The differences in the discriminator thresholds of the delay lines are due to the different noise levels. Especially X2 shows a high noise level, which could not be reduced by changing cables, amplifier or discriminator channels. Thus the noise has to be picked up inside the vacuum chamber or being created in the FT12TP. X1 and Y2 have the lowest noise while Y2 is somewhat intermediate.

Table 2.9.: Amplification factors and threshold settings of the main MCP and delay line signals as used during the calibration. Listed are also the amplifier and discriminator modules.

Channel	Amplification Factor	Amplifier Module	Threshold	Discriminator Module
MCP-Back	60	Roentdek FAMP1+	- 200 mV	Roentdek CFD1x
X1	100	LeCroy 612 A	-430 mV	LeCroy 821 CS
X2	100	LeCroy 612 A	-490 mV	LeCroy 821CS
Y1	100	LeCroy 612 A	-460 mV	LeCroy 821
Y2	100	LeCroy 612 A	-430 mV	LeCroy 821 CS

2.3.3. Recorded information in 2011

Each recorded event in the CAMAC DAQ contains the following information:

- 1 trigger number information. A counter increases by 1 when it gets a trigger from the MCP back signal. This variable will be called N_S.

- 1 pulse height information encoded in the time delay between the start trigger signal from the MCP back and a separate stop signal. The CFD1x creates a delay depending on the pulse height of the MCP back signal which is recorded wit the CAMAC TDC module. This variable will be called A_{PH}.

- 2 timing informations for each delay line, 4 in total. This is the stop time – after the start time, set by the MCP main read-out – that the charge pulse arriving at a certain position on the delay line needs to travel to each end. The length of one delay line is roughly 90 ns for 80 mm. These 80 mm are discretized in the CAMAC TDC with 1800 channels. Thus the upper limit for the position resolution is given by the ratio $\frac{80\,\mathrm{mm}}{1800} \approx 0.05\,\mathrm{mm}$. This is below the limit of 0.1 mm given by the manufacturer. These four time informations will be called t_{x1}, t_{x2}, t_{y1} and t_{y2}. Histograms of the individual X1, X2, Y1 and Y2 events for the measurement with the uncollimated source are shown in fig. 2.35.

From these variables first ROOT TTrees containing the following informations were created:

- The differences of the two corresponding delay line times: $t_{dx} = t_{x1} - t_{x2}$ and $t_{dy} = t_{y1} - t_{y2}$. This is the actual position information. Two histograms for the time differences t_{dx} and t_{dy} for the measurement with the uncollimated source are shown in fig. 2.36. In both histograms the events are distributed approx. in $[-90\,\mathrm{ns}, 90\,\mathrm{ns}]$. The position distribution on the detector will be derived by plotting t_{dy} versus t_{dx} (see fig. 2.46). This will be discussed in detail in sec. 2.3.7.
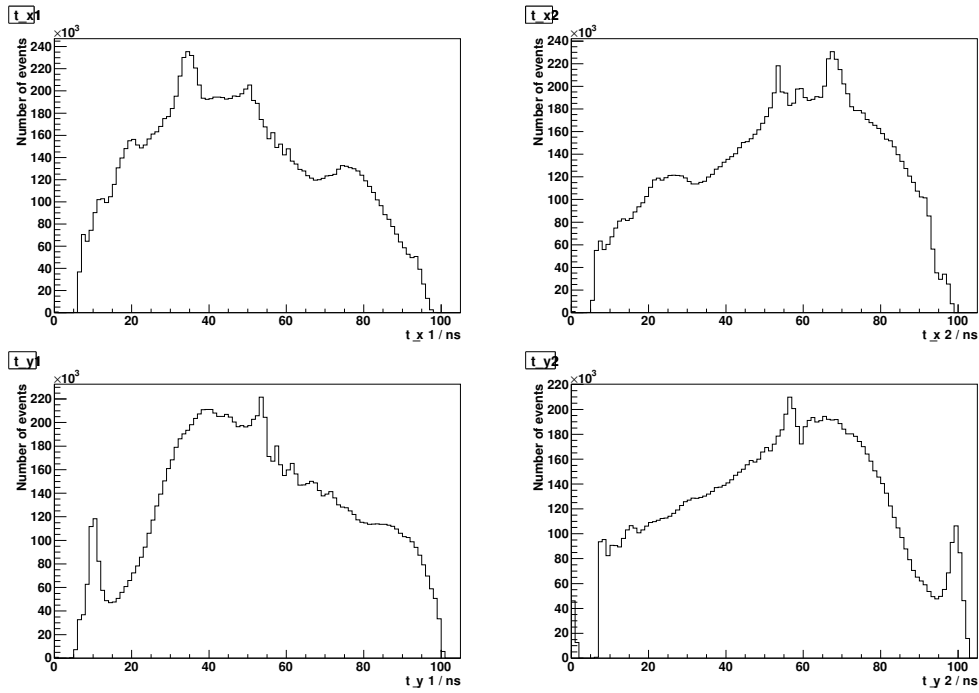
Figure 2.35.: Histograms of the individual t_{x1}, t_{x2}, t_{y1} and t_{y2} events for the measurement with the uncollimated source. The events spread over approx. 90 ns.
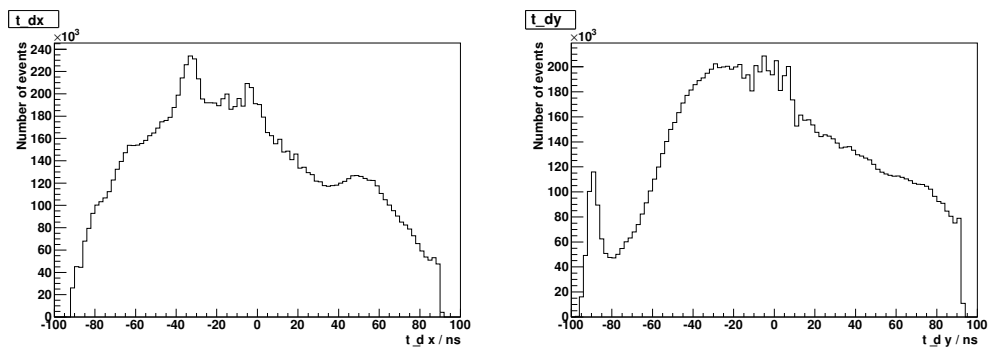

Figure 2.36.: Histograms of t_{dx} (left) and t_{dy} (right) in the range where the cut in fig. 2.47 has been placed. The events spread over approx. 90 ns.

- The sum of the two corresponding delay line times: $t_{sx} = t_{x1} + t_{x2}$ and $t_{sy} = t_{y1} + t_{y2}$. These sums should in principle be constant and show a well defined peak. This peak becomes broadened due to the walk of the discriminators and the use of a leading edge discriminator in stead of a CFD for the delay line signals. This information can be used to cut out artifacts created by noise or timeouts on one channel.
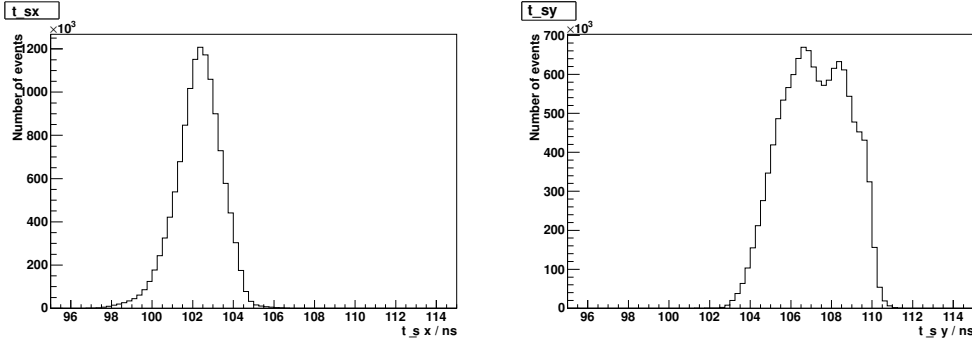

Figure 2.37.: Histograms of t_{sx} (left) and t_{sy} (right) in the range where the cut in fig. 2.47 has been placed. t_{sx} shows a symmetric peak with a FWHM of about 3 ns and a longer tail to the left side then to the right. t_{sy} shows a broader distribution and it has a double peak and a FWHT of about 6 ns.

Fig. 2.37 shows histograms of the sums t_{sx} and t_{sy} of the measurement with the uncollimated source. t_{sx} has a symmetric peak with a FWHM of about 3 ns and a longer tail to the left side then to the right. t_{sy} shows a broader distribution and it has a double peak and a FWHT of about 6 ns.

To find the origin of this double peak, we plot t_{dy} vs. t_{sy}. This way we can see which part of the detector contributes to which part of the sums t_{sy}. In fig. 2.38 scatterplots of t_{dx} vs. t_{sx} and t_{dy} vs. t_{sy} are shown. t_{dx} vs. t_{sx} has tails at the top, the bottom and slightly below the center. These tails are responsible for the long tails in the t_{sx} histogram. t_{dy} vs. t_{sy} shows a wobble which explains the double peak structure of the t_{sy} histogram. The events in approx. $t_{dy} \in [90\,\mathrm{ns} : -20\,\mathrm{ns}]$ contribute to the first peak, the events in approx. $t_{dy} \in [-20\,\mathrm{ns} : -90\,\mathrm{ns}]$ to the second peak. A reason for this could be the use of leading edge discriminators.

- The radial time position: $t_r = \sqrt{(t_{x1} - t_{x2})^2 + (t_{y1} - t_{y2})^2}$. This is the radial position of an event and can be used to cut out artifacts occurring on the outer ring. Fig. 2.39 shows a histogram of the radius t_r of the events of the measurement with the uncollimated source.

- The pulse height A_{PH} as described above. Fig. 2.40 shows a histogram of the pulse height A_{PH} of the MCP back signal of the measurement with the uncollimated source. The threshold was set to -200 mV, where the distribution is cut on the left.

- The corrected CAMAC counter information N'_S as described in sec. 2.3.4.

Tab. 2.10 lists the X and Y position of the collimated source, number of recorded events N_E, number of scaler counts N'_S, the calculated dead time correction factor $f_{dt} = \frac{N'_S}{N_E}$, measurement time t_m and the count rate R_c for each measurement. N'_S is recorded by a scaler that increases each time the MCP main signal is triggered. N_E is the number of registered events (with complete position information) in the corresponding data file. For details on the calculation of the dead time correction factor and the corrected scaler counts N'_S see sec. 2.3.4. Note that measurement 14 with the collimated source is corrupted and could not be used for the data analysis.
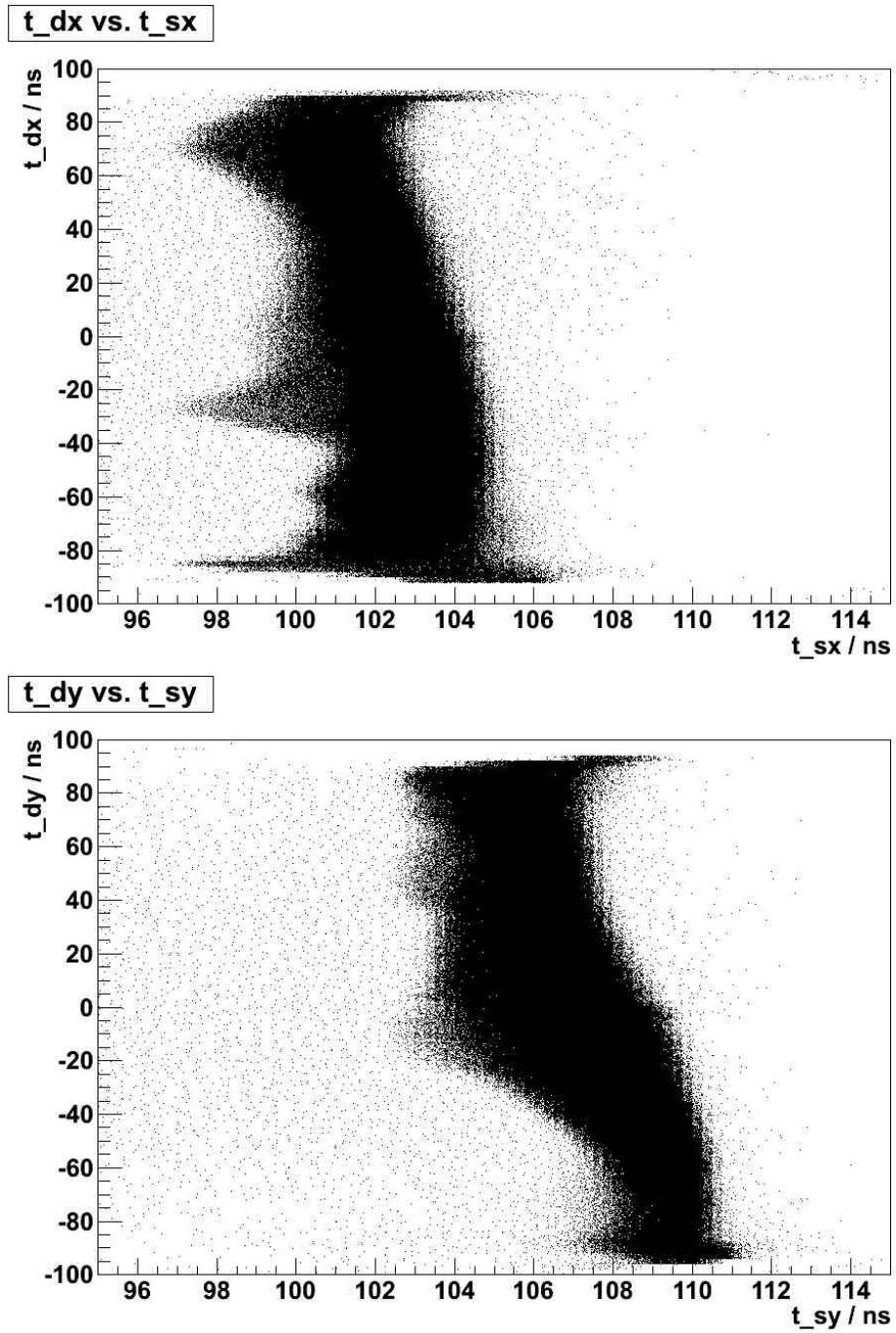
Figure 2.38.: Scatter plots of t_{dx} vs. t_{sx} (top) and t_{dy} vs. t_{sy} (bottom). t_{dx} vs. t_{sx} has tails at the top, the bottom and slightly below the center. These tails are responsible for the long tails in the t_{sx} histogram. t_{dy} vs. t_{sy} shows a wobble which explains the double peak structure of the t_{sy} histogram. The events in approx. $t_{dy} \in [90\,\text{ns} : -20\,\text{ns}]$ contribute to the first peak, the events in approx. $t_{dy} \in [-20\,\text{ns} : -90\,\text{ns}]$ to the second peak.
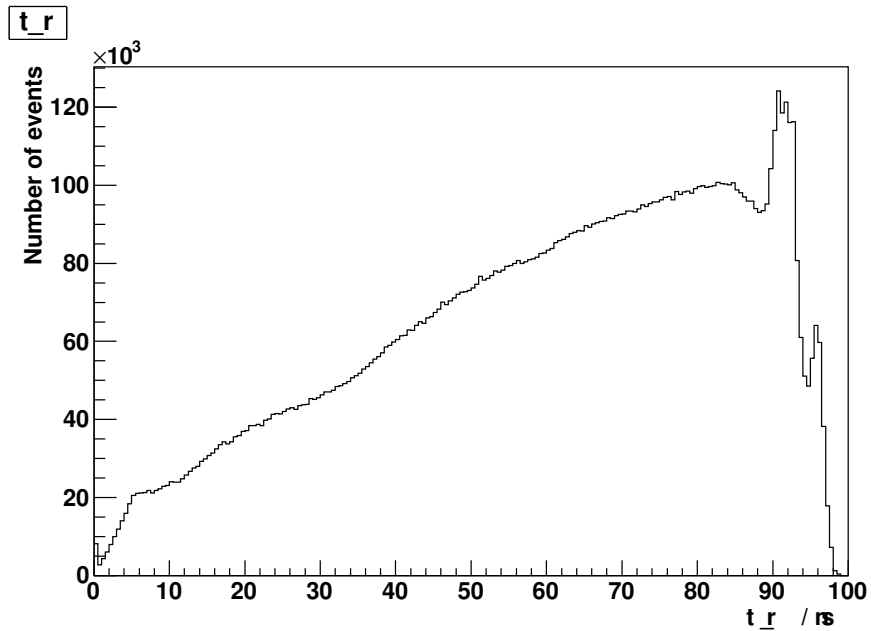
Figure 2.39.: Histogram of the radius t_r of the events of the measurement with the uncollimated source. The threshold was set to -200 mV. The events spread over roughly 100 ns.
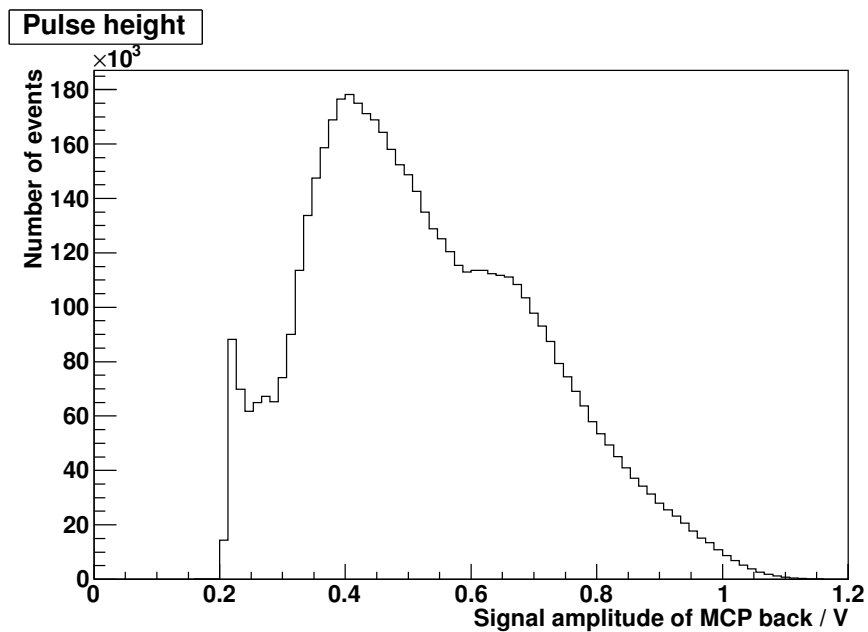
Figure 2.40.: Histogram of the pulse height A_{PH} of the MCP back signal. The threshold was set to -200 mV, which is where the distribution starts. The tail of the distribution reaches up to about 1.2 V.

63

Table 2.10.: List of the X and Y position of the collimated source, number of recorded events N_E, corrected scaler counts N'_S, the calculated dead time correction factor $f_{dt} = \frac{N'_S}{N_E}$, measurement time t_m the count rate $\dot{N}'_S = \frac{N'_S}{t_m}$ for each measurement and the dead time τ_{dead} (see eq. 2.3.10). Note that measurement 14 with the collimated source is corrupted and could not be used for the data analysis.

Measurement	X / mm	Y / mm	N'_S	N_E	f_{dt}	t_m / s	$\dot{N}'_S$ / Hz	t_{dead} / ms
Collimated source								
1	-35	-6	50285	40494	1.24	3902	12.89	18.76
2	-33	12	89935	75476	1.19	6345	14.17	13.53
3	-27	23	76177	68171	1.12	6672	11.42	10.29
4	-21	-27	38543	35410	1.09	4320	8.92	9.917
5	-18	-13	38824	34760	1.12	3596	10.80	10.83
6	-15	5	75378	69016	1.09	6613	11.40	8.09
7	-11	21	36100	33935	1.06	3816	9.46	6.74
8	-7	37	32378	28769	1.13	3440	9.41	13.32
9	-5	-36	29942	28325	1.06	3805	7.87	7.25
10	-3	-19	88280	82071	1.08	8831	10.01	7.56
11	-2	1	42247	39280	1.08	3751	11.26	6.706
12	2	17	71575	67564	1.06	9194	7.78	7.62
13	7	34	37745	35191	1.07	3866	9.76	7.43
15	13	-24	48294	45285	1.07	5926	8.15	8.153
16	18	-10	43823	37617	1.16	3864	11.34	14.55
17	20	8	27246	25664	1.06	3119	8.73	7.05
18	21	28	48841	45911	1.06	4495	10.86	5.87
19	30	-12	58426	55530	1.05	6174	9.46	5.51
20	37	3	26557	25339	1.05	3735	7.11	6.76
Background	-	-	$1.87 \cdot 10^5$	$1.80 \cdot 10^5$	1.04	36979	5.05	7.69
Uncollimated source	-	-	$1.26 \cdot 10^7$	$6.69 \cdot 10^7$	5.310	63115	200	4.07

2.3.4. Dead time correction

To take into account the dead time of the CAMAC DAQ due to readout and data storage, the signal from the MCP *Back* is being counted by a scaler and stored as N_S. Fig. 2.41 shows the number of scaler counts as function of the entry number in the CAMAC DAQ for different regions of the entry number. On the left the full range of the measurement is shown, right hand side we zoomed in to the first 1000 events. From this figure we can learn the following:

- The Scaler is a 24 bit scaler. Thus it gets a reset at $2^{24} \approx 1.68 \cdot 10^7$ (see fig. 2.41, left).

- The counting shows two different kinds of steps (see fig. 2.41, right) and has an offset of 2560 (see fig. 2.41 right). This can be explained due to the fact, that two bits cannot be reset and are constantly at 1. This offset can be written a the sum $2560 = 2048 + 512 = 2^{11} + 2^9$. This means that bit 9 and 11 are the wrong ones and thus the jumps appear always when these bits are set.

The wrong scaler bits can be corrected. Let's look to the beginning of the scaler sequence as it is shown in fig. 2.43 on the left hand. The scaler can have four different states, as it is indicated in
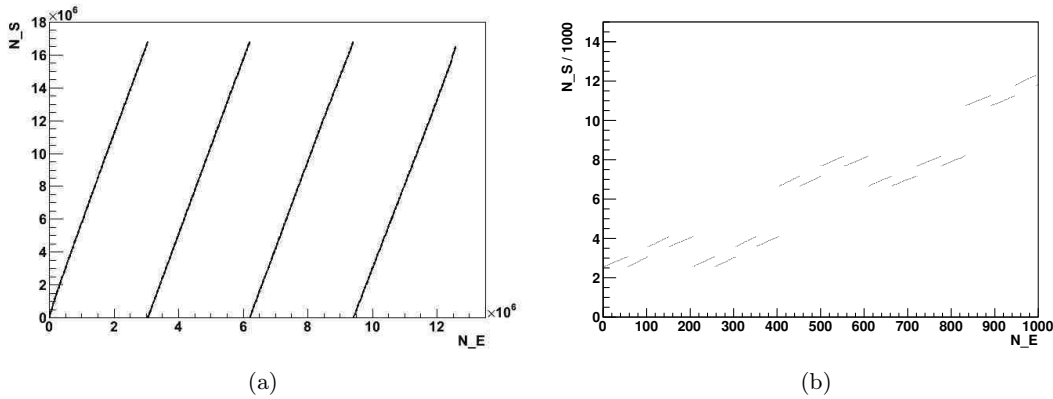
Figure 2.41.: Scaler counts as function of event number in the CAMAC DAQ for the measurement with the uncollimated source. Left hand side the region $N_E \in [0, 13 \cdot 10^6]$ is shown (a) and to the right we zoomed in to the region $N_E \in [0, 1000]$ (b) by what the two different types of steps the scaler makes are better visible.

that picture.

a) Bit 11 and bit 9 are wrong, we have to subtract 2560.

b) Bit 11 is wrong, bit 9 is right, we have to subtract 2048.

c) Bit 11 is right, bit 9 is wrong, we have to subtract 512.

d) Bit 11 and bit 9 are right, we have to subtract 0.

We define the actual state of the scaler for a certain event as Z_a and the state of the scaler in the event before as Z_v. The recorded scaler counts in the corresponding event will be called N_a and the recorded sealer counts in the event before will be called N_v. The scaler starts counting in state 1 with 2560 counts: $Z_v = 1$, $N_v = 2560$. With this we can define the actual scaler state Z_a by applying a case-by-case analysis:

Table 2.11.: Conditions to define the actual scaler state. Z_a is the new state to which the scaler will be set and Z_v is the state in which the scaler was before.

Condition	Actual scaler state
$Z_v = 1$, $N_a < N_v$	$Z_a = 2$
$Z_v = 2$, $N_a < N_v$	$Z_a = 3$
$Z_v = 2$, $N_a \geq (N_v + 512)$	$Z_a = 1$
$Z_v = 3$, $N_a < N_v$	$Z_a = 4$
$Z_v = 4$, $N_a \geq (N_v + 2560)$	$Z_a = 1$
$Z_v = 4$, $(N_v + 2560) > N_a \geq (N_v + 512)$	$Z_a = 3$
All other cases	$Z_a = Z_v$

The first sequence of the four scaler states is shown in fig. 2.42. This sequence will be repeated periodically until the scaler reached its maximum number of counts. Using the list above in combination with the actual state of the scaler defined by tab. 2.11 we can correct the actual scaler

counts. The result is shown in fig. 2.43. To correct for the dead time we calculate a factor f_{dt} and take into account the systematic correction of the scaler as described before:

$$f_{dt} = \frac{N'_S}{N_E} \tag{2.3.9}$$

where N'_S is the corrected total number of counts registered by the CAMAC scaler and N_E is the total number of events registered by the CAMAC DAQ. This factor is listed in tab. 2.10 for every measurement taken. The dead time factor f_{dt} as function of the count rate is shown in fig. 2.44. It shows a fluctuating behavior with a rising tendency towards larger count rates. This is unexpected, the reason for this is probably a random dead time contribution from the CAMAC DAQ. Moreover we can now deduce the dead time τ_{dead} for each measurement. We start with the relation [Kno10]:

$$\dot{N'_S} = \frac{\dot{N_E}}{1 - \tau_{dead} \cdot \dot{N_E}}$$

$$\Rightarrow \frac{\dot{N_E}}{\dot{N'_S}} = 1 - \tau_{dead} \cdot \dot{N_E}$$

$$\Rightarrow \tau_{dead} = \left(\frac{1}{\dot{N_E}} - \frac{1}{\dot{N'_S}} \right) \tag{2.3.10}$$

with $\dot{N_E} = \frac{N_E}{t_m}$ and $\dot{N'_S} = \frac{N'_S}{t_m}$, where t_m is the measurement time.

Figure 2.42.: Scaler counts as function of event number in the CAMAC DAQ for the measurement with the uncollimated source. Shown is the uncorrected scaler information with the number of the actual state, the scaler is in for the first eight steps. This sequence will be repeated over and over again.
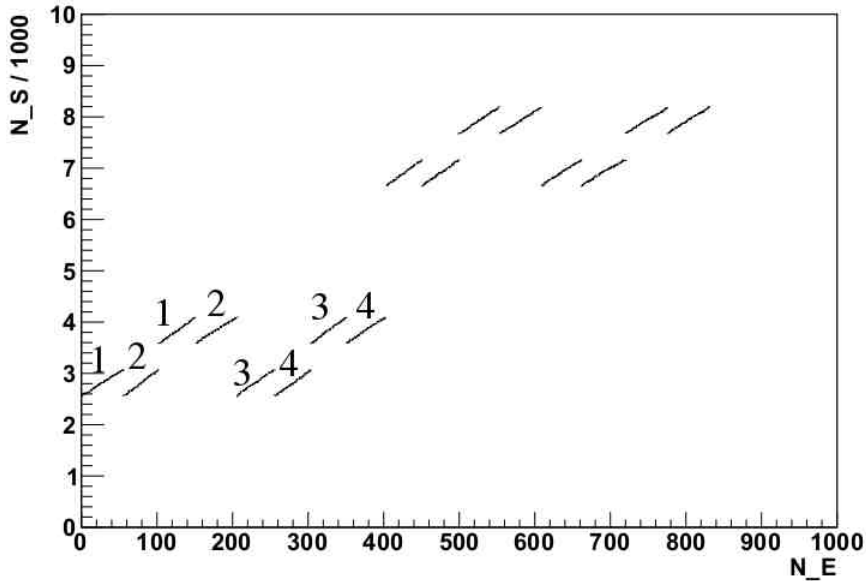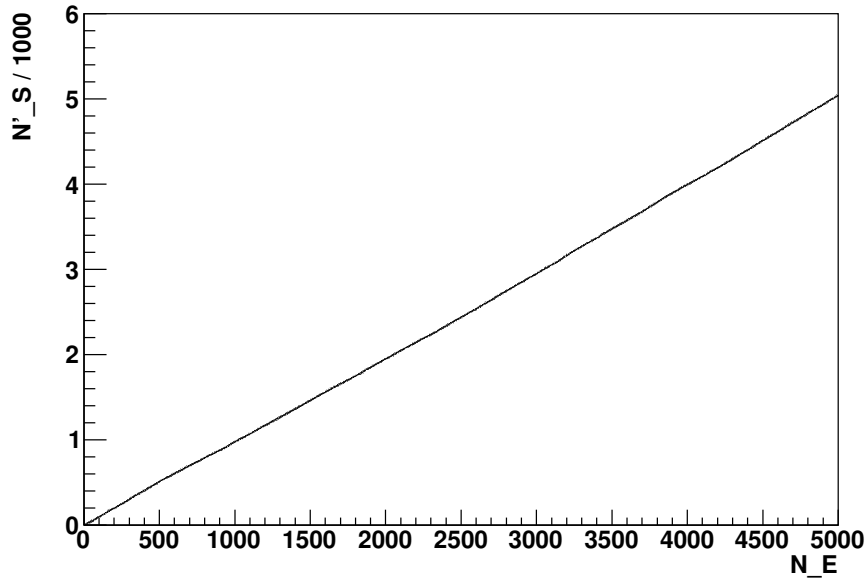
Figure 2.43.: Scaler counts as function of the event number in the CAMAC DAQ for the measurement with the uncollimated source. Shown is the corrected scaler information. As we can see, we can correct for the odd behavior and get a straight line as a result.
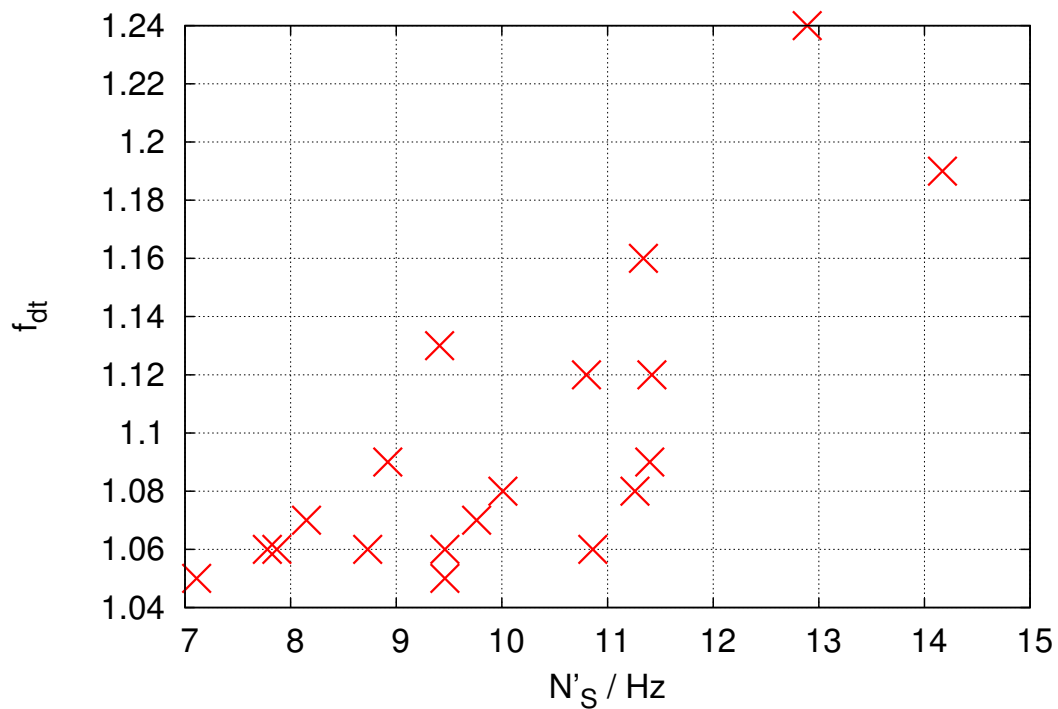

Figure 2.44.: Dead time correction factor f_{dt} as function of the count rate. These event scatter somewhat randomly, which is unexpected. The reason for this probably is probably an inappropriate programmed DAQ software in combination with a Windows XP operating system which is unsuited for such a purpose.

2.3.5. Background measurement

The background count rate of the MCP was measured:

$$\dot{N'}_{S,bg} = \frac{1.87 \cdot 10^5}{36979 \, \text{s}} = 5.05 \, \text{Hz} \tag{2.3.11}$$

where N_S is the corrected number of counts from the CAMAC scaler and t_m is the measurement time. The position distribution of the background counts accumulated in 36979 s is shown in fig. 2.45. In the left part of the detector one can see parts with more background counts and several small hot spots. To the right and at the bottom we see several parts with less count rate. To the left an area with more events appears. On the outer radius a ring of artifacts is visible in the upper half of the picture.
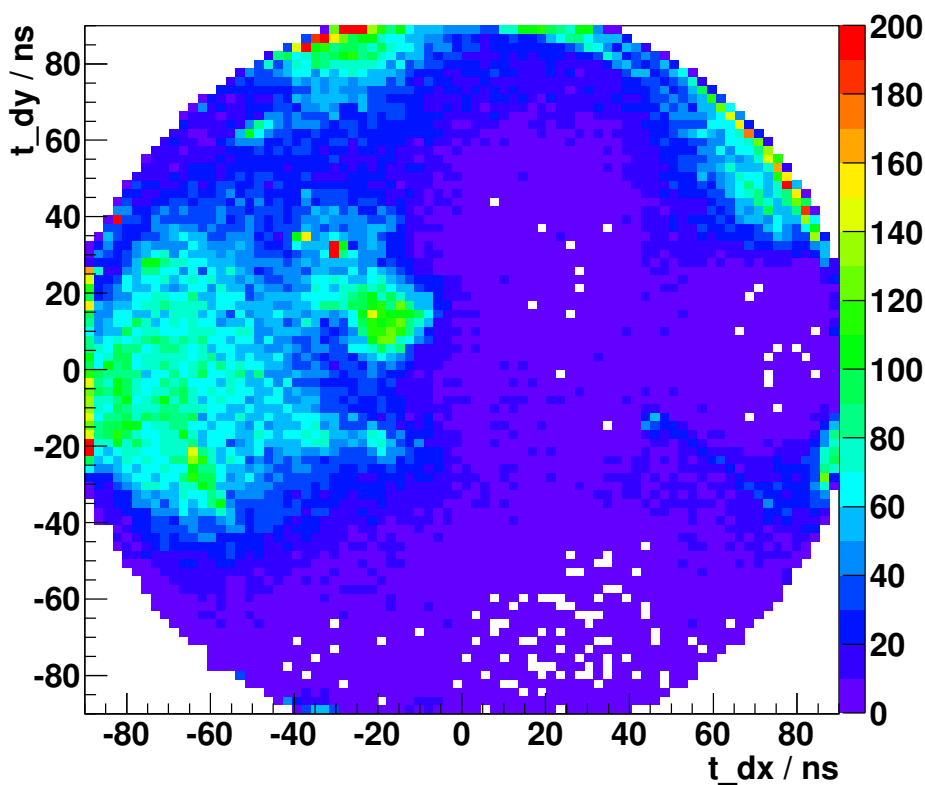

Figure 2.45.: Position distribution t_{dy} versus t_{dx} of the background measurement accumulated in a 36979 s measurement. The background events spread very unevenly over the detector surface. Most of the events show up on the upper left of the MCP and on a ring at the very outer radii on the upper half. At the very bottom and to the right only few background events are present.

2.3.6. Timeouts

A timeout is created when the TDC channel gets a start but no stop signal. Tab. 2.12 lists the total number of counts, the number timeouts and its ratio for all four delay line channels for the uncollimated measurement and the background measurement along with their durations and the time and date when the measurements were started.

Table 2.12.: Number of timeouts in each channel of the background measurement and the measurement with the uncollimated source. Besides this the date and stat time, the duration of the whole measurement and the total number of events are listed.

	Uncollimated source	Background
Date	12/10/11	11/10/11
Start time	21:00	22:45
Duration / s	61335	36979
Channel	Number of timeouts	Number of timeouts
X_1	7973	2389
X_2	7427	2131
Y_1	12977	3934
Y_2	154264	13285
X_1 and X_2	7371	2113
Y_1 and Y_2	7289	2086
Total events	12570089	197349

We see that the amount of timeouts for the measurement with uncollimated source is dominated by the Y_2-channel which has approx. 1.2% timeouts. This is due to a higher threshold setting on the Y_2-channel, which was necessary to be above the noise level and avoid double pulses. All channels have less then 0.2% timeouts in that measurement. For the background measurement the amount of timeouts is higher. Here again the Y_2-channel shows the most timeouts but the amount is 6.7%. This can be explained by the fact that background pulses have predominantly smaller amplitudes and alphas with several MeV energy like from the ^{241}Am create in average very large pulses.

2.3.7. Measurement with the uncollimated source in 2011

For the efficiency calibration of the detector the measurements listed in tab. 2.12 were used. The step-by-step procedure to calculate the relative efficiency over the surface of the detector is described below.

2.3.7.1. Relative detection efficiency

To reconstruct the position of an event in one dimension we calculate the difference in the arrival times at the both ends of the delay line, e. g. $t_{dx} = t_{x1} - t_{x2}$. Each delay line has a length of approx. 90 ns. Thus the events will be distributed in one dimension in $t_{dx} \in [-90 \, \text{ns}, 90 \, \text{ns}]$. The active radius of our MCP is 41.5 mm. To convert the measured time difference into a spatial distance, one needs to multiply the time t_{dx} with a conversion factor:

$$f_c = \frac{83 \, \text{mm}}{180 \, \text{ns}} = 0.46 \, \frac{mm}{ns} \tag{2.3.12}$$

Applying the same procedure to the other dimension t_{dy} and displaying the events in a 2-dimensional histogram where t_{dy} is drawn versus t_{dx} one can create a two-dimensional position picture. This way the orientation is defined by the location of the ends of the delay lines: X1 is left, X2 is right Y1 it the top and Y2 the bottom. These are marked outside on the edge of the detector flange and it has been confirmed by the measurement.

To get a rough estimate of the position resolution let's have a look on the sum of the arrival times. Let's take for instance the x-coordinate. As explained before we would in principle expect a sharp peak at a defined position which is broadened by the signal processing. For the standard deviation of this peak we find the following relation:

$$\sigma_{sx}^2 = \sigma_{x1}^2 + \sigma_{x2}^2 = \sigma_{dx}^2 \tag{2.3.13}$$

So we see that the standard deviation of the sums of two corresponding delay line signals should be equal to the one of the differences. Since the position is encoded in the difference of the signals (e. g. t_{dx}) this will give an estimate on the position resolution. t_{sx} has a standard deviation of about $\sigma_{sx} = 1 \, \text{ns}$ (compare fig. 2.37). Utilizing the conversion factor from eq. 2.3.12 we find:

$$\Delta x = \sigma_{sx} \cdot f_c \approx 0.5 \, \text{mm} \tag{2.3.14}$$

From now on we describe stepwise how to get to the final efficiency calibration. Each step performed in this calibration will be documented with a separate figure. We start with the measurement with the uncollimated source. Drawing the differences of the timing information $t_{dx} := t_{x1} - t_{x2}$ and $t_{dy} := t_{y1} - t_{y2}$ for each delay line in a two-dimensional histogram results in the graph shown in fig. 2.46. Note that the maximum in this histogram has been limited to 250.
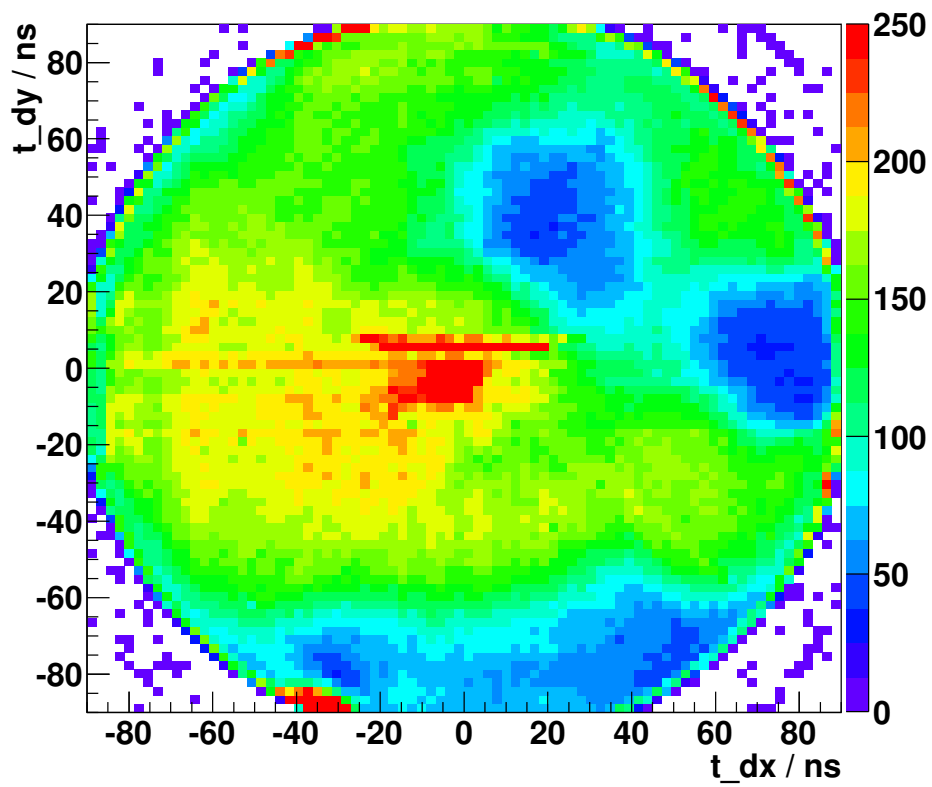
Figure 2.46.: Two-dimensional histogram with the differences of the timing information t_{dy} versus t_{dx} for the measurement with the uncollimated source.

One can see a dominant peak close to the center, that is shifted a bit to the left and to the bottom. Hotspots and a ring of small artifacts on the edges. In between there are areas showing more or less intensity. In the four corners one can see some noise and in the center above the peak there is a dominant straight line parallel to the x-axis crated by timeouts on one delay line. The propagation time of both corresponding signals e. g. $t_{sx} := t_{x1} + t_{x2}$ and $t_{sy} := t_{y1} + t_{y2}$ should in principle be constant. Due to effects of the electronics e. g. the walk caused by the discriminators, these sums are broadened. Fig. 2.37 shows histograms for the two sums of the arrival times of the two corresponding ends of the delay line t_{sx} and t_{sy}. The sums for the x-coordinate have a Gaussian shape. The sums of the y-coordinate show a double peak structure. The artifacts in fig. 2.46 can be eliminated by setting a condition to the sums of the delay line times: $t_{sx} \in [95\,\text{ns}, 115\,\text{ns}]$, $t_{sy} \in [95\,\text{ns}, 115\,\text{ns}]$. The result is shown in fig. 2.47.
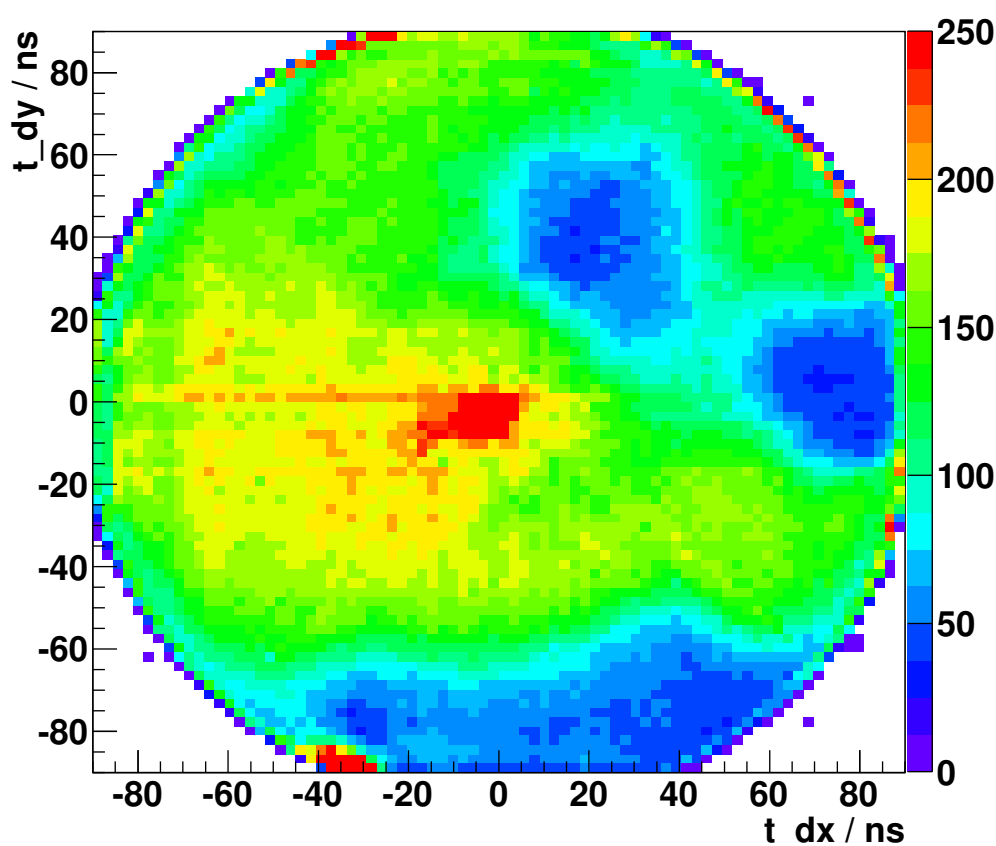

Figure 2.47.: Two-dimensional histogram with the differences of the timing information t_x and t_y with a cut on the sums of the signal traveling time: $t_{sx} \in [95\,\text{ns}, 115\,\text{ns}]$, $t_{sy} \in [95\,\text{ns}, 115\,\text{ns}]$.

In fig. 2.48 the outer ring with artifacts has been cut out by the conditions $t_r := \sqrt{t_{sx}^2 + t_{sy}^2} \leq 85.5$ ns. Moreover the time coordinates t_{dx} and t_{sy} were transformed into spatial coordinates by applying the conversion factor from eq. 2.3.12.
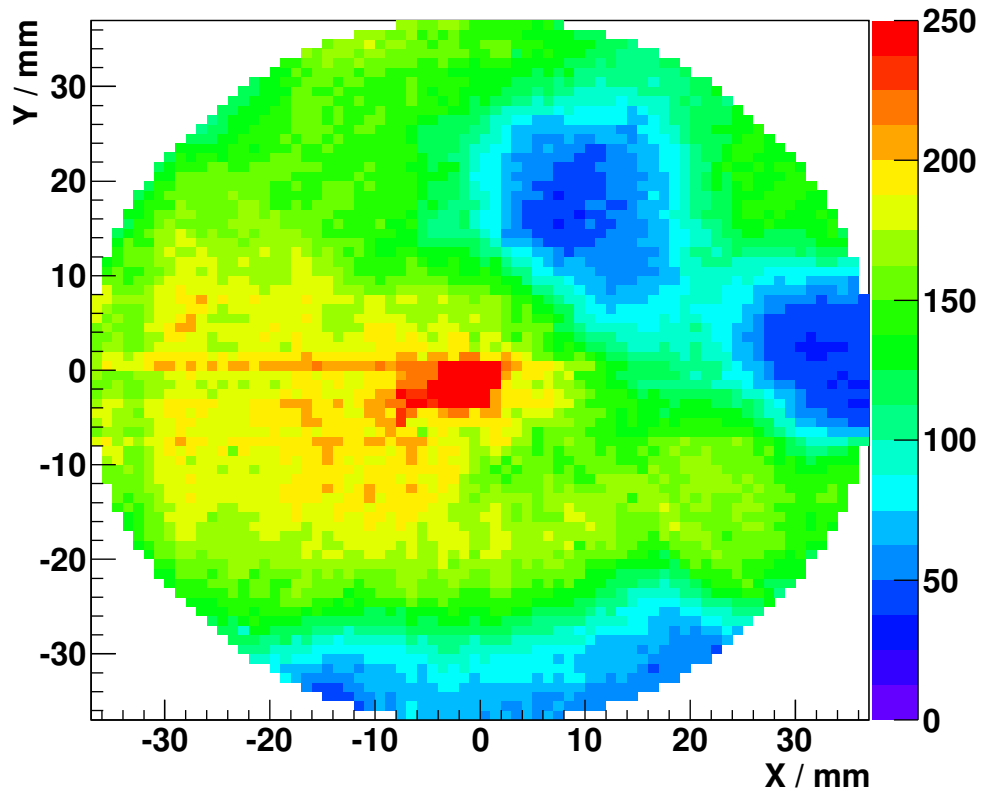
Figure 2.48.: The same two-dimensional histogram like in fig. 2.47 but with an additional cut on the outer radius $t_r \leq 85.5$ ns. The dimensions of x and y scale have been changed to mm by multiplying with the conversion factor $f_c = 0.46 \frac{mm}{ns}$.

In fig. 2.49 we subtracted the background normalized to the measurement time and the dead time factor from tab. 2.10.

Figure 2.49.: The same two-dimensional histogram as in fig. 2.48 but with subtracted background.

Figure 2.50.: Schematic drawing of how the radial dependency of the source intensity on the surface of the MCP or two different radii R_1 and R_2. See text for details.
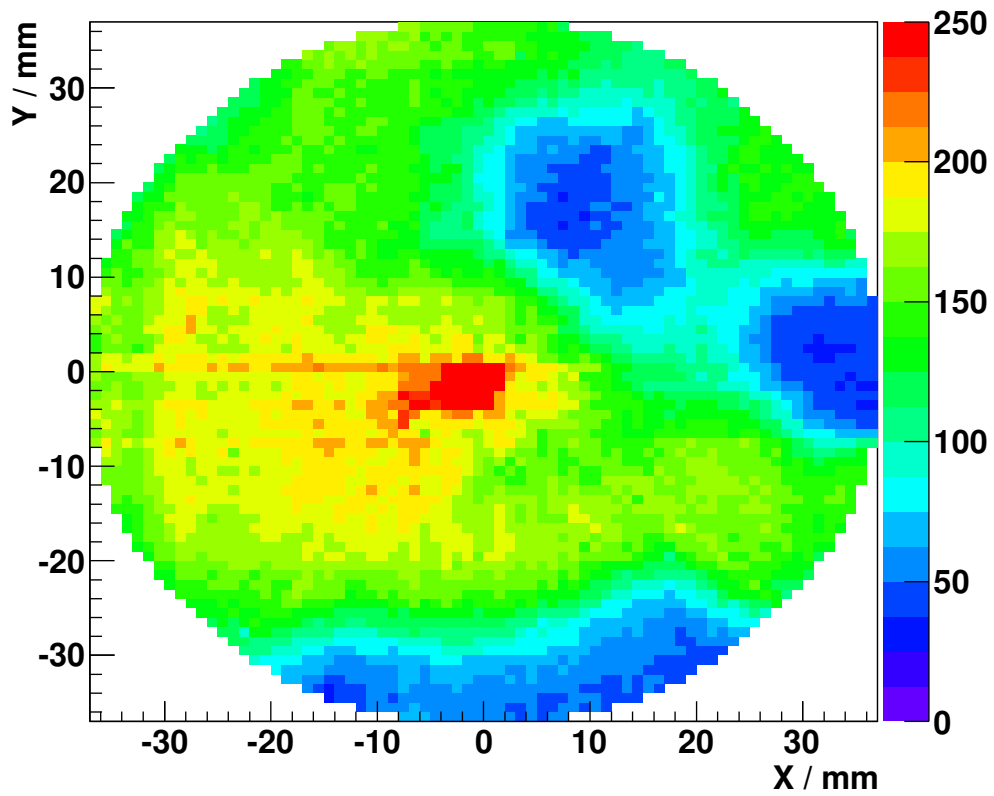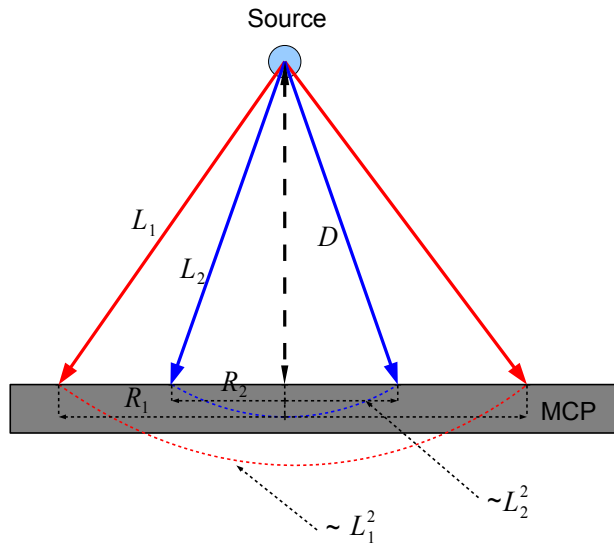
In the next step we take into account the distance from the source by dividing the measured intensity on the detector by the factor:

$$f_{dist} = \frac{D^2}{D^2 + R^2} = \frac{D^2}{L^2} \qquad (2.3.15)$$

where D is the distance between the source and the center of the MCP and R is the radial distance from the center of the MCP from which we calculate the distance from the source to the place at radius R as $L = \sqrt{D^2 + R^2}$. In other words: The intensity on the detector is inversely proportional to the distance from the source L squared. This is illustrated in fig. 2.50 for two different radii R_1 and R_2.
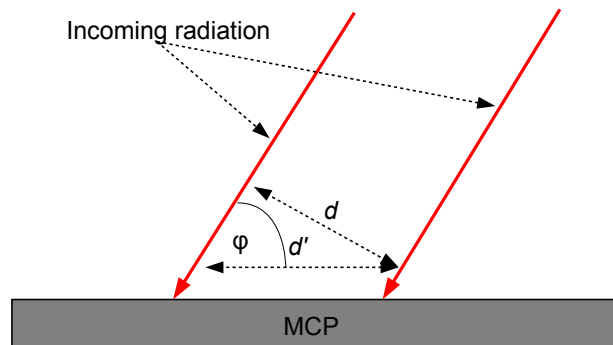

Figure 2.51.: Schematic drawing of how the angle of impact influences the intensity on the surface of the MCP. The smaller the angle φ gets, the larger becomes the surface ($\propto d' \propto \sin \varphi$) on which the intensity is distributed.

A second factor comes into play, which depends on the incidence angle φ. Let's have a look on fig. 2.51. The flux density of radiation coming from the source depends on the angle of incident. The flux density I_0 under an angle of $\varphi = 90°$ is larger than the flux density $I(\varphi)$ under an angle φ smaller than $90°$. This we consider by dividing the intensity by the factor:

$$f_{ang} = \frac{I(\varphi)}{I_0} = \frac{d}{d'} = \sin\varphi \tag{2.3.16}$$

If the angle φ becomes more shallow the same amount of incoming radiation is spread over a larger surface. If we apply analogue labeling as in fig. 2.50 we can substitute $d = D$ and $d' = L$, by what we can express $\sin\varphi$ by:

$$\sin\varphi = \frac{D}{L} = \frac{D}{\sqrt{R^2 + D^2}} \tag{2.3.17}$$

These two factors f_{dist} and f_{ang} we can combine as one factor f_{tot}:

$$f_{tot} = f_{dist} \cdot f_{ang} = \frac{R^2}{R^2 + D^2} \cdot \frac{D}{\sqrt{R^2 + D^2}} = \frac{R^2 \cdot D}{(R^2 + D^2)^{\frac{3}{2}}} \tag{2.3.18}$$

The resulting detector image is shown in fig. 2.52 where the intensity on the detector has been divided by the factor f_{tot}.
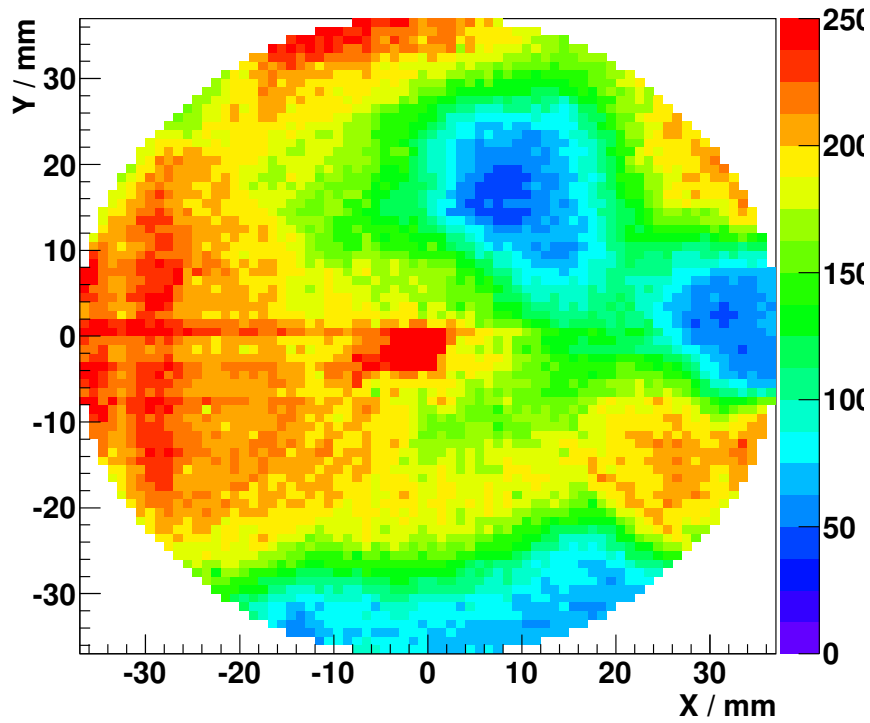

Figure 2.52.: Two-dimensional histogram of the intensity on the detector with subtracted background, normalized to the distance from the source and the angle of impact by division by a factor f_{tot} (see text for explanation). The time coordinates t_{dx} and t_{dy} have been transformed by multiplying with f_c (see eq. 2.3.12).

The origin of this central peak is not clear. We discussed two possible explanations:

- The manufacturer suggested the following explanation: Gamma photons coming from the source (see sec. 2.3.1.1) interact with the channel walls predominantly, when they shine into the channels, entering the channel parallel to its axis. Regrettably they did not provide a consistent explanation why the gamma photons should have a higher probability to interact when they shine into the channels [Roe12]. Their reasoning for this explanation is that the events in this peak have a low pulse height distribution (see section 2.3.7.2), which is true for gamma photons.

  Anyway, if the activity of the source is not spread homogeneously over the surface but concentrated in a defined spot this could result in a defined spot on the detector, given the assumption made above is true. It is well possible that the source disposes of a defined spot of activity due the production process, e. g. if the activity is implanted into the foil by an ion beam. If this explanation would be true one would expect the peak to occur in a distance from the center that is:

$$d_{peak} = D \cdot \tan \theta_{channels} = 10 \, \text{mm} \tag{2.3.19}$$

  where D is the distance from the source to the center of the MCP and $\theta_{channels}$ is the bias angle of the microchannels. Contrary to this we find the peak about 2–3 mm away from the center. The measurement is not consistent with this assumption. So either the explanation is not correct or the source or the spot of the activity is off-center by about 1 cm.

- However, we favor another explanation: The source is placed in the source holder and – since both are made from conductive material[5] – it is on ground potential. The front surface of the microchannel plates is on -3230 V with respect to ground potential. The source is sealed with a 1.8 μm Palladium layer (see also sec. 2.3.1.1). When alphas of an average energy of about 5.5 MeV penetrate this sealing they can sputter some of the Palladium ions which can then leave the foil in direction towards the detector. These ions will travel along the electric field lines towards the MCP and end up in a defined spot in the center. This is illustrated in fig. 2.53. In eq. 2.3.8 we estimated the rate of these Palladium ions form simulations with the program SRIM to be about 20 Hz.

  Now let's compare the count rate in the spot. Therefore we estimate the number of events in that peak. In the histogram for t_{dx}, shown in fig. 2.36 left, we can see the peak sticking out. We can roughly estimate the number of events in that peak as

$$N_{E,peak,2011} \approx 120000.$$

To calculate the count rate in this peak we have to divide this number by the measurement time $t_{m,uncoil.,2011}$ and multiply with the dead time factor $f_{dt,uncoll}$ from tab. 2.10:

$$\dot{N}_{S,peak,2011} = \frac{N_{E,peak,2011}}{t_{m,uncoll.,2011}} \cdot f_{dt,uncoll.} = 10 \, \text{Hz} \tag{2.3.20}$$

To compare this to the value from eq. 2.3.8 we have to divide eq. 2.3.20 by the open area ratio (eq. 2.2.3), which results in a count rate of about 20 Hz which agrees with the rate given in eq. 2.3.8.

Since these ions have three orders of magnitude less energy (about 3 keV if singly charged compared to a few MeV of energy of the alphas), it is expected that they create in average

---

[5]the source consists of a silver foil which is fixed to a stainless steel plate. The source holder is made of aluminum which is in electrical contact with the test chamber

smaller signals then the alphas. Anticipating one result that is shown in sec. 2.3.7.2, this is possibly the reason for the observation that the events in this peak have a smaller pulse height distribution.
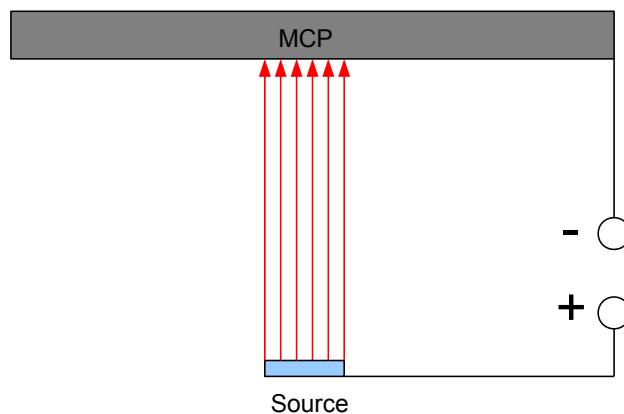
Figure 2.53.: The favored explanation for the peak in the center of the detector: The source is on ground potential and MCP *Front* is on −3230 V with respect to ground potential. The source is sealed by a 1.8 μm Palladium layer. Alpha particles with energy of about 5.5 MeV pass through this sealing and can create low energetic positively charged ions, which would travel along the electric field lines towards the detector and end up in a defined spot in the center.

The central peak will be eliminated by hand. The area that has been deleted from the center has approx. a width of 10 mm and a height of 5 mm and is shifted approx. 5 mm to the left and 2 mm to the bottom. The result is shown in fig. 2.54.

Figure 2.54.: Two-dimensional histogram of the intensity on the detector with subtracted background, normalized to the distance from the source and the angle of impact by division by a factor f_{tot} (see text for explanation). The time coordinates t_{dx} and t_{dy} have been transformed by multiplying with f_c (see eq. 2.3.12). The central park has been deleted by hand.

To reconstruct the content in the center we use linear interpolation. Finally we normalized on the maximum, such that the graph now describes the relative intensity. This is shown in fig. 2.55. The upper plot has a linear scale, the lower one a logarithmic scale. The mean value of the relative efficiency is:

$$\bar{\epsilon}_{rel,2011} = 0.61 \tag{2.3.21}$$

About 12% of the detector surface has $\geq 80\%$ relative efficiency, 1% has $\geq 90\%$ relative efficiency and approx. 33% of the surface has $\leq 20\%$ relative efficiency.
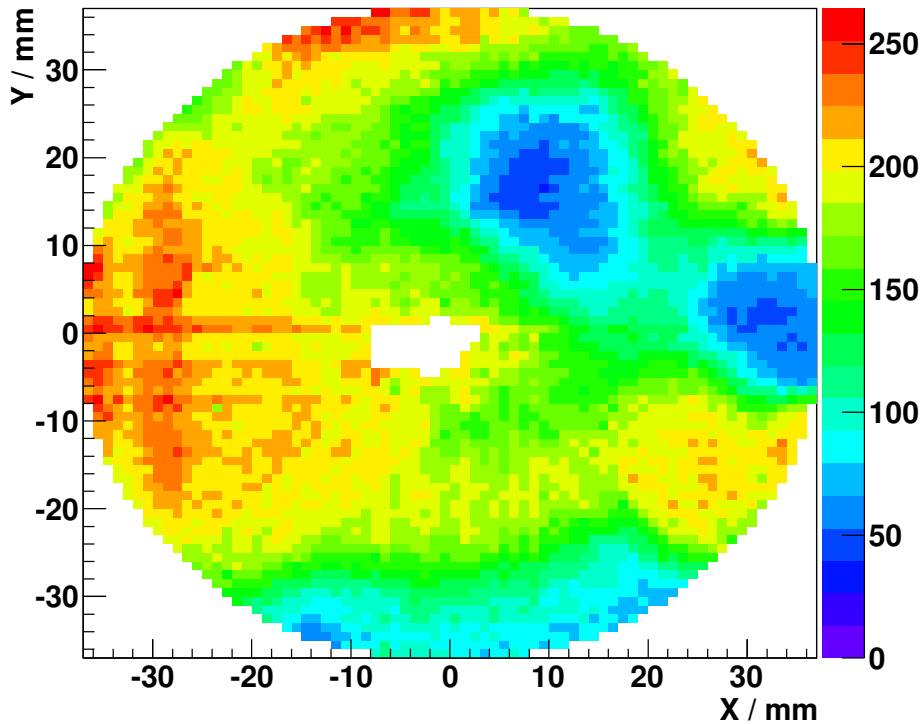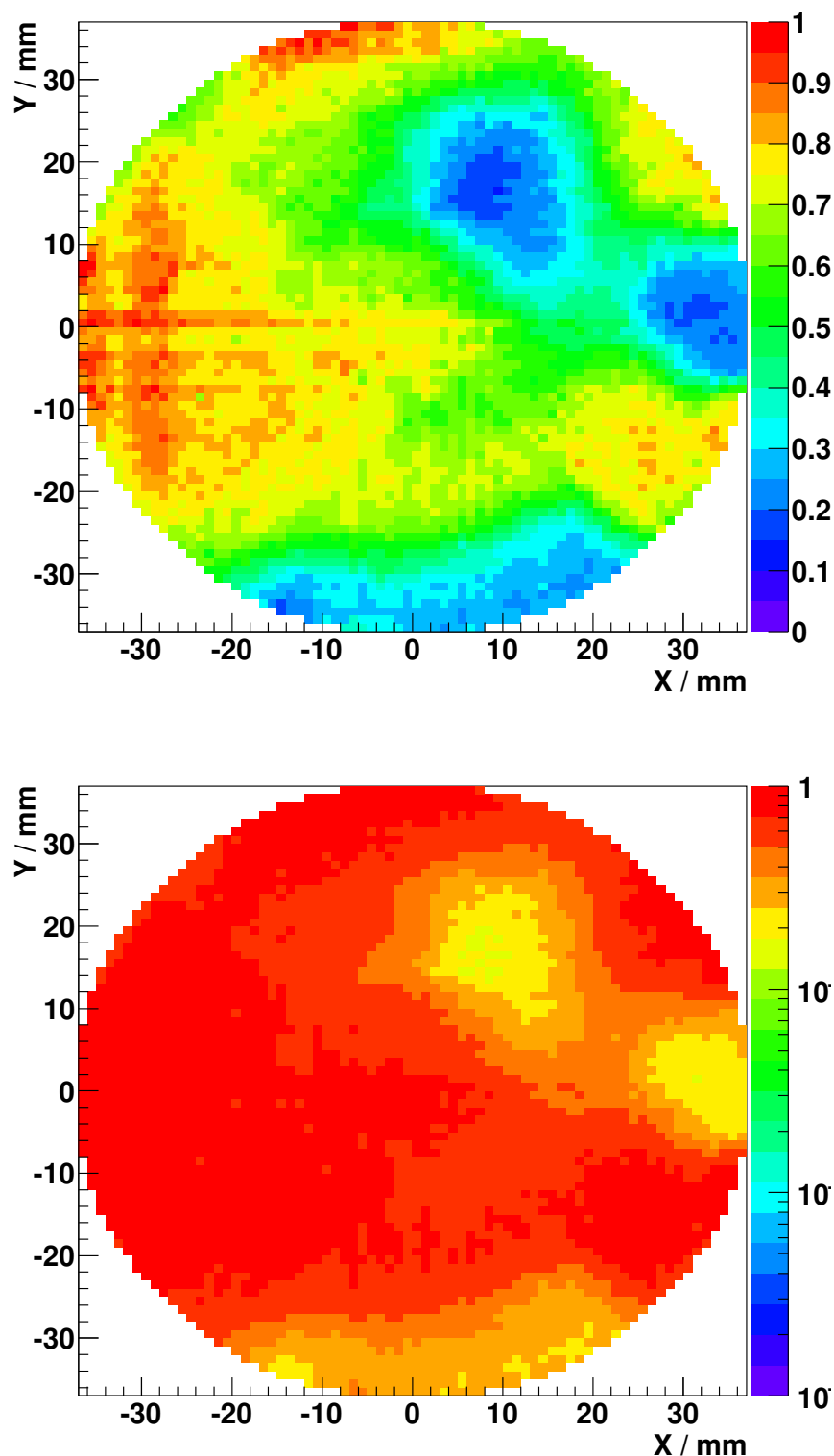
Figure 2.55.: Two-dimensional histogram of the intensity on the detector with subtracted background, normalized to the distance from the source and the angle of impact by division by a factor f_{tot} (see text for explanation). The time coordinates t_{dx} and t_{dy} have been transformed by multiplying with f_c (see eq. 2.3.12). The central park has been deleted by hand. The deleted bins have been replaced by linear interpolation from neighboring bins. The count rate has been normalized to the maximum. The upper graph has a linear scale. The lower graph shows a logarithmic scale.

2.3.7.2. Pulse height distribution

As already described in sec. 2.3.3, the CFD which is used for the main MCP signal has the ability to encode the height of the incoming signal either in a delayed pulse returned by the discriminator. Therefore it inverts the incoming signal and decreases the maximum with a constant rate of 2.5 V per 15 ns. For proper operation is is important to set the start of the ramp and the maximum of the inverted signal to the same time. This can be achieved by choosing a suitable delay cable between A_{in} and A_{out} of the CFD1x. The resolution of $0.1\bar{6}$ V / ns is fixed. When it reaches 0 the CFD1x returns a pulse at the *stop* output. The trigger from the MCP main signal serves as the start trigger for the TDC while the *stop* trigger from the CFD1x is used as stop signal on channel 5 of the TDC. Thus it is possible to record the pulse height of the MCP main signal with a TDC instead of using an analogue to digital converter (ADC).
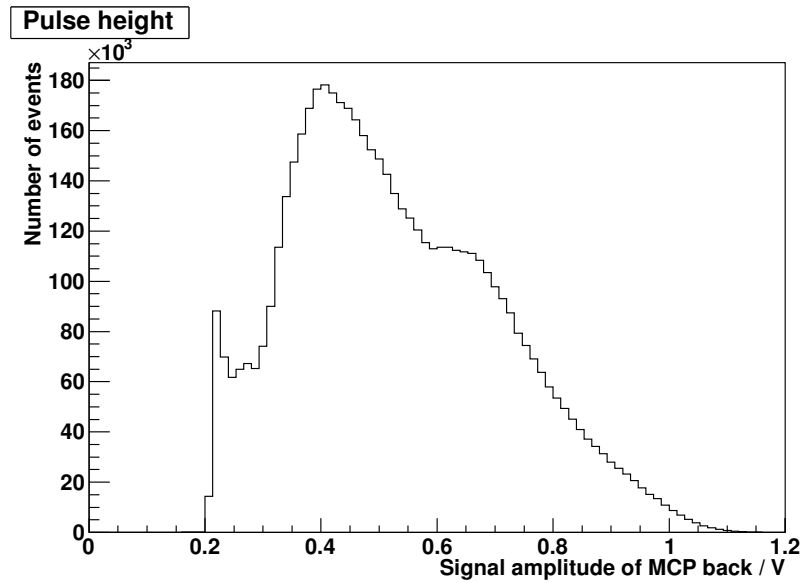
Figure 2.56.: PHD of the measurement with the uncollimated source. The tail of the distribution is cut at 1.2 V for better visibility. The threshold of the main signal was set to 200 mV, which is the reason why the distribution starts at this value.

Fig. 2.56 shows the pulse height distribution PHD obtained for the measurement with the uncollimated alpha source. The distribution starts at 0.2 V. This is to where the threshold for main MCP trigger was set. The long tail of this distribution is cut in this graph at 1.2 V. One can see a steep rise with a peak in the beginning and then again a rise of the distribution. Afterwards it shows a slow decay with a plateau between 0.6 and 0.7 V. The mean value of the PHD for alphas is

$$\bar{A}_{PHD,2011} = 0.53\,\text{V}. \tag{2.3.22}$$

The PHD of the background measurement its shown in fig. 2.57. Here the peak in the beginning is more dominant and it is much more separated from the rest of the distribution. Between 0.6 and 0.9 V there are relatively less events compared to the measurement with the uncollimated source. The reason for this can be that dark counts predominantly produce low pulse heights. The distribution in fig. 2.57 has a mean value of

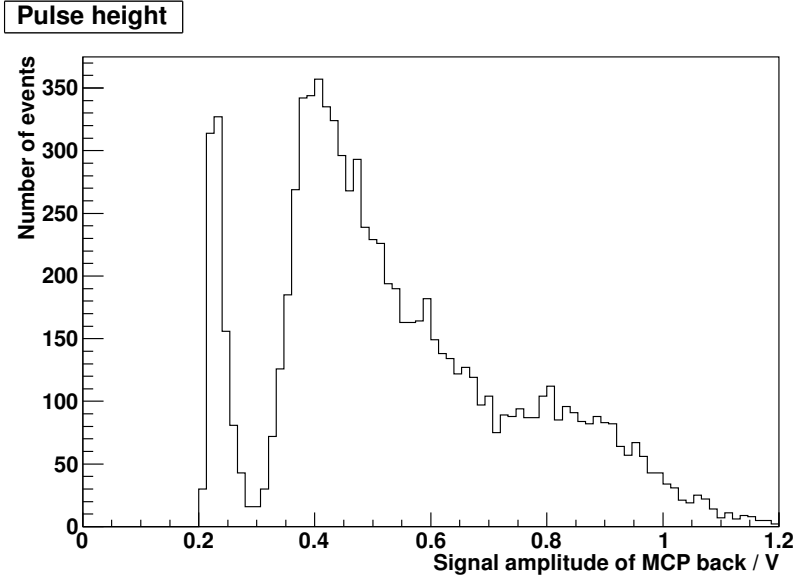$$\bar{A}_{PHD,bg,2011} = 0.54\,\text{V}. \tag{2.3.23}$$

Figure 2.57.: PHD of the background measurement. The tail of the distribution is cut at 1.2 V for better visibility. The threshold of the main signal was set to 200 mV, which is the reason why the distribution starts at this value.

Usuallay for alphas one would expect a bell-shaped distribution with its maximum at high amplitudes, since they have very high kinetic energies (several MeV) and thus creating large signal amplitudes [Roe12, Lie05]. This is obviously not the case for this measurement. This can be explained by the fact that our MCP stack shows an inhomogeneous gain factor over its surface. This can be shown by placing cuts on the pulse height when plotting the position distribution of the MCP. Fig. 2.58 show the position distributions of events with amplitudes between 0.2 and 0.4 V (top) and between 0.4 and 0.6 V (bottom).

Some areas at the top, on the right and at the bottom show more events for lower pulse heights, while an ares on the left stays dark (fig. 2.58 top). If we place the cut between 0.4 and 0.6 V (bottom) we can see that two areas at the bottom and at the top right of the MCP become darker while the center and the left part of the MCP become lighter. The events in the peak in the center have small amplitudes since the peak is present in the cut from 0.2 to 0.4 V but vanishes for a cut with amplitudes larger then 0.4 V.

Figure 2.58.: Events with pulse heights between 0.2 V and 0.4 V (top) and events with pulse heights between 0.4 V and 0.6 V (bottom). See text for further explanations.
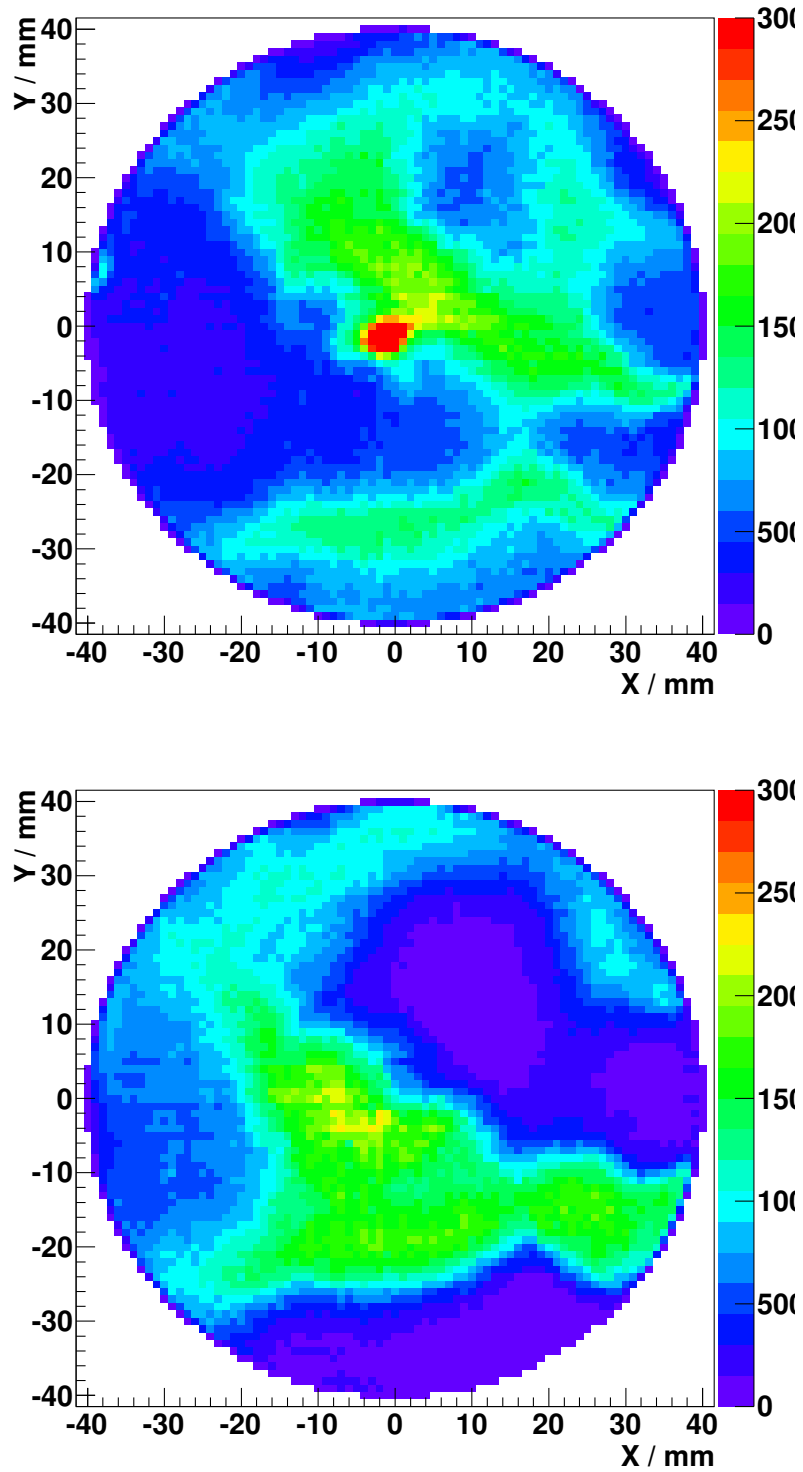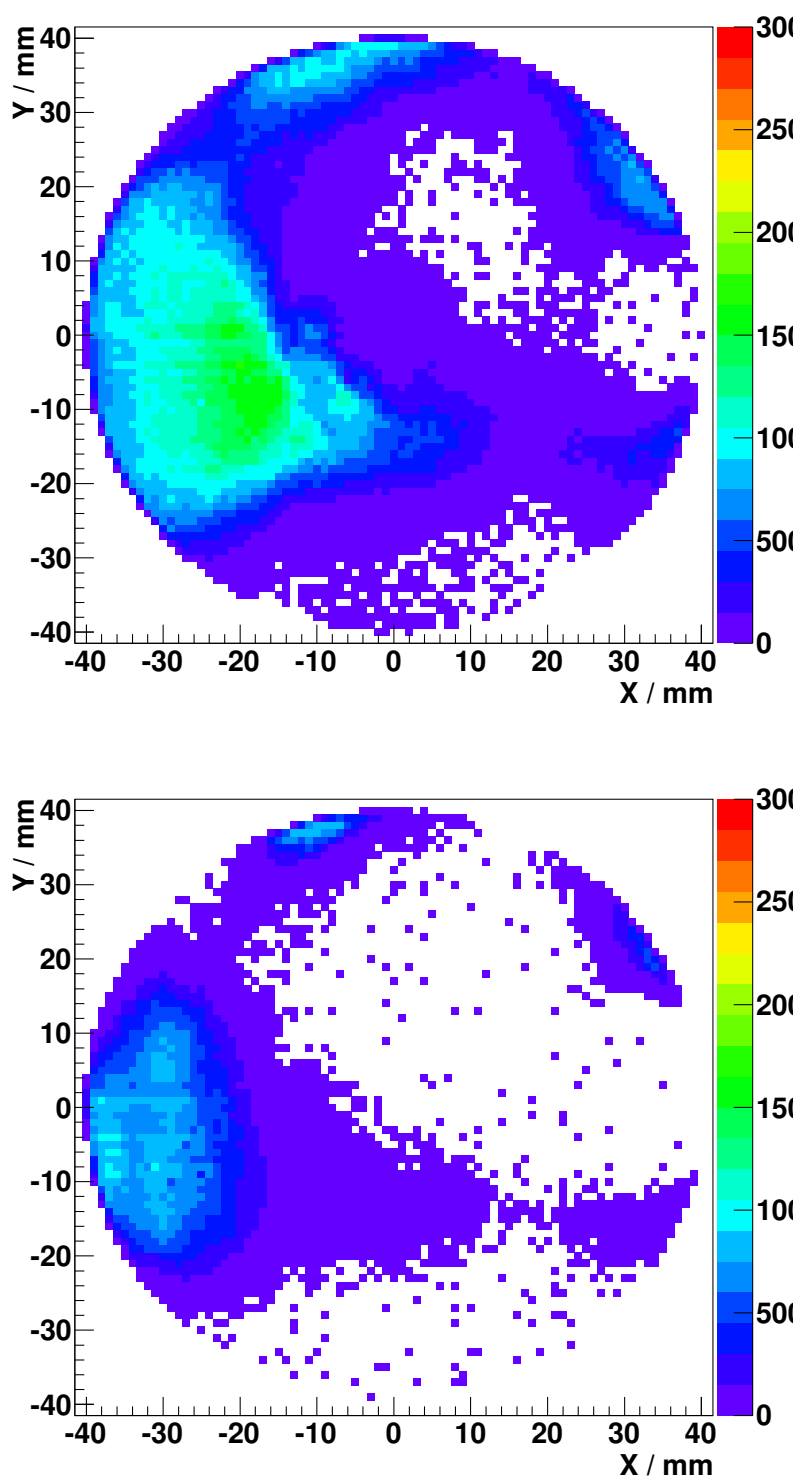
Figure 2.59.: Events with pulse heights between 0.6 V and 0.8 V (top) and events with pulse heights between 0.8 V and 1.0 V (bottom). See text for further explanations.

If we further increase the limit of the cut the right and the bottom part of the detector becomes darker while the amount of events on the left side of the detector increases. This is shown in fig. 2.59, top, where the cut is placed at amplitudes between 0.6 and 0.8 V. Already some parts of the MCP are completely blind. Further increasing the limits of the cut results in a large area ranging from the right to behind the center where the MCP is almost blind. The right side of the detector shows the most events. This is shown in fig. 2.59, bottom, where the cut is amplitudes between 0.8 and 1.0 V. By plotting the distribution of events with the weight of their pulse height and normalizing on the number of counts in a certain area one can create a map of the mean pulse heights. This is shown in fig. 2.60. On average, the largest pulse heights appear at the very left side of the distribution. The upper right and the very bottom have in average a factor 2–3 smaller pules heights.

Figure 2.60.: Mean PHD of the measurement with the uncollimated source. The large pulse heights appear in a spot on the left side. The upper right and the very bottom have in average a factor 2–3 smaller pules heights. This illustrates the inhomogenous gain factor of the MCP stack.

2.3.7.3. Absolute detection efficiency
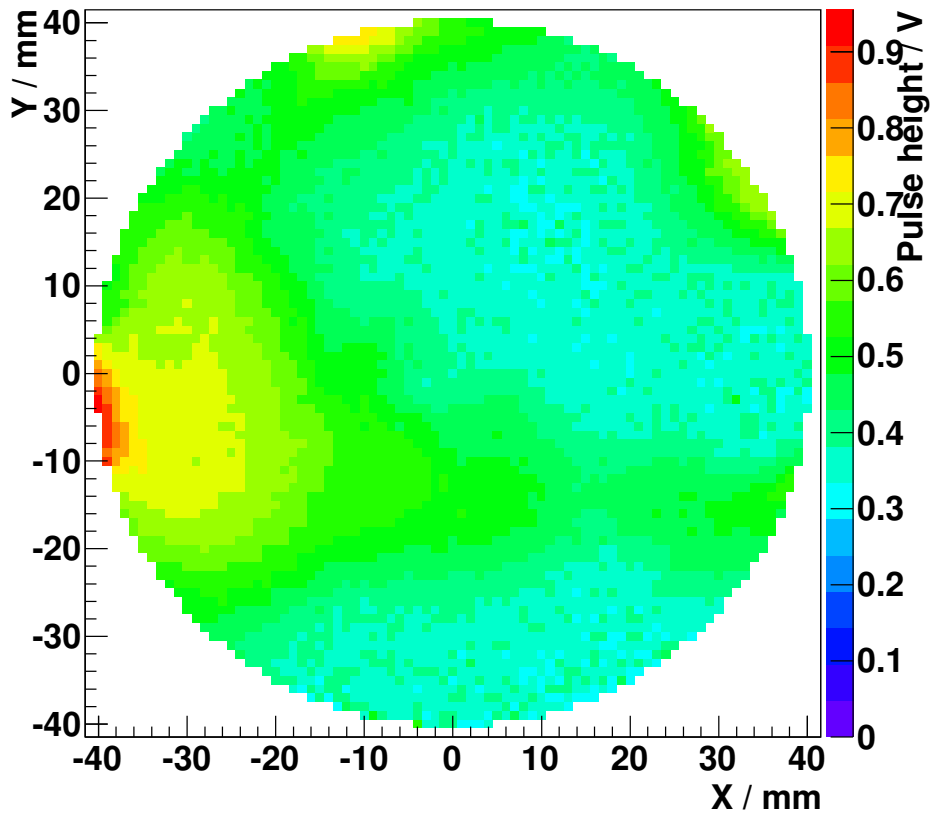
The absolute efficiency can be estimated from the corrected CAMAC scaler counts N'_S and the measurement time t_m. For the uncollimated measurement the count rate is

$$\dot{N}'_{S,uncoll.} = \frac{N'_{S,uncoll.}}{t_{m,uncoll.}} = \frac{6.9 \cdot 10^7}{6.13 \cdot 10^4 \,\mathrm{s}} = 1.13 \,\mathrm{kHz}. \tag{2.3.24}$$

Calculating the same quantity for the background measurement, we find

$$\dot{N}'_{S,bg} = \frac{N'_{S,bg}}{t_{m,bg}} = \frac{184818}{36457 \,\mathrm{s}} = 5 \,\mathrm{Hz}. \tag{2.3.25}$$

The background count rate is about two orders of magnitude smaller then the uncertainty of the expected count rate (see below, eq. 2.3.28) and will be neglected. The activity of the source is emitted isotropically in $\Omega_S = 4\pi$. The source is placed in $D = 70$ mm in distance from of the MCP which has an active diameter of $d = 83$ mm. The solid angle of the detector can be calculated as:

$$
\begin{aligned}
\Omega_D &= \int_0^{2\pi} d\phi \int_0^{\theta_{max}} \sin\theta d\theta \\
&= 2\pi \int_0^{\theta_{max}} \sin\theta d\theta \\
&= 2\pi \left[1 - \cos\theta\right]_0^{\theta_{max}} \\
&= 0.88 = 0.28 \cdot \pi \tag{2.3.26}
\end{aligned}
$$

where in line three the constant of integration has been chosen such that $\Omega_d(\theta = 0) = 0$ and the upper limit $\theta_{max} = \arctan(\frac{83\,\mathrm{mm}}{2 \cdot 70\,\mathrm{mm}}) = 30.7°$. The ratio of the solid angle of the source to the solid angle of the detector is:

$$R_{SD} = \frac{\Omega_D}{\Omega_S} = \frac{0.28 \cdot \pi}{4 \cdot \pi} = 0.07 \tag{2.3.27}$$

The expected count rate can be calculated as the product of two factors: the modified activity of the source $\tilde{A}_S$ (see eq. 2.3.7) and the ratio of the solid angle of the source to the solid angle of the detector (see eq. 2.3.27):

$$
\begin{aligned}
\dot{N}_{S,exp.} &= \tilde{A}_S \cdot R_{SD} \\
&= (54 \pm 15)\,\mathrm{kHz} \cdot 0.07 \\
&= (3.78 \pm 1.05)\,\mathrm{kHz} \tag{2.3.28}
\end{aligned}
$$

Finally we can estimate the total efficiency of the detector as the ratio of measured to expected count rate:

$$\epsilon_{tot,2011} = \frac{\dot{N}_{S,uncoll.}}{\dot{N}_{S,exp.}} = (0.30 \pm 0.08) \tag{2.3.29}$$

In this calculation we neglect the uncertainty of the geometry of the setup and the contribution of sputtered ions. The latter has been estimated in eq. 2.3.8 and after multiplication with the open area ration (eq. 2.2.3) it is about 30 times smaller then the uncertainty of $\dot{N}'_{S,exp.}$.

2.3.8. Measurement with the collimated source in 2011

As described in sec. 2.3.1 a problem occurred to the reproducibility of the position of the collimated source. So it will not be possible to use this measurement to calibrate the absolute position resolution of the detector but only the relative position resolution. Nevertheless it can be used for efficiency calibration and for a comparison this result with the measurement with the uncollimated source.

2.3.8.1. Relative detection efficiency

To compare the measurement with the collimated source with the uncollimated measurement for efficiency studies, the following procedure was applied: We took every measurement with collimated source, cut out a region with 2 mm radius in the center of the beam spot, summed up all events in that region and corrected the measurement for the dead time by multiplication with the factor f_{dt} from tab. 2.10.

Then we applied the same cut to the measurement with the uncollimated source, summed up all events in that region and took into account the distance from the source and the angle of impact as described in the section before and then we multiplied the corrected the measurement for the dead time by multiplication with the factor f_{dt} from tab. 2.10. Finally we divided both results by their measurement time.

The result is shown in fig. 2.62. The black circle indicate the active area of the MCP. The count rate of the measurement with the uncollimated source (red impulses) is in general higher than the one with the collimated source (grey impulses). For better visibility, we scaled the measurement with the collimated source by a factor of 5 (blue impulses). Comparing the uncollimated and the scaled collimated measurement, one can see that the intensity shows a similar behavior in both measurements. Small deviations appear in some points, but show no sign for systematics. The factor 5 less intensity in the measurements with the collimated source compared to the uncollimated measurement can have two reasons:

- The source is spread over a larger surface then the actual part that can contribute to the spot on the detector surface. Due to the geometry of the two apertures the area of the source that contributes to the events in the spot can be calculated by:

$$A_{spot} = \pi \cdot \left(\frac{d_A}{2} + \frac{d_2 \cdot d_A}{d_1} \right)^2 = \frac{\pi d_A}{4} \cdot \left(1 + \frac{2d_2}{d_1} \right)^2 = 32\,\mathrm{mm}^2 \qquad (2.3.30)$$

  where $d_1 = 22$ mm is the distance between the two apertures, $d_2 = 7$ mm the distance from the lower aperture to the surface of the source and $d_A = 4$ mm the diameter of the aperture (see fig. 2.61). The left part of the sum is the solution for infinitely large apertures ($d_1 >> d_2$), the second term is the correction for short apertures. The metal foil on which the activity of the source is deposited has an area of [Cer11]:

$$A_{src} = 6\,\mathrm{mm} \cdot 20\,\mathrm{mm} = 120\,\mathrm{mm}^2 \qquad (2.3.31)$$

  With these numbers we find a factor of $\frac{A_{src}}{A_{spot}} = \frac{120\,\mathrm{mm}^2}{32\,\mathrm{mm}^2} \approx 6$, which is in the right order.

- The activity of the source is not deposited accurately in the center but slightly off. To support this theory, we already saw that the peak coming from the uncollimated source was not in the center but approx. 2 mm shifted to the left. In this case a large part of the activity is shielded by the collimator and cannot contribute to the events in the spot on the detector surface. To quantify this we would need more information on how exactly the activity is deposited on the sources surface which is not available.
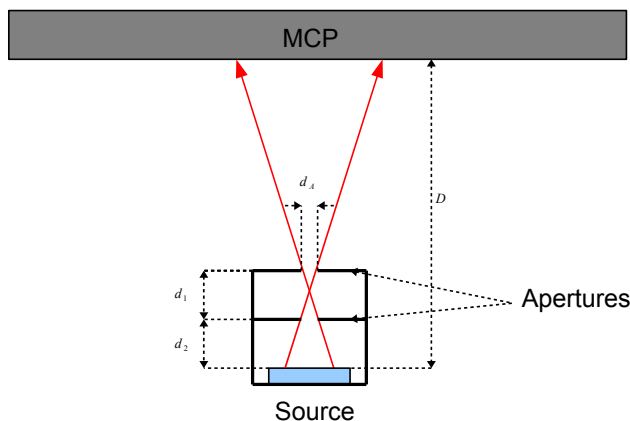
Figure 2.61.: Illustration of the geometrical properties in the measurement with the collimated source. d_1 is the distance between the surface of the source and the first aperture, d_2 the distance between the first and the second aperture and d_A is the diameter of the aperture. $D = 70$ mm is the distance from the surface of the source to the MCP front.
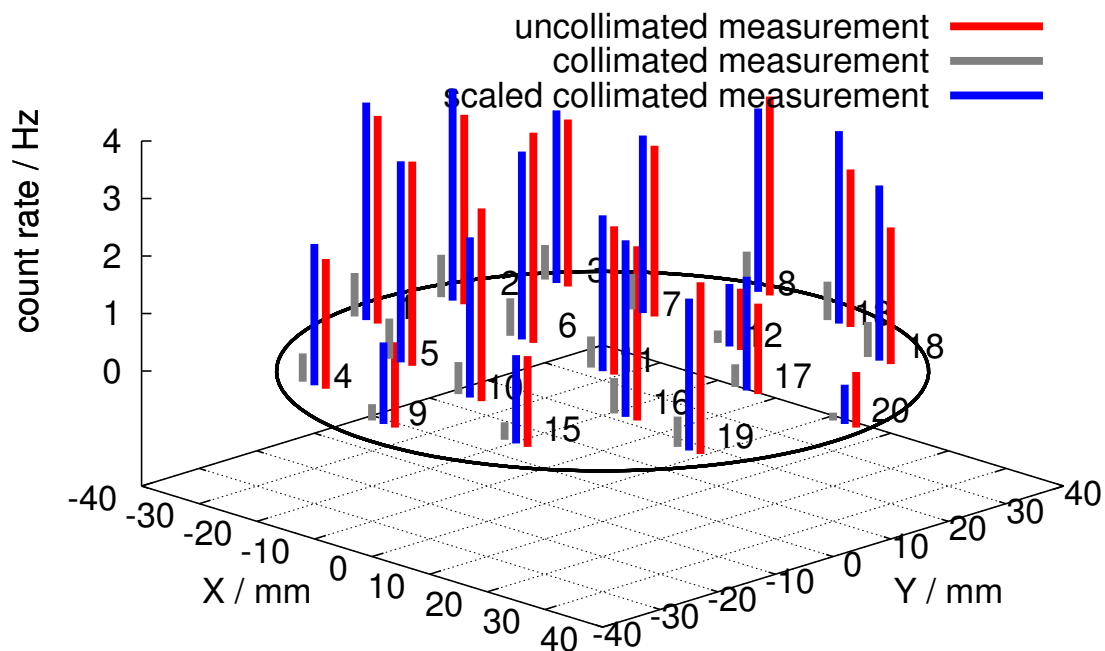

Figure 2.62.: Comparison of the measurements with collimated and uncollimated source.

2.3.9. Discussion of the detector calibration in 2011

The big advantage of the measurement with the uncollimated source is, that it is relatively easy to carry out. Nevertheless it shows several systematic effects which have to be taken into account in the data analysis. These are in particular the $1/L^2$-dependence of the source intensity, the dependence on the angle of impact and the orientation of the MCP channels. The latter has been measured in [Lie05] with ^{6}Li$^+$ and ^{23}Na$^+$ ions of several keV energy for incident with respect to the channel axises of the front microchannel plate between -22° and +15° for a detector that is identical in construction to our detector. Also the MCPs have the same specifications. No significant effect was found (see [Lie05]). Since we have alpha particles with average energies of a few MeV and incident angles (with respect to the channel axises) ranging from –38° to +22° (estimated from the geometry of the calibration setup) our situation might not be fully comparable.

Our result shows deviations in the efficiency by a factor of approx. 10. Especially on the bottom edge and in the upper right quarter we can see a significant lack in the efficiency. The reason for this could be an in homogenous gain factor of the MCP stack in combination with high MCP *Back* threshold.

Another explanation could be a so-called Moiré pattern. A Moiré pattern appears if two regular patterns, e. g. the holes in two plate, are overlaid with a slight shift or twist with respect to each other or if the distance between them is not constant and can be observed at transparent curled window curtains for instance. A very simple example is shown in fig. 2.63, where two identical grids are overlaid with a small angel.
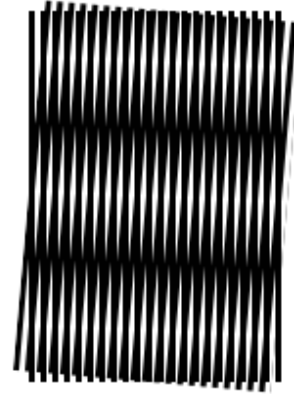

Figure 2.63.: A simple example of a Moiré pattern with two identical grids are overlaid with a small angel (taken from ref. [Wik12]).

The PHD of the uncollimated measurement shows an unexpected shape. By placing cuts on the different ranges of the PHD one can show that the mean amplification over the whole detector surface varies by almost one order of magnitude. This behavior explains the very inhomogeneous detection efficiency. We can see that the areas with low efficiency, e. g. at the very bottom and on the top right, produce predominantly smaller signal amplitudes while the areas with a high efficiency, e. g. the left side, create larger signals.

The value for the total efficiency of the detector of $\epsilon_{tot,2011} = (0.30 \pm 0.08)$, given in eq. 2.3.29 is significantly lower then the open area ratio (eq. 2.2.3) which is the upper limit for the total efficiency. This is not unexpected if we consider the large fluctuations we observed in sec. 2.3.7. We calculated the average value of the relative detection efficiency in eq. 2.3.21. The product

$$R_{OA} \cdot \bar{\epsilon}_{rel,2011} = (0.31 \pm 0.03)$$

agrees within the error bars with eq. 2.3.29. In this calculation we neglected the uncertainty of the geometry and the uncertainty from the ions that are sputtered from the protective Pd sealing. The latter will only contribute with about 10 Hz to the count rate (the product of eq. 2.3.8 and eq. 2.2.3).

The measurement with the movable collimated source had several problems which were caused by a disfunction of the mechanics. Because of this, the position information of the collimated source could not be used for a calibration purpose. Anyway, the recorded information is still suitable, to calibrate the efficiency of the MCP. It is very important to consider the dead time of each individual

measurement as it was calculated in sec. 2.3.4.

This measurement has different systematics then the one with uncollimated source. The $1/L^2$-dependance of the source intensity and the dependance on the angle of impact are not appearing in this measurement, since the distance from the source to the detector is always identical. This measurement avoids the systematic dependance due to the orientation of the MCP channels. The good accordance of the measurement with the collimated source and the interpolated spot in the center indicates that the interpolation procedure in fig. 2.55 is mostly valid.

2.4. Modifications in 2012

In the 2011 calibration we found a significant inhomogeneity of the relative detection efficiency over the surface of the MCP. Variations of a factor of 10 have been observed. This is a severe problem for a precision measurement even if it has been calibrated.

A method to increase and smoothen the gain factor and avoid Moiré patterns (see also sec. 2.3.7) of the two stacked MCPs over its surface is to place a shim ring between these two plates. Such a ring creates a larger but also well defined distance in-between the two plates which has the effect that the electron cloud leaving the first plate its spread over more channels of the second plate. The gain factor contribution from the second plate is higher, since the secondary electrons from the first MCP will be spread over more channels of the second MCP. The disadvantage off this method is that the spatial resolution will be reduced since the pulse height distribution gets broadened, but this is not of concern for the WITCH experiment at the moment. First measurements with a shim ring from the manufacturer Roentdek, resulted in discharges between the shim ring and the electrode of the ceramic ring of the MCP stack. The situation improved when insulating the ring with Teflon tape. Fig. 2.64 shows the first successful measurement with a shim ring as conducted on the 30/04/2012 on 09:50.
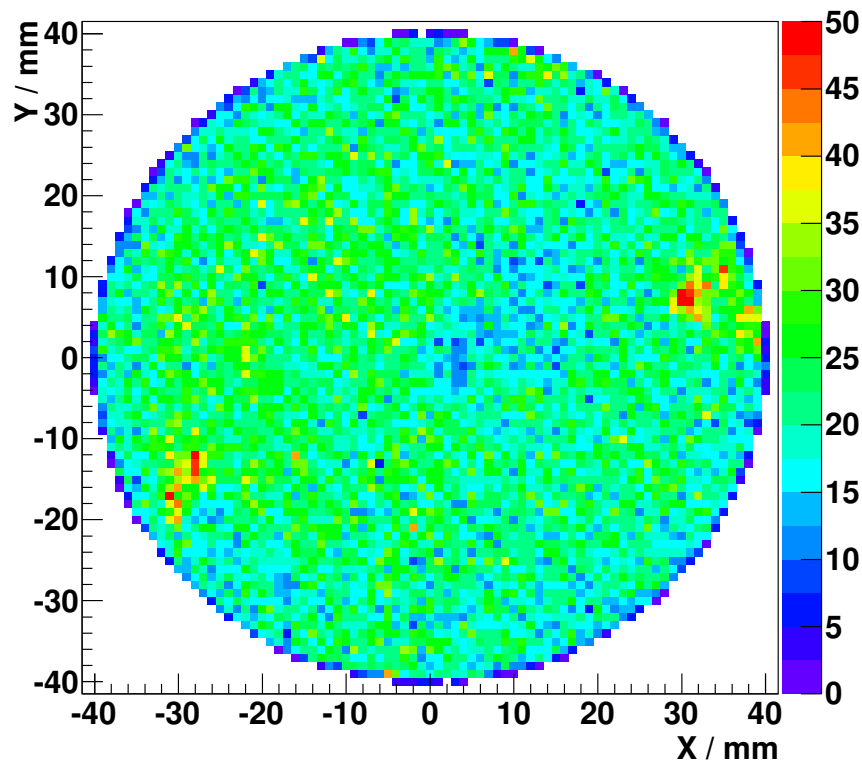
Figure 2.64.: The first successful measurement with a shim ring conducted on 30/04/2012 at 09:50. Insulating the shim ring with Teflon tape could temporarily avoid discharges at the MCP stack but in a long term the situation was not stable.

But the situation was short-lived and got worse after a few hours again. Fig. 2.65 shows a measurement with the same detector setup approx. 6 hours later. The half-moon shaped figure at the bottom was caused by discharges from the shim ring to the bottom electrode of the ceramic holders. The electrons leaving that ring see a potential difference of approx. 1 kV and can create X-rays when hitting the bottom electrode.
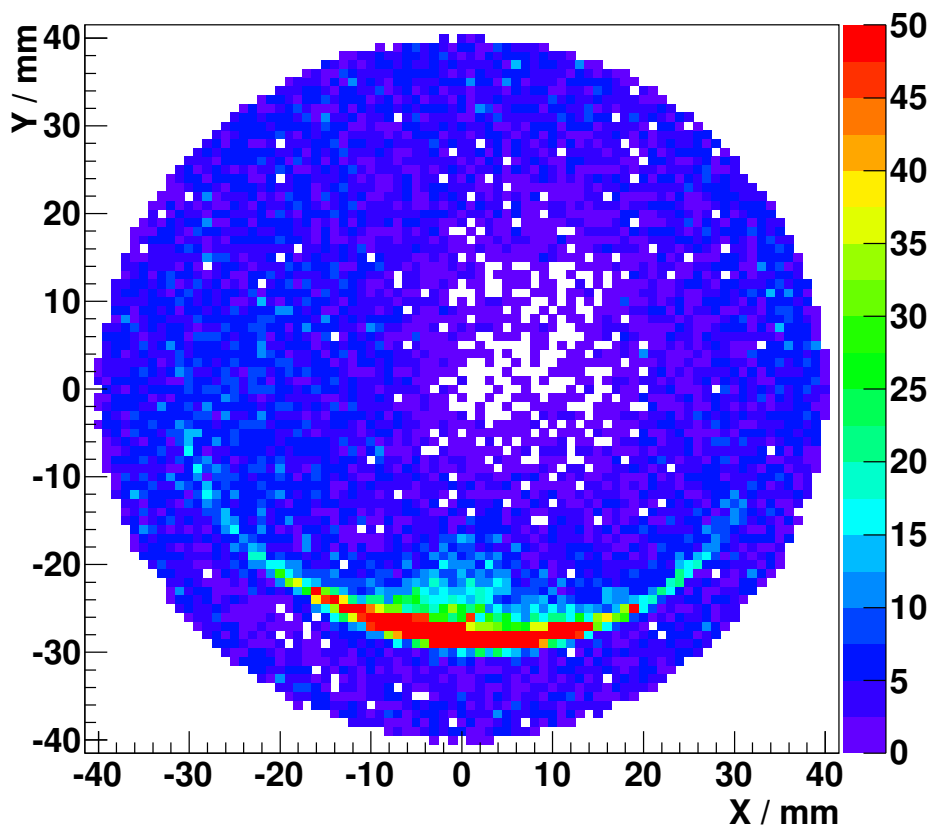
Figure 2.65.: A measurement with the same detector setup as in fig. 2.64 approx. 6 hours later (conducted on 30/04/2012 at 15:35). The half circle in the lower part of the picture is cased by a off-centered shim ring, that slipped off during the measurement. At this time the MCP stack did not feature the pintles and washers made from Peek (see sec. 2.4.2) and the shim ring that was used in this measurement did not have lugs.

2.4.1. The shim rings

The first versions of the shim rings came from Roentdek, three of them were ordered. On the first ring we received from them the outer lugs have been removed by cutting them away with a scissors, which left sharp edges that increased the rise of discharges. These shim rings keep a defined distance of 100 μm between both MCPs. The properties of the ring are listed in tab. 2.13.

A picture of the shim ring is shown in fig. 2.66. The ring has three lugs with two holes each. The inner holes fit with the holes of the ceramics. When screwing the MCP stack together, the shim ring will be adjusted by these lugs. The lugs can also be used to apply a potential between the front plate and the back plate. This is necessary if the MCPs are not matched in resistance but in our case it is not needed (see sec. 2.2.1).

Figure 2.66.: Picture of one of the shim rings from Roentdek with three lugs to support the ring and connect an electrical contact.

Table 2.13.: Mechanical properties of the shim rings from Roentdek and the mechanical workshop in Münster.

Manufacturer	Material	Method of treatment	Thickness	Inner diam.	Outer diam.
Roentdek	CuSn6 bronze	Etching	100 μm	83 mm	86.6 mm
Münster workshop	CuSn8 bronze	Wire-electro discharge machining	100 μm	80 mm	84 mm

The discharges occur either at places where the removed lugs left a sharp edge or where the electrical contacts of the ceramics were attached and the rings from Roentdek, which have the same dimeter at the MCPs, flush with the MCPs or leaped over. Thus we decided to manufacture shim rings in the mechanical workshop in Münster, which have a smaller diameter and thus are shielded

by the edges of the MCPs. These rings have been wire-electro discharge machined from a standard 100 μm SnCu8 bronze sheet. Their properties are listed in tab. 2.13 and a photograph of it is shown in fig. 2.67.

Figure 2.67.: Picture of the shim ring manufactured in the mechanical workshop in Münster, which is placed between the MCPs. This ring was manufactured from a sheet of CuSn8 bronze by the use of wire-electro discharge machining.

2.4.2. Revised MCP stack

To reduce the risk of discharges, we decided to polish the ceramic rings on the side of the electrodes. Fig. 2.68 and 2.69 show the polished front and back ceramic rings. A problem when using the shim ring is that the MCP stack has no lateral support in the ceramic rings. It once happened that the bottom MCP slipped a few millimeters to the side and the shim ring lapped over which caused discharges to the electrode of the ceramic ring.

Figure 2.68.: Pictures of both sides of the revised ceramic ring for the front MCP. The holes for the pintles are labeled with numbers acceding to tab. 2.14.

On the pictures one can see that each ceramic ring has two types of holes: Twelve on an outer radius and four on a smaller radius marked in fig. 64 with numbers. Using a turning machine with a microscope we measured the distance of each hole to the center of the ceramic ring. The enumeration of the holes is according to fig. 2.68 and 2.69. The results of the measurement are listed in tab. 2.14.
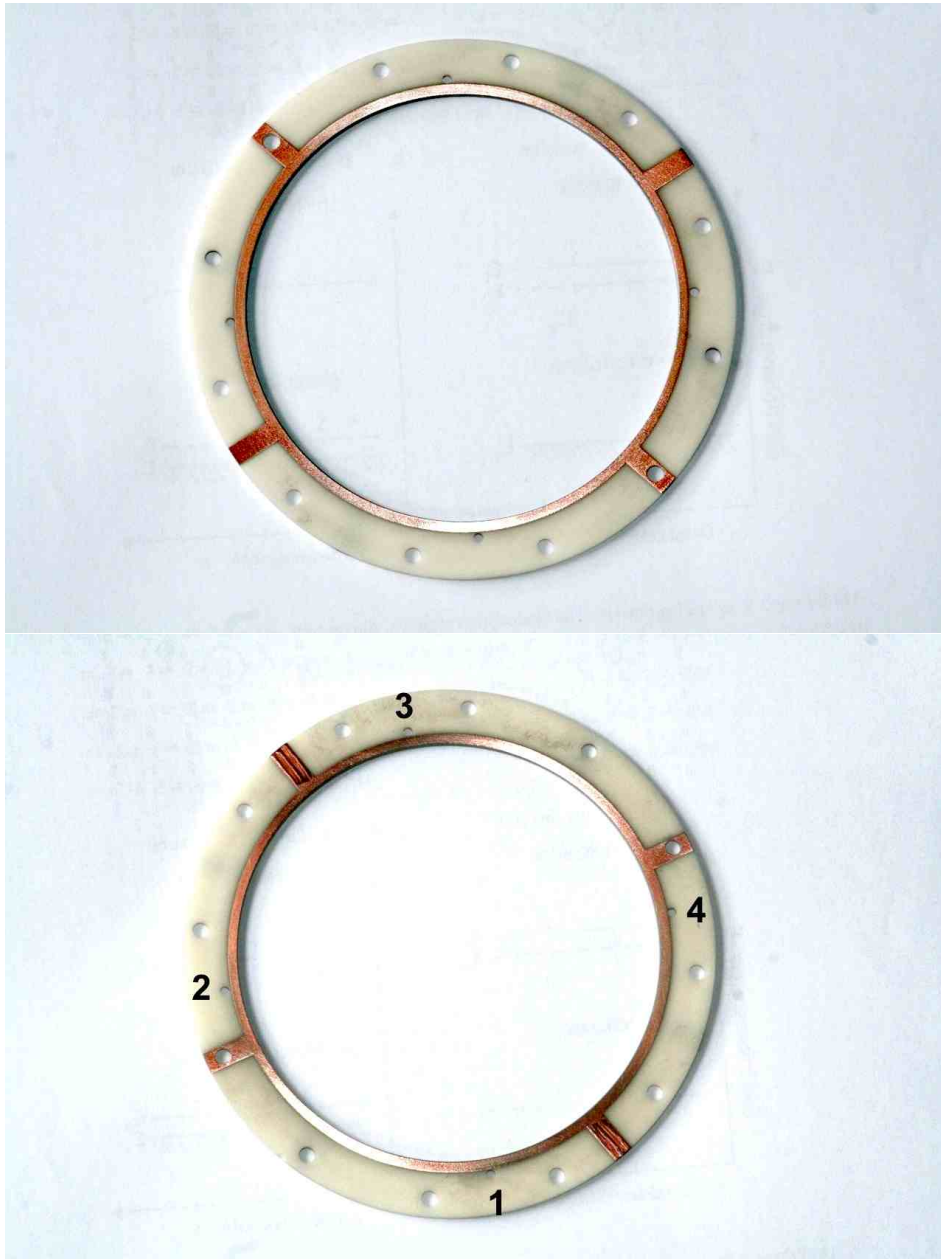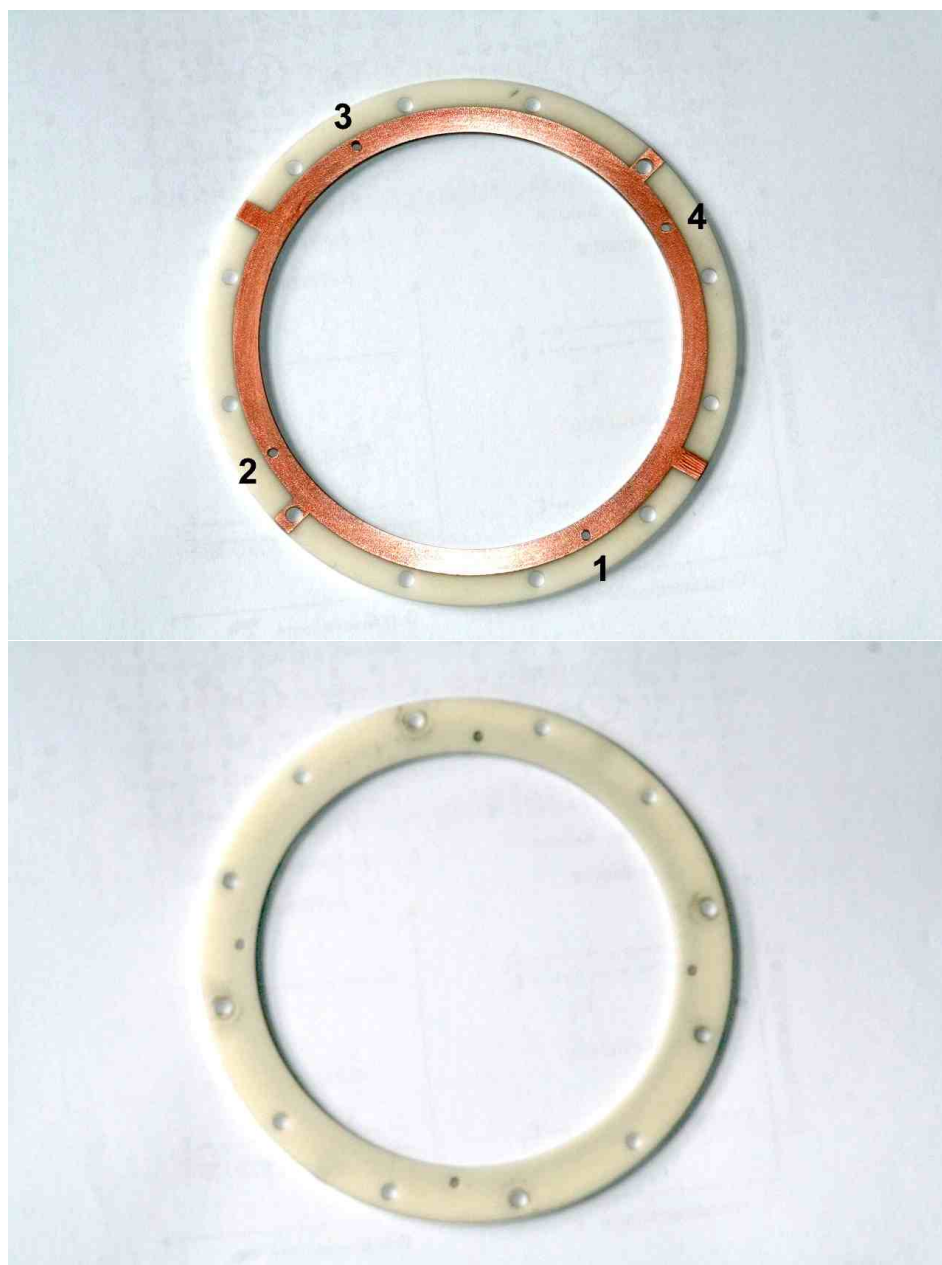

Figure 2.69.: Pictures of both sides of the revised ceramic ring for the back MCP. The holes for the pintles are labeled with numbers acceding to tab. 2.14.

Table 2.14.: Measured coordinates of the holes for the pintles in the front ceramic ring (left) and the back ceramic ring (right). The measurement was arranged in the mechanical workshop in Münster.

Hole	X / mm	Y / mm	Hole	X / mm	Y / mm
1	0.00	44.78	1	0.00	44.80
2	44.73	0.11	2	44.65	0.04
3	0.00	-44.58	3	0.08	-44.60
4	-44.65	0.10	4	-44.46	0.05

Small pintles were constructed, which fit into the four small inner holes and which are made of Peek. From tab. 2.14 one can see that the four holes were not drilled accurately. The distance of opposing holes varies about 200 μm for the back ring. To correct this, two types of pintles have been manufactured, one with a diameter of 2.8 mm and one type with a diameter of 2.6 mm.

Figure 2.70.: Picture of both types of pintles, 2.80 mm (left), 2.60 mm (center) and the washer (right). The pintles and the washer are made of Peek.

To support the three lugs of the shim rings from Roentdek, washers made of Peek have been manufactured. These can be placed between the lugs of the shim ring and the ceramics. Fig. 2.70 shows a picture of the pintles and the washer and in fig. 2.71 the ceramics equipped with the pintles and washers are shown.

Figure 2.71.: The bottom ceramic ring equipped with the pintles and the washers (top). The ceramic stack equipped with the pintles and the washers (bottom).

The contact screw for the MCP back connection as been replaced by a metal clamp with better mechanical properties than the screws that had been used. This clamp fits into the outer holes of the ceramic rings. Fig. 2.72 shows a picture of the MCP stack with the clamped MCP back contact.
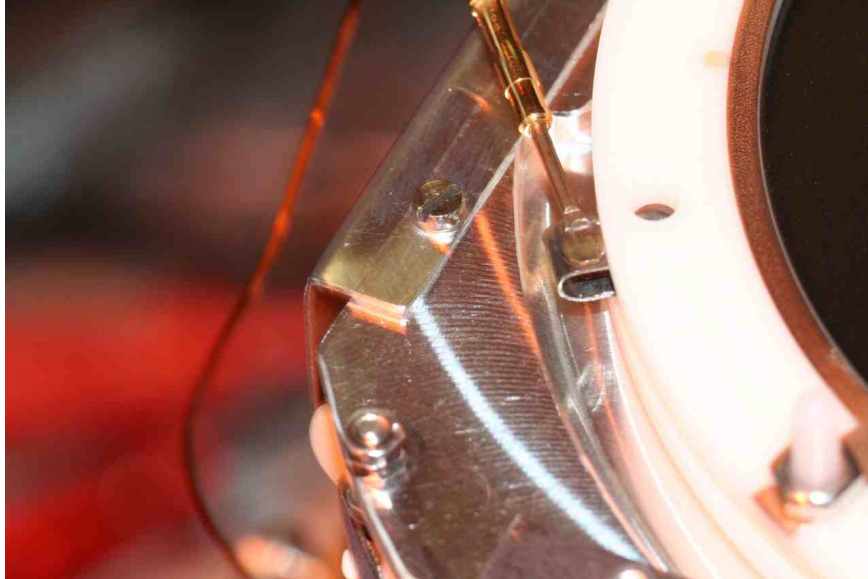

Figure 2.72.: Picture of the metal clamp, used to connect the MCP back contact. The wire which provides the electrical contact to the electrical feedthrough is crimped to the gold plated metal plug.

2.4.3. Final configuration

After a short period of trail and error we finally found a stable configuration in which the detector could run uneventfully. In this configuration the shim ring from the mechanical workshop in Münster was installed between the two MCPs. The four pintles were used to correctly align the two microchannel plates but the washers were not needed, because the shim ring has no lugs. The MCP *Front* was placed with the mark facing towards the delay line anode. Also the MCP *Back* was placed with the side with the mark facing in direction of the delay line anode. To achieve a Chevron configuration the marks of the MCP *Front* and MCP *Back* have to be on opposite sides like it is shown in fig. 2.73, which also shows the locations of the connectors for MCP *Front* and *back*. The *Front* contact was screwed to the front ceramic ring and the *Back* contact was clamped using the metal clamp shown in fig. 2.72. The mark of the front MCP is facing downwards. So the channel axises point in opposite direction then the label *MCP mark* in this figure.

2.4.4. Storage box for the detector equipment

To keep the equipment for detector together we organized a big plastic box where small parts, special tools, the MCP transport box etc. are placed in. Fig. 2.74 shows a picture of this box.
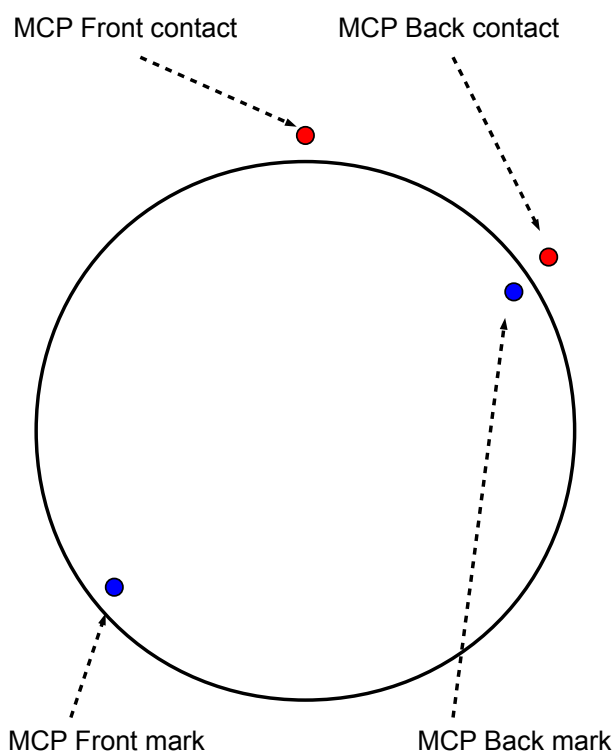
Figure 2.73.: Schematic drawing of the orientation of the MCP marks of the front and back MCP (blue dots) and the electrical front and back connections. When looking from the top onto the detector both MCP marks were facing downwards. Due to an accident where a drop of machine oil from contaminated pressurized air was spilled on the MCP back plate (see sec. 2.5) it is not possible to place the MCP marks face-on-face. To equal a Chevron configuration the MCP marks of the front and the back MCPs have to face to opposite directions.

Figure 2.74.: The storage box for the detector equipment.

2.5. Detector calibration in 2012

The improvements described in the chapter before allow us to run the detector stable. Using almost the same calibration setup like in 2011, three calibration measurements have been conducted.

2.5.1. Calibration setup

The setup for the calibration was almost identical to the one described in section 2.3.1 but the following changes had to be applied:

- **The Source:** We had to return the 40kBq ^{241}Am source which was used in 2011 for the calibration measurement (number 4263RP). It was not possible to get the same source again but the radiation protection source Group provided us a source with identical specifications. Its number is 4292RP.

- **The manipulator flange:** The horizontal tilter, a loan of the group of Prof. Khoukaz from the IKP Münster, had to be returned. The source holder is now attached to the linear feedthrough which was mounted with a CF-100 to CF-40 reduction piece directly to one of the side flanges of the test chamber.

- **The source holder:** The source holder is adjustable in height. It now was lowered by 13 mm to reduce the systematic effect of the $1/L^2$-dependency of the source intensity and the incident angle.

- **The vacuum gauge:** The Penning gauge used in 2011 meanwhile was installed in another setup. Now the pressure now is determined with a full range gauge. The pressure was measured before and after each measurement below $1 \cdot e^{-6}$ mbar.

The other parts were identical to the calibration in 2011.

2.5.2. Detector settings

When modifying the MCP stack we took special care of the orientation of the MCP mark and the connectors for *Front* and *Back*. This was important to solve the problem of discharges. For the final setup used in the following measurements the orientation of the connectors and the MCP mark of the front plate is shown in fig. 2.73. Notice, the mark of the front is facing downwards. The channel axises point in opposite direction then the label *MCP mark* in this figure.

Fig. 2.75 shows a schematic overview of the signal processing, cable delays and amplification factors used in this calibration measurement. Due to the higher amplification factor of MCP stack caused by the shim ring, one amplification stage in the processing of the delay line signals has been removed. Instead of $100\times$ the signals were now only $10\times$ amplified. This increased the signal-to-noise ratio.

Because of its better signal quality and lower noise level, this time the MCP *Front* signal was used as main MCP signal to provide the common start trigger for the TDC. The amplification of this signal was identical ($60\times$) as in 2011. Due to a broader pulse the delay cable of the CFD have been changed from 1 ns to 2 ns and the delay between A_{in} and A_{out} was adjusted to the same length of 2 ns. The setting of the constant fraction f of the Roentdek CFD1x did not change ($f = 0.35$).

With the shim ring the amplification factor of the MCP stack is in average approx. 4 times larger than without for identical bias voltages. This was estimated by eye, using the oscilloscope. So the potential between MCP *Front* and MCP *Back* was reduced to 2.16 kV, respectively to 2.90 kV between MCP *Front* and ground potential. Compared to the configuration in 2011 the amplification is about 2.5 times larger with this bias voltage and shim ring. The amplification factors and thresholds along with the modules used in these measurements are listed to tab. 2.15.
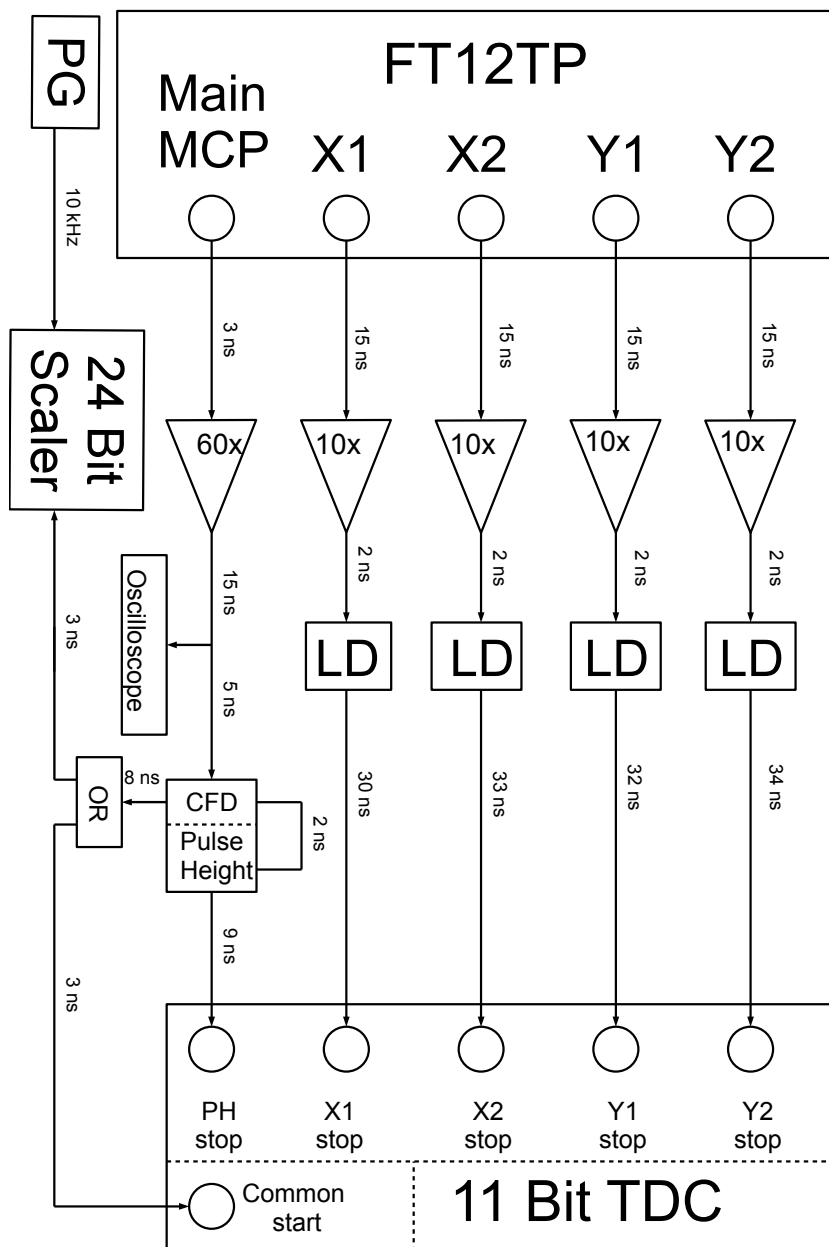
Figure 2.75.: Schematic drawing of the signal processing with cable lengths and amplification factors used for the calibration in june 2012. The lengths of the cables are written new to the lines. A pulse generator (PG) creating a periodic 10 kHz rectangular pulse is used to create a time stamp for the events.

Table 2.15.: Amplification factors, threshold settings, constant fraction f and CFD delay cable as used during the calibration in june 2012.

Channel	Amplification factor	Amplifier module	Threshold	Discriminator module	Fraction f	Delay cable
MCP Front	60	Roentdek FAMP1+	- 380 mV	Roentdek CFD1x	0.35	2 ns
X1	10	LeCroy 612 A	-45 mV	LeCroy 821	-	-
X2	10	LeCroy 612 A	-60 mV	LeCroy 821	-	-
Y1	10	LeCroy 612 A	-70 mV	LeCroy 821 CS	-	-
Y2	10	LeCroy 612 A	-83 mV	LeCroy 821	-	-

The cable length between the *Stop* output of the CDF 1x and the TDC stop for channel 5 has been reduced to 9 ns. Additionally a pulse generator (PG) providing a 10 kHz rectangular pulse is connected to the second channel of the scaler module.

2.5.3. The Recorded information in 2012

The way the recorded information was arranged and processed did not change compared to the calibration measurement in 2011, except for one small detail: now for each event an additional scaler information with the measurement time t_m is available.

Three different measurements were made: one with an uncollimated ^{241}Am source centered in 83 mm distance from the MCP surface, one where additionally the aperture mask (see section 2.88) was screwed on the ceramic holder of the from MCP and a background measurement, where the source was removed from the detector chamber but the mask was left on. The Properties are listed in tab. 2.16.

Table 2.16.: Recorded information of the three measurements used for this calibration. For each measurement we list the date, the start time, the duration of the measurement t_m, the CAMAC scaler counts N_S, the number of events registered by the CAMAC DAQ N_E, the dead time correction factor $f_{dt} = \frac{N_S}{N_E}$ and the total count rate $\dot{N}_S = \frac{N_S}{t_m}$ of each measurement.

Measurement	Date	Start time	t_m / s	N_s	N_E	f_{dt}	$\dot{N}_S$ / Hz
Uncollimated	03/06/12	20:30	47841	54540937	11638329	4.686	$1.14 \cdot 10^3$
Mask	04/06/12	20:00	49644	19716298	8516355	2.32	397
Background	05/06/12	17:40	61293	503633	486726	1.035	8.22

Nevertheless the graphs made from these recorded data now look different compared to what was shown in section 2.3.3. In the following subsections we show these graphs and discuss the differences compared to 2011. All graphs in that section are made from the measurement with the uncollimated source.

Unless otherwise indicated all the plots are made with a cut on events that fulfill the conditions: $t_{sx} \in [85\,\text{ns}, 105\,\text{ns}]$, $t_{sy} \in [90\,\text{ns}, 110\,\text{ns}]$ & $t_r \in [0, 85.5\,\text{ns}]$. This is done to cut out artifacts and will be exactly the region in the parameter space that will be used for the coming analysis.

2.5.3.1. The t_{X1}, t_{X2}, t_{Y1} and t_{Y2} histograms

Fig. 2.76 shows the t_{X1}, t_{X2}, t_{Y1} and t_{Y2} histograms, recorded with the TDC channels 1 to 4. The detector surface has a circular shape. If we assume the whole surface gets illuminated homogeneously by the source, one would expect that the shape of these histograms look hemicycle-like, spread over the full length of the delay lines, 85.5 ns (due to the cut). If we take into account the fact, that the intensity from the source drops towards the edge of the detector, the hemicycle-like shape should be flattened towards the beginning and the end of these distributions.
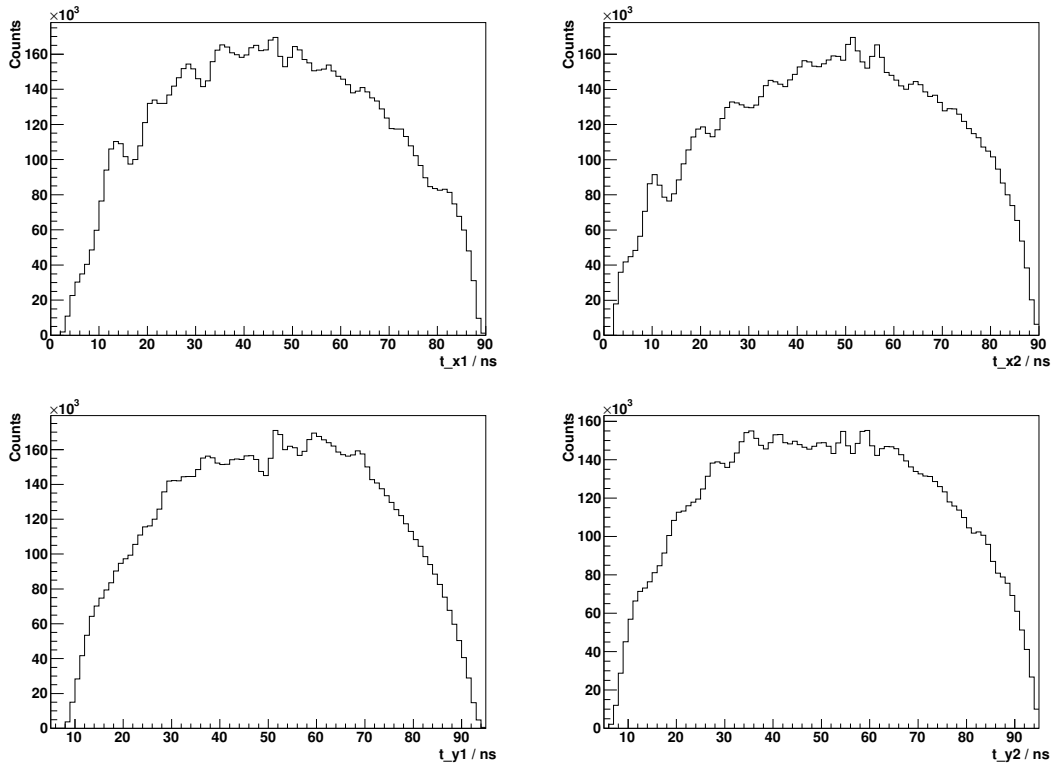
Figure 2.76.: Histograms of t_{X1}, t_{X2}, t_{Y1} and t_{Y2} for the measurement with the uncollimated source. The distributions look almost hemicycle-like with small structure superposed.

This is essentially what we can see in fig. 2.76. Moreover $Y1$ and $Y2$ show fluctuations around the center, which is also true for $X1$ and $X2$ but with additional fluctuations to the left sides of both histograms. These fluctuations are beyond the statistical expectations. Nevertheless this looks better then in 2011 (see fig. 2.35). These fluctuations could be caused by inhomogeneities in the efficiency or artifacts (e.g. hot spots) on the MCP.

2.5.3.2. The sums t_{sx} and t_{sy}

Fig. 2.77 shows the histograms of the sums $t_{sx} = t_{x1} + t_{x2}$ and $t_{sy} = t_{y1} + t_{y2}$. Here one expects a single peak at a time that is equal to the length of the delay line. Due to various delays in the cables and the electronics this can be shifted towards larger times. The electronics of the signal processing (e. g. the walk of the discriminators) and the dispersion of the signals lead to a broadening of these pulses.

This is what we almost see in fig. 2.77. These sums now look more symmetric as in 2011. The double peak structure of the t_{sy} sums is gone but now a small knee on the left side appears. The sums have a standard divination of approx. $\sigma_{sx} \approx 2$ ns. Comparing this to 2011, where t_{sx} had a standard divination of about $\sigma_{sx} \approx 1$ ns and we now see an approx. two times broader distribution. This is expected due to the effect from the shim ring which spreads the electron pulse from the first MCP over a larger surface on the second one, that causes a larger pulse. This will lead also to a broader pulse height distribution.

(a) t_{sx} (b) t_{sy}

Figure 2.77.: Histograms of the sums t_{sx} (a) and t_{sy} (b) of the corresponding signal arrival times for the measurement with the uncollimated source. t_{sx} shows a symmetric peak. t_{sy} has a small bump on the left side and is somewhat asymmetric. Compared to in 2011 the distributions are broader by about a factor 2 ($\sigma_{sx} \approx 2$ ns compared to $\sigma_{sx} \approx 1$ ns, see fig. 2.37). The double-peak structure of the t_{sy} distribution is gone.

2.5.3.3. The differences t_{dx} and t_{dy}

Fig. 2.78 show the histograms of the differences $t_{dx} = t_{x1} - t_{x2}$ and $t_{dy} = t_{y1} - t_{y2}$. One would expect these histograms to have again the hemicycle-like shape with flattened ends like for the t_{X1}, t_{X2}, t_{Y1} and t_{Y2} histograms but now spread over double the length of the delay line, 171 ns (due to the limits in the cut).

In fig. 2.78 t_{dy} shows some small fluctuations near the center. For t_{dx} the fluctuations are spread over a broader range and they are larger. Again the fluctuations are beyond the statistical expectations. To estimate the position resolution form the standard deviation of the sums of the X times σ_{sx} we multiply with the conversion factor f_c:

$$\Delta X \approx \sigma_{dx} \cdot f_c = \sigma_{sx} \cdot f_c \approx 1\,\text{mm} \tag{2.5.1}$$

We see that the expected position resolution is reduced by about a factor of 2 compared to in 2011. This is probably the effect of the shim ring.
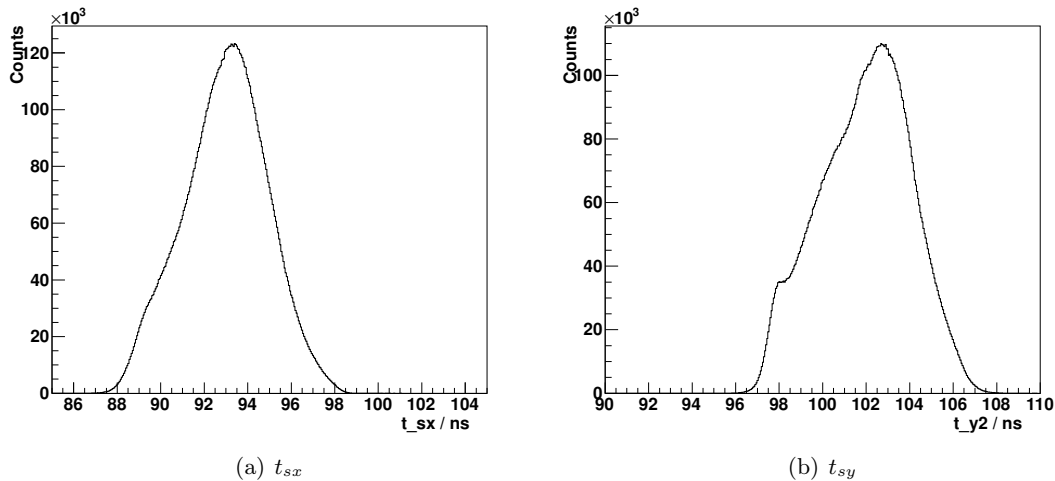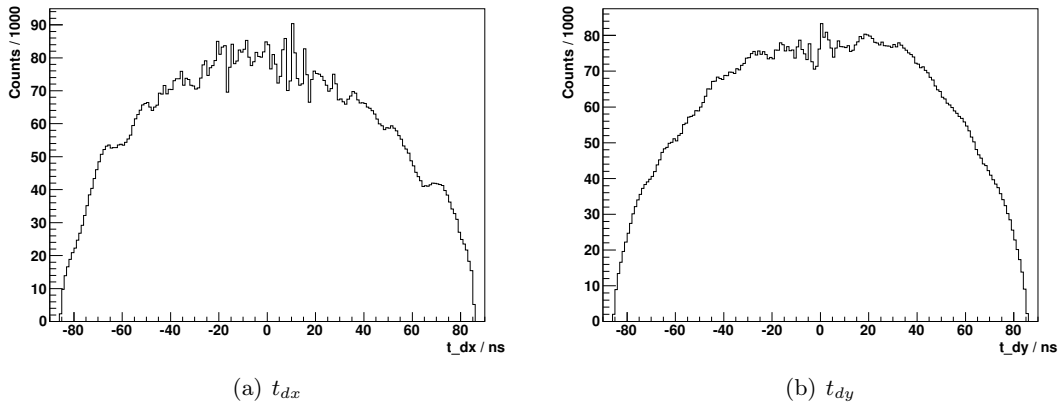

(a) t_{dx} (b) t_{dy}

Figure 2.78.: Histograms of the differences t_{dx} (a) and t_{dy} (b) of the corresponding signal arrival times for the measurement with the uncollimated source.

2.5.3.4. The radial distribution

Fig. 2.79 shows the radial distribution of events over the detector surface. In the ideal case of an homogeneously illuminated detector, the number of counts in each bin of this graph is proportional to t_r we would expect a linear rise and due to the reduced intensity on the outer radii a bend-down towards larger radii. The result shown in fig. 2.79 is almost like we expect it. Around 40 ns the distribution has a small kink and some small ripples appear after 60 ns. The small peak around 85 ns is caused by a hotspot on the outer radius (see section. 2.5.4)
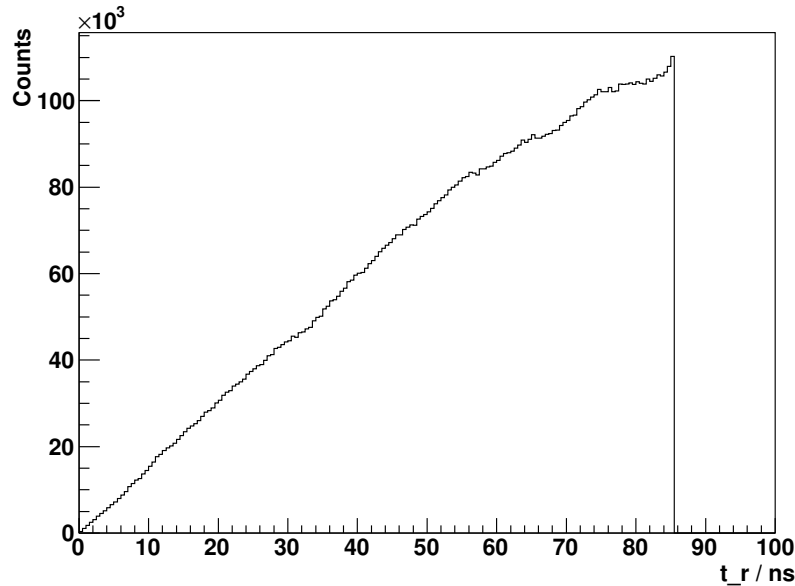

Figure 2.79.: Histogram of the radial distribution for the measurement with the uncollimated source. We expect a linear rise and due to the reduced intensity on the outer radii one would expect a bend-down towards larger radii. In fact the t_r distribution looks very much like we would expect it.

2.5.3.5. Pulse height information

In fig. 2.80 the PHD of the measurement with the uncollimated source is shown. This distribution starts at 380 mV, which is to where the threshold of the main signal is set and reaches to 2.4 V. We would expect a bell-shaped distribution around large pulse heights which is typical for alpha particles with some MeV energy [Lie05]. This is not exactly what we see in fig. 2.80. In the beginning, the distribution shows a peak around 400 mV, which might originate from noise or an electronic artifact. Afterwards is rises from approx. 30000 to 60000 events. The maximum of this distribution is around 1.4 V. Between 2.2 V and 2.3 V it shows a knee and a steep decay from 2.4 to 2.5 V. The step at the end indicates that the distribution is cut artificially by the electronics (the CFD1x). This is what we also observed during the tuning phase beforehand of this measurement. A higher voltage between *Front* and *Back* could not shift the endpoint of this distribution but produced a more dominant knee in the end. This lead to the conclusion that events with pulses over 2.4 V are cut and added on top of the distribution at the place where the knee is positioned.

Overlaid to this curve one can see fluctuations with a regular pattern which are beyond the statistical fluctuations. Although it looks similar to artifacts caused by a faulty binning of the histogram, this has been checked thoroughly and been ruled out. Eventually it stems from the

107
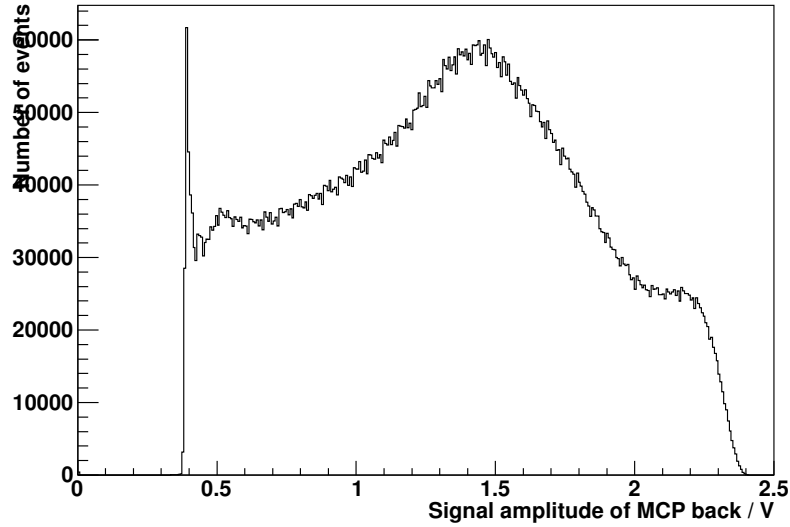
Figure 2.80.: Pulse height distribution of the measurement with the uncollimated source. We would expect bell-shaped distribution around large pulse heights which is typical for alpha particles with some MeV energy. tho is not exactly what we see. In the beginning the distribution shows a peak around 400 mV, which might originate from noise or an electronic artifact.

analogue signal processing electronics (e. g. the CFD1x). The mean value of the PHD is

$$\bar{A}_{PHD,2012} = 1.30 \, \text{V} \tag{2.5.2}$$

Compared to 2011 the maximum of the PHD is shifted from 0.5 V to 1.5 V. The end of the distribution moved from 1.1 V to 2.4 V (but artificially cut). From this we can conclude that now the amplitudes are enlarged by a factor of 3 in average. Considering that the measurement in 2011 was performed with a 210 V higher bias voltage between *Front* and *Back*, this may agree with the observation from the oscilloscope that for identical bias voltage the pulses are about 4 times higher.

2.5.3.6. Background measurement

Fig. 2.81 shows a scatter plot of the background measurement. At the top right corner one can see a hotspot which was present in all of the measurements. Apart from this more background events occur at the outer radius and less in the center of the detector.
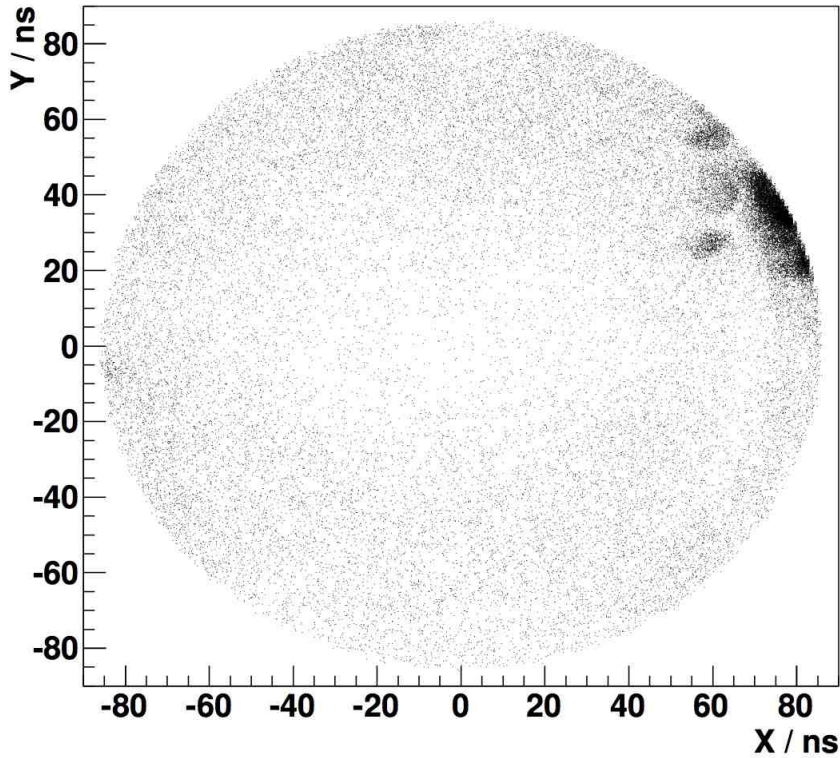
Figure 2.81.: Scatter plot of the background measurement as conducted on 05/06/2012 at 17:40. In the top right corner a spot with more events appears. In the center less background events appear than on larger radii.

The background count rate can be determined from the CAMAC scaler information:

$$\dot{N}_{S,bg} = \frac{5.04 \cdot 10^5}{61293\,\text{s}} = 8.2\,\text{Hz} \tag{2.5.3}$$

Compared to 2011 the count rate is approx. 3 Hz higher. The reason for this is the contribution from the two hot spots. Placing a cut on the events in these two peaks (the condition is: $x > 72$ ns & $y > 12$ ns) we can estimate the count rate contribution in this measurement:

$$\dot{N}_{S,peak} = \frac{N_{E,peak}}{t_m} \cdot f_{dt} = 4.1\,\text{Hz} \tag{2.5.4}$$

So, we see that if we subtract this contribution we find a count rate of 4.1 Hz which is comparable to the measurement in 2011.

2.5.4. Measurement with the uncollimated source in 2012

This measurement was started at 20:30 on 03/06/12 taking 47841 s of measurement time. 83 mm away from of the MCP surface a 40 kBq ^{241}Am alpha source was centered in front of the detector. From the accumulated data we derive an efficiency map of the detector surface similar to the measurement in 2011. Afterwards discuss the pulse height measurement. All the plots are made with a cut on events that fulfill the conditions: $t_{sx} \in [85\,\text{ns}, 105\,\text{ns}]$, $t_{sy} \in [90\,\text{ns}, 110\,\text{ns}]$ & $t_r \in [0, 85.5\,\text{ns}]$.

2.5.4.1. Relative detection efficiency

Fig. 2.82 shows a two-dimensional histogram from histogram of t_{dy} versus t_{dx} for the measurement with the uncollimated alpha source. In the top right corner one can see two larger hotspots. More to the center, around the coordinates (0 ns,40 ns) and (-10 ns,20 ns), two smaller hotspots appear.
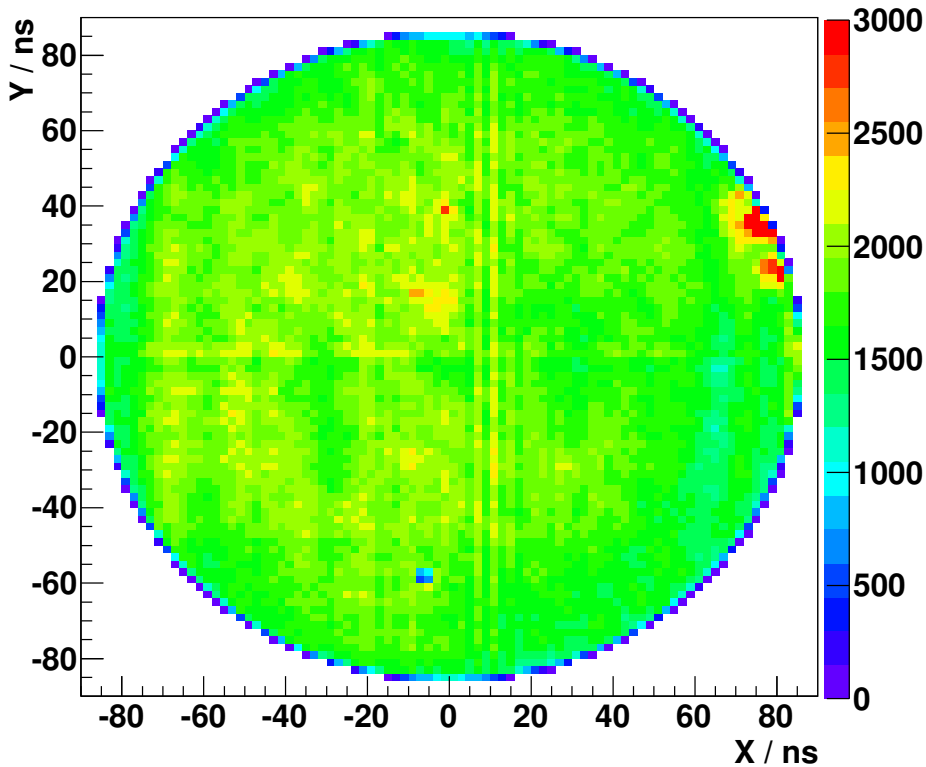
Figure 2.82.: A two-dimensional histogram of t_{dy} vs. t_{dx} for the measurement with the uncollimated alpha source, conducted on 03/06/2012 at 20:30. In the top right corner one can see two larger hotspots. More to the center, around the coordinates (0 ns,40 ns) and (-10 ns,20 ns), two smaller hotspots appear. Around (-10 ns,-60 ns) a blind spot is visible. Apart from this the distribution is rather even.

Around (-10 ns,-60 ns) a blind spot is visible. This originates from an accident with a contaminated pressurized air line. While cleaning the back MCP with pressurized air, a drop of machine oil was spilled on that MCP. This spot is located on the former front side of the back MCP. To avoid having this spot in-between both MCPs and eventually contaminating the front MCP we flipped over the back MCP so this spot of oil is now located on the backside of the back MCP. Probably the oil

chokes the microchannels, hindering the electrons from leaving.

One thing that is particularly noticeable is, that we do not see a dominant peak in the center. In 2011, as described in section 2.3.7, this peak was correlated to the position of the source. One possible explanation can be that the source has been exchanged. According to the CERN Radiation Protection Sources Group the now used source has the same specifications but eventually some details, e. g. how exactly the activity is spread over the surface of the source may be different.

Now we proceed like explained in detail in section 2.3.7, to create a map of the relative efficiency of the detector. This time we don't have to delete the center of the distribution and replace the missing bins. As a reminder we list the individual steps of this procedure:

a) Plot t_{dy} versus t_{dx} of the measurement with the uncollimated source and cut out all events that don't fulfill the condition $t_{sx} \in [85\,\mathrm{ns}, 105\,\mathrm{ns}]$, $t_{sy} \in [90\,\mathrm{ns}, 110\,\mathrm{ns}]$ & $t_r \in [0, 85.5\,\mathrm{ns}]$. This is already shown in fig. 2.82.

b) Subtract the background measurement.

c) Change the scale from ns to mm by using the conversion factor $f_c = \frac{83\,\mathrm{mm}}{180\,\mathrm{ns}} = 0.46\,\frac{mm}{ns}$ (see eq. 2.3.12).

d) Normalize on the distance from the source squared and the incident angle by dividing by the factor $f_{tot} = \frac{R^2 \cdot D}{(D^2 + R^2)^{2/3}}$, where $D = 83$ mm is the distance from the source to the center of the detector surface and R is the radial distance from the center of the detector (see 2.3.18).

e) Normalizing on the maximum. The maximum we define as $N_{max} = 265.5$ in this graph. All entries above that value are set to 1.[6]

f) There are four hotspots in this measurement. All bins in these spots are set to 1 for the efficiency graph.

The result is shown in fig 2.83 with a linear (top) and a logarithmic scale (bottom). Disregarding the blind spot at the bottom center, we still see deviations in the relative efficiency by a factor of almost 2. These appear at some places on outer radii, especially in the 2nd quadrant. Around the coordinate $(15\,\mathrm{mm}, 0\,\mathrm{mm})$ an area with reduced efficiency appears. From the efficiency graph we calculate the mean value of the relative efficiency in this measurement:

$$\bar{\epsilon}_{rel, 2012} = 0.88 \tag{2.5.5}$$

About 84% of the detector surface has a relative detection efficiency $\geq 80\%$ and over 44% of the surfaces has a relative efficiency $\geq 90\%$.

---

[6]because of the hot spots we cannot simply use the bin with the highest content.

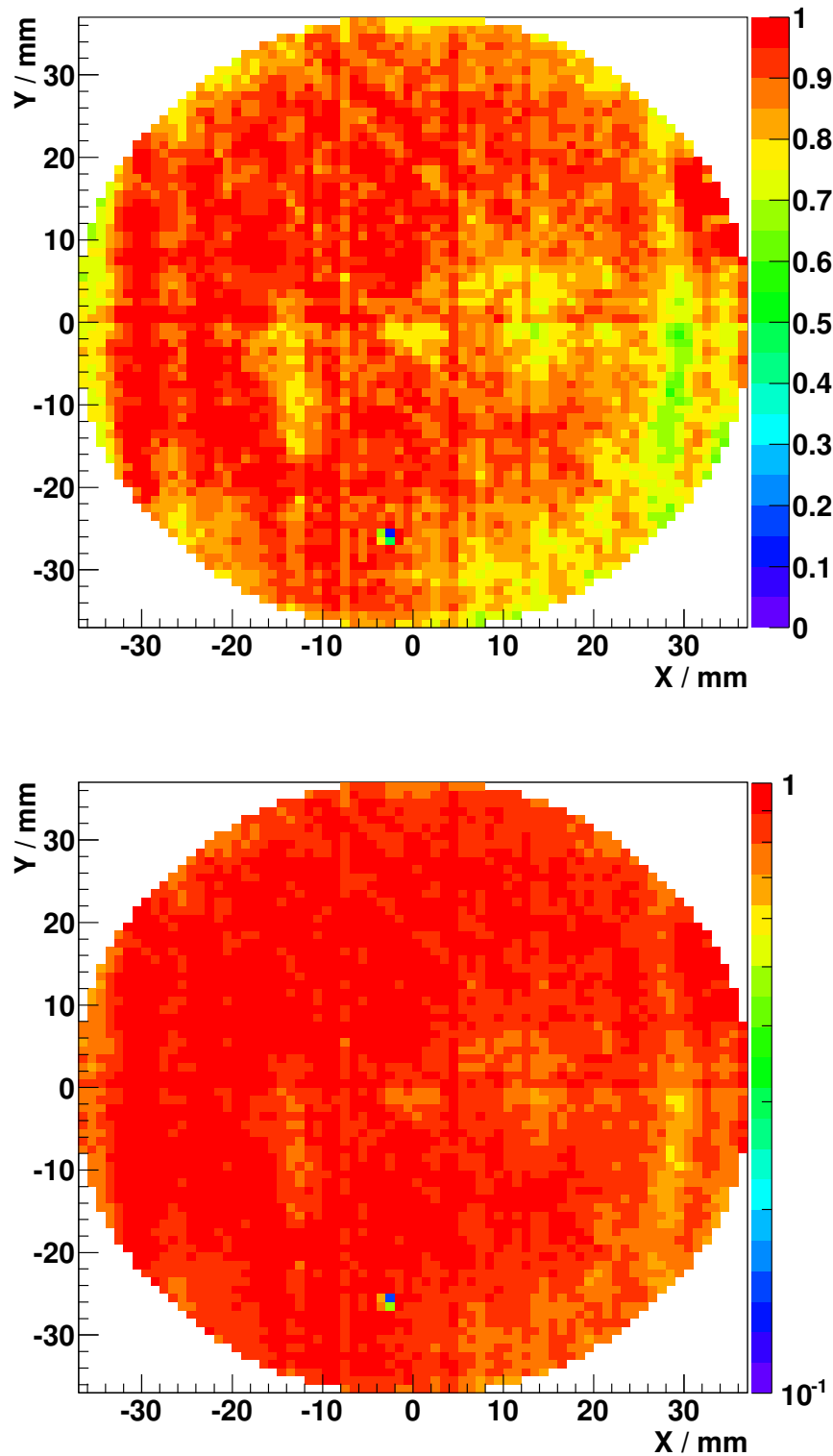**Figure 2.83.:** Relative detection efficiency derived from the measurement with the uncollimated alpha source june 2012. The procedure was analogous to the one described in fig. 2.55 but this time no central peak had to be deleted and replaced. On the lower right corner the detector has areas with slightly decreased efficiency. The mean value of the relative efficiency in this measurement is $\bar{\epsilon}_{rel,\,2012} = 0.88$.

2.5.4.2. Puls height distribution

Alphas usually produce a bell-shaped PHD with a maximum at large amplitudes. To fully understand the PHD shown in fig. 2.80 we have to consider three things. One of them is the fact that pulses with amplitudes larger then 2.4 V are cut and added on top in the end of that spectrum. This was already explain in section 2.5.3.5.

The second thing is the fact that the relative efficiency over the detector surface is not constant. This can be explained by an inhomogeneous gain factor of the MCPs. This will have the effect that the PHD is deformed such that less events appear at higher pulse amplitudes and more for smaller ones. This is one part of the explanation why there are more events between 0.5 V and 1.5 V then we would expect for a bell-shaped curve.

The third thing is that hot spot – like we had at least two rather dominate in our measurement – contribute to small pulse heights. These events will be added on top in the beginning of the bell-shaped curve. This can be the explanation why there are more events between 0.5 V and 1.5 V then we would expect for a bell-shaped curve. The PHD shown in fig. 2.80 has a mean value of

$$\bar{A}_{PHD,2012} = 1.30\,\text{V} \tag{2.5.6}$$
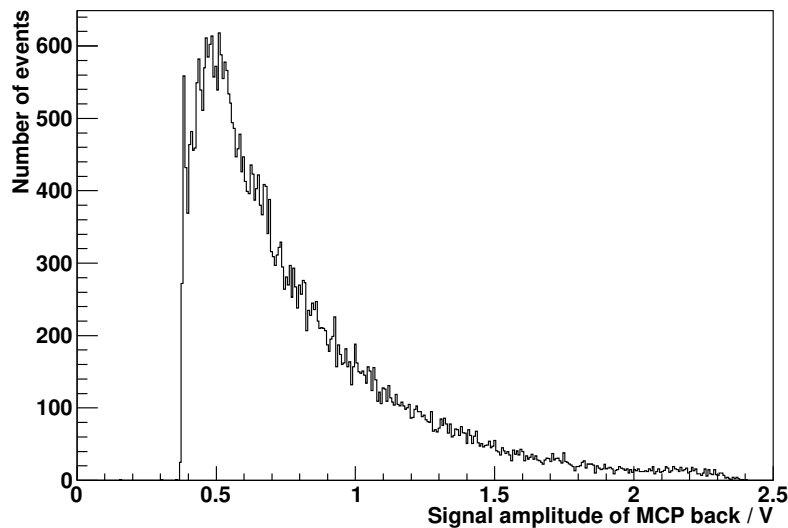
Figure 2.84.: PHD of the background measurement from 05/06/2012 at 17:40. The duration of the measurement was 61293 s. We see a steep rising distribution with an almost exponential decay afterwards, reach up to amplitudes of 2.4 V.

The PHD of the background measurement is shown in fig. 2.84 for the measurement from 05/06/2012 at 17:40. We see a steep rising distribution with an almost exponential decay afterwards. According to ref. [Lie05] this is typical for background pulses of a MCP. The mean value of the background pulse height distribution is:

$$\bar{A}_{PHD,bg,2012} = 0.76\,\text{V} \tag{2.5.7}$$

If we now place cuts on the pulse heights we can locate the areas of the detector that contribute to the different regions of the PHD. We start with small amplitudes. This is shown in fig. 2.85 for the region $A_{PH} \in [0.38\,\text{V}, 1.0\,\text{V}]$ (left) and the region $A_{PH} \in [1.0\,\text{V}, 1.5\,\text{V}]$ (right).
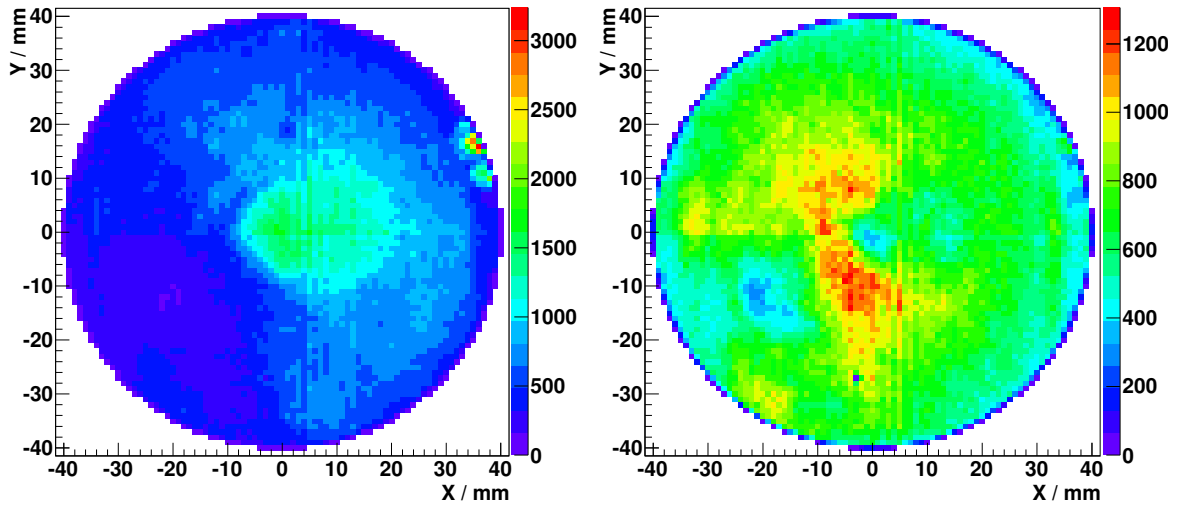
Figure 2.85.: Plot of the position distribution with a cut on $A_{PH} \in [0.38\,\text{V}, 1.0\,\text{V}]$ (left) and the region $A_{PH} \in [1.0\,\text{V}, 1.5\,\text{V}]$ (right). See text for explanation. Amplitudes of $A_{PH} \in [0.38\,\text{V}, 1.0\,\text{V}]$ predominantly appear in a spot in the center of the MCP and less on outer radii. Amplitudes with $A_{PH} \in [1.0\,\text{V}, 1.5\,\text{V}]$ predominantly appear in two sports around the left side of the center.

The small amplitudes ($A_{PH} \in [0.38\,\text{V}, 1.0\,\text{V}]$) appear mostly in the center and the right side of the MCP. The two hotspots on the right side also contribute to this pulse height region. Apart from this the outer radius of the MCP shows less counts. Especially the bottom left corner is dark.
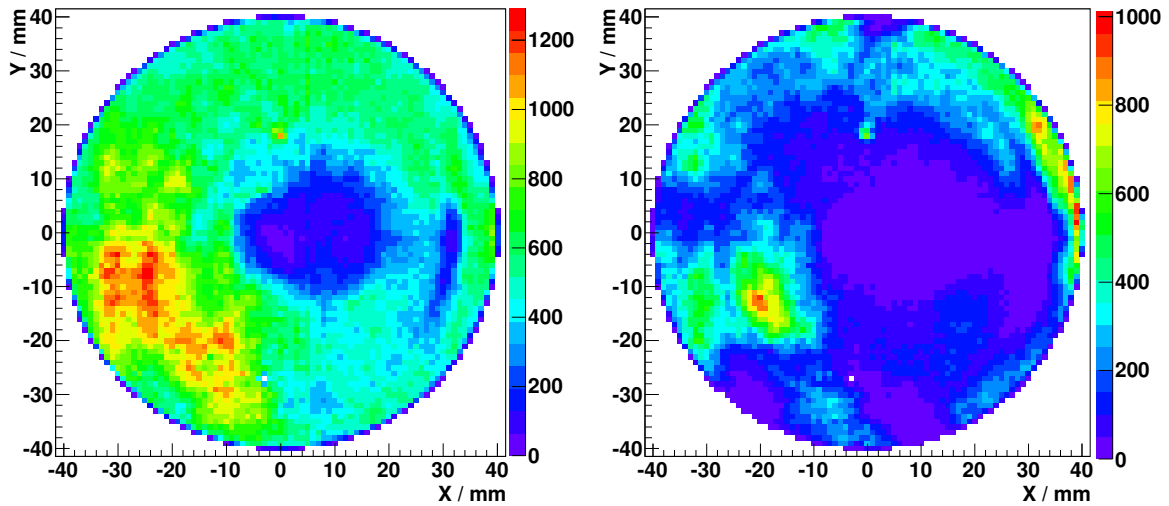
Figure 2.86.: Plot of the position distribution with a cut on $A_{PH} \in [1.5\,\text{V}, 2.0\,\text{V}]$ (left) and the region $A_{PH} \in [2.0\,\text{V}, 2.5\,\text{V}]$ (right). See text for explanation. Amplitudes with $A_{PH} \in [1.5\,\text{V}, 2.0\,\text{V}]$ appear mostly on outer radii especially in the lower left corner. $A_{PH} \in [2.0\,\text{V}, 2.5\,\text{V}]$ show up mostly in a defined ring at the top right and a spot on the lower left.

If we go to larger pulse heights ($A_{PH} \in [1.0\,\text{V}, 1.5\,\text{V}]$), we see that the contributing area moves from the very center to intermediate radii. Still the bottom left corner contributes less. We see a vertical dividing line ranging from (-40 ns, 0) to (8 ns, 0). The hot spot around (0, 20 ns) also has some contributions.

Similar cuts are shown in fig 2.86 for the regions $A_{PH} \in [1.5\,\text{V}, 2.0\,\text{V}]$ (left) and the region $A_{PH} \in [2.0\,\text{V}, 2.5\,\text{V}]$ (right). In the left figure we see that the center region becomes darker. A ring of medium to large radii show some contribution while the most dominant part comes from the bottom left. The hot spot around (0, 20 ns) is still present. The bottom right is slightly suppressed. Moving on with the pulse heights to $A_{PH} \in [2.0\,\text{V}, 2.5\,\text{V}]$ (see fig. 2.86 right), we see that the center and the very bottom becomes almost dark. A ring-like structure on very large radii appears in the upper half of the MCP and two spots at the bottom left are contributing.
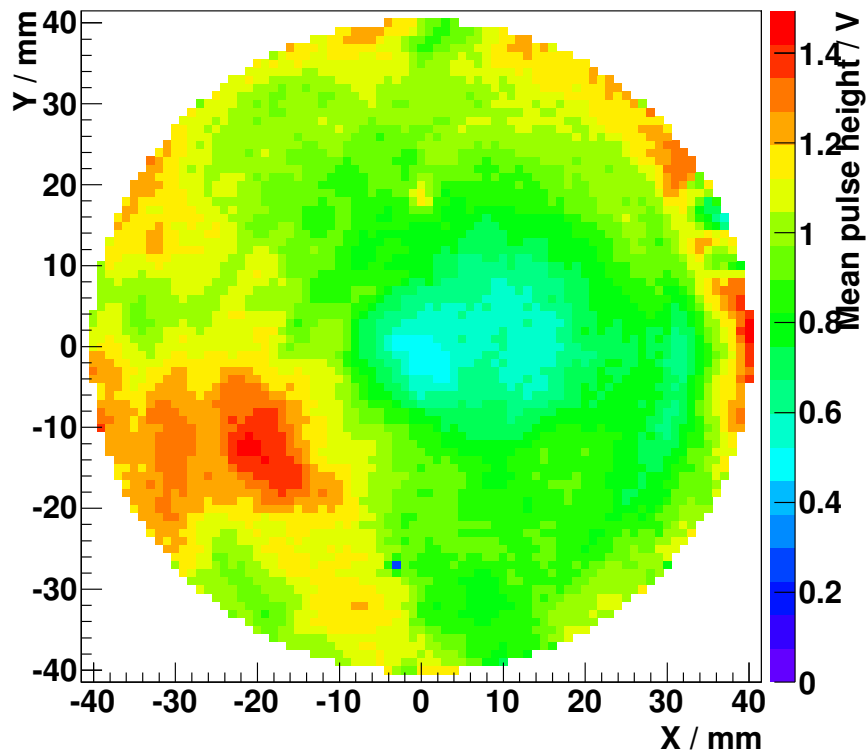
Figure 2.87.: Mean pulse height distribution over the MCP surface. The center and the bottom right show rather low values from 0.5 V up to 1.0 V. The largest mean values of the amplitude appear in a spot on the left side and on the very outer radii at the top right.

By plotting the distribution of events with the weight of their pulse height and normalizing on the number of counts in each bin, one can create a map of the mean pulse heights (compare sec. 2.3.7.2). This is shown in fig. 2.87. The mean value of the plus height ranges from 0.5 V up to 1.5 V over the whole area of the MCP. The center and the bottom right show rather low values from 0.5 V up to 1.0 V. The largest mean values of the amplitude appear on the left side and on the very outer radii. According to the manufacturer this is uncommon. Usually the pulse heights should be almost constant over the surface, eventually with a small decrease of about 10 to 20 % to the edge [Roe12].

2.5.4.3. Absolute detection efficiency

The absolute efficiency can be estimated from the CAMAC scaler information. For the uncollimated measurement the count rate is

$$\dot{N}_{S,uncoll.} = \frac{N_{S,uncoll.}}{t_{m,uncoll.}} = \frac{5.454 \cdot 10^7}{4.78 \cdot 10^4 \, \text{s}} = 1.14 \, \text{kHz}. \tag{2.5.8}$$

The background count rate is

$$\dot{N}_{S,bg} = \frac{N_{S,bg}}{t_{m,bg}} = \frac{5.04 \cdot 10^5}{61293 \, \text{s}} = 8.22 \, \text{Hz}. \tag{2.5.9}$$

The background count rate is about 30 times smaller then the uncertainty of the expected count rate (eq. 2.5.12), why it will be neglected.

These count rates in eq. 2.5.8 and eq. 2.5.9 includes also the rate coming from the two hot spots at the top right corner. These spots contributed to the background count rate with $\dot{N}_{peak,bg} = 4.08$ Hz (see section 2.5.3.6). These peaks showed a time evolution. In the uncollimated measurement their contribution is

$$\dot{N}_{S,peak} = \frac{N_{E,peak}}{t_{m,uncoll.}} \cdot f_{dt,uncoll.} = 20.0 \, \text{Hz}. \tag{2.5.10}$$

This contribution is less then a tenth of the uncertainty of the expected count rate (eq. 2.5.12) why we will neglect this. The alphas and gammas from the source are emitted isotropically in $\Omega_S = 4\pi$. It is placed in $l = 83$ mm in distance from of the MCP which has an active diameter of $d = 83$ mm. The solid angle of the detector can be calculated in analogy to eq. 2.3.26:

$$\begin{aligned} \Omega_D &= \int_0^{2\pi} d\phi \int_0^{\theta_{max}} \sin\theta d\theta \\ &= 0.211 \cdot \pi \end{aligned} \tag{2.5.11}$$

where the upper limit for the integration is $\theta_{max} = \arctan(\frac{83\,\text{mm}}{2 \cdot 83\,\text{mm}}) = 26.57°$. We expect a rate of

$$\dot{N}_{S,exp} = \tilde{A}_S \cdot \frac{\Omega_D}{\Omega_S} = (2.85 \pm 0.79) \, \text{kHz}. \tag{2.5.12}$$

where $\tilde{A}_S$ is the modified activity (see eq. 2.3.7), taking into consideration the gammas coming from the source and the assumed efficiency of the MCP for gammas. Here we neglect sputtered ions coming from the protective sealing of the source. Since this is in the order of about 10 Hz (see sec. 2.3.7 for explanation) this contribution is an order of magnitude smaller then the uncertainty of $\tilde{A}_S$. The total efficiency for this measurement is the ratio of the measured count rate $\dot{N}_S$ and the expected count rate $\dot{N}_D$:

$$\epsilon_{tot,2012} = \frac{\dot{N'}_{S,unc}}{\dot{N}_{S,exp}} = (0.40 \pm 0.11) \tag{2.5.13}$$

Comparing this to the product

$$R_{OA} \cdot \bar{\epsilon}_{rel,2012} = (0.44 \pm 0.04) \tag{2.5.14}$$

where R_{OA} is the open area ratio (eq. 2.2.3) and $\bar{\epsilon}_{rel,2012}$ the averaged relative detection efficiency (eq. 2.5.5), we find both values in agreement within their uncertainties.

2.5.5. Measurement with the aperture mask in 2012

To test the position resolution of the detector a longtime measurement with an aperture mask was performed. In fig. 2.88(a) the mask is shown separately and in fig. 2.88(b) it is shown, installed on the detector. Fig. 2.89 shows a technical drawing of the aperture mask. The mask has 13 rows and 13 columns of holes with a diameter of 4 mm and a center-to-center spacing (the distance between the centers of two neighboring holes) of 6 mm. To create an asymmetry, the hole in the center (column 7, row 7) and one in the upper right corner (column 9, row 3) have a diameter of 6 mm instead of 4 mm. The mask has 145 holes in total It is made from a 0.5 mm thick sheet of aluminum. For the measurement it was attached with two nylon screws and stainless steel counter nuts to the front ceramic ring of the MCP stack. The distance from the mask to the front MCP surface is defined by the thickness of the ceramics, which is 2 mm.

(a)   (b)
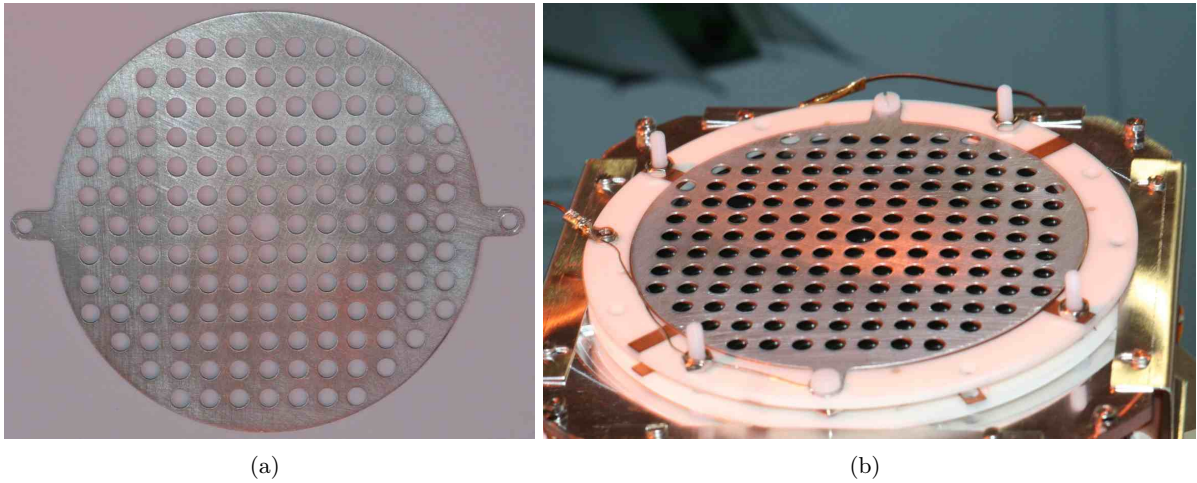
Figure 2.88.: Picture of the aperture mask with 4 mm diameter holes (a) and the detector with the mask screwed on top of the MCP stack (b). Two of the holes, the central one and one in the upper right corner have 6 mm instead of 4 mm diameter to create an asymmetry. The aperture mask is attached with two screws to the ceramic ring and is electrically connected with the MCP *Front*.

Fig. 2.90 shows a plot of t_{dy} vs. t_{dx} derived from the raw data for the measurement with the aperture mask from the 04/06/2012 started at 20:00. One can see that the holes of the aperture mask are resolved. Also the positions of both larger holes is perceptible. In this measurement the columns and rows of the holes in the mask were aligned in parallel to the X- and Y-axis of the detector. We start with the calibration of the position resolution of the detector. Afterwards we compare the efficiency in each spot with the measurement of the uncollimated source.

Figure 2.89.: Technical drawing of the aperture mask. The mask has 13 rows and 13 columns of holes with a diameter of $d_{hole} = 4$ mm and a center-to-center spacing of $d_{ctc} = 6$ mm, which is the distance between the centers of two neighboring holes. The hole in the center (column 7, row 7) and one in the upper right corner (column 9, row 3) have a diameter of 6 mm instead of 4 mm, to create an asymmetry.

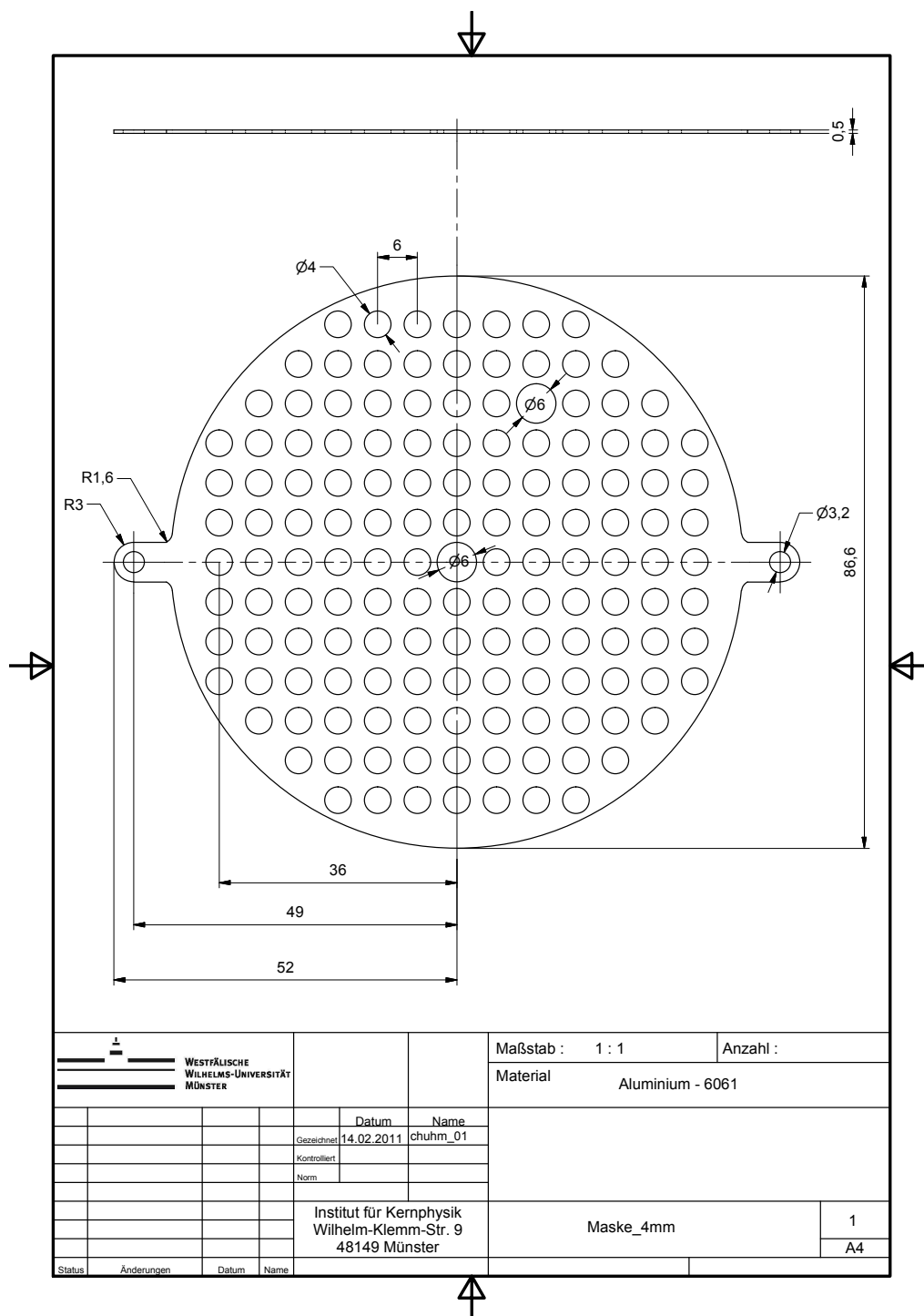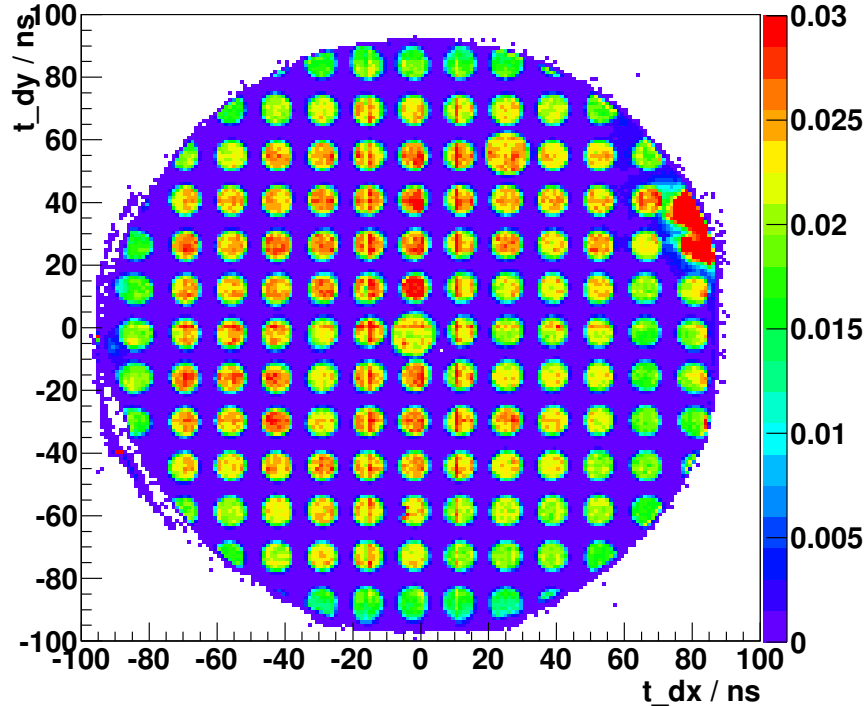**2.5.5.1. Position calibration with aperture mask**

Figure 2.90.: Plot of the t_{dy} vs. t_{dx} divided by the measurement time, derived from the raw data for the measurement with the aperture mask as conducted on 04/06/2012 at 20:00 with subtracted background. The color scale is given in counts per second. On the upper right corner a hotspot appears. All holes are resolved pretty well. The two larger hole appear at the positions we expected and are distinguishable from the others.

First we apply a correct scaling of the outer holes of the mask image. This is done in three steps:

- We plot the data recorded from the measurement with the aperture mask, subtract the background measurement, normalize to the distance from the source squared and the angle of incidence (see sec. 2.5.4). We chose a resolution of 0.1 mm, which is the the value given by the manufacturer (which is only reached with fast amplifiers and CFDs for the delay line signals).

- Then we shifted by eye the image of the mask such that the images of the holes in row 7 are centered on the X-axis and the ones of the holes in the seventh column centered on the Y axis.

- Lastly we scale by eye the X-axis so that the outer edges of the holes in the first and the last column appear at $\pm(13 \cdot d_{hole} + 12 \cdot d_{gap} + 2 \cdot c_{geo})/2 = \pm 39\,\mathrm{mm}$, where $d_{hole} = 4$ mm is the diameter of the holes, $d_{gap} = 2$ mm is the gap between two holes and $c_{geo} \approx 1\,\mathrm{mm}$ a geometrical correction that takes into account the distance between the mask and the detection plane (see fig. 2.91 for explanation). Thereafter the procedure was repeated for the Y-axis.

119

The axis transformations for the timing signals t_{dx} and t_{dy} into x- and y-positions (in mm) we found as:

$$X = t_{dx} \cdot \frac{81\,\text{mm}}{180\,\text{ns}} + 1.0\,\text{mm} \tag{2.5.15}$$

$$Y = t_{dy} \cdot \frac{77\,\text{mm}}{180\,\text{ns}} + 0.6\,\text{mm} \tag{2.5.16}$$

We see that the inner delay line (X) is shorter because it has a larger scaling factor ($\frac{81\,\text{mm}}{180\,\text{ns}}$ instead of $\frac{77\,\text{mm}}{180\,\text{ns}}$).

The result is shown in fig. 2.92 where a resolution of $\frac{83\,\text{mm}}{922}$ in X-direction and $\frac{83\,\text{mm}}{970}$ in Y-direction[7]. Please note that the minimum of the Z axis was set to 1 mHz for a better visibility of the hole images. To recapitulate: In equation 2.5.1 we estimated the relative position resolution as $\frac{\Delta X}{X} \approx \frac{2\,\text{ns}}{171\,\text{ns}}$. If we apply the conversion from equation. 2.5.15 we find:

$$\Delta X \approx 2\,\text{ns} \cdot \frac{81\,\text{mm}}{180\,\text{ns}} \approx 1\,\text{mm} \tag{2.5.17}$$
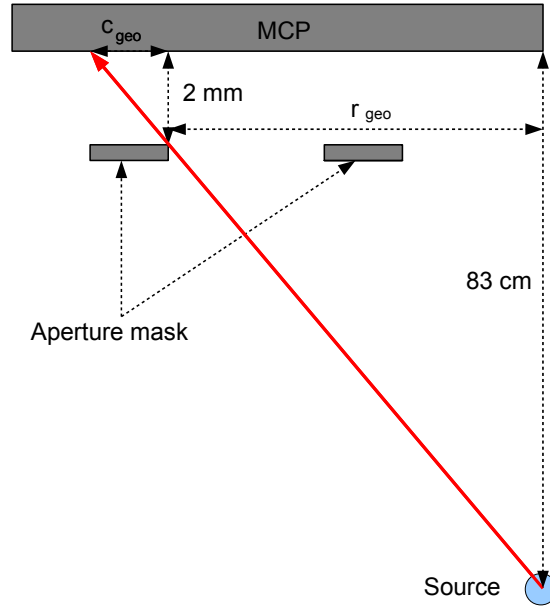
Figure 2.91.: Explanation of the correction factor c_{geo}. The source is located in 83 mm distance from the center of the MCP. The distance between the aperture mask and the MCP front surface is 2 mm. The distance between the center and the outer rim of the outer hole of the aperture mask can be calculated by: $r_{geo} = (13 \cdot d_{hole} + 12 \cdot d_{gap})/2 = 38\,\text{mm}$. Utilizing the incept theorem we find $c_{geo} = 2\,\text{mm} \cdot \frac{38\,\text{mm}}{83\,\text{mm} - 2\,\text{mm}} \approx 1\,\text{mm}$.

---

[7] the values for X and Y differ because of the different conversion factors given in eq. 2.5.15 and eq. 2.5.16 and have been chosen such to ensure a correct binning of the histograms in fig. 2.92, fig. 2.93 and fig. A.1 to A.12. Moreover these values have been chosen so, to be below the value given by the manufacturer which is 0.1 mm.
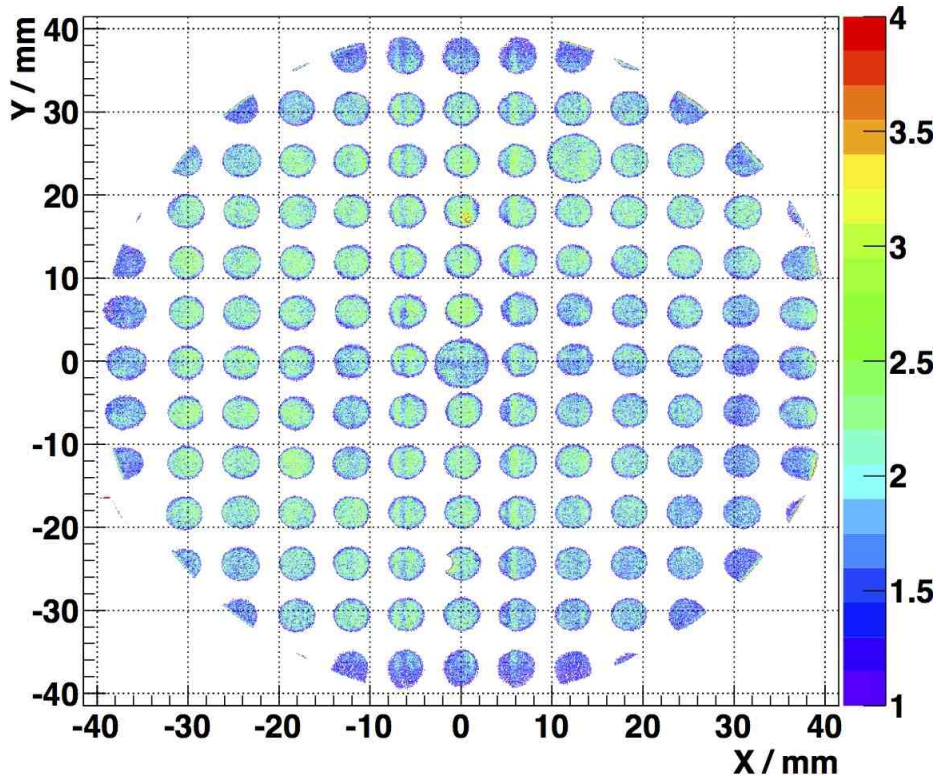
Figure 2.92.: Image of the recorded data from the measurement with the aperture mask and the scaling of the axis coordinates given in eq. 2.5.15 and eq. 2.5.16. The radius has been limited to 40 mm. See text for further explanation.

To test the position resolution of the detector we applied the following method:

- Along the center of each row (in X-direction) and each column (Y-direction) 22 bins wide slices (which is approx. 2 mm) of the histogram shown in fig. 2.92 were cut out.

- Each slice along each row is projected on the X-axis and each slice along each column is projected on the Y-axis. The results for the row $Y = 0\,\mathrm{mm}$ and the column $X = 0\,\mathrm{mm}$ are shown fig. 2.93 as an example, the remaining ones can be found in the Appendix A in fig. A.1–A.12 . These are in total 13 slices in X- direction 13 in Y-direction.

- Then we used these slices to determine in each spot the mean values in X- and in Y-direction. The results for the row $Y = 0\,\mathrm{mm}$ and the column $X = 0\,\mathrm{mm}$ are listed in tab. 2.17. The remainder can be found in tab. A.1–A.12 in Appendix A.

- Finally we compared these results with the expected mean values, taking into account the actual geometry of the mask. For this we assumed a point-like source centered in 83 mm distance from the detector surface, a distance of 2 mm between the mask and the MCP front surface and a thickness of 0.5 mm of the mask. To exemplify this we define for each hole a radius vector $\vec{r} = (r_x, r_y)$ that points from the center of the mask to the center of the hole.

The expected mean $\vec{M}$ value of a certain hole can be calculated via:

$$\vec{M} = ((r_x + 2\,\text{mm} \cdot \frac{r_x}{81\,\text{mm}}), (r_y + 2\,\text{mm} \cdot \frac{r_y}{81\,\text{mm}})) \tag{2.5.18}$$

in this equation the 81 mm is the distance between source and mask plus the thickness of the mask and the 2 mm is the distance between mask and MCP.
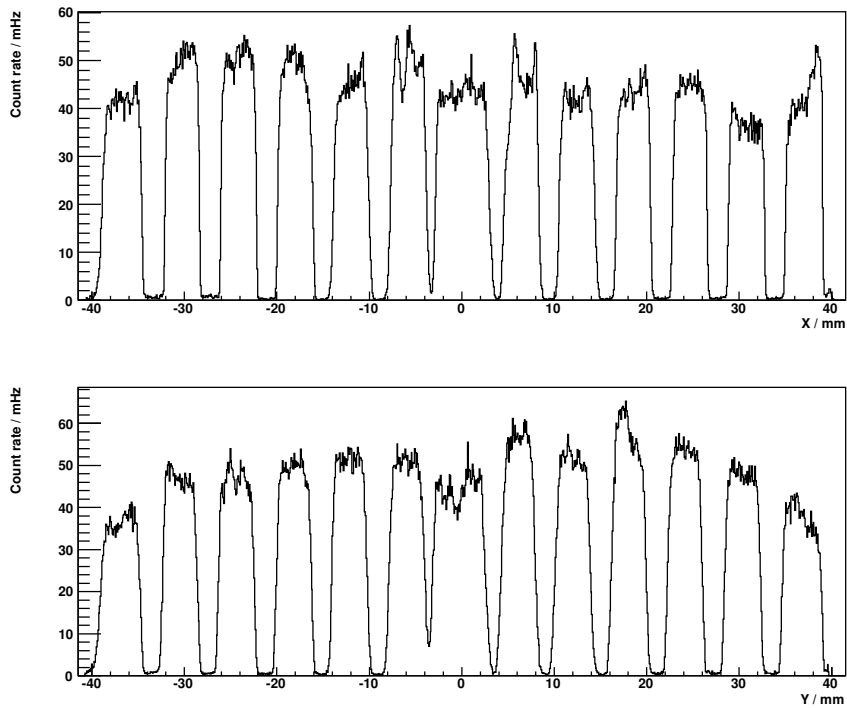

Figure 2.93.: Top: 2 mm thick slice of the X-Z-plane along Y = 0 mm projected on the X-axis. Bottom: 2 mm thick slice of the Y-Z-plane along X = 0 mm projected on the Y-axis.

Table 2.17.: Expected mean and measured mean of the spots from the mask for the slices along Y = 0 mm (left) and X= 0 mm (right) as returned by the algorithm.

Expected mean value	Measured mean value	Expected mean value	Measured mean value
0	0.090878	0	0.090878
0	0.144385	0	0.144385
0	0.211268	0	0.455634
0	0.185403	0	0.211268
0	0.381935	0	0.185403
0	0.115352	0	0.381935
0	0.311884	0	0.115352
0	0.250214	0	0.311884
0	0.144078	0	0.250214
0	0.155134	0	0.144078
0	0.106303	0	0.155134
0	0.059354	0	0.106303

From this we can now create a correction matrix which in each spot shifts the measured to the expected mean value. Therefore we calculate in each spot in row i and column j the vector:

$$\vec{C}_{ij} = (\vec{e}_x \cdot (M_{x,exp,ij} - M_{X,meas,ij}) + \vec{e}_y \cdot (M_{y,exp,ij} - M_{y,meas,ij})) \qquad (2.5.19)$$

where $M_{x,exp,ij}$ is the expected x value, $M_{y,exp,ij}$ the expected Y-value, $M_{x,meas,ij}$ the measured X-value and $M_{y,meas,ij}$ the measured y value of the mean value and $\vec{e}_x$ and $\vec{e}_y$ the unit vectors in X- and Y-direction. The resulting correction matrix $\vec{C}_{ij}$ shifts each measured mean value to its expected position. Spots that were not entirely displayed have been discarded. Apart from the spots on the outer edge, this also included the spot that interfered with the blind spot (row 11, column 7, see fig. 2.92).

The result is displayed as a vector field in fig. 2.94. For better visibility the lengths of these vectors are enlarged by a factor of 5. The edge of the active surface is marked by the black circle. We see a tendency from the top right corner towards the bottom left. This is a clear indication the the scaling is not correct. Therefore we fit the expected mean values to the measured ones, like we explain in the following.
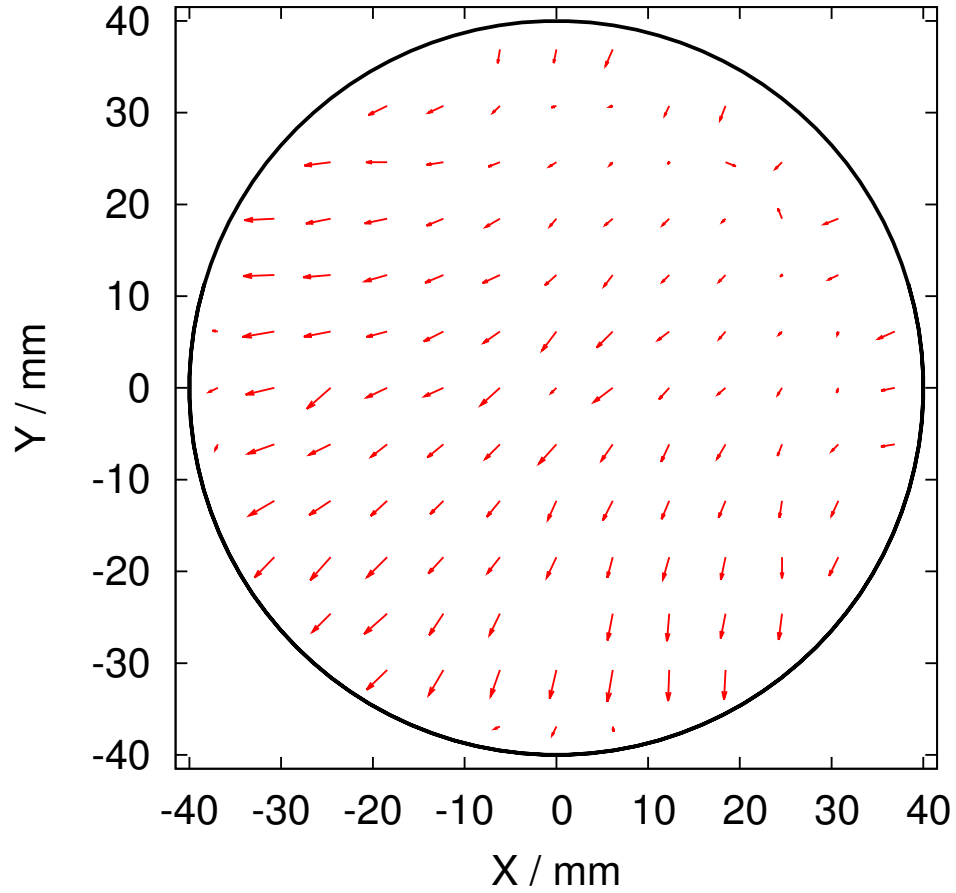
Figure 2.94.: Vector field of the correction matrix $\vec{C}_{mean,ij}$ created from the measured and the calculated mean values. Here the lengths of these vectors are enlarged by a factor of 5 for better visibility. The edge of the active surface is marked by the black circle.

To do so, we first allocate a unique index n to each data point. Starting in the outer left column of fig. 2.94 with the lowermost data point getting $n = 1$ and then moving upwards and then continuing to the right. For each data point we increase n by 1 and so the uppermost data point in the outer right column finally is indexed $n = 120$. Then we create two data files with three columns each: One with the index number n, the measured mean x value and a constant error of 0.114808 and one with the index number n, the measured mean y value and a constant error of 0.119327.[8] In a next step we defined two functions:

$$f_x(n) = a_x \cdot M_{x,exp}(n) + b_x \tag{2.5.20}$$
$$f_y(n) = a_y \cdot M_{y,exp}(n) + b_y \tag{2.5.21}$$

where $M_{x,exp}(n)$ and $M_{y,exp}(n)$ are the expected X and Y values of the data point with index n, a_x and a_y are stretching factors in X and Y direction and b_x and b_y are offsets in X and in Y direction. Finally we fitted the function of eq. 2.5.20 to the x data file and the function of eq. 2.5.21 to the y data file. The fits results in:

---

[8]The values of the constant errors were chosen to achieve $\chi^2/N_{dof} = 1$ for a better error estimation.

- $a_x = (0.9936 \pm 0.0006)$ and $b_x = (0.255 \pm 0.011)$ mm with $\chi^2/N_{df} = 1.0$

- $a_y = (0.9939 \pm 0.0006)$ and $b_y = (0.259 \pm 0.011)$ mm with $\chi^2/N_{df} = 1.0$

(a) X-coordinate   (b) Y-coordinate
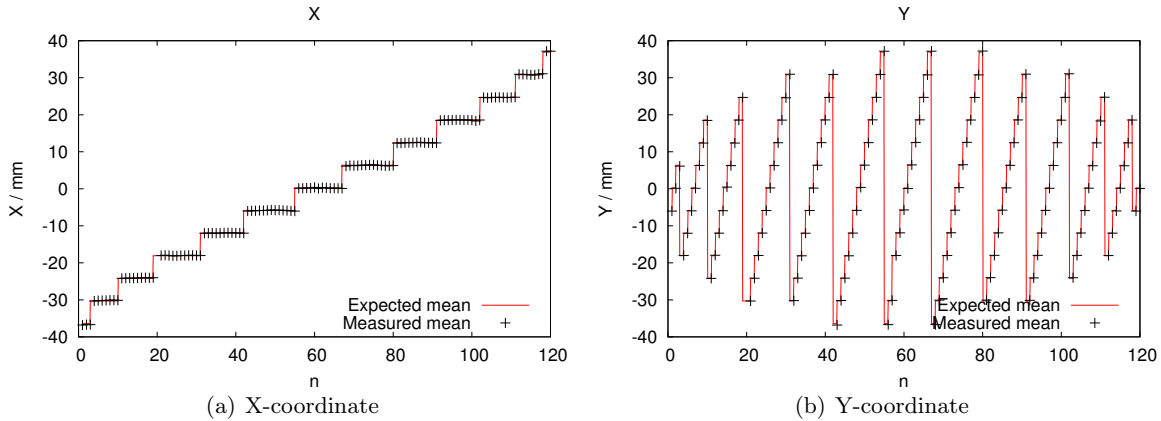
Figure 2.95.: Fit function (eq. 2.5.20) and data points for the X-coordinate (a) and fit function (eq. 2.5.21) and data points for the Y-coordinate (b). n is a unique index allocated to each data point. Steps in the fit functions appear when leaping to another row respectively another column. See text for further explanations.

One should remark that in this fit we neglect a rotation in the X-Y-plane. Fig. 2.95 shows the fit functions and data files for the X- ad Y-coordinate. The residuals for the fit are displayed in fig. 2.96. One can see that the deviations for both coordinates scatter nearly randomly without an obvious systematic. In fig. 2.97(a) a contour plot of the χ^2 as function of the fit parameters a_x and b_x for the fit of the X-coordinate is shown. Fig. 2.97(b) shows the same plot, but for the Y-coordinate. From the orientation of the ellipses we can see that these parameters are not correlated.

(a) X-coordinate   (b) Y-coordinate
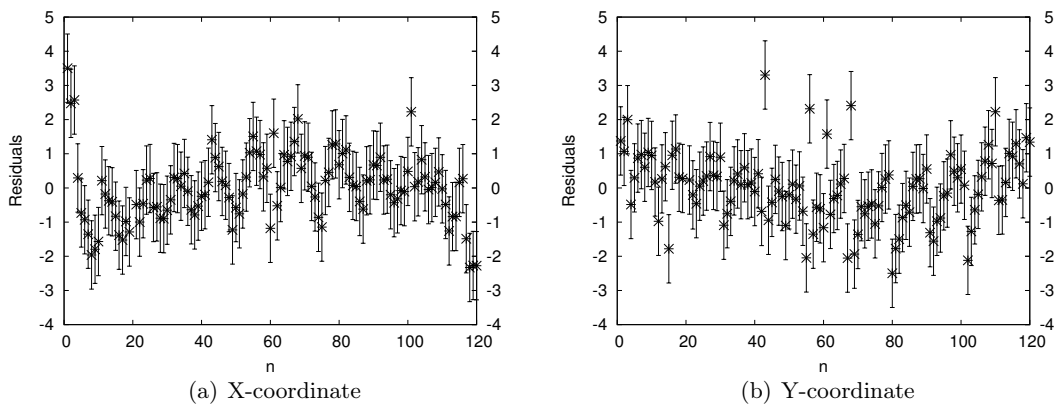
Figure 2.96.: Residuals of the fit for the X-coordinate (a) and the Y-coordinate (b). We cannot see an obvious systematic. In the left plot there are a few runaways to the very left and the very right, as well in the right plot in the very center.

(a) X-coordinate

(b) Y-coordinate

Figure 2.97.: Contour plot of the χ^2 as function of the parameters a_x and b_x for the fit for the X-coordinate (a) and the χ^2 as function of the parameters a_y and b_y for the fit of the Y-coordinate (b). The ellipses show no sign that the parameters a_x and b_x respectively a_y and b_y are correlated.
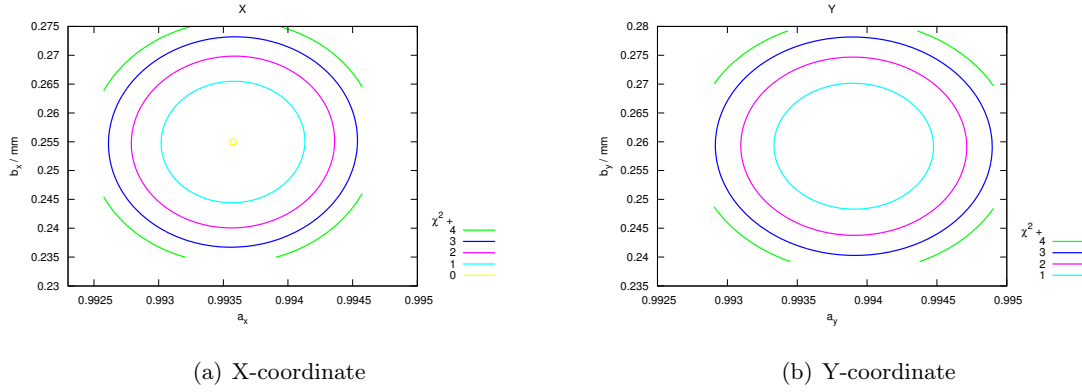
From reverse transformation we get the final scaling of the X- and Y-axises:

$$\tilde{X} = \frac{X - b_x}{a_x} = t_{dx} \cdot \frac{81.54 \,\mathrm{mm}}{180 \,\mathrm{ns}} + 0.751 \,\mathrm{mm} \tag{2.5.22}$$

$$\tilde{Y} = \frac{Y - b_y}{a_y} = t_{dy} \cdot \frac{77.48 \,\mathrm{mm}}{180 \,\mathrm{ns}} + 0.746 \,\mathrm{mm} \tag{2.5.23}$$

If we now create a vector field such as in fig. 2.94 but with the corrected transformations we get the result which is shown in fig. 2.98. Here the amplitudes of the vectors are enlarged by a factor 10. As one can see, now the vectors scatter without an obvious systematics but the deviation seem to become larger to the very edge, especially to the vey top and bottom and the very left and right. These vectors are pointing towards the center.

As we don't observe a curl in the direction of the vectors the negligence of a rotation in the X-Y-plane seems to be a valid assumption. If we now plot the differences of the expected and measured X- and Y-mean values in histograms $(M_{x,exp} - M_{x,meas})$ and $(M_{y,exp} - M_{y,meas})$ we get the distributions shown in fig. 2.99. We see that the differences scatter around 0 with a root mean square of $\sigma_{RMS,x}$ and $\sigma_{RMs,y}$. This will define our position resolution in either X- or Y-direction:

$$\Delta X = \sigma_{RMS,x} = 0.12 \,\mathrm{mm} \tag{2.5.24}$$

$$\Delta Y = \sigma_{RMS,y} = 0.12 \,\mathrm{mm} \tag{2.5.25}$$

For the radial position resolution we transform ΔX and ΔY as follows:

$$\Delta R = \sqrt{\Delta X^2 + \Delta Y^2} = 0.17 \,\mathrm{mm} \tag{2.5.26}$$
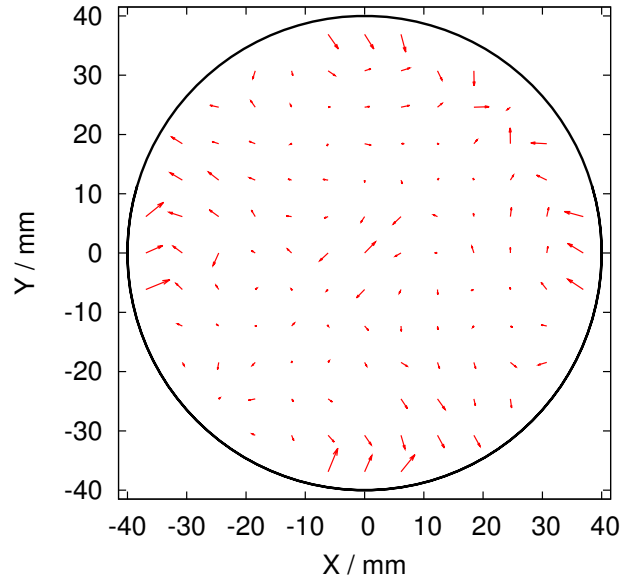
Figure 2.98.: Deviations between expected and measured mean values shown as a Vector field $\vec{C}_{mean,ij}$. The lengths of these vectors are enlarged by a factor of 10 for better visibility. The edge of the active surface is marked by the black circle. One can see that the largest deviations occur at the ends of the delay line anode. See text for details.

(a) X-component
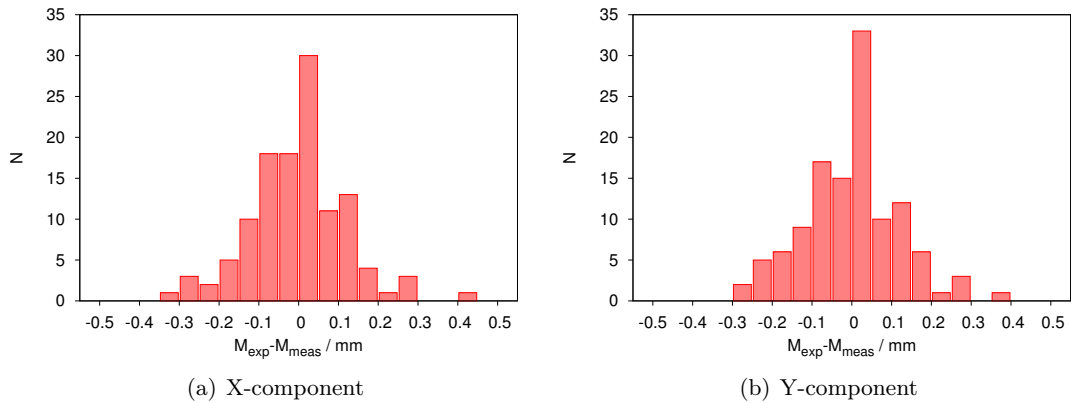
(b) Y-component

Figure 2.99.: Difference between the expected and the measured mean values $(M_{x,exp} - M_{x,meas})$ for the X-component (a) and $(M_{y,exp} - M_{y,meas})$ for the Y-component (b). The distributions scatter around 0 with a root mean square of 1.3 μm each.

2.5.5.2. Relative detection efficiency with aperture mask

We compare the count rate of the measurements with and without the aperture mask. If we neglect the two bigger holes, the open area ratio of the mask can be estimated to:

$$R_{OA,mask} = \frac{\pi \cot(2\,\mathrm{mm})^2}{(6\,\mathrm{mm})^2} \approx 0.35 \tag{2.5.27}$$

For the count rate we would expect roughly a fraction of 0.35 of the count rate without the mask:

$$\dot{N}_{S,mask,expected} = 0.35 \cdot \dot{N}_{S,uncoll.} = 398\,\mathrm{Hz} \tag{2.5.28}$$

Comparing this with tab. 2.16 where $\dot{N}_{S,mask} = 397$ this is in good agreement. If we subtract the mask measurement from the measurement with the uncollimated source, normalized on the measurement time and corrected for the dead time, the intensity drops to zero at the places of the holes. This is shown in fig. 2.100.
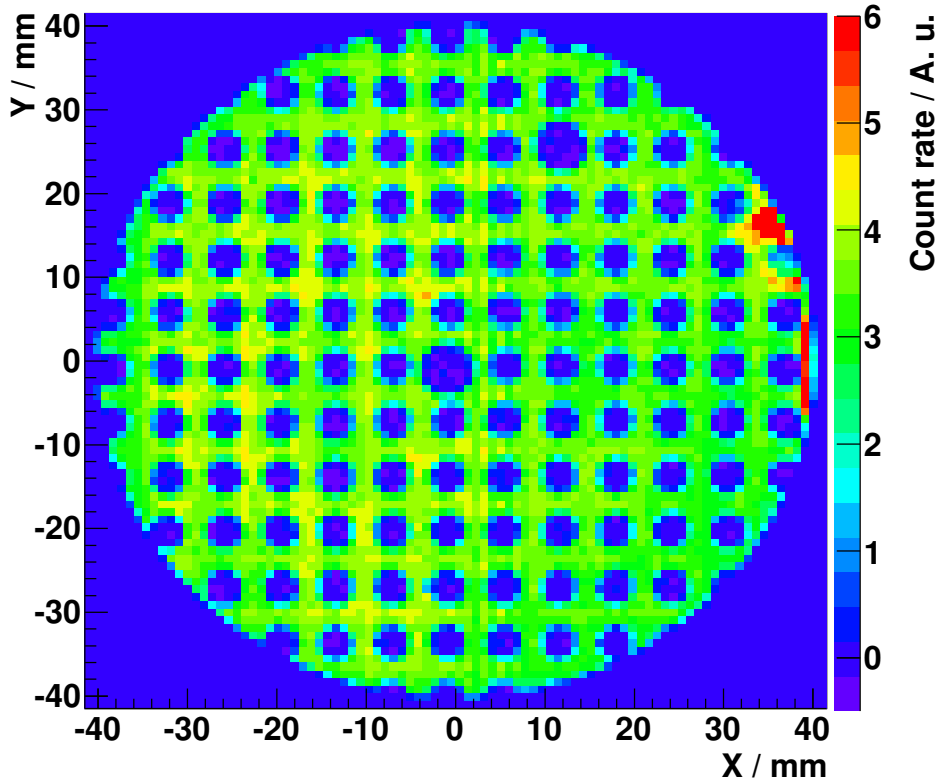
Figure 2.100.: Measurement of the uncollimated source with subtracted measurement with aperture mask. Both measurements have been normalized to the measurement time. At the positions of the holes the difference in count rate is compatible with zero. Both measurements are good agreement.

Like it is expected, the count rate in each spot of the mask drops to zero. Only small fluctuations occur in some spots. From this we can conclude that these two measurements are in good agreement.

2.5.6. Discussion of the detector calibration in 2012

During the tests with the shim ring we have seen that very accurate positioning of the shim ring is mandatory to avoid discharges. Finally a stable situation was found with the shim ring from the workshop in Münster, which has a 2.6 mm smaller diameter then the outer radius of the MCPs. Small pintles, made of Peek, keep the MCPs centered. These small details helped to created a situation where we could run the detector in stable conditions over four days without problems. It was possible to apply up to 2.24 kV between *Front* and *Back* without discharges, a further increase of the voltage was not tested[9].

In this section it was shown that the effect of the shim ring is huge. The amplification factor from the MCP stack increased approx. by a factor of 3 compared to the measurement in 2011 although the potential difference between *Front* and *Back* was 200 V smaller. With this the relative detection efficiency now deviates by less then a factor of two over the whole MCP surface. Nevertheless we see some smaller areas, especially at the right bottom, that are less efficient. Comparing this to 2011 where we saw deviations in the efficiency by about a factor of 10, we reduced the relative deviations by a factor of 5!

The areas of reduced efficiency are now more confined. They either appear on the very outer radii where they do not harm us or at the bottom right part of the MCP. Over 84% of the active detector surface has equal or more than 80% relative detection efficiency and 44% has equal or more than 90% relative efficiency. The mean value of the relative detection efficiency increased from 61% to 88%. We found that the total efficiency of this detector is $\epsilon_{tot,2012} = (0.40 \pm 0.11)$ (see eq. 2.5.13). This value is in agreement with the open area ratio (see eq. 2.2.3). The uncertainties on these values are huge, due to the uncertainty of the source activity and the estimated contribution of gammas to the count rate. We could not observe a peak in the center like in 2011.

The measurement with the aperture mask has shown that we are able to nicely resolve the holes of the mask. We can easily distinguish the larger holes from the small ones and find them at their predicted positions. By comparing the measured with the expected mean values and the FWHM of the spots from the mask we find that with the current setup, we can achieve an absolute position resolution $\Delta R < 0.2$ mm. This is almost the value that the manufacturer gives in the manual[10], which they achieve with the use of fast amplifiers and CFDs for the delay line signals and no shim ring between the MCPs.

We still see an inhomogeneous gain factor of the MCPs stack. The means pulse height deviates by about a factor 3 over the whole surface. Especially areas in the center and at the bottom seem to have less good amplification. The highest gain factors were observed on the very outer radii and the bottom left corner. A small drawback is that, due to the accident with the contaminated pressurized air line, a small blind spot, about 2 mm × 2 mm in area, now appears in the lower part of the detector.

---

[9]In November 2012 the same detector setup was used in an online measurement. During the course of the measurement and several weeks of preparation the detector was operating stable without any incident. In the preparation time a voltage of 2.4 kV between *Front* and *Back* was tested for several days without problems.

[10]the value given in ref. [Roe11] is a position resolution better then 0.1 mm

2.6. Summary and conclusion of the detector calibration

Over a period of almost two and a half years the WITCH detector system has been improved subsequently. Starting with a mere copy of the old detector design we found that this was not stable in operation. Showing a high vulnerability to a shortcut delay line anode, it happened that the position read-out was disabled all of a sudden, during regular operation. As the most probable source for the shortcuts we identified conductive dust coming from the hull of the coax signal cables. Since this is not a solution for a long term, we decided to replace the old signal decoupling by the standard solution offered by the manufacturer. Through this we achieved fourfold improvements:

- The probability for a shortcut delay line has been reduced significantly – during the last one and a half years we only had three incidents – such that it is now possible to operate the detector over weeks and even months without a shortcut delay line.

- The signal quality and signal-to-noise ratio improved significantly.

- The vacuum in the detector chamber improved by one order of magnitude, due to the fact that the soldered electronics has been moved to the outside.

- The decoupling and signal processing outside of the vacuum allows to troubleshoot in many cases without intervening in the vacuum system.

Detailed descriptions of the individual components of the WITCH detector system, starting with the microchannel plates and the delay line anode then moving on to the analogue electronics like the amplifiers and discriminators and finally arriving at the DAQ system, were presented and suitable settings were given.

For the calibration of the detector we developed a procedure to calibrate the relative and absolute detection efficiency. We used an ^{241}Am alpha source in a defined distance in front of the detector. This type of measurement can be performed in the short period of about two days with minimum interventions on the detector itself. A second measurement, with the help of an aperture mask screwed onto the ceramic holder ring of the MCP *Front* is an easy way to test the position resolution of the detector. Thereby it is possible to measure the position resolution in one cycle also with a minimum intervention to the detector. *A full calibration measurement of the WITCH detector is possible in about 4 days.*

In a first series of calibration measurements performed in summer 2011 we found significant fluctuations in the relative detection efficiency of the WITCH detector of about a factor 10. This was shown in two independent series of measurements with different systematics: one a longtime measurement with an uncollimated alpha source in a defined position in front of the detector and second with a collimated source attached to a movable manipulator (see sec. 2.3.7 and 2.62). The absolute efficiency was determined at this time to $\epsilon_{tot,2011} = (0.30 \pm 0.08)$ (see eq. 2.3.29).

This situation was dissatisfactory though, the reason for this inhomogeneous efficiency might be a so-called Moiré pattern, created by the two MCPs stacked closely together. By installing a shim ring between the two MCPs which could avoid such a Moiré pattern and increase the amplification of the MCP stack. First tests with a shim ring, ordered from the manufacturer of the detector, showed another problem: discharges at the MCP stack. By manufacturing a new ring with reduced diameter and building lateral support for the MCPs we found a stable situation that allowed us to run the WITCH detector without problems. Moreover this shim ring increased the gain factor of the MCP by about 3 times (see section 2.5.4.2) and reduced the relative detection inhomogeneities to less then a factor 2 (see fig. 2.83).

This followed a measurement with an aperture mask which was attached to the ceramic ring of the MCP stack. We fitted the measured to the expected mean values that we calculated from the known geometry of that setup. This way we could determine the correct scaling factors for the X-

and Y-axises. From the distribution of the differences between measured and calculated mean values we could deduce a position resolution of $\Delta R = 0.17$ mm. This is close to what the manufacturer gives as reference (0.1 mm) and one should notice that they reach this value with better analogue electronics and without shim ring. The shim ring is known to deteriorate the spatial resolution. This value is probably sufficient for the experiment at the moment, since we are limited by the uncertainty of the geometry.

We summarize the key features of final detector configuration again in the following list:

- Shortcut delay lines, and disabled position read-out as a consequence of it, are not an issue anymore. The risk for a shortcut delay line has been reduced significantly. Only three incidents occurred in the last 2 years, that were easy to solve. This is a requirement for a stable operation of the detector.

- A stable mode of operation has been proven over a period of one week[11].

- A pressure below $6 \cdot 10^{-6}$ mbar can be reached within 3 hours after installation of the detector. The detector has to stay at least 1 hour below $2 \cdot 10^{-6}$ mbar. So after approx. 4 hours after its installation the detector is ready to operate.

- The vacuum in the detector chamber improved by about one order of magnitude, due to the fact that the soldered electronics for the electronics have been moved to the outside.

- The background count rate was measured:

$$\dot{N}_{S,bg} = 8.2 \, \text{Hz}$$

- The mean pulse height for alphas and background events are

$$\bar{A}_{PHD,2012} = 1.30 \, \text{V} \quad \& \quad \bar{A}_{PHD,bg,2012} = 0.76 \, \text{V}.$$

Compared to 2011 ($\bar{A}_{PHD,2011} = 0.53$ V and $\bar{A}_{PHD,bg,2011} = 0.54$ V) the mean pulse height of alphas increased by about a factor 3 and the difference to the one of the background increased.

- We see relative efficiency differences of about a factor 2 only in small areas which are mostly located on outer radii.

- The relative detection efficiency is the ratio of the detection efficiency at a distinct place to the maximum possible efficiency value which is the open area ration (see eq. 2.2.3). Over 84% of the detector surface has $\geq 80\%$ relative efficiency and about 44% has $\geq 90\%$ relative efficiency. The mean value of the relative efficiency is

$$\bar{\epsilon}_{rel,2012} = 0.88.$$

- The absolute detection efficiency is the probability with which events that are homogeneously distributed over the whole detector surface are detected. For alphas of about 4.5 MeV energy this was determined as

$$\epsilon_{tot,2012} = (0.40 \pm 0.11).$$

---

[11]In Nov. 2012 the detector was used in the same configuration for an online measurement. Only the DAQ has been exchanged.

- The transformations from the time into space domain for the X and Y axises are:

$$\tilde{X} = t_{dx} \cdot \frac{81.54\,\text{mm}}{180\,\text{ns}} + 0.751\,\text{mm}$$

$$\tilde{Y} = t_{dx} \cdot \frac{77.48\,\text{mm}}{180\,\text{ns}} + 0.746\,\text{mm}$$

- We achieve a position resolution of

$$\Delta R = 0.17\,\text{mm}.$$

The results presented in this chapter document the progress at the WITCH detector. We showed that the detector is now fully operational and calibrated. During the work we experienced situations, e. g. the problems with shortcut delay lines or the relative inhomogeneity of the detection efficiency of the MCPs, that were unexpected. This and the insufficient documentation of the old detector system lead to delays in the calibration and stable operation of the new WITCH detector.

In a more sophisticated state of the experiment we suggest the following modifications and improvements for the detector and the calibration procedure:

- The biggest uncertainty in this calibration procedure comes from the source. Its activity is only known with a precision of 10%. Moreover the source provides alphas with a mean energy of about 5 MeV and gammas in the soft X-ray regime. The experiment however, aims to measure ^{35}Cl ions with charge states of $0 \leq q \leq +5$ e and incident energies of $\approx q \cdot 3$ keV.

  For a good determination of the absolute efficiency this is too imprecise and also the situation is not fully comparable. A better option would be an ion source that could deliver ions of comparable masses and energies. For such a purpose commercial ion sources are available that can provide ions such as ^{23}Na$^+$ or ^{6}Li$^+$ ions with tunable energies of 0.5 - 7.5 keV [Lie05]. It is highly recommended to use such a source for upcoming calibration procedures.

- One major problem during the calibration are vibrations on the WITCH platform caused by the pre-vacuum pump, people walking around and occasionally dewars that are craned onto the platform. We could circumvent this problem by installing a calibration source right underneath the detector chamber, that could be moved in and out with a linear feedthrough. This would allow us to calibrate the detector right before and after a measurement and by this we could eliminate another uncertainty when having to move the detector from the calibration chamber to the top of the spectrometer.

- The CAMAC DAQ system shows a large, not constant, dead time with a random behavior, which is in the order of 10 to 100 ms. Usually CAMAC systems can handle event rates of approx. 10 to 100 kHz. The individual components of the CAMAC system, the crate, the controller, the TDC and the scaler, have been replaced and checked and found to be operational. The most probable source for this misbehavior is the software that controls the data readout and storage. It is at the moment a Windows XP system with a LabView based code, which is typically not dimensioned for handling high rates with little and reproducible dead time. If this is somehow not feasible, another solution for this problem could be the replacement of the CAMAC system and the current DAQ computer and software.

The last and most urgent item has been tackled in the meantime. The CAMAC DAQ system and the discriminators have been replaced by a system named FASTER which was developed at LPC CAEN. This system has eight channels, each consisting of a CFD, a scaler and a TDC. All settings can be made softer ware-based. An online analysis software is installed on a separate PC which is based on RHB – a ROOT-based routine (see also chapter 4).

Part II.

Analysis of a test run optimizing the WITCH experiment

Data analysis of the October 2011 beam time

3.1. Introduction

In October and November 2011 two beam times were conducted. The first measurement was scheduled from October the 29th to November the 1st. Despite the fact that the actual measurements took place on November this measurement will be called October beam time in 2011, since the major part of the preparations took place in October. This is the first time a measurement with ^{35}Ar has been performed with the WITCH experiment, with a fully working spectrometer. The other measurement was conducted from November the 9th to November the 11th, which will be called November beam time in 2011. An earlier measurement with ^{35}Ar was performed during June 2011 where several problems hindered the correct operation of the MAC-E filter spectrometer (see ref. [Gor11a]). In 2007 a first measurement with ^{35}Ar and following in 2009 a second test measurement couldn't provide valuable data [Tan11a]. A first successful measurement of a recoil spectrum with ^{122}In in 2009 is described in detail in ref. [Bec11].

Before the October measurement that will be described here, a severe problem of the target which was arranged for this measurement appeared. In the curse of the preparation time, the target completely broke and could not be used anymore. As a last resort an old target from 2008 was installed, which allowed us to measure, but only with reduced beam intensity. In a second measurement, the November measurement, scheduled about one week later a new target was provided by the ISOLDE which allowed us to measure with higher statistics. The analysis of this measurement will eventually be described elsewhere [Bre13].

This chapter is fourfold: An introductory part describes in detail the measurement principle starting with the choice of the isotope and its production at the ISOLDE, continue with the measurement cycle of the WITCH experiment and finally discussing problems with the data taking. In the second part we introduce the simulation tool SimWITCH. We describe its components and discuss some more general results of simulations that used this routine. In the third part we describe in detail the analysis process of the data taken on November 1st, where we first tackle a critical problem with the synchronization of the data acquisition, continue with the combined fit of the raw data, generate a fit function with the help of tracking simulations and finally discuss the least square fit of the recoil spectrum. The fourth part of this chapter is a discussion of the systematic effects of this measurement. These are in particular the effect of the so-called anti-ionization wire on the shape of the recoil spectrum and the effect of the initial kinetic motion of the ions in the decay trap. We finish this section with a discussion of the results.

3.2. The measurement

In the following subsections we explain the measurement principle of the WITCH experiment and how it was realized in the October beam time in 2011. The first section concentrates on the selected isotope ^{35}Ar. Thereafter we explain how the measured recoil energy spectrum is expected to look like. Afterwards we explain the details of the measurement cycle and discuss the problems that occurred in this measurement.

3.2.1. Isotope selection ^{35}Ar

The isotope of choice has to fulfill certain requirements as it is partially described in [Gor12]. In particular the requirements are:

- A high production yield at ISOLDE, about 10^6 to 10^7 ions per second.

- The isotope should have a low ionizing potential.

- The half-life should be around 0.5 to 3 s, such that it fits into the experimental cycle of the experiment.

- It should decay to a stable daughter isotope, so that its decay products do not contaminate the spectrometer or the MCP detector.

- It should have a simple decay scheme.

- The ion beam should have minimal isobaric contamination. The mother nucleus ^{35}Ar has an atomic mass of $M(^{35}\text{Ar}) = (34.9752567 \pm 0.0000008)$ u [Aud95] and the daughter nucleus ^{35}Cl has an atomic mass of $M(^{35}\text{Cl}) = (34.968852 \pm 0.0000000)$ u [Aud95] where the uncertainties of the latter value are an order of magnitude smaller than the shown number of digits and therefore are negligible with respect to the ^{35}Ar value. The mass resolving power that is necessary to separate the mother an the daughter ions from the ^{35}Ar decay can be estimated as[1]:

$$
\begin{aligned}
\frac{\Delta M}{M}\left(^{35}\text{Ar},^{35}\text{Cl}\right) &= \frac{M(^{35}\text{Ar}) - M(^{35}\text{Cl})}{M(^{35}\text{Ar})} \\
&= \frac{(34.9752567 \pm 0.0000008)\,\text{u} - (34.968852 \pm 0.0000000)\,\text{u}}{(34.9752567 \pm 0.0000008)\,\text{u}} \\
&= 1.8882 \cdot 10^{-4} \\
&\approx \frac{1}{5000}.
\end{aligned}
\tag{3.2.1}
$$

    This is at the limit of what mass resolving power the HPS can provide at best. In previous measurements most of the ^{35}Cl contamination was created in the source. These ^{35}Cl impurities were brought into the target material by a treatment with cleansing agent which contains chlorine. Improved handling of the target material could reduce the contaminations of ^{35}Cl in the ^{35}Ar beam to about 1%

---

[1]Here we neglect the binding energy of the valence electron, since only singly charged ions are provided by the separator. The ionization energy is usually in the order of a few eV and therefore about 6 orders of magnitude smaller than the mass difference of the atomic masses. The masse of the valence electrons will even out when calculating the mass difference and change the denominator by less than 0.01%. These effects are negligible for our estimation.

- To search for scalar interaction the isotope should decay via a pure Fermi decay. A pure Gamow-Teller decay is favored to search for tensor interaction. Alternatively mirror nuclei are suitable as well, in this case it is possible to precisely calculate the Fermi-to-Gamow-Teller ratio (see eq. 1.1.13).

- A β^- emitter is preferred, ions with a 1^+ charge state become neutral after β^+ decay and only the fraction which undergoes electron shake-off can be detected. The neutral atoms cannot be detected and are lost.

^{35}Ar fulfills most of these requirements. The decay scheme of ^{35}Ar is shown in fig. 3.1. ^{35}Ar decays to with 100% to ^{35}Cl, which is stable. 98.23 % decay to the ground state of ^{35}Cl [Nud12]. The remaining (summed up less than 2%) decay to various excited states of ^{35}Cl. About 0.08% undergo electron capture [End90]. These ions have a monoenegrtic recoil energy of

$$E_{rec,\,EC} = \frac{Q^2}{2 \cdot M_{rec}} \approx \frac{(6\,\text{MeV})^2}{2 \cdot 35\,\text{GeV}} = 514\,\text{eV}. \tag{3.2.2}$$

Since these ions are singly charged they will contribute to the end of the recoil energy spectrum. ^{35}Ar has a half-life of 1.7756(10) s [Nud12]. The ^{35}Ar decay to ^{35}Cl is a mirror transition. In ref. [Sev08] the Gamow-Teller-to-Fermi ratio (see also eq. 1.1.13) for ^{35}Ar has been calculated from the measured half life of the ^{35}Ar to ^{35}Cl decay

$$\rho(^{35}\text{Ar}) = (-0.2841 \pm 0.0025). \tag{3.2.3}$$

where the value of the half-life has been averaged from four measurements taken from refs. [Azu77, Iac06, Jan60, Wic66]. From this the Standard Model value of small a can be calculated [Sev08]:

$$a_{SM}(^{35}\text{Ar}) = \frac{1 - \rho(^{35}\text{Ar})^2/3}{1 + \rho(^{35}\text{Ar})^2} = (0.9004 \pm 0.0012) \tag{3.2.4}$$

A disadvantage is that ^{35}Ar is a β^+ emitter, whereby the singly positively charged ^{35}Ar ions become neutral after decay. 28(10)% of the daughter ions undergo electron shake-off [Gor12]. This results in a charge state distribution from 1^+ to 5^+ with relative contributions of each charge state as it shown in tab. 3.1. ^{35}Ar is a noble gas, which means it has a high electron affinity. This can result in an artificially shortened half-life of the isotope since singly charged ions stored in the decay Penning trap can undergo charge exchange, grab electrons from residual gas atoms, become neutral and get lost from the trap. In 2010 a major update to the vacuum system of the experiment has been executed which improved the vacuum above the decay trap from about $5 \cdot 10^{-8}$ mbar to approx. $5 \cdot 10^{-9}$ mbar [Tan11a].

Table 3.1.: Charge state distribution of the daughter ^{35}Cl ions after β^+ decay of ^{35}Ar measured at LPC CAEN in 2011, taken from ref. [Gor12].

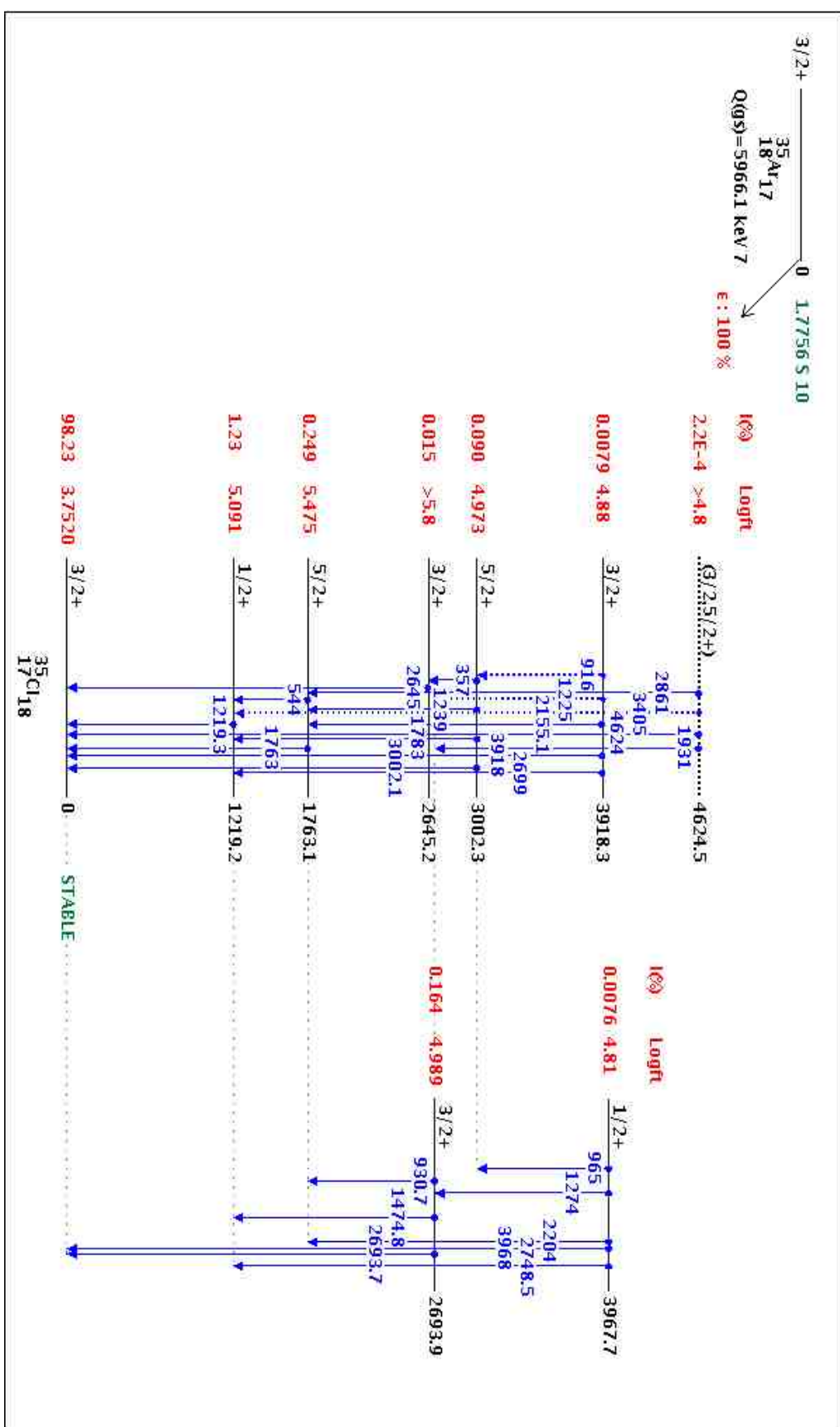| Charge state	Relative occurrence
1^+	74.6(1.0)%
2^+	17.3(0.4)%
3^+	5.7(0.2)%
4^+	1.7(0.2)%
5^+	$< 1\%$

Figure 3.1.: Decay scheme of ^{35}Ar taken from ref. [Nud12]. The levels for the daughter nucleus are split into two columns for better clarity. About 98% decay to the ground state of ^{35}Cl. About 0.08% undergo electron capture (not shown in the scheme). The rest decay to various excited levels of ^{35}Cl.

3.2.2. The recoil energy spectrum

As described in sec. 1.3.5 the WITCH experiment uses a MAC-E filter to determine the energy of the recoil ions, which is an integrating spectrometer. In a simplified picture this means, that all ions above a certain threshold energy $E_{thresh} = q \cdot U_{ret}$, where q is the charge state of the ion and U_{ret} is the applied retardation potential, are able to pass the spectrometer and will be detected. Ions with a lower energy will be reflected and don't reach the detector. By scanning the retardation potential, starting at 0 and increasing the potential stepwise we measure an integrated spectrum. This has been simulated for the ^{35}Ar recoil energy spectrum for different values of a. This is shown in fig. 3.2. The solid lines take into account the charge state distribution form tab. 3.1, the dashed lines are for charge 1^+ only.
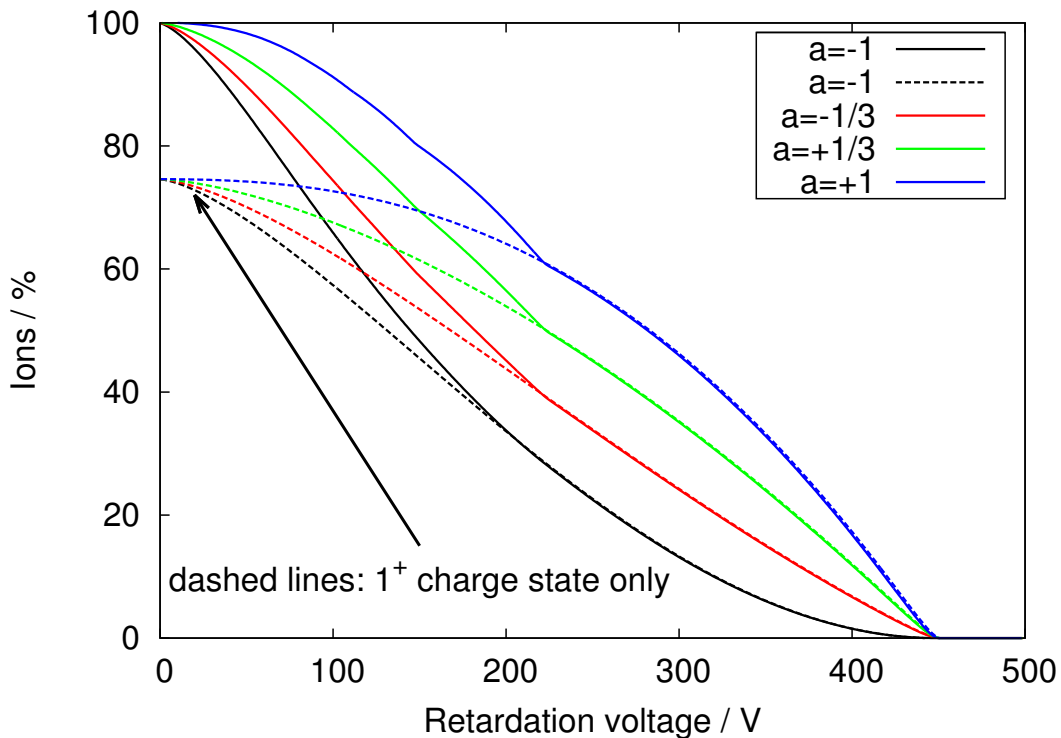

Figure 3.2.: Simulated integrated recoil energy spectrum of ^{35}Ar for different values of a. The solid lines take into account the charge state distribution form 3.1. The dashed lines are for charge 1^+ only.

3.2.3. Creation and delivery of radioactive ions to the WITCH setup

At CERN the protons used for our experiment are first created in a **LIN**ear **AC**elerator (LINAC) with an energy of 50 MeV and afterwards transferred to the **P**roton **S**ynchrotron **B**ooster (PSB) where their energy is increased to 1.4 GeV before they are delivered to the ISOLDE (**I**sotope **S**eparator **O**nline **DE**vice) [Kug00, Gor12]. At this time the protons are already bunched with a time separation of 1.2 s and an average intensity of 2 μA [Gor12].

In the beam time in 2011 scheduled from 20:00 at 29th of October 2011 until 14:00 on the 1st of November 2011 the protons were shot on a CaO target which was installed in the (**G**eneral **P**urpose **S**eparator (GPS)). A problem emerged during the preparation of the initial CaO target by what the target broke. So we had to switch to another CaO target, which was already used before and

was installed for this beam time for the third time (it was used already in the run in june 2011 and in 2009). A target of similar properties is described in ref. [Ram11]. The CaO target was used in combination with a **V**ersatile **A**rc **D**ischarge **I**on **S**ource (VADIS) [Pen10].

The GPS delivers a continuous 30 keV beam to REXTRAP - a cooler and buncher Penning trap ([Ame05]). After cooling, the ion bunches are transferred with a time separation of 1.2 s to the WITCH beam line, using the trigger signal of the proton pulses from the PSB. In the **H**orizontal **B**eam **L**ine (HBL) several focussing and steering electrodes guide the bunched ion beam to a 90°-bender that injects the beam into the **V**ertical **B**eam **L**ine [Del05]. In the VLB with the help of a **P**used **D**rift **T**ube (PDT) the energy of the bunched ions is reduced from 30 keV to between 0 and 250 eV [Coe07]. These slowed down ions are afterwards injected into the cooler Penning trap. This is where the measurement cycle begins.

3.2.4. The measurement cycle

On Nov. the 1st 2011 four different recoil energy spectra have been measured. In this section we first describe the measurement cycle, which is in principle identical for each measurement except that the sequence of retardation potentials has been varied for each measurement. Afterwards we address the problems that appeared in the analysis of the data.

The measurement cycle consists of three cycles that ran in parallel and are initiated by the same start trigger. The first is the trap cycle which consists of five stages: the injection into the cooler trap, the cooling of the ion cloud, the transfer to the decay trap, the storage in the decay trap and the ejection from the decay trap. Simultaneously the data acquisition cycle runs two branches: a **M**ulti **C**hannel **S**caler (MCS) card and a CAMAC system. The MCS scaler records the main MCP counts in steps of 25 ms. The CAMAC system records event-by-event but with a high and not reproducible dead time (see sec. 3.2.5). A third cycle defines which retardation potential is set on the retardation electrodes of the spectrometer which is controlled by a Keithley 2410 source meter.

3.2.4.1. Trap cycle

The voltages of the trap electrodes are set by a multi channel power supply which is controlled by a FPGA (**F**ield **P**rogramable **G**ate **A**rray). The Operation of the FPGA is integrated in the WITCH CS – the computer control system of the WITCH experiment [Tan11].

The measurement cycle starts with the injection of the ion bunch into the cooler trap. The proceeding from one to another step in the measurement cycle is accompanied by a change in the potential settings of the two Penning traps. In the end of the cycle the ions are ejected in direction of the horizontal beam line system to empty the traps. Simulated electric potentials along the symmetry axis of the two Penning traps for the different settings are shown in fig. 3.3. The potential settings of the trap electrodes are listed in tab. 3.2. The measurement cycle can be divided into five steps:

a) **Filling of the cooler trap:** The ions are filled into the cooler trap. The electric potential of the cooler trap is asymmetric consisting of a 5 V quadrupole potential superposed with a 200 V potential of the two upper end cap electrodes to stop the ion bunch from flying through the cooler trap.

b) **Preparation of the ion cloud:** After 100 μs the lower end cap potential is raised to prevent the ions from flying back and leaving the trap again. Notice that the lower potential on the bottom end of the cooler trap is caused by the field penetration of the neighboring electrodes, not a wrong potential setting of these electrodes (see fig. 3.3). The ion cloud is kept for $t_{cooler} = 200$ ms in this state, during which the ions interact with the buffer gas, losing their kinetic energy and fall into the quadrupole potential.
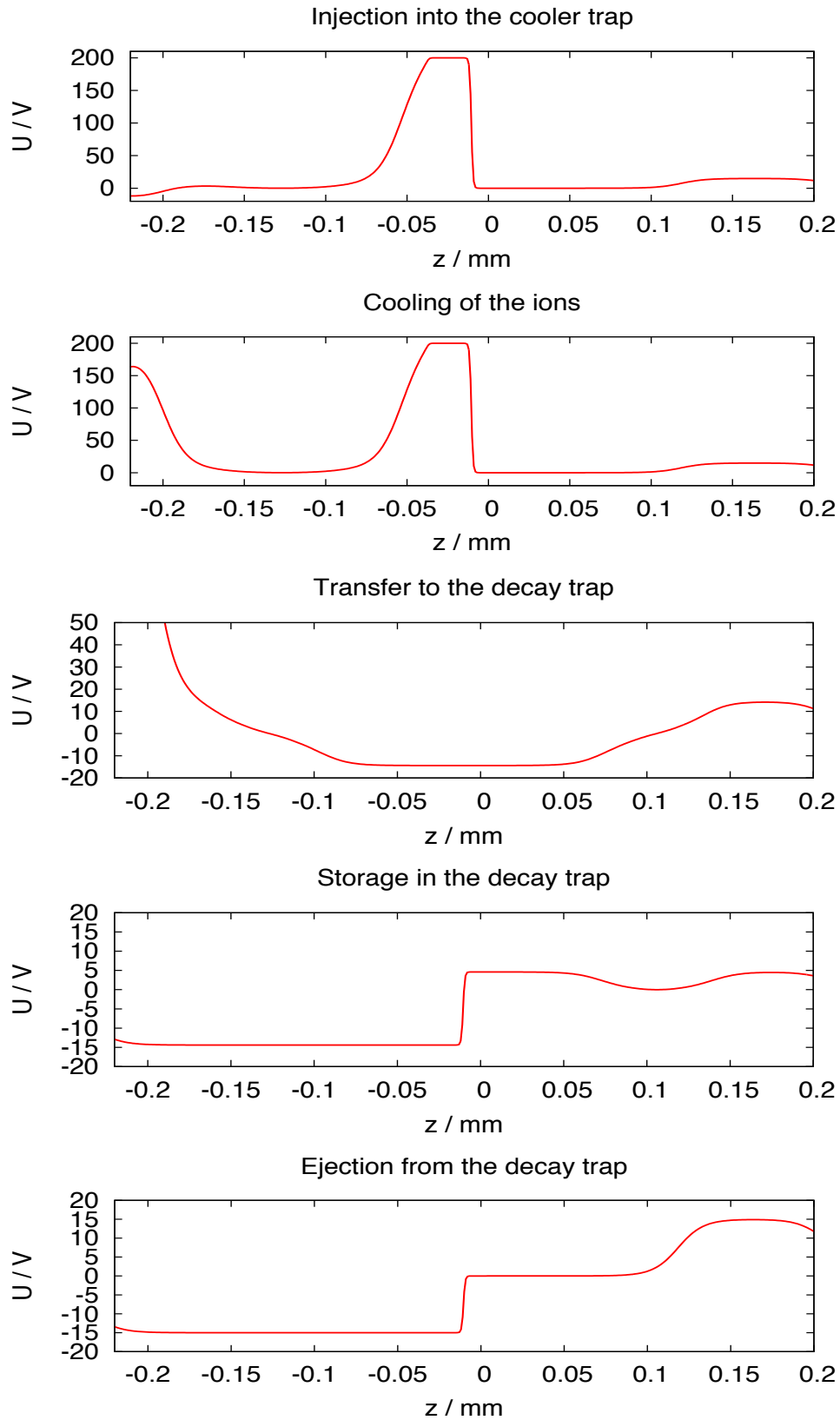
Figure 3.3.: Simulated electric potentials along the symmetry axis of the two Penning traps for the five different sequences of the measurement cycle. $z = 0$ is the center of the trap magnet. The center of the cooler trap is located at $z = -0.093$ m and the center of the decay trap is located at $z = 0.106$ m.

c) **Transfer to the decay trap:** To transfer the ions from the cooler to the decay trap the potentials of the upper end cap electrodes of the cooler trap and the lower end cap electrodes of the decay trap are lowered for $t_{trans} = 35\,\mu s$ to -15 V.

d) **Storage in the decay trap:** After $t_{trans} = 35\,\mu s$ the potentials of the lower end cap electrodes of the decay trap are raised and the correction electrodes are adjusted to capture the ions in a 5 V quadrupole potential. The ions are kept in this potential for $t_{decay} = 5$ s.

e) **Ejection of the ion cloud:** When the storage time ends, the potentials of the electrodes of the cooler trap are lowered to -15 V. By this the ion cloud is ejected in direction of the vertical beam line. This state is kept for $t_{ejection} = 7$ ms. Afterwards all trap electrodes are reset to their initial state and a new cycle begins.

Table 3.2.: Cooler and decay trap electrode potentials for the five different trap potential sequences. The electrode labels are explained in fig. 1.5. These settings have been used to simulated the electric potential along the symmetry axis, shown in fig. 3.3.

Trap electrode	Cooler trap filling potential / V	Cooler trap preparation potential / V	Transfer potential / V	Decay trap storage potential / V	Decay trap ejection potential / V
CEE8	-15	200	200	-14.4	-15
CEE7	-15	200	200	-14.4	-15
CEE6	4.6	4.6	14.4	-14.4	-15
CEE5	4.6	4.6	14.4	-14.4	-15
CCE4	3	3	11.5	-14.4	-15
CCE3	0.4	0.4	4.4	-14.4	-15
CRE1	-0.4	-0.4	0	-14.4	-15
CCE2	0.4	0.4	-4.4	-14.4	-15
CCE1	3	3	-11.5	-14.4	-15
CEE4	4.6	4.6	-14.4	-14.4	-15
CEE3	4.6	4.6	-14.4	-14.4	-15
CEE2	200	200	-14.4	-14.4	-15
CEE1	200	200	-14.4	-14.4	-15
DEE1	-14.4	-14.4	-14.4	4.6	0
DEE2	-14.4	-14.4	-14.4	4.6	0
DEE3	-14.4	-14.4	-14.4	4.6	0
DCE1	-11.5	-11.5	-11.5	3	0
DCE2	-4.4	-4.4	-4.4	0.4	0
DRE1	0	0	0	-0.4	0
DCE3	4.4	4.4	4.4	0.4	15
DCE4	14.4	14.4	14.4	3	15
DEE5	14.4	14.4	14.4	4.6	15
DEE6	14.4	14.4	14.4	4.6	15

3.2.4.2. Retardation cycle and measurement of the retardation potential

Simultaneously with the trap cycle, a cycle which controls the setting of the retardation potential is started. The retardation potential is applied by a Keithley 2410 source meter. The output of

the source meter is connected to the electrical feedthroughs of the retardation electrodes. During the beam time in Oct. 2011 one of the seven retardation electrodes (SPRETA05, the fifth looking from the side of the traps) was shortcut to ground potential. Thus only the two upper retardation electrodes (SPRETA06 and SPRETA07) were connected to the output of the retardation power supply. The lower retardation electrodes (SPRETA01–SPRETA04) have been manually shortcut to ground potential[2].

In the beginning of the cycle the retardation power supply gets the same start trigger as the one for the trap cycle. With this trigger the Keithley 2410 source meter begins to run a 5.5 s long sequence of different retardation voltages. The retardation voltage can be defined via the WITCH control system [Tan11]. This sequence is divided into steps of 25 ms. At the end of the cycle the power supply keeps the actual potential and waits for a new trigger, which is sent each 6 s[3]. Then the next cycle is started.

In the October beam time in 2011 four measurements with different retardation sequences have been conducted. Time and date of these measurements, together with the number of measurement cycles and the applied retardation potentials are listed in tab. 3.3.

Table 3.3.: List of retardation spectrum measurements. Listed is the time and date, when the measurement was conducted, the number of measurement cycle repetitions recorded in the measurement and the retardation potentials that were applied.

Start time	Date	Number of cycles	Retardation potentials
06:40	01/11/2011	999	0 V, 75 V, 150 V, 225 V, 300 V, 375 V, 450 V, 525 V & 600 V
08:45	01/11/2011	999	0 V, 75 V, 150 V, 225 V, 300 V, 375 V, 450 V, 525 V & 600 V
11:15	01/11/2011	499	0 V, 50 V, 100 V, 150 V, 200 V, 250 V, 300 V, 350 V 400 V, 450 V, 500 V, 550 V & 600 V
12:25	01/11/2011	526	0 V, 150 V, 300 V, 450 V & 600 V

3.2.4.3. Data acquisition cycle

During the October beam time in 2011 the **D**ata **AQ**uisition (DAQ) consisted of two branches: a CAMAC system composed of an 8 channel TDC module and an 8 channel scaler module and a MCS scaler card:

- **The CAMAC branch:** A detailed description of the CAMAC system can be found in chapter 2.6. This branch of the DAQ can deliver two-dimensional position information along with information on the pulse height of the MCP main signal in an event-by-event structure. A scaler information triggering on the MCP main signal serves as a dead time correction. A 100 kHz pulse generator signal registered with the scaler provides a time stamp for each event. After 6 s the DAQ cycle ends and the CAMAC scaler is reset.

- **The MCS branch:** The MCS scaler registers the triggers of the MCP main signal. Every 25 ms the counter information is saved on an internal memory and the counter is reset. After 5.5 s the internal memory is written to the hard disk of the DAQ PC and the counter and the internal memory is reset. 500 ms later the next cycle starts.

---

[2]See fig. 1.6 for electrode labeling.
[3]this corresponds to 5 cycle lengths of the PSB

3.2.5. The CAMAC DAQ branch

During the analysis of the data two distinct problems with the DAQ have been found, which show up in the data. The first problem concerns the CAMAC scaler information. When plotting the registered CAMAC scaler counts as function of the time information we see that the CAMAC system doesn't register every reset trigger. This means we can find events with $t > 6$ s, where 6 s is the cycle length. It also happened that the system did not register two or even three resets in a row. A clear indication for this is that we find events with $t > 6$ s and $t > 12$ s. This is shown fig. 3.4(a), where the number registered counts as function of the time is shown. The events with $t > 18$ s are not shown in this figure because they are hardly visible.
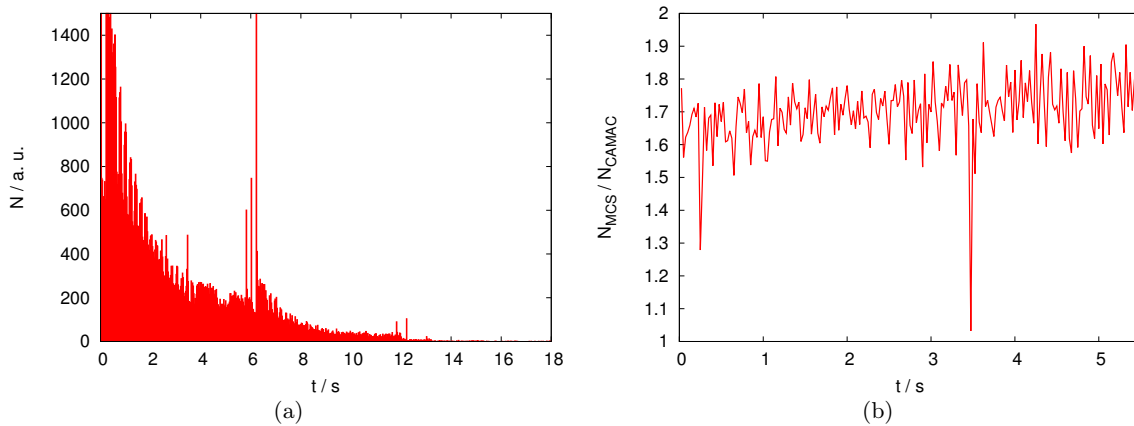

Figure 3.4.: Number of registered counts as function of the time in the CAMAC DAQ (a). Ratio of registered MCP main triggers with the MCS scaler to triggers registered with the CAMAC scaler (b).

Another problem shows a discrepancy between the CAMAC scaler counts and the MCS scaler counts. We added up the CAMAC scaler counts between 0 and 6 s into a histogram with 25 ms time bins. Then we took the events between 6 s and 12 s, subtract 6 s and add them to the same histogram. Analogously we proceeded with the events between 12 s and 18 s and between 18 s and 24 s. The resulting histogram should be in principle identical to the histogram recorded with the MCS scaler. Fig. 3.4(b) shows the ratio of these two histograms as function of the time. Both histograms had an identical binning of 25 ms. The events in the CAMAC histogram with $t > 6$ s have been shifted by 6 respectively 12 s to the left. We see that the MCS scaler registered about 1.7 times more count than the CAMAC scaler and that the ratio is not constant over the whole cycle length but fluctuates without an obvious systematic.

It is a pity that these two problems did not show up beforehand of the beam time during preparations. The reasons for this deviation could be either that the CAMAC scaler misses some triggers or the MCP scaler counts pulses twice or a combination of the two. To clear things up we performed a test with a pulse generator which showed that the CAMAC scaler channel that was used to register the main MCP pulses occasionally misses some pulses and the MCS scaler counted correctly.

At the time when the four measurements were conducted, the WITCH experiment was not the only experiment using proton pulses from the PSB. Thus the proton pulses of the PSB were distributed over multiple experiments. The proton pulses have a time separation of 1.2 s, the WITCH measurement cycle is 6.0 s long and so 5 proton pulses could fit into the WITCH measurement cycle.

During our measurement other experiments were asking for proton pulses as well. So it was not always possible to have a proton pulse available right after our measurement cycle ends. This would

mean waiting time until the next start trigger is sent from the PSB. For instance if the WITCH measurement cycle just finishes but the next proton pulse is reserved for another experiment and the following proton pulse is available for WITCH, then the PSB would wait one proton pulse length (1.2 s) before it sends the next start trigger.

This means we could still have events in the CAMAC DAQ branch after 6.0 s where no retardation was applied. These events will mix with the events that missed one start trigger. Thus we would have to discard all events with $t_{CAMAC} > 6$ s in the analysis of the CAMAC data. With all theses problems in mind we decided to concentrate on the data of the MCS scaler in the following analysis and discard the data from the CAMAC branch.

3.3. Electric and magnetic field calculations and particle tracking simulations

As tracking simulations are an important part of the data analysis we introduce the simulation package SimWITCH in a separate section. This is also where we discuss a few other results obtained with these simulations, which are not directly linked to the data analysis but are of importance for experiment. This includes for instance the development of a compensation magnet in the einzel lens region of the spectrometer.

The electrode and magnet geometry of the experiment is an important input for these calculations. The original technical drawings were used to implement these into the simulation. Since they are only accurate to about 1–2 mm this is limiting the spatial accuracy of the simulations.

Since its first application [Fri08] the simulation tool underwent several modifications. Throughout this development process this simulation package was used at many occasions, such as to determine the ion cloud size by comparison of simulation results with online measurement data [Mad10], understanding secondary ionization processes in the spectrometer [Tan11] or the data analysis of the june 2011 measurement [Gor12].

To take into account the systematics of the retardation spectrometer we performed a series of Monte Carlo simulations. In the following subsection we first introduce the simulation tool SimWITCH and give an overview about its key features. In the next two subsections we discuss several results of magnetic and electric field calculations performed with SimWITCH, before we come to the particle tracking a detailed description of how the source is modeled in this simulation tool is given. This is of particular importance since the results are strongly dependent on it. Finally we show results of the particle tracking and close with a discussion.

3.3.1. The simulation tool SimWITCH

The simulation tool SimWITCH is in essence a combination of different simulation routines. The main ingredients are routines to calculate electric and magnetic fields and perform tracking of charged particles inside these fields. These routines have been developed for the KATRIN experiment by the author Ferenc Glück (see ref. [Glu11, Glu11a, Glu13]) and have been adapted to the needs of the WITCH experiment. The essential similarity between these two experiments is the use of a MAC-E filter spectrometer. Besides its application in KATRIN (see e. g. [Cor09, Val09]) the routines are also used by another MAC-E filter experiment, aSPECT [Glu05], which aims to measure a from the beta decal of the neutron (see sec. 1.2).

All electric field, magnetic field and tracking simulations make use of cylindrical symmetry of the experimental setup. So it is not possible to simulate deviations from this assumption. The key features of this tool set are:

- **Magnetic field calculations:** The routine for the magnetic field calculation uses the zonal harmonic expansion, which is a special version of the spherical harmonic method, applied for

axisymmetric systems [Glu11a]. This method is about 100–1000 times faster than the widely known method for the magnetic field computation of axisymmetric coils by elliptic integrals.

- **Electric field calculations:** Zonal harmonic expansion method can also be applied for electric field computation of axisymmetric electrodes. For this the charge density distribution on the surface of the electrode system is needed, which is calculated by using the boundary element method. More details can be found in [Glu11]. The advantage of this method is its high accuracy, which is orders of magnitude better than commercial systems. The zonal harmonic expansion method is about 100–1000 times faster than the elliptical integral method.

- **Particle tracking:** To simulate the motion of charged particles in vacuum, the exact relativistic equations of motion of charged particles with Lorentz force was employed, using explicit 8th order Runge-Kutta methods to solve the ordinary differential equations [Glu13, Ver78, Pri81]. A more detailed description will be given in [Glu13]. Its advantages are again the high accuracy.

- **Recoil spectra:** A formerly used Fortran code [Bec12] was translated into C++ and integrated into the SimWITCH package [Mad10]. This allows in Monte Carlo simulations to draw the recoil energy from an afore simulated recoil spectrum. The calculation of the recoil spectrum is described in sec. 1.1.6. A comparison with two refersnce spectra is shown in fig. 1.1.

- **Initial kinetic ion motion in the source:** Due to the ion motion in the Penning trap the recoil ions can gain additional energy. This energy gain is particularly sensitive to the transfer time between the two Penning traps of the system as it was shown in ref. [Gor12]. Since this energy gain can easily be as much as several eV, its effect on the measurement of a recoil energy spectrum is significant and has to be taken into account in the analysis.

- **Monte Carlo generator:** At many places in the data analysis process and study of systematic effect it is necessary to perform simulations of many ions – numbers of 10^4 up to 10^6 events can easily occur. Therefore in SimWITCH the random number generator *Ran2* from Numerical Recopies in C/C++ [Pre92] is implemented. As mentioned before it is e. g. possible to randomly draw a recoil energy from a simulated spectrum or generate an emission angle equally distributed in $\cos\theta$[4] (see sec. 3.3.4.1).

More details on the individual items will be described in the following subsections.

3.3.2. Magnetic field calculations

The usual, widely known method for the magnetic field computation of axisymmetric coils is by using elliptic integrals. Another possibility is by using zonal harmonic expansion, which is a special version of the spherical harmonic method, applied for axisymmetric systems. This method can be 100–1000 times faster than the elliptic integral method, and is more general than the similar radial series expansion. It has not only high speed but also high accuracy, which makes the method especially appropriate for trajectory calculations of charged particles. Due to these properties, no interpolation is necessary when the magnetic field during particle trajectories is computed with the aid of the zonal harmonic method [Glu12].

The zonal harmonic field series formulae are convergent at field points within the central and remote regions, which have spherical boundaries and their center, the source point, can be arbitrarily chosen on the symmetry axis. The rate of convergence of the field series depends on the distance

---

[4]θ it the angle between the recoil momentum vector and the magnetic field line at the starting position. In the region of the source the magnetic field lines are parallel to the z-axis.

of the field and the source point; smaller distance for central field points and a larger distance for remote field points correspond to a higher convergence rate. For a given field point, one can improve the convergence properties of the zonal harmonic method by optimal choice of the field expansion method (central or remote) of the source point and of the source representation method [Glu12]. For more details about magnetic field calculation with the zonal harmonic expansion method see Refs. [Gar51, Glu11a].
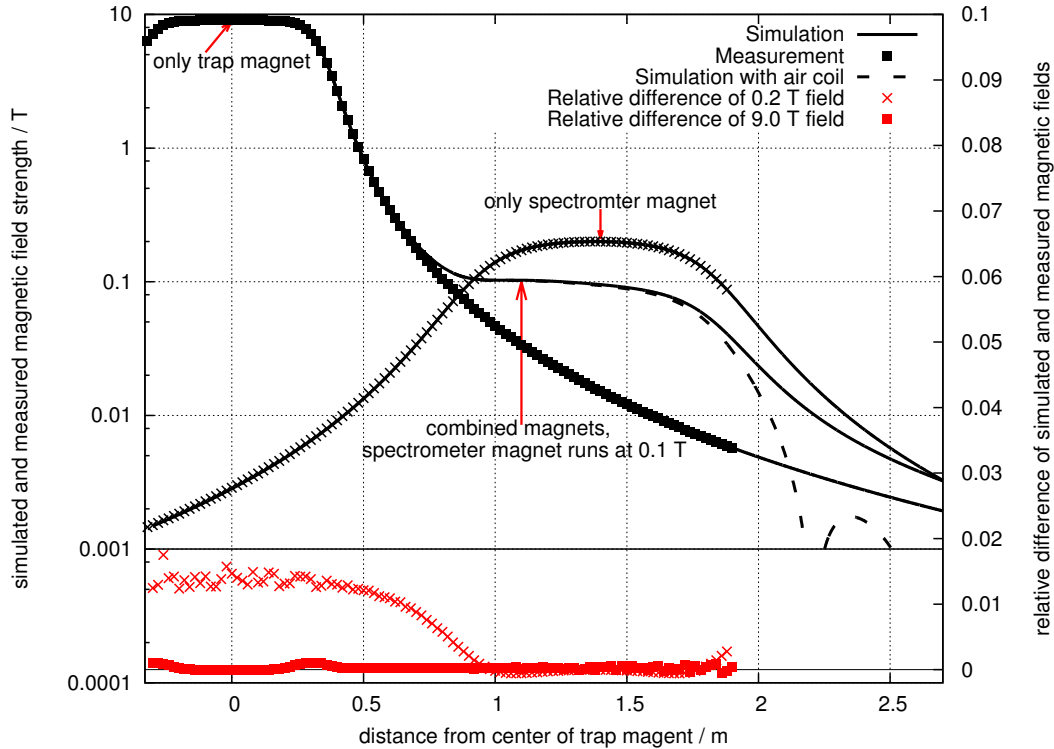

Figure 3.5.: Simulated and measured [Oxf02] magnetic fields in the traps and spectrometer region on the symmetry axis of the spectrometer. Simulated data are displayed with solid (only superconducting magnets) and dashed (superconducting magnets and air coil) black lines. Measured data provided by the manufacturer are displayed with black data points. Relative deviations between measurement and simulation are displayed with red data points. Measures on the x-axis are given with respect to the center of the 9 T magnet.

3.3.2.1. The WITCH magnet system

The magnet system of the WITCH experiment consists of three magnets (see fig. 1.6 in sec. 1.3.5): Two superconducting magnets located in a common cryostat and an air coil which is installed on top of the cryostat. The lower super conducting magnet can provide field strengths up to 9 T, the upper one up to 0.2 T. The lower superconducting magnet borders the two Penning traps and will be called trap magnet. The upper superconducting magnet encloses the main spectrometer electrode (SPRETA06[5]) and will be called spectrometer magnet. The air coil is located in the region of the einzel lens and is used to eliminate an unintentional Penning trap for electrons in this region by lowering the magnetic field in this region to below 0. It will be called compensation magnet and a detailed description will follow in section 3.3.2.2.

Both superconducting magnets have been delivered by the supplier Oxford Instruments, together with measured fields along the symmetry axis as well as the configuration of the coils themselves

---

[5]See fig. 1.6 for electrode labels

[Oxf02]. This allows us to implement the magnet geometry in the source code, while cross-checking the simulation results with the measurements. For the compensation magnet such measurements do not exist, but the manufacturer delivered the necessary geometrical information to simulate the fields.

Fig. 3.5 shows the simulated fields (solid black lines) compared to the measurements (black data points) of the fields of the individual magnets. Measures are with respect to the center of the trap magnet. In this plot the relative deviations between measurement and simulation are shown with red data points. These are less then 0.2% for the trap and less than 2% for the spectrometer magnet. Anyway, the error bars on the measured fields for both magnets are given as 2.5 % on the absolute value [Oxf11].

The simulated combined fields with the trap magnet operated at 9.0 T and the spectrometer magnet operated at 0.1 T are shown as well (solid black lines). For this configuration we reach a plateau of 0.1 T in the analysis plane (around 1.0 m). The dashed black line shows the combined fields of both superconducting magnets operated at 9 T and 0.1 T and the compensation magnet at 0.01 T in opposite direction to the two super conducting magnets. One can see the drop of the magnetic field below 0 at $z = 2.2$ m. The purpose of the compensation magnet is to avoid an unintentional Penning trap for electrons in the einzel lens region.
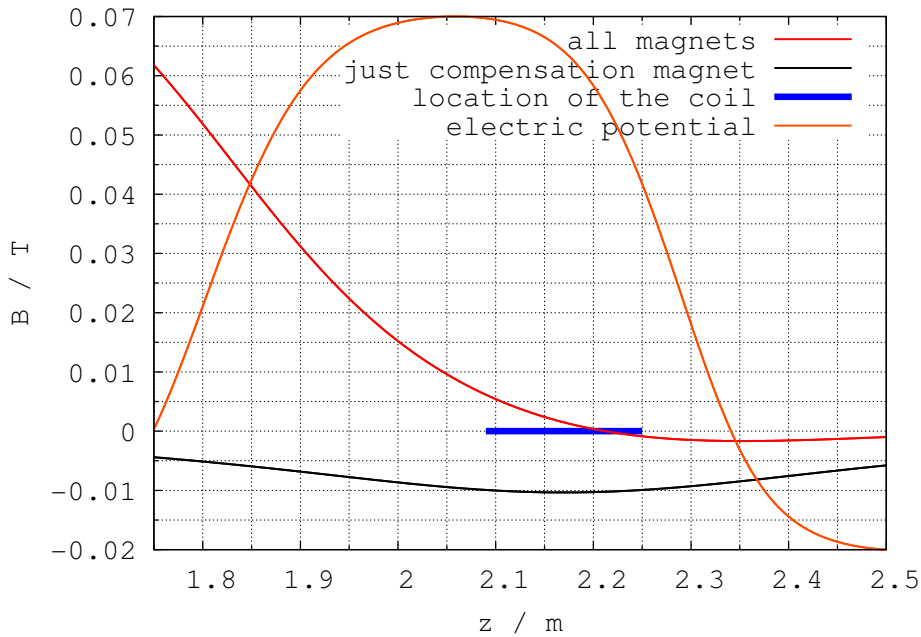
3.3.2.2. The compensation magnet

Figure 3.6.: Magnetic field along the symmetry axis with and without compensation magnet. The location of the compensation coil on the symmetry axis (z-axis) is indicated with a bold blue line.

Right on top of the cryostat an air coil has been installed. Its purpose is to eliminate an unintentional Penning trap for electrons created by the more positive potential of the einzel lens (usually minus several 100 V) surrounded by the more negative electrodes of the post-acceleration (in the order of minus several kV). To remove this electron trap, it is important to lower the magnetic field in this area to zero or below. So the magnetic field lines in this region are led astray and the electrons following them collide with the electrodes, whereas the recoil ions are following the electric field lines. Applying the field calculation routine from ref. [Glu11a] it was possible to design

Figure 3.7.: Pictures of the compensation magnet just unpacked right after delivery from the company (a). The compensation magnet after installation on top of the cryostat, holding the two superconducting magnets (b).

a sufficient solution [Bec11]. Mechanical and technical restrictions denied the use of water cooling and caused limitations in weight. The solution is an air coil built from an aluminum band, kept together by epoxy that is stable enough to be mounted without a coil bobbin. Regardless of the fact that the coil is large in volume due to the aluminum material and construction method, its weight is approx. 5 times less than that of a comparable coil made of copper while at the same time, it is more robust. The coil is placed on small aluminum blocks right on top of the cryostat. In fig. 3.6 the magnetic field along the symmetry axis with and without the air coil is shown and the location of the compensation magnet on the axis is indicated as well.
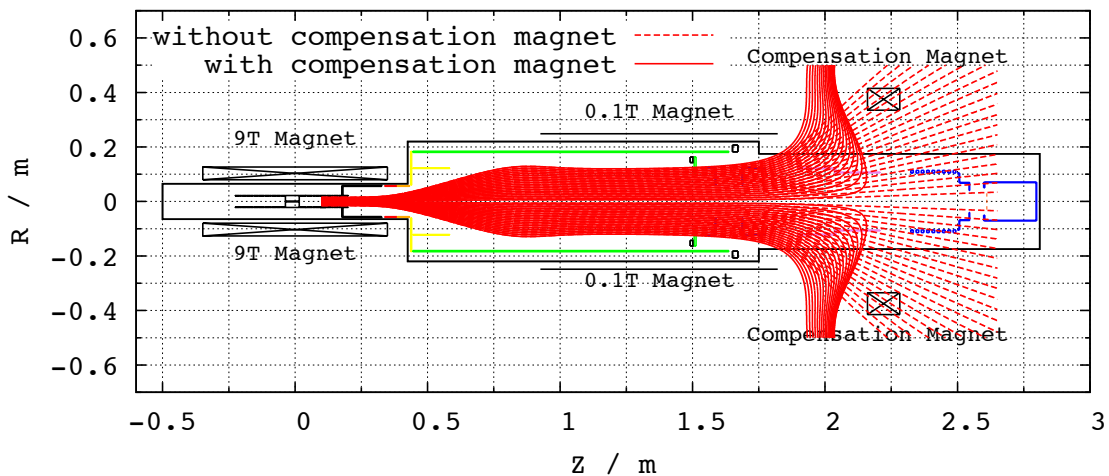
Figure 3.8.: Simulated magnetic field lines in the WITCH setup with the compensation magnet (solid red lines) and without the compensation magnet (dashed red lines). The compensation magnet bends the field lines in the upper part of the system to the outside.

In practice this unwanted Penning trap can create secondary ionization leading to discharges

and hampering the normal operation of the neighboring electrodes and causes a dominant background contribution on the main detector. Experimental tests and the measurements in October an November in 2011 have proven the correct operation of this compensation magnet. A picture of the compensation magnet just unpacked right after delivery from the company Anoxal[6] is shown in fig. 3.7(a). The compensation magnet after installation on top of the cryostat, holding the two superconducting magnets is shown in fig. 3.7(b). In fig. 3.8 simulated magnetic field lines in the WITCH setup are shown, with and without the compensation magnet. As we can see, the compensation magnet bends the magnetic field lines to the outside by lowering the magnetic field below 0.

3.3.3. Electric field calculations

The zonal harmonic expansion method can also be applied for electric field computation of axisymmetric electrodes [Glu11]. For this purpose, one needs the charge density distribution on the electrode surfaces. This can be computed by the finite difference or the finite element method, but the more natural possibility is using the boundary element method (BEM). The electrode system is discretized into many conical subelements, assuming that each of them has constant charge density. The potential of each subelement is composed from a linear superposition of the charge densities of all subelements weighted with a geometrical factor (from the definition of a capacitor $U = Q/C$); thus, we get a linear algebraic equation system for the unknown charge densities, which can be solved by a direct method (like the simple Gauss-Jordan elimination). Close to the electrodes, the electric potential and field can be calculated by elliptic integrals [Glu13, Cor09]. Farther from the electrodes, the zonal harmonic expansion provides a much faster computation method, which at the same time keeps the high accuracy of the elliptic integral calculation. The electric field calculation using the zonal harmonic expansion method is similar to the magnetic field calculation, for example, the same Legendre polynomial and convergence formalism can be used in both cases. In axisymmetric electric fields the zonal harmonic expansion method is 100–1000 times faster than the elliptic integral method, while the combination of boundary element method and zonal harmonic expansion method provides a higher accuracy than the finite element method or the finite differences method [Glu12]. More details are described in refs. [Glu11, Glu13].

For the tracking simulations the geometrical and electrical settings of the decay trap and all electrodes above (in particular the retardation, post-acceleration, einzel lens and detector electrodes) are of concern. The cooler trap is also implemented in the geometry of the tracking routine, but plays a minor role. Its field is shielded by the differential pumping diaphragm between the two traps and practically does not influence the field in the decay trap, where the actual tracking starts. Therefore we describe in the following sections the decay trap, the retardation section and the post-acceleration and detection section.

3.3.3.1. Decay trap

The decay trap is a cylindrical Penning trap consisting of 10 cylindrical gold plated copper electrodes with Macor insulators in between[7]. Its total length is 184 mm. All electrodes are arranged together with the cooler trap and the differential pumping diaphragm in one stack, mounted in a titanium structure. The decay trap features three lower and two upper end cap electrodes, two lower and two upper correction electrodes and a central ring electrode. Thus the decay trap is not fully mirror symmetric.

It is possible to apply various types of potentials to the trap electrodes. Usually either a box or a quadrupole potential or a superposition of both is used to trap the ions. For the box potential the

---

[6]Homepage: www.anoxal.de

[7]Meanwhile the Macor insulators have been replaced by Peek insulators, for its better mechanical properties.

end caps are set to the maximal trap potential while all other electrodes are set to ground potential. In the quadrupole mode the correction electrodes are used to form the potential more gently. Tab. 3.4 shows the configuration of the trap electrodes for box and quadrupole potentials applied to the trap. The numbers in the second and third column are given as ratio of the maximum trapping potential (taken from ref. [Coe07]).

Table 3.4.: Electrode configuration for box and quadrupole potentials in the decay trap. The numbers in the second and third column are the ratio of the maximum trapping potential [Coe07].

Electrodes	Ratio of max. trap potential	
	Quadrupole pot.	Box pot.
End cap electrodes	1	1
Outer correction electrodes	0.65	0
Inner correction electrodes	0.165	0
Central ring electrodes	0	0

In Fig. 3.9(a) the simulated potential in the decay trap along the central axis is shown. It is clear that the potential in the center of the trap does not go down to 0, but, depending on the maximal trapping potential U_{trap} and the potential form (box or quadrupole potential), reaches a different value U_{cen}. This effect can be compensated by adding a negative offset to the central potential. This dependence is shown in fig. 3.9(b). A linear fit results in:

$$U_{cen} = 0.013 \cdot U_{trap} \qquad \text{(Box)} \qquad (3.3.1)$$

$$U_{cen} = 0.0773 \cdot U_{trap} + 0.0042\,\text{V} \qquad \text{(Quadrupole)} \qquad (3.3.2)$$

This offset has to be taken into account when calculating the effective retardation potential (see sec. 3.3.3.2). With this we can define an effective trap potential $U_{eff} = U_{trap} - U_{cen}$, which can be calculated via:

$$U_{eff} = 0.987 \cdot U_{trap} \qquad \text{(Box)}$$

$$U_{eff} = 0.9227 \cdot U_{trap} - 0.0042\,\text{V} \qquad \text{(Quadrupole)} \qquad (3.3.3)$$

3.3.3.2. The retardation section

Half of the recoil ions escaping the decay trap (the upwards 2π of the solid angle) enter into the low magnetic field region, where they keep their orbital magnetic moment constant, provided the magnetic field change is sufficiently slow so that the motion can be considered as adiabatic. The retardation section of the WITCH spectrometer features seven electrodes (see fig. 1.6 in sec. 1.3.5). The first five electrodes increase the electric potential in the spectrometer subsequently. The sixth electrode provides the maximum retardation potential over a long range along the symmetry axis, while the seventh electrode is used to shield the more negative potential of the post-acceleration electrodes from the retardation section.

Nevertheless, the more negative potentials from the post-acceleration and the trap region influence the retardation in the analysis plane. For the potential on the z-axis, this influence can be described by a linear relation given in equation 3.3.4, where U_{ret} is the applied retardation voltage and U_{nom} is the resulting potential in the analysis plane on the symmetry axis. If we simulate the electric potential along the symmetry axis of the spectrometer for a quadrupole decay trap potential of 5 V,
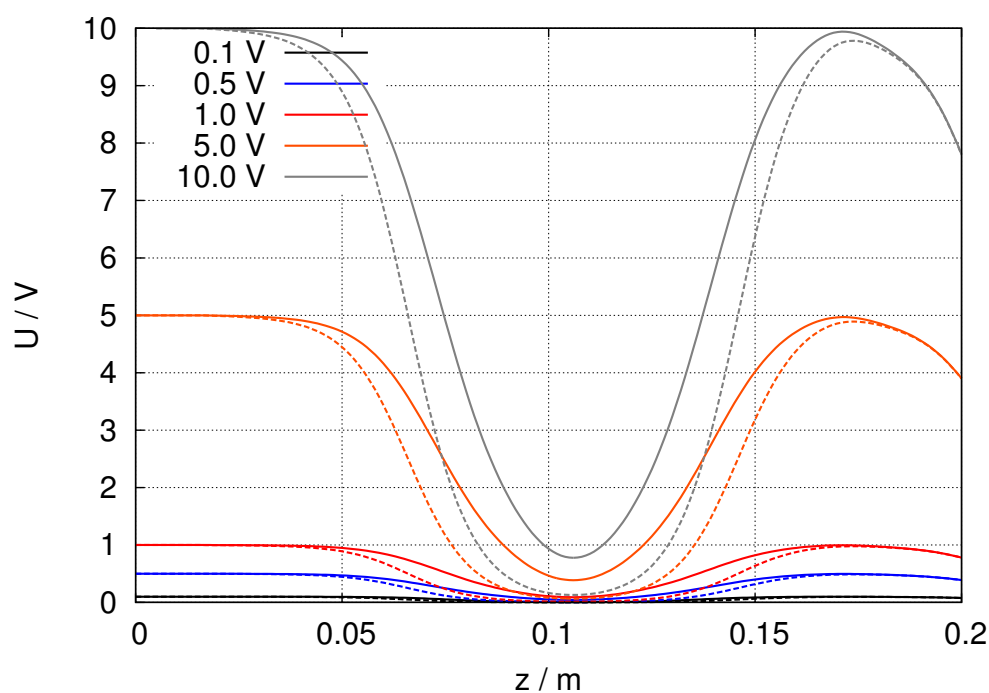
(a) Simulated electric potential in the decay trap for different max. trap potentials.
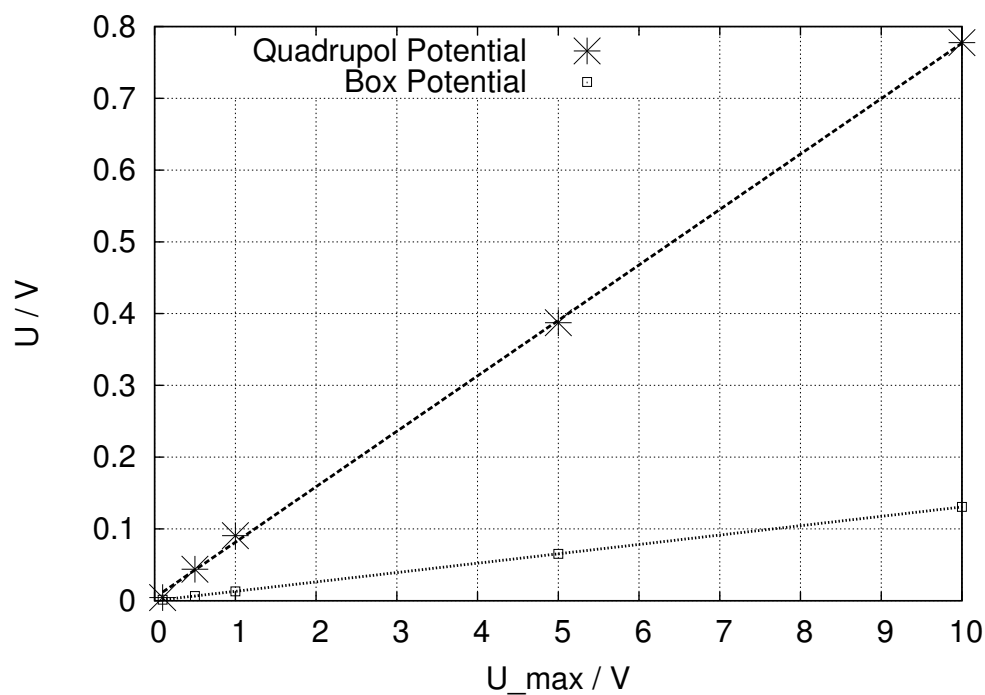
(b) Central trap potential versus the max. trap potential.

Figure 3.9.: Simulated electric potential in the decay trap for different maximal trap potentials (a). Solid lines are for quadrupole potentials, dashed lines are for box potentials. The center of the trap is located at $z = 0.106$ m. Plotting the central potential versus the max. trapping potential leads to a linear relation (b).

-2.0 kV applied at SPACCE01 and -8.0 kV applied at SPACCE02 we find the following relation[8]:

$$U_{nom} = 0.998 \cdot U_{ret} - 0.29 \, \text{V}. \tag{3.3.4}$$

In conjunction with this, we find a shift of the potential maximum, i.e. of the analysis plane with the applied retardation voltage. The position of the potential maximum on the z-axis can be expressed by the following equation[9]:

$$z_{AP}(U_{ret}) = \frac{-15.3 \, \text{V m}}{U_{ret} + 113.4 \, \text{V}} + 0.993 \, \text{m}. \tag{3.3.5}$$

3.3.3.3. The post-acceleration and detection section

Right above the retardation section one can find the post-acceleration and detection section. For the proper use of the MCP detector it is necessary to accelerate the ions to energies of several keV (about 3 keV is sufficient, according to ref. [Lie05]). This section consists of two electrodes usually operated at a negative potential of a few kV, followed by an einzel lens at minus several 100 V[10], used to electrostatically focus the ions onto the MCP. It is followed by a long, drift electrode operated at similar potentials as the post-acceleration. The MCP detector is mounted inside another electrode operated at the same potential as the MCP *Front* plate.

The focussing of this einzel lens depends on the charge and mass of the ions. Since the ions start from an extended ion cloud in the center of the decay trap and enter the einzel lens with different energies on different radii, it is not possible to express the best settings in a simple formula. Usually this is handled by Monte Carlo simulations, where the the applied potentials are systematically varied. This was done in preparation of the October beam time in 2011. A suitable set of electrode settings we found the potentials listed in tab. 3.5[11]. Anticipating one result from the following section 3.3.4 it is possible to focus all ^{35}Cl recoil ions onto the detector within a radius for $r \leq 30$ mm.

Table 3.5.: Potential settings for the post-acceleration and focussing section used in the October beam time in 2011. Simulations shows that with these settings it is possible to focus all ^{35}Cl recoil ions onto the detector. For an illustration of the electrode system see fig. 1.6 in sec. 1.3.5. See text for further explanations.

Electrode	SPACCE01	SPACCE02	SPEINZ01	SPDRIF01	SPDRIF02 & MCP front
Electric potential	-2000 V	-8000 V	-200 V	-5000 V	-3230 V

3.3.4. Tracking simulations

In order to simulate the motion of charged particles in vacuum, the exact relativistic equation of motion of charged particles with Lorentz force was employed, using explicit 8th order Runge-Kutta methods to solve the ordinary differential equations [Glu13, Ver78, Pri81]. The parameters of the 6 first order ordinary differential equations are the 3 spatial coordinates and the 3 momenta of the particle. The step size of the Runge-Kutta method in our C/C++ codes is controlled by the

---

[8]See fig. 1.6 for electrode labels.

[9]This is an approximation, here we neglect the anti-ionization wire (see also sec. the wire)

[10]positive voltages should not be applied to the einzel lens electrode, because they would act as a retardation for the recoil ions

[11]See fig. 1.6 for electrode labeling.

cyclotron period and by the particle path length during a step. For example: the time step is 50 times smaller than the cyclotron period (in high magnetic field), but the path length of the step is maximum 0.1 mm (the second requirement is important in the small magnetic field region). The 8th order Runge-Kutta methods were found to be more accurate and stable than the classical 4th order Runge-Kutta methods, while for a given precision, the 8th order Runge-Kutta methods are faster then the 4th order Runge-Kutta methods [Glu12]. The electric and magnetic fields used for the tracking require a cylindrical symmetry.

3.3.4.1. Modeling the source

Apart from the electric and magnetic field configurations the most crucial parameter for the result of a Monte Carlo simulation is the generation of the starting parameter for the tracking simulations or the modeling of the source. Although the motion of a single ion or even a few ions in a Penning trap has been studied and is well understood (see e. g. [Bro86, Bla03]), up to now only little information about the behavior of large ion numbers (about $10^4 - 10^5$) in Penning traps is available. The adaption of a many-body simulation code, which was invented for astrophysical simulations and which can be run on fast multi core GPUs [Gor11] showed first results for the behavior of ^{35}Ar ions in the WITCH Penning trap system for ion numbers up to $3 \cdot 10^3$ [Gor12]. To simulate the Coulomb interaction of the ions the gravitational force implemented in the original code is scaled to the coulomb force. This is possible because both forces show the same $1/r^2$-dependency. The results for the final ion distribution in the decay trap can be summarized as [Gor12]:

- The positions of the ions in the space coordinates (x, y) follow a Gaussian distribution around the trap center.

- The velocity coordinates (v_x, v_y) follow a Gaussian distribution centered around 0.

- The axial position (z) and the axial velocity (v_z) form a harmonic oscillator and are coupled. This leads to a correlation between the position in z-direction and the corresponding velocity component v_z. (see fig. 3.10 and below for details).

- The widths of the distributions show only small or no dependency on ion numbers between $N = 100$ and $N = 2600$.

- The widths of the distributions in axial direction (z, v_z) strongly depends on the transfer time t_{trans} between both traps. In ref. [Gor12] a transfer time of $t_{trans} = 31.5 \, \mu$s corresponds to $\sigma_z = 28$ mm and $\sigma_{vz} = 3290 \, \frac{m}{s}$, while a transfer time of $t_{trans} = 38 \, \mu$s corresponds to $\sigma_z = 4$ mm and $\sigma_{vz} = 424 \, \frac{m}{s}$. More details on the effect of the transfer time and the methods of the simulations can be found in ref. [Gor12].

  This means in particular that a not optimal transfer time (in our case around $31.5 \, \mu$s) produces an approx. 10 times broader velocity distribution in the z-component, therefore leading to an about 100 times broader initial kinetic energy distribution in the decay trap.

- The widths of the distributions in radial direction $(\sigma_x, \sigma_y, \sigma_{vx}, \sigma_{vy})$ show no dependency on the transfer time t_{trans}.

Verification of these simulation results by measurements are still a long time coming. Furthermore there have been indications that the double Penning trap system was misaligned with respect to the magnetic field lines of the trap magnet. This will be discussed in sec. 3.6 and especially in fig. 3.44 in more detail. *So the above mentioned results are questionable and the assumptions for the modeling of the source to some extend arbitrary. More realistic assumptions for the source will probably not affect the final result, as the moderate statistics and many experimental problems of*

this measurement are limiting its accuracy, and will have to be followed by further research and simulations.

So we decided to consider the source in the simulation tool SimWITCH in the following way:

- The space coordinates x and y are randomly drawn from Gaussian distribution with standard divinations (σ_x, σ_y) and mean values 0 (which equals to the center of the decay trap) in the intervals $x \in [-2 \cdot \sigma_x, +2 \cdot \sigma_x]$ and $y \in [-2 \cdot \sigma_y, +2 \cdot \sigma_y]$.

- The velocities of the x and y coordinate are randomly drawn from Gaussian distribution with standard divinations $(\sigma_{vx}, \sigma_{vy})$ and mean values 0 in the intervals $v_x \in [-2 \cdot \sigma_{vx}, +2 \cdot \sigma_{vx}]$, $v_y \in [-2 \cdot \sigma_{vy}, +2 \cdot \sigma_{vy}]$. This is a simplification, since the space and the velocity coordinates are coupled via the equations of motion of a single particle in a Penning trap (see for instance refs. [Bro86, Bla06]. For a few thousand particles, this problem is not fully understood, yet. In ref. [Gor12] the author explains that the biggest contribution for an energy gain in the initial kinetic energy of the stored ions is cased by a non-optimal transfer between the cooler and the decay Penning trap. This predominantly affects the z component of the space and the velocity coordinates. Therefore this simplification will only have little effect on the final result of the simulations.

- The z-component of the spatial coordinate z follows a sine distribution or in other words: the following expression is equally distributed in $\arccos(\frac{z}{2 \cdot \sigma_z}) \in [-\frac{\pi}{2}, +\frac{\pi}{2}]$.

- The velocity coordinate v_z is calculated from the afore drawn axial postion:

$$v_z = 2 \cdot \sigma_{vz} \cdot \cos(\arcsin(z/2/\sigma_z))$$

Afterwards both coordinates are randomly smeared out by about 10%. This is shown for a simple example in fig. 3.10.
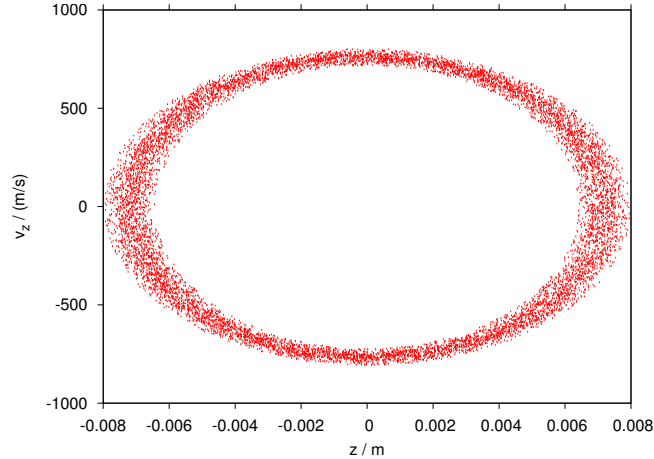

Figure 3.10.: Correlation between the axial position z in the decay trap and the axial velocity component v_z. See text for details. The standard deviations for the spatial and the velocity components for this simulation are $\sigma_z = 4\,\mathrm{mm}$ and $\sigma_{vz} = 425\,\mathrm{m/s}$.

With this the initial ion position and velocity before the decay is defined and considered in the simulation. Thereafter the recoil momentum is generated and added vectorially to the initial momentum of the ion. This works as follows:

- The recoil energy E_{rec} of the ion in the moving system of the mother ion according to fig. 3.10 is randomly drawn from a simulated recoil energy spectrum.

- The two emission angles θ and φ are randomly generated. θ is the angle between the momentum vector and the magnetic field lines (which are parallel to the z-axis in the decay volume) and φ is the corresponding azimuthal angle (in our case the angle between the momentum vector and the x-axis). $\cos\theta$ is equally distributed in $\cos\theta \in]0,1[$ and φ is equally distributed in $\varphi \in [0, 2\pi]$. This way, only ions emitted in forward direction (solid angle of 2π) are generated (to also generate ions in backward direction one needs to draw $\cos\theta \in]-1,1[$).

- From theses three values the three velocity components $v_{rec,x}, v_{rec,y}, v_{rec,z}$ are calculated[12]:

$$
\begin{aligned}
v_{rec,x} &= \sqrt{\frac{2E_{rec}}{m}} \cdot \cos\varphi \cdot \sin\theta \\
v_{rec,y} &= \sqrt{\frac{2E_{rec}}{m}} \cdot \sin\varphi \cdot \sin\theta \\
v_{rec,z} &= \sqrt{\frac{2E_{rec}}{m}} \cdot \cos\theta
\end{aligned}
\tag{3.3.6}
$$

where m is the mass of the ion.

- After all, the velocity vectors from the initial ion motion $\vec{v}$ and the velocity vector of the ion recoil $\vec{v}_{rec}$ are added to a final velocity vector $\vec{v}_{fin}$:

$$
\vec{v}_{fin} = \vec{v} + \vec{v}_{rec}
\tag{3.3.7}
$$

The resulting final energy in the laboratory system consists of three components:

$$
E_{fin} = \frac{1}{2}m(\vec{v} + \vec{v}_{rec})^2 = \frac{1}{2}m(\vec{v}^2 + 2\cdot\vec{v}\cdot\vec{v}_{rec} + \vec{v}_{rec}^2) = E_{ini} + m\cdot\vec{v}\cdot\vec{v}_{rec} + E_{rec}
\tag{3.3.8}
$$

with $E_{ini} = \frac{1}{2}m\vec{v}^2$. So it becomes obvious that the initial kinetic energy in the decay trap is not simply added on top of the recoil energy but the mixing term $m\cdot\vec{v}\cdot\vec{v}_{rec}$ has a more dominate effect (see also fig. 3.11 as well as sec. 3.4.4.1).

In fig. 3.11 the kinetic broadening in the decay trap due to the ion motion is simulated. Shown are simulated recoil spectra for different values of a and different transfer times t_{trans} with thermal broadening in the decay trap (solid lines) and without (dashed lines). For the ideal transfer time $t_{trans} = 38\,\mu s$ the effect is small while for $t_{trans} = 31.5\,\mu s$ the effect is dominant. For $t_{trans} = 31.5\,\mu s$ the energy distribution gets smeared out towards higher energies and the endpoint of the spectrum shifts by about 100 eV towards lager energy values due to the mixing term $m\cdot\vec{v}\cdot\vec{v}_{rec}$. For a better explanation the shift of the endpoint for a distinct example will be calculated in sec. 3.4.4.1.

---

[12]The typical recoil energies are $E_{rec} \leq 1000$ eV and can be considered as non-relativistic.
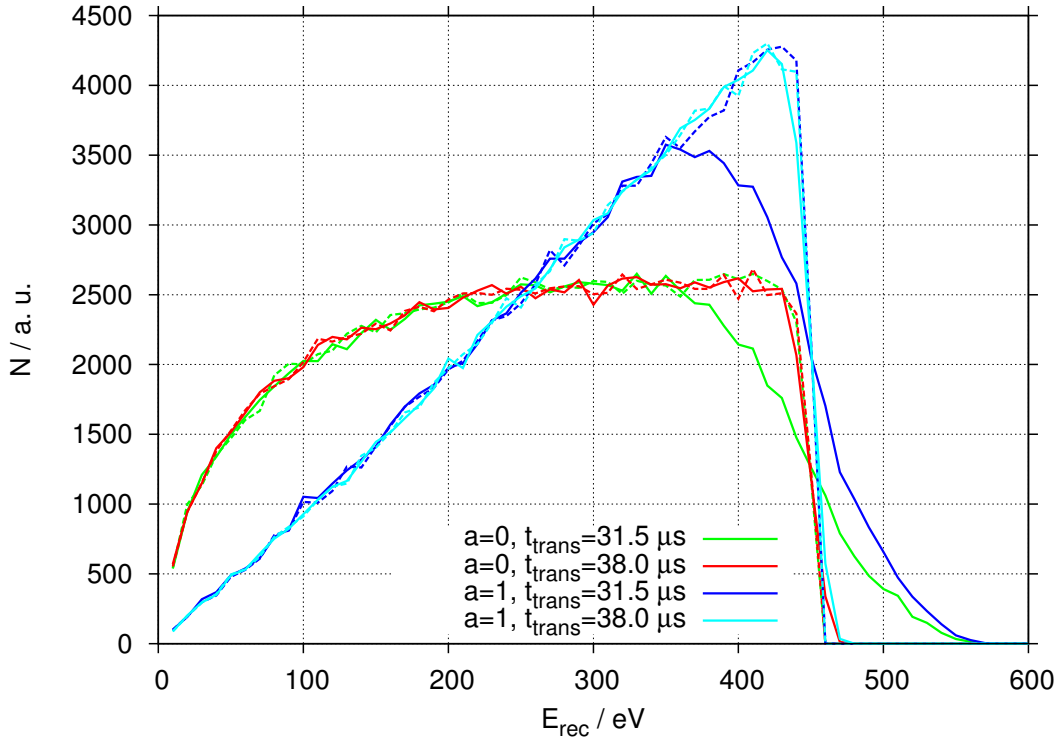
Figure 3.11.: Broadening of the energy distribution due to the ion motion in the decay trap: Shown are simulated recoil spectra for different values of a and different transfer times t_{trans} with thermal broadening in the decay trap (solid lines) and without (dashed lines). For the ideal transfer time $t_{trans} = 38\,\mu$s the effect is small while for $t_{trans} = 31.5\,\mu$s the effect is dominant.

3.3.4.2. Particle tracking

After its creation, each simulated ion is tracked inside the magnetic and electric field. The exact details of the particle tracking will eventually be described in [Glu13]. The tracking stops if one of the following stopping conditions are fulfilled. These are in full detail:

- **The ion is detected:** Ions are regarded as detected when they reach the detection plane within a radius of $r = \sqrt{x^2 + y^2} \leq 40$ mm, which is the active radius of the MCP detector (see sec. 2). The detection plane is located at $z = 2.60$ m with respect to the center of the trap magnet.

- **The ion hits an electrode:** If an ion gets closer than one computation step size of a typical length of $300\,\mu$m to the surface of an electrode the ion is regarded as absorbed and is lost.

- **Absorption by the anti-ionization wire:** Ions that pass the volume of the anti-ionization wire are considered as absorbed. The wire is implemented as a cylindrical volume with its symmetry axis aligned in y-direction. More details are given in sec. 3.5.2.

- **Reflection of the ion:** If the ions velocity component v_z changes sign, meaning it becomes negative, the ion is regarded as reflected. Since there is almost no possibility that the ion will be reflected again and could reach the detector, these ions are considered as lost. Apart from ions that are reflected because of the retardation potential, a significant amount of ions cannot leave the decay trap due to the $\theta - E-$cut-off, described in ref. [Fri08].

- **The maximum number of Runge-Kutta steps is exceeded:** As a safety condition a maximum number of Runge-Kutta is defined. Through this we avoid that the routine could hang-up. For the simulations discussed in this chapter the maximum allowed number of Runge-Kutta steps was set to 50000[13].

Each of these stopping conditions can afterwards be identified via a certain stopping index. For each simulated particle the initial conditions like the spatial coordinates x, y, z, the initial velocity coordinates v_x, v_y, v_z, the recoil energy E_{rec} and the emission angles θ and ϕ are stored in a file, together with the stopping index, the final position $x_{fin}, y_{fin}, z_{fin}$, energy conservation error [Glu13], the flight time and the total path length are stored. This allows us to analyze where and under which conditions, ions are lost inside the system, which will be discussed in the next chapter.

3.3.4.3. Tracking results

In this section we discuss a few more general results that the Monte Carlo simulation revealed. That part of the simulations which is directly linked to the data analysis and the fit of the recoil spectrum will be discussed in sec. 3.4. The extend of the simulations we performed will be described in sec. 3.4.4.1.

Let us first have a look on a few exemplary ion tracks. Each 100 randomly generated and simulated simulated ^{35}Cl ion tracks inside the setup are shown in fig. 3.12 for ion distribution corresponding to the two different simulated transfer times $t_{tans} = 31.5 \, \mu$s (a) and $t_{tans} = 38 \, \mu$s (b). The electrode and magnet configurations were chosen as those of during the October beam time in 2011 measurement, with $U_{ret} = 0$ V retardation potential. No significant difference can be observed between the ion tracks for $t_{trans} = 31.5 \, \mu$s and $t_{trans} = 38 \, \mu$s. In both cases the ions are well guided through the setup and don't come close to the electrodes.

Table 3.6.: Reflected ions and ions absorbed by the anti-ionization wire for the different simulated transfer times $t_{trans} = 31.5 \, \mu$s and $t_{trans} = 38 \, \mu$s and the simulated different values of $a = 0$ and $a = 1$ for singly charges ^{35}Cl ions. Each simulation was performed for $N = 100000$ initial events in the decay trap.

$t_{trans} \, / \, \mu$s	a	ions reflected in the decay trap	ions absorbed by the wire
31	0	10559	7658
38	0	15502	7587
31	1	8754	6791
38	1	12782	6754

Each set of Monte Carlo simulations performed was thoroughly checked and we found the following similarities:

- No simulated ion track has too many Runge-Kutta steps.

- No simulated ion hit an electrode in the system. This is very important since this has been always a problem in former simulations [Mad10, Gor12]. There are two reasons for this. On one hand, during this measurement we were able to apply more negative potentials to the post-acceleration and focussing electrodes. This was often not possible during past runs, because ionization in the spectrometer occurred. On the other hand this is the first time the ion cloud has been considered fully in the simulations. Before the ions were assumed to be uniformly distributed in the decay trap within a cylindrical volume and a too large radial

---

[13]typically it takes between 5000 to 15000 Runge-Kutta steps to simulate the track of an ion from the decay trap to the detector

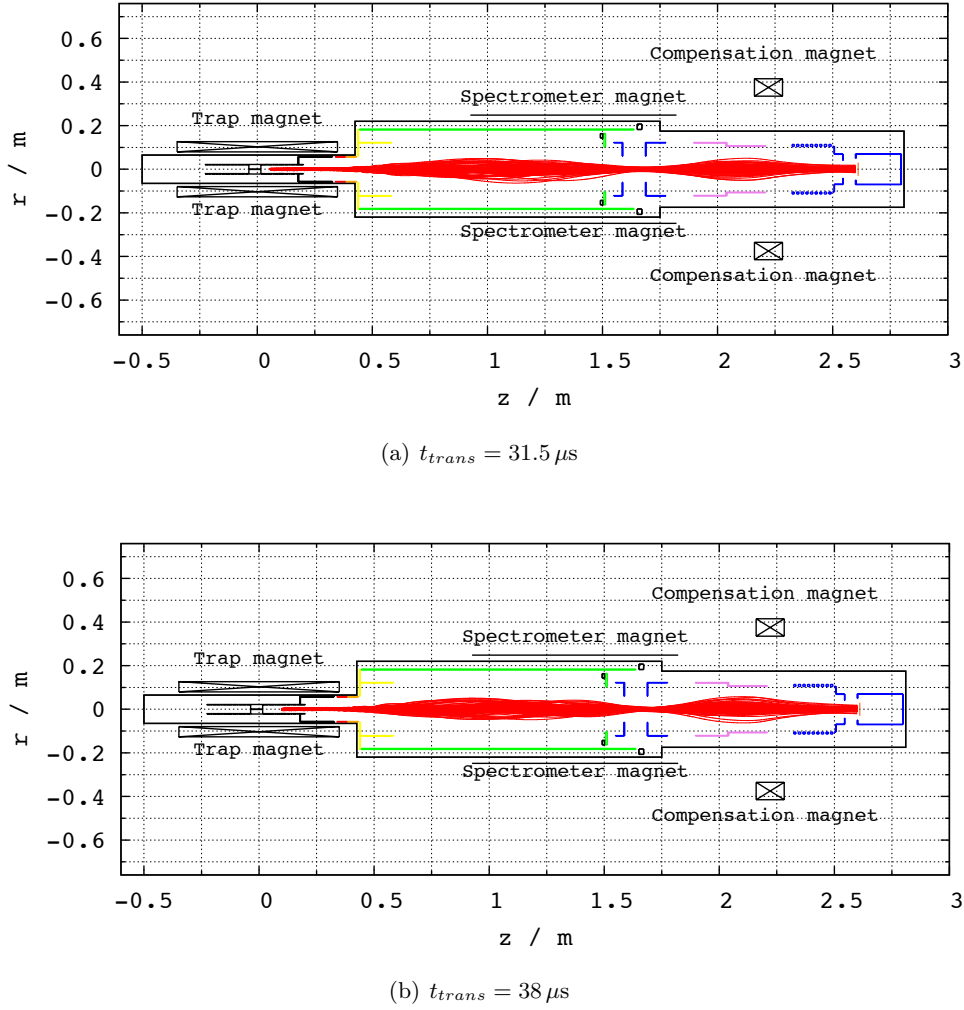(a) $t_{trans} = 31.5\,\mu$s

(b) $t_{trans} = 38\,\mu$s

Figure 3.12.: 100 randomly generated ^{35}Cl ion tracks plotted in the WITCH spectrometer geometry for $U_{ret} = 0$ V retardation potential. The upper graph (a) was simulated for an ion cloud distribution corresponding to $t_{trans} = 31.5\,\mu$s, $\sigma_x = \sigma_y = 5.0 \cdot 10^{-2}$ mm, $\sigma_z = 28$ mm, $\sigma_{vx} = \sigma_{vy} = 460\,\frac{m}{s}$ and $\sigma_{vz} = 3290\,\frac{m}{s}$. The lower graph (b) was simulated for an ion cloud distribution corresponding to $t_{trans} = 38\,\mu$s, $\sigma_x = \sigma_y = 3.3 \cdot 10^{-2}$ mm, $\sigma_z = 28$ mm, $\sigma_{vx} = \sigma_{vy} = 385\,\frac{m}{s}$ and $\sigma_{vz} = 424\,\frac{m}{s}$. Both simulations have been performed for a quadrupole potential with a depth of 5 V in the decay trap, energy drawn from an ^{35}Ar recoil spectrum for $a = 1$ and charge state 1^+. No significant difference can be observed.

extend [Fri08, Mad10] or like in the simulations discussed here but without a correlation between the z and v_z [Gor12, Gor11a]. It emphasizes the importance of the correct modeling of the source in the simulations.

- The two simulated transfer times $t_{trans} = 38\,\mu$s and $t_{trans} = 31.5\,\mu$s influenced significantly the number of detected and reflected ions (see tab. 3.6 and sec. 3.4.4.1 for details) but not the number of ions absorbed by the anti-ionization wire (see tab. 3.6 and sec. 3.5.2 for details). The number of ions that hit electrodes or exceeded numbers of Runge-Kutta steps is 0 for all simulations.

- For all simulations the ions were focussed within a radius of $r \leq 30$ mm (see e. g. figs. 3.25 and 3.27 in sec. 3.4.4.2). This means that under the assumption made, the size of our

detector is sufficient, but the old detector with an active radius of 20 mm was not large enough. Since this has been a problem in the past with wrongly assumed ion cloud properties, where simulations showed that ions had too large radii when they arrived in the detector plane.

- The amount of reflected ions in the decay trap is constant for all applied retardation potentials but differs for the different transfer times and the recoil energy distribution, respectively the value of a of the simulated spectrum. This is due to the so-called $\theta - E$-cut-off [Fri08]: For a point-like mono energetic source a certain emission angle θ_{max}[14] exists, above which the ion is not able to escape the decay trap due to the magnetic mirror effect.
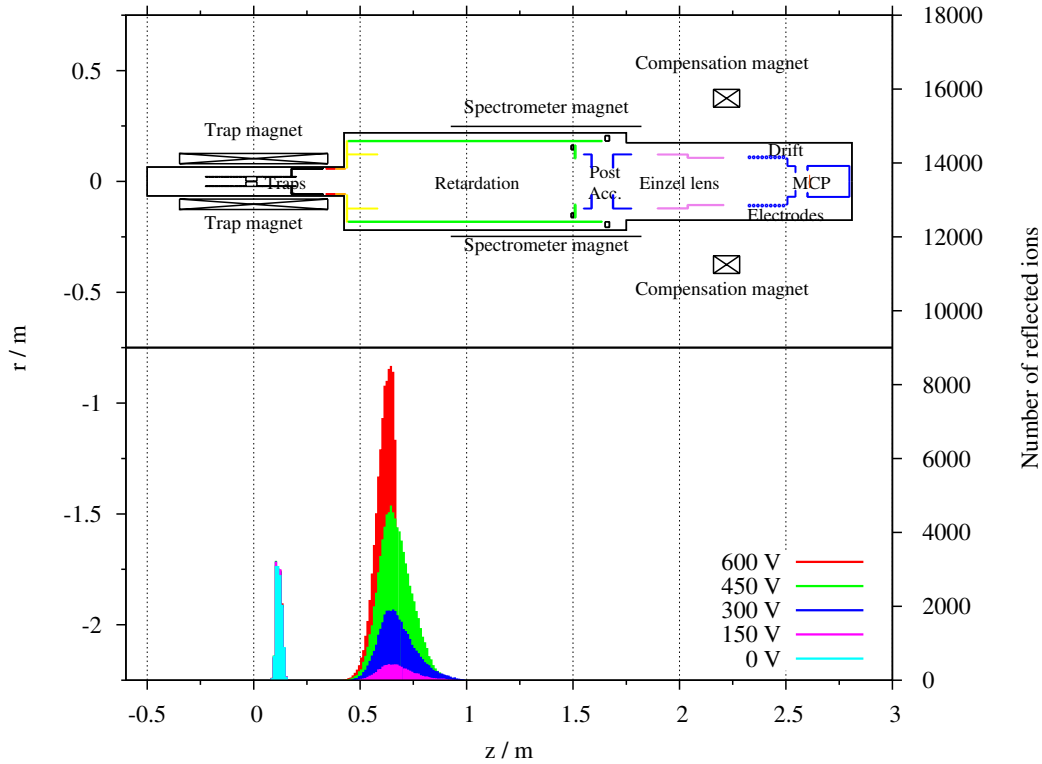
Figure 3.13.: Number of simulated reflected ions as function of the position on the symmetry axis (z-axis) shown for different retardation potentials U_{ret} and $t_{trans} = 38\,\mu s$. For each simulation 10^5 initial event were randomly created (see sec. 3.3.4.1). The number of reflected ions in the source is constant. With rising retardation potential a larger amount of ions is reflected in the spectrometer near the analysis plane.

Let's see what happens to the reflected ions. Fig. 3.13 shows on top a schematic of the electrode an magnet geometry as it is assumed in the simulations, below histograms with the amount of reflected ions as function of the axial position are shown. This simulation was performed for a simulated recoil energy spectrum corresponding to $a = 1$, an ion cloud distribution corresponding to $t_{trans} = 38\,\mu s$ with $N = 10^5$ initial events in the decay trap. We see that the amount of ions that are reflected in the trap is constant for the different retardation potentials, like we would expect it. From tab. 3.6 we know that for singly charged ^{35}Cl ions this ranges from about $9 - 16\%$ depending on the values of a and the transfer time t_{trans}. As expected, the amount of ions reflected in the spectrometer changes with the applied retardation potential U_{ret} from 0 for $U_{ret} = 0$ to all ions

---

[14]this is the angle between the magnetic field lines, which are parallel to the symmetry axis in the decay volume and the momentum vector of the ion

for $U_{ret} = 600$ V. One can also see that the position of the reflection shifts slightly more to the beginning with higher retardation potential.

3.3.4.4. Discussion of the electromagnetic field calculations and the tracking simulations

In the beginning of this section we introduced the simulation tool SimWITCH and presented an overview over its key features. Over the years since its introduction this tool has found many applications [Fri08, Mad10, Gor12, Tan11, Bec11].

In this chapter we discussed several simulation results. We showed that the simulated magnetic fields are in good agreement with the measurement data form the manufacturer Oxford Instruments. Small deviations might be explained by the additional dielectric material of the cryostat.

Simulations of the electric potential showed that the form of the potential and the absolute value of the potential applied to the end cap electrodes influences the potential in the center of the trap and can create an offset which has to be taken into account when calculating the applied retardation potential. A similar result shows, that due to the field penetration from the post-acceleration electrodes the effective retardation potential in the spectrometer is actually lower than the applied retardation potential. This is now understood and can be calculated via eq. 3.3.4 and tracking simulations take this into account automatically.

It is the first time that the ion distribution and motion in the decay trap is fully considered in the tracking simulations. Contrary to older simulations, the tracking simulations now showed that with the electrode configuration shown in tab. 3.5 it is possible to focus all ^{35}Cl recoil ions onto the detector within a radius of $r \leq 30$ mm. No ions hit electrodes in the setup, the only loss of ions happens in the decay trap due to the so-called $\theta - E$-cut-off described in [Fri08]. It was shown that for a distinct ion distribution the amount of ions reflected in the decay trap is constant. This systematic effect is automatically taken into account by the simulations. Another systematic effect, the initial motion of the ions in the decay trap, was described and is considered by the tracking simulations as well. Further details on this will follow in sec. 3.4.4.1 and 3.5.1. We showed that with rising retardation potentials the recoil ions will be reflected earlier in the spectrometer.

Finally we list some key result from the simulations that are either of relevance for the experiment or might be of interest for the execution of further simulations.

- The typical flight time for a singly charged ^{35}Cl ions from the decay trap to the detector is about $30 - 50\,\mu$s.

- The total path length for a typical trace for a singly charged ^{35}Cl ion from the decay trap to the detector ranges between $2.5 - 4.2$ m.

- The storage of one uncompressed ion track takes about 1.5 MB of disk space in ASCII format.

- Typically it takes about 1-2 s per ion track to simulate on a typical Intel Core2Duo PC. E. g. one can simulate about 100000 tracks in 1.5-2 days.

- The calculation of the magnetic fields in the setup takes less than 10 s on a typical Intel Core2Duo PC.

- The calculation of the electrical source points in the electrode geometry takes about 20 min on a typical Intel Core2Duo PC.

We should emphasize that, under the assumptions made, it is not necessary to apply more negative potentials to the focussing and detector electrodes than we did in this simulation, to focus all ions onto the detector.

3.4. Analysis of the raw data and fit of the recoil spectrum

This section describes the data analysis. We limit the analysis to data recorded with the MCS scaler (**M**ulti **C**hannel **S**caler), for the reasons described in sec. 3.2.5. Before we can fit the raw data we have to tackle a synchronization problem between the DAQ and the retardation voltage. This is done by rather uncommon but effective way of fitting the retardation sequence to the data and is described in sec. 3.4.2. Subsequent measurements of mimicked conditions like in the October beam time in 2011 proved these results [Bre12, Zak121]. In a second subsection, a fit of the raw data is discussed. The resulting retardation spectrum is used to extract a value for a with the help of tracking simulations. We finish this part with a discussion of two important systematic effects.

3.4.1. The raw data
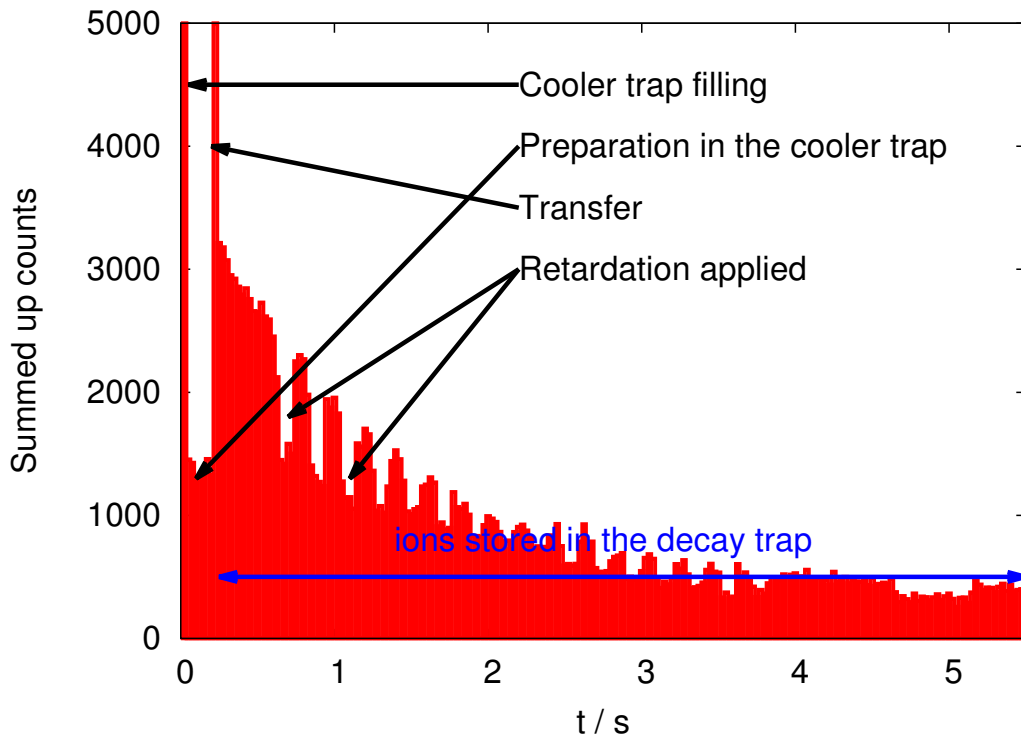
Figure 3.14.: Raw data of the 06:40 measurement. The 999 individual measurements are summed up to one histogram. The first peak around $t = 0$ originates from ions that are injected into the cooler trap with too much kinetic energy to be stopped by the electric potential of the upper end caps of the cooler trap. These ions are shot through the trap system and reach the main detector. The second peak around $t = 0.25$ s originates from the transfer of the ion cloud from the cooler into the decay trap. At $0.25\,\text{s} < t \leq 5.5\,\text{s}$ the ions are stored in the decay trap while part of them decay.

In fig. 3.14 the raw data of the 06:40 measurement is shown. The 999 individual measurements are summed up to one histogram. Similar figures for the measurement from 08:45, 11:15 and 12:25 can be found in fig. B.1 to B.3 in the Appendix B. The first peak around $t = 0$ originates from ions that are injected into the cooler trap with too much kinetic energy to be stopped by the electric potential of the upper end caps of the cooler trap. These ions are shot through the trap system and reach the main detector. The second peak around $t = 0.25$ s originates from the transfer of the ion cloud from the cooler into the decay trap. The second peak (from the transfer) is about 20

times higher than the first one, which cannot be seen in the histogram in fig. 3.14, since y-axis is zoomed in to visualize the decay curve withe the retardation patterns at $t > 0.25$ s. This gives rise that there has been a severe problem with the cooling and preparation of the ion cloud in the cooler trap. In-between these two peaks, at $0.25\,\text{s} < t < 0.225\,\text{s}$, the ions are kept in the cooler trap and cooled by collisions with buffer gas atoms.

At $0.25\,\text{s} < t \leq 5.5\,\text{s}$ the ions are stored in the decay trap while part of them decay and the daughter recoil ions can escape into the spectrometer. At certain time intervals a retardation voltage $U_{ret} > 0$ is applied which hinders, depending on its value, part of the recoil daughter ions to pass the analysis plane. These retardation patterns are different for the four measurements. Around $4.65\,\text{s} < t < 5.2\,\text{s}$ a retardation potential of $U_{ret} = 600$ V was applied, which is common for all four measurements 06:40, 08:45, 11:15 and 12:25.

3.4.2. Synchronization problem and fit of the retardation sequence

The following subchapter describes a problem with the synchronization between the data acquisition and the setting of the retardation voltage. This was found in the end of the November beam time in 2011 which followed the run that is part of the data analysis presented here. Since the identification and description of this problem via a measurement took a large amount of time after the beam time we choose a rather uncommon but effective way to solve this problem. Our approach is to fit a certain pattern of retardation sequences to the recorded data. The results of this method will be used in the upcoming analysis.

As a result of this analysis an internal report was written to share this information with the collaboration. This report is the basis for this subchapter.

3.4.2.1. Introduction

During the October and November 2011 beam times the data acquisition and the retardation power supply were not correctly synchronized. The data acquisition ran in steps of 25.0 ms while the retardation power supply should have operated with the same time steps, but added internally a time offset due to the so-called *command processing time*. Consulting the data sheet of the retardation voltage supply (a Keithley 2410 source meter) this value is given as 0.7 ms. Additionally, time is needed to reach the set voltage at the output. The manual gives a value of 100 μs as the time required to reach 99.9 % of the set voltage at the output of the power supply and 30 μs as minimum time for the output to recover to its specification following a step change in load. We don't know whether we have to add to the 0.7 ms another short period of 0.1 ms or 0.13 ms. A measurement with the oscilloscope results in 0.80 (10) ms[15]. To be sure an alternative way by fitting the retardation sequence was approached, whose result will be used in the data analysis.

We apply the following procedure to fit the retardation sequence to the measurement data:

- First we create a so-called switching file from the raw data (06:40, 08:45, 11:15 and 12:25 of 01/11/2011): We checked by eye from the recorded count rate in which bins retardation voltage was applied, where retardation voltage was switched and where no retardation was applied. Each time bin of the recorded data gets marked with a number: 1 if retardation was applied, 0.5 if the retardation was switched and 0 if no retardation was applied. These switching files are shown in tab. B.2 and B.3 in Appendix B).

- We use the idealized retardation sequences with 25.0 ms time steps (see tab. B.1 in Appendix B) for all four data sets and combined them to one fit function ($f(t)$), by using the same time delays as above.

---

[15]Elog entry 438, Thu. Nov. 10 08:01:12 2011

- We fit the function $F(t) = f((t + t_{off}) \cdot \frac{t_{step}}{t_{step} + \Delta t_{off}})$ to the switching files while assuming constant errors of $\sigma = 0.1565$[16]. Here $t_{step} = 25.0$ ms is the length of one time step of the data acquisition, Δt_{off} the offset per time step and t_{off} the global time offset per cycle. Each switching file has 220 data points, so it are 880 in total. All four data sets are fitted simultaneously to receive common values for t_{off} and Δt_{off}.

We use a C-based version of Minuit, release 93.08, to fit the data. The fit results in:

$$\Delta t_{off} : 767.6 \pm 0.2 \, \mu\text{s} \tag{3.4.1}$$

$$t_{off} = -4.805 \pm 0.004 \, \text{ms} \tag{3.4.2}$$

with a $\chi^2/N_{dof} = 1.00$ with a constant σ of 0.1565. The fit function with the switching files is drawn in fig. 3.16 together with the residuals of the fit. The parameter errors given by Minuit are only valid in case of a Gaussian error distribution which is not right in our case because the χ^2 increases step-wise in steps of $\frac{1}{\sigma^2} = \frac{1}{(0.1566)^2} = 41$ (see fig. 3.15). This happens always when, by varying a parameter one additional data point and the function value don't comply anymore. So we have to think of another way to estimate the errors on the parameters. Fig. 3.15 shows levels where such a step in the χ^2 happens. The yellow line encloses the χ^2 level, which ranges from $\Delta t_{off} = 0.74$ ms to 0.78 ms, while t_{off} reaches from -7.2 ms to -3.4 ms. So we use the mean value and half of the difference between upper and lower value as result:

$$\Delta t_{off} = (0.76 \pm 0.02) \, \text{ms} \tag{3.4.3}$$

$$t_{off} = -(5.3 \pm 1.9) \, \text{ms} \tag{3.4.4}$$

In retrospect theses two values have been determined with an oscilloscope from the emulated sequences as they were used during the beam time. These values for Δt_{off} and t_{off} are in good agreement with the values our method extracted from the raw data [Zak121, Bre12]:

$$\Delta t_{off} = (0.8 \pm 0.1) \, \text{ms} \tag{3.4.5}$$

$$t_{off} = (6.1 \pm 1.0) \, \text{ms} \tag{3.4.6}$$
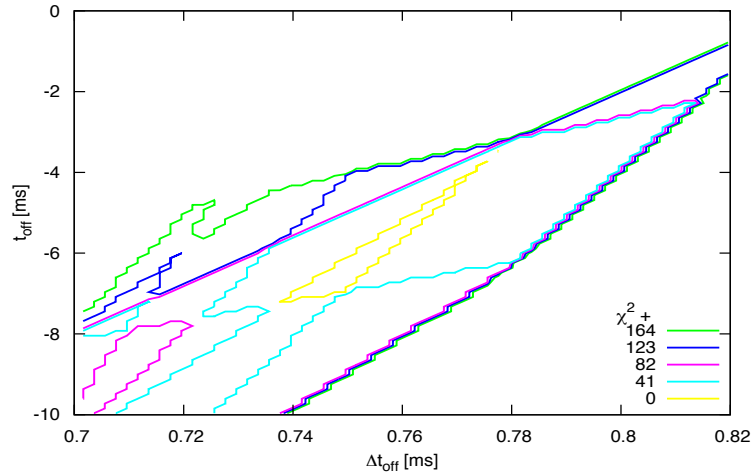
Figure 3.15.: Contour plot of the χ^2, $\chi^2 + 41$, $\chi^2 + 82$, $\chi^2 + 123$ and $\chi^2 + 164$ levels for the parameters Δt_{off} and t_{off} of the fit of the retardation sequence. See text for explanation.

---

[16]The value σ was chosen to obtain a final $\chi^2/N_{dof} = 1$ to get a better estimate on the uncertainties
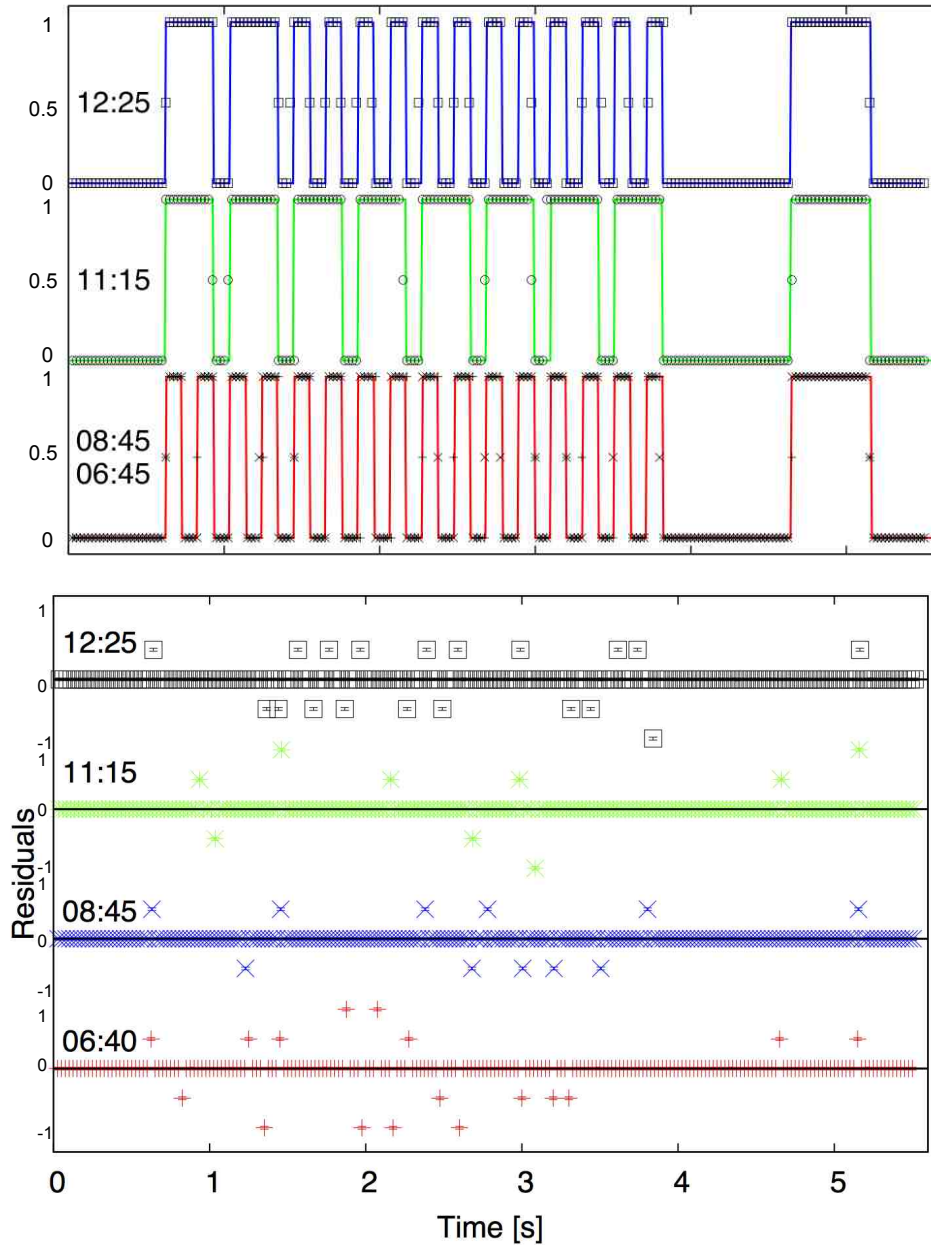
Figure 3.16.: Fit function with switching files. The fit function is drawn with a solid line in red for the 06:40 and 08:45 measurements, green for 11:15 and blue for the 12:25 measurement. The switching files are drawn with + for 06:40, x for 08:45 circles for 11:15 and squares for 12:25. The function value can be either 1 (reiteration is applied), 0.5 (retardation is switched) or 0 (no retardation is applied). Therefore the residuals are either 1, 0.5, 0, -0.5 or 1.

3.4.3. Fit of the raw data

Following the description and resolution of synchronization problem presented in sec. 3.4.2, we fitted the raw data to extract a recoil spectrum. In a first approach we fitted the individual data sets. Afterwards we performed a combined fit of all four data sets. Again as a result of this work, an internal report was written to share this information with the rest of the collaboration. This report is the basis for the following section.

3.4.3.1. Introduction

On Nov. 1st we performed 4 measurements of retardation spectra where we applied four different sequences of retardation voltages. The measurement cycle length of 6 s, was repeated 999 times for the first two measurements (06:40 and 08:45), 499 times for the third measurement (11:15) and 526 times for the fourth measurement (12:25) (compare tab. 3.3). The analysis described here concerns the data acquired with a **M**ulti **C**hannel **S**caler (MCS). The events are measured from the MCP back signal and discriminated by a CFD and lead to a MCS PC card. The events are registered in steps of 25 ms, stored internally and were written after 5.5 s to the hard disk. 0.5 seconds later the next cycle started. The recorded count rate is shown in fig. 3.14 for the 06:40 measurement and in fig. B.1–B.3 in Appendix B for the remainder.

As explained in sec. 3.4.2, the retardation voltage and the MCS data acquisition were not properly synchronized. We sorted out all bins in which a switch of the retardation voltage happened. We defined switching functions for a lower limit ($F_l(t)$) and an upper limit ($F_r(t)$):

$$F_l(t) = f\left((t - t_{step} + t_{off,l}) \cdot \frac{t_{step}}{t_{step} + \Delta t_{off,l}}\right) \tag{3.4.7}$$

$$F_r(t) = f\left((t + t_{off,r}) \cdot \frac{t_{step}}{t_{step} + \Delta t_{off,r}}\right) \tag{3.4.8}$$

with $t_{step} = 0.025$ s, $t_{off,l} = 0.0072$ s, $\Delta t_{off} = 0.00078$ s, $t_{off,r} = 0.0034$ s, $\Delta t_{off,r} = 0.00074$ s and f is the ideal retardation sequence function, described in sec. 3.4.2.

Using these functions we take into the $1\,\sigma$ uncertainties of the time offset t_{off} and the time step offset Δt_{off} obtained in sec. 3.4.2. $F_l(t)$ probes if at the beginning of each bin retardation voltage is applied and $F_r(t)$ does so for the end of the bin. The time signature of the bin is the time when the data in the bin was saved which is the end of the bin. Thus we had to subtract the length of one bin $t_{step} = 0.025$ s in $F_l(t)$ to check for the beginning of a bin. We accept only bins in which both functions return the same value.

In a second step we sorted the data by the retardation voltage which was applied. For each value of retardation voltage, we used an artificial time delay of additional 10 s. For better understanding let's have a look at the 06:40 measurement. The values of the retardation potential that were applied in this measurement are: 0 V, 75 V, 150 V, 225 V, 300 V, 375 V, 450 V, 525 V and 600 V. All data points with $U_{ret} = 0$ V get a time delay of 0 s, all data points with a retardation voltage of $U_{ret} = 75$ V get a time delay of 10 seconds, all data point with $U_{ret} = 150$ V are delayed by 20 s and so on.

In a third step we fitted the function

$$F_{fit}(t) = A(U_{ret}) \cdot e^{-\frac{t}{\tau_1}} + B \cdot e^{-\frac{t}{\tau_2}} + C\,, \tag{3.4.9}$$

which consists of a constant background C, an exponentially decaying background $B \cdot e^{-\frac{t}{\tau_2}}$ and an exponential decay $A(t) \cdot e^{-\frac{t}{\tau_1}}$ with different amplitudes for each retardation potential U_{ret} to the

data. The function $A(U_{ret})$ is defined as follows:

$$A(U_{ret}) = \begin{cases} A_0 & \text{for } U_{ret} = 0 \\ A_{75} & \text{for } U_{ret} = 75 \text{ V} \\ \vdots \\ A_{550} & \text{for } U_{ret} = 550 \text{ V} \\ 0 & \text{for } U_{ret} = 600 \text{ V} \end{cases}$$

The amplitudes A_i are indexed with the value of the retardation potential in volts so that for each retardation potential the signal contribution of the fit function has a separate amplitude.

A retardation potential of $U_{ret} = 600$ V is in principle enough to stop all recoil ions of charge state 1^+ or higher. Anticipating the simulation results in sec. 3.4.4.1 and the estimation in eq. 3.4.14 in the worst case recoil ions could still contribute to the count rate of $U_{ret} = 550$ V. Maybe recoil ions from the electron capture could still be present in the measurement with $U_{ret} = 600$ V but since the branching ratio of the electron capture for ^{35}Ar is below 0.1% [End90] its contribution is negligible. The exponentially decaying background $B \cdot e^{-\frac{t}{\tau_2}}$ is fitted to the measurement with 600 V retardation potential. The exponential background should in principle be composed out of betas from the decay of ^{35}Ar but two other contributions might be present as well:

- It cannot be fully excluded that there are contaminations of other isotopes in the ion beam.

- Part of the radioactive ions that are shot over the cooler trap potential while injecting the ion bunch are implanted into the MCP. The same appears to ions that are shot over the decay trap potential while transferring the prepared ion cloud from the cooler trap into the decay trap. These implanted ions can decay in the MCP and create a signal in the detector which is detected. This contributes to the background. As some of the implanted radioactive ions may diffuse out of the MCP they could mimic a different lifetime than the ions have that are stored inside the decay trap.

So we assumed a separate lifetime τ_2 for the exponential background. We assume the square root of the count rate as error bars for the data points.

3.4.3.2. Individual fits of the raw data

For the fit a C-based version of Minuit, release 93.08, was used. The fit results as they are returned from the program can be obtained from tab. C.1 to C.4 (see Appendix C). The χ^2 and χ^2/N_{dof} of the fits are:

- 06:40: $\chi^2 = 319$ and $\chi^2/N_{dof} = 2.07$

- 08:45: $\chi^2 = 367$ and $\chi^2/N_{dof} = 2.39$

- 11:15: $\chi^2 = 392$ and $\chi^2/N_{dof} = 2.61$

- 12:25: $\chi^2 = 393$ and $\chi^2/N_{dof} = 2.49$

Using instead of 1 σ, 2 σ uncertainties for the upper and the lower limit of the offset times of the switching function, meaning $t_{off,l} = 9.1$ ms, $\Delta t_{off,l} = 0.8$ ms, $t_{off,r} = 15$ ms, $\Delta t_{off,r} = 0.72$ ms has the effect, that 11 additional bins are sorted out. This does not improve the χ^2/N_{dof} significantly:

- 06:40: $\chi^2 = 299$ and $\chi^2/N_{dof} = 2.09$

- 08:45: $\chi^2 = 329$ and $\chi^2/N_{dof} = 2.30$

- 11:15: $\chi^2 = 371$ and $\chi^2/N_{dof} = 2.67$

- 12:25: $\chi^2 = 355$ and $\chi^2/N_{dof} = 2.41$

The fit functions, together with the data and the residuals are shown in fig. C.1, C.2, C.3 and C.4 (see Appendix C).

We first concentrate on the results of the 06:40, 08:45 and 12:25 measurements. The result of the 11:15 data will be discussed at the end of this section. The values for the lifetime τ_1, found by the fits of the 06:40, 08:45 and 12:25 measurements, range from (2.00 ± 0.05) s to (2.51 ± 0.16) s. The largest value is in agreement with the literature value of ^{35}Ar the ($\tau_{dec} = (2.562 \pm 0.002)$ s [Che11]). This indicates that there were no significant losses of ^{35}Ar ions from the decay trap.

$$\Gamma = \Gamma_{decay} + \Gamma_{loss} \qquad \Rightarrow \qquad \frac{1}{\tau} = \frac{1}{\tau_{decay}} + \frac{1}{\Gamma_{loss}} \tag{3.4.10}$$

Fig. 3.17 shows the amplitudes of the fit with the error bars calculated by Minuit as function of the retardation voltage. The amplitudes of the different retardation voltages show a falling tendency with rising retardation potential. The 0 V amplitude is significantly larger then the other amplitudes. The reason for this will be discussed in sec. 3.4.4.2. Between 75 V and 300 V we can see a slow decrease in the amplitudes. The amplitudes for the retardation voltage of 525 V are all compatible with 0. This shows no sign of energy gain of the ^{35}Cl ions due to non-optimal transfer of the ion cloud from the cooler to the decay trap.
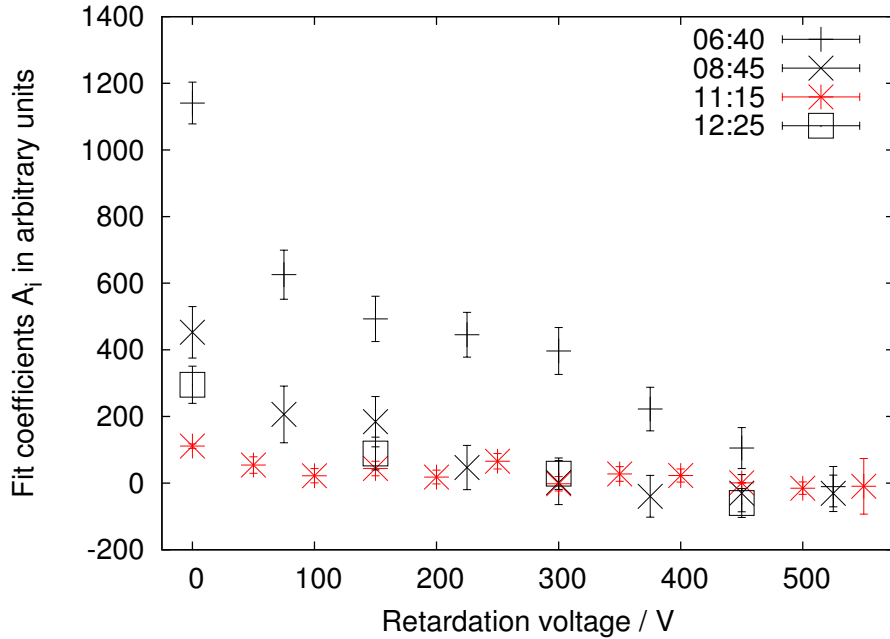
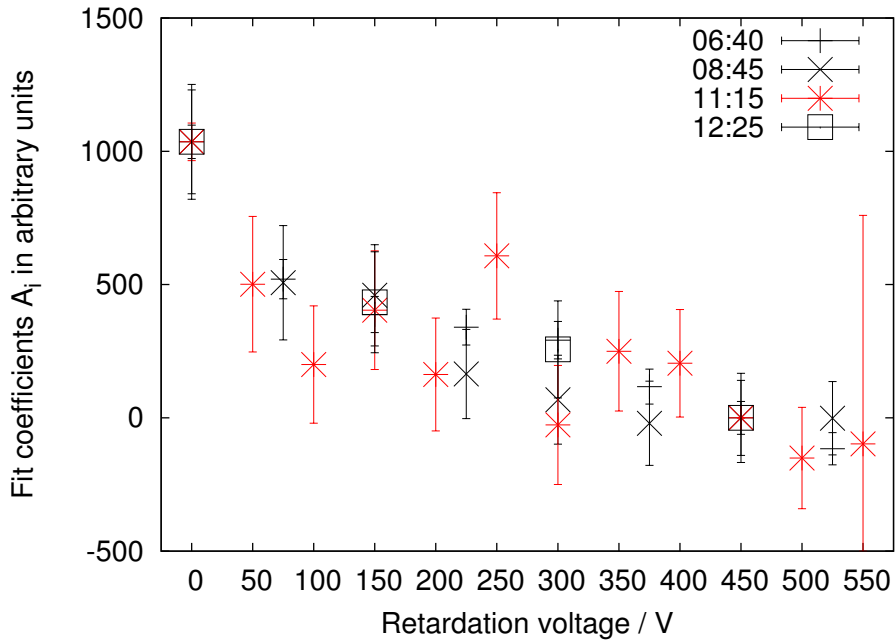**Figure 3.17.:** Recoil spectrum of the data from the 06:40, 08:45, 11:15 and 12:25 measurement from 01/11/11. The amplitudes differ because of a decrease in the target performance and different measurement times. The error bars are drawn with the values calculated by Minuit. The result of the 11:15 measurement is marked in red because it is not in good agreement with the other data.

Regarding the uncertainties on the fit parameters given by the program Minuit we have to take into account that the large reduced χ^2. Let us look on the result of the 06:40 measurement for instance. The reduced χ^2 of 2.07 with $N_{dof} = 158$ shows a 9.5 σ deviation from the expected value

1, where $\sigma(\chi^2_{\text{reduced}}) = \sqrt{2/N_{dof}} = 0.1125$. This deviation is even bigger for the other measurements. This is an indication that the errors on the data are not purely statistical, but have a systematic contribution.

Hence, to find a more reliable estimate on the uncertainties of the amplitudes, we multiplied them by a factor of $\sqrt{\chi^2/N_{dof}}$ to receive a reduced χ^2 of 1. Furthermore we normalized the spectra to the amplitude of the 0 V measurement A_0 and used the amplitude of the 450 V retardation voltage as the zero line. This is necessary because some amplitudes of the higher potentials were shifted to negative values. In principle one could also normalize on the amplitude of the background B but this would only be possible if the performance of the target would be constant over the whole measurement period, which was not the case. One can see a decrease in the 0 V amplitude by about a factor 4 from 1150 for the 06:40 measurement to 300 for the 12:25 measurement. The result of this is shown in fig. 3.18. One can see that within the error bars all three measurements (06:40, 08:45 and 12:25) are in agreement.

Figure 3.18.: Recoil spectrum of the data from the 06:40, 08:45, 11:15 and 12:25 measurement from 01/11/11. All measurements are normalized to the amplitude A_0 of the 0 V retardation voltage measurement. Error bars are enlarged to receive $\chi^2/N_{dof} = 1$ of the fits.

The constant background C has a value of approx. 300 for the 06:40 and 08:45 measurements and approx. 170 for the 12:25 measurement. The amplitude B of the exponentially decaying background of approx. 2500 for the 06:40 and 08:45 measurements and about 1100 for the 12:25 measurement. This can be due to the shorter measurement period. The ratio C/B, of constant to exponential background, is somewhat similar (approx. 0.13 to 0.15) for all three measurements and the lifetime of the exponentially decaying background is always about one second.

Contour plots of the amplitude of the exponential background B and the constant background C is shown in fig. 3.19(a). For the amplitude B and the lifetime τ_2 of the exponential background it is shown in fig. 3.19(b). A contour plot of the lifetime τ_1 and the lifetime of the background τ_2 is shown in fig. 3.19(c) for the 06:45 measurement. All ellipses show practically no correlation between the parameters. The residuals of all fits scatter randomly and show no sign of systematic effects.

(a)

(b)

(c)
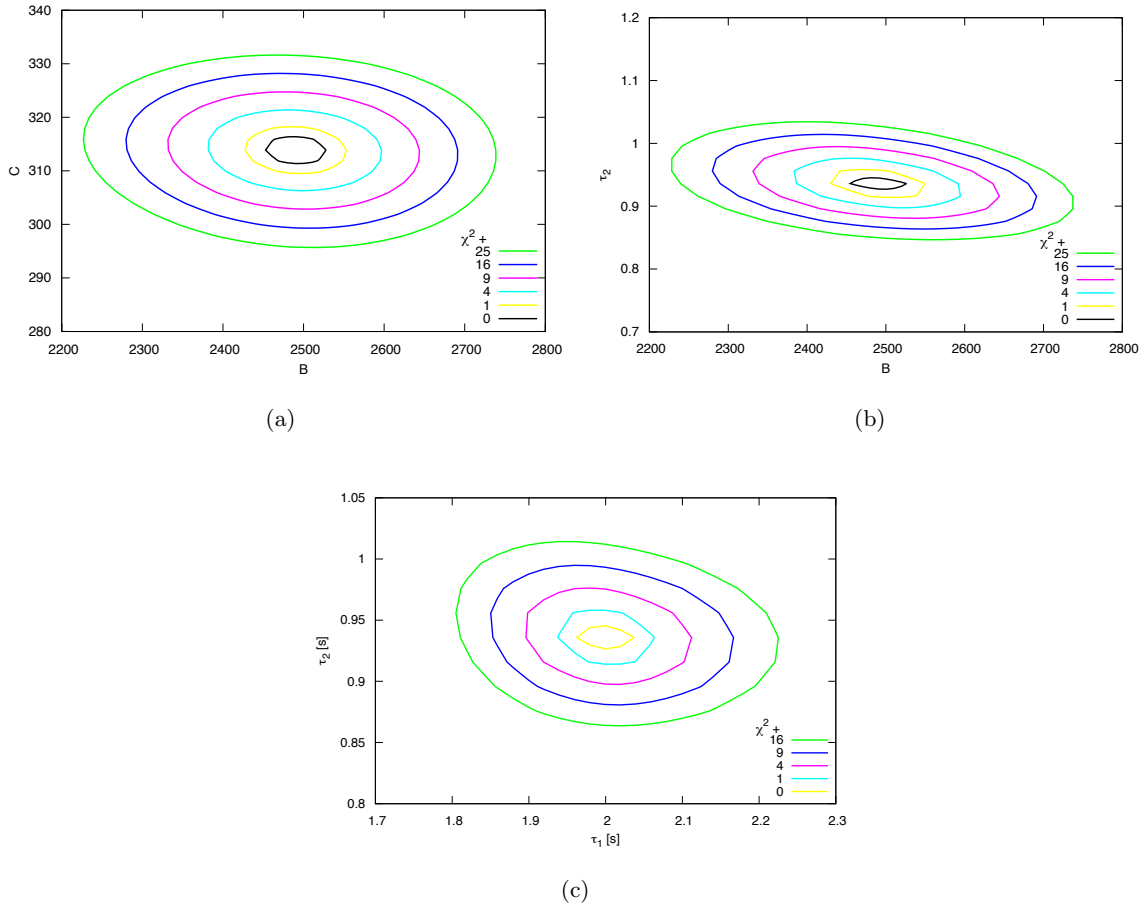
Figure 3.19.: (a) Contour plot of the amplitude of the exponential background B and the constant background C for the 06:40 measurement. The contour shows an ellipse with little correlation. (b) Contour plot of the lifetime τ_2 and amplitude of the exponential background B for the 06:40 measurement. The orientation of the ellipse indicates a small correlation between these two factors. (c) Contour plots of the lifetime τ_1 and the lifetime of the background τ_1 for the 06:45 measurement. The ellipse shows no correlation between the two lifetimes.

For the 11:15 data the result of the fit was somewhat contradictory. It showed a lifetime which was about 1.5 times larger then the ^{35}Ar lifetime. Also the amplitudes for the different voltages are not in the right order and show significant fluctuations. Trying to fix certain parameters and refitting them later did not improve the result. The lifetime of the background is somehow in the right order of magnitude but shows a huge uncertainty of nearly 50%, calculated by Minuit. The ratio of constant background to the amplitude of the exponential background is comparable to the results of the other data sets.

3.4.3.3. Combined fit

Finally a combined fit off all four data sets was performed. The advantages of this method are a better error estimation and the problem of normalization is being bypassed. To fit all four sets of data simultaneously, we applied the following procedure:

- The four data sets are combined to one file by adding an additional time offset of 200 s between each file.

- Each retardation voltage has a separate amplitude, 16 amplitudes in total: A_i with $i \in [0, 50, 75, 100, 150, 200, 225, 250, 300, 350, 375, 400, 450, 500, 525, 500]$.

- Additionally each set of data gets a separate amplitude indexed with the measurement time, so one for 06:40, one for 08:45 and so on: A_k with $k \in [0640, 0845, 1115, 1225]$. This amplitude is multiplied with the amplitude for the retardation voltage. It is important to notice that the amplitude A_{0640} was fixed to 1 otherwise one would have two degenerated parameters.

- All of these amplitudes are multiplied with an exponential decay with the same lifetime τ_1: $A_i \cdot A_k \cdot e^{-\frac{t}{\tau_1}}$

- Each set of data (06:40, 08:45 and so on) gets a separate background amplitude B_k indexed with the measurement time, with $k \in [0640, 0845, 1115, 1225]$. This amplitude is then multiplied with an exponential decay with time constant τ_2 and a constant offset C for all four measurements: $B_l \cdot e^{-t/\tau_2} + C$.

In a nutshell we can write the fit function as:

$$f_{fit, raw}(t) = \sum_k \sum_i \left(A_k \cdot A_i \cdot e^{-t/\tau_1} + B_k \cdot e^{-t/\tau_2} + C \right) \tag{3.4.11}$$

with $i \in [0, 50, 75, 100, 150, 200, 225, 250, 300, 350, 375, 400, 450, 500, 525, 500]$ and $k \in [0640, 0845, 1115, 1225]$. The fit results as returned from the program are displayed in tab. C.5 (see Appendix C). The reduced χ^2 of the fit is 2.95. The fit function and the data are shown in fig. C.5 in the Appendix C. The residuals are shown in fig. C.6 in the Appendix C.

The lifetime of the signal is $\tau_1 = (1.91 \pm 0.08)$ s. This gives rise to the conclusion that the losses of Ar ions from the decay trap are significant. The lifetime of the exponential background of $\tau_2 = (0.97 \pm 0.02)$ s is smaller than the lifetime of the signal amplitudes τ_1. This indicates that the exponential background originates not form the betas of the ^{35}Ar decay alone but has other contributions. The ratio of the constant background to the amplitude of the exponential background is given by $C/B = (0.148 \pm 0.004)$. With a measurement cycle length of 6 s the background is dominated in the upper part of the spectrum by the exponential component, while to the end of the spectrum the background is dominated by the constant contribution.

The signal-to-noise ratio of the exponential background at the beginning of each measurement cycle can be obtained from the ratio $(A_0 \cdot A_k)/B_k$ with $k \in [0640, 0845, 1115, 1225]$. The result is given in tab. 3.7. One can see a significant decrease from 0.56 ± 0.05 at 06:40 to 0.12 ± 0.02 at 12:25 with progressing time. This might indicate a decrease of the performance of the target through the course of the measurement.

Table 3.7.: Signal to noise ratio of the exponential background at the beginning of each measurement cycle. Uncertainties are enlarged by a factor of $\sqrt{\frac{\chi^2}{N_{dof}}}$ (see text for explanation).

k	$(A_0 \cdot A_k)/B_k$
06:40	0.56 ± 0.05
08:45	0.29 ± 0.04
11:15	0.21 ± 0.04
12:25	0.12 ± 0.02

A zoom to the 0 V measurement from the four data set 06:40 is shown in fig. 3.20 without enlarged uncertainties. It shows that the fluctuations in the count rate are beyond the statistical fluctuations. It is the reason for the bad χ^2/N_{dof} and an indication for experimental problems. In fig. 3.21 the first extracted ion recoil spectrum with the full statistics of all measurements of November 1, 2011 is shown. With enlarged error bars, by $\sqrt{\chi^2/N_{dof}}$, the spectrum looks smooth. The runaway at 250 V retardation voltage stems from the 11:15 measurement but is still compliant within the uncertainties.
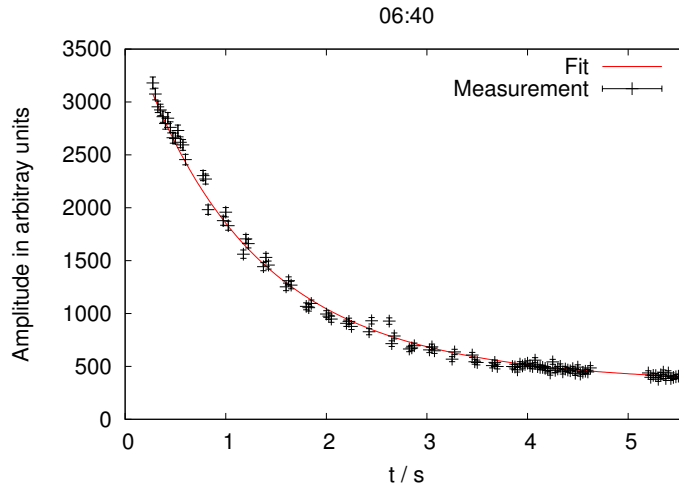
Figure 3.20.: Zoom to the 0 V measurements from the 06:40 data with uncertainties of $\sqrt{N}$. The fluctuations in the count rate are beyond the statistical fluctuations.
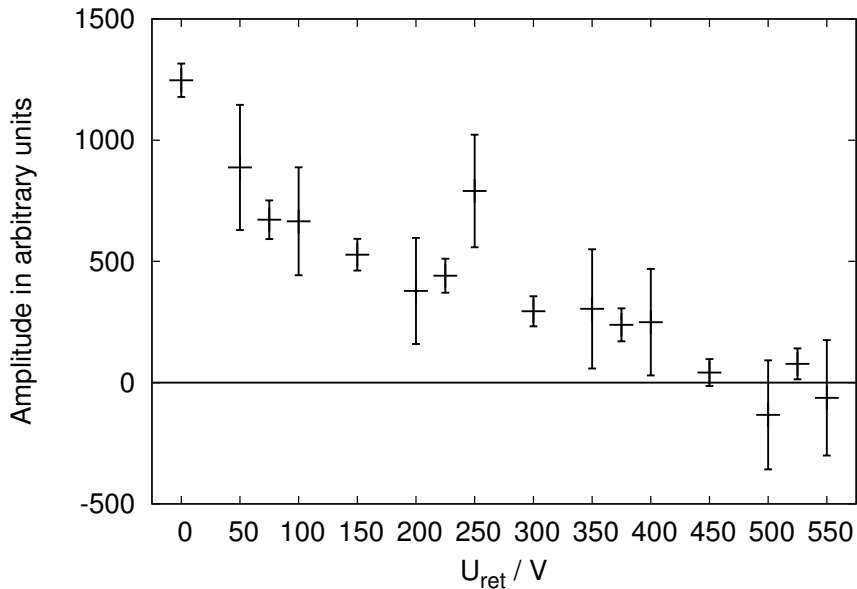
Figure 3.21.: Recoil spectrum of the combined fit of all four measurements from 01/11/2011. Error bars are enlarged to receive $\chi^2/N_{dof} = 1$ of the fits.

3.4.4. Least square fit of the recoil spectrum

To fit the recoil spectrum which we extracted from the combined fit (shown in fig. 3.21) we combined the simulation results to a fit function. This is described in the following paragraph. In the next section we present the fit results. Thereafter we discuss two important systematic effects. This section finishes with a summary and conclusion.

3.4.4.1. Generation of the fit function

To create the fit function we start with the simulation results. For each retardation potential and each charge state between 1^+ and 4^+ we have four different Monte Carlo simulations each with $N = 100000$ events: One for $t_{trans} = 31.5\,\mu$s and $a = 0$, one for $t_{trans} = 38\,\mu$s and $a = 0$, for $t_{trans} = 31.5\,\mu$s and $a = 1$ and for $t_{trans} = 38\,\mu$s and $a = 1$. The numbers of detected ions from these simulations were combined to four different spectra: $N_{sim}(U_{ret}, 31.5\,\mu\text{s}, 0, \text{i} \cdot \text{e})$, $N_{sim}(U_{ret}, 38\,\mu\text{s}, 0, \text{i} \cdot \text{e})$, $N_{sim}(U_{ret}, 31.5\,\mu\text{s}, 1, \text{i} \cdot \text{e})$ and $N_{sim}(U_{ret}, 38\,\mu\text{s}, 1, \text{i} \cdot \text{e})$, where U_{ret} is the retardation potential, $31.5\,\mu$s respectively $38\,\mu$s denotes the transfer time t_{trans}, 0 or 1 denotes the value of a and $i \cdot e$ is the charge of the recoil ion. Each spectrum contains all retardation potentials from the measured spectrum in fig. 3.21: 0 V, 50 V, 75 V, 100 V, 150 V, 200 V, 225 V, 250 V, 300 V, 350 V, 375 V, 400 V, 450 V, 500 V, 525 V, 550 V and 600 V.

Fig. 3.22 shows a comparison of the simulated spectra between $a = 0$ (dashed lines) and $a = 1$ (solid lines) for $t_{trans} = 31.5\,\mu$s (left hand side) and $t_{trans} = 38\,\mu$s (right hand side) for the charge states 1^+ (red), 2^+ (blue), 3^+ (grey) and 4^+ (black). The curves for $a = 0$ show a more shallow slope compared to $a = 1$ while the endpoint of these spectra stays the same. One would expect this, since for $a = 0$ the ions have predominantly lower energies compared to $a = 1$. Moreover, we see that for $U_{ret} = 0$ V, depending on the charge of the ions, different amounts of ions are transmitted. This number decreases with higher charge states (about 85000 for 1^+ to approx. 60000 for 4^+). The missing ions are the ones that cannot leave the trap due to the $\theta - E$-cut-off (see sec. 3.3.4.3 and ref. [Fri08]). For instance, doubly chargedions will experience double the Coulomb force compared to singly charged ions, which is why a larger fraction of ions cannot overcome the trapping potential. Furthermore, at $U_{ret} = 0$ V more ions are transmitted for a=1 than for a=0. For $a = 0$, the ions have predominantly lower energies compared to $a = 1$, why a larger fraction is unable to escape the decay trap.

Fig. 3.23 shows a comparison of the simulated spectra between $t_{trans} = 31.5\,\mu$s (solid lines) and $t_{trans} = 38\,\mu$s (dashed lines) for $a = 1$ (left hand side) and $a = 0$ (right hand side) for the charge states 1^+ (red), 2^+ (blue), 3^+ (grey) and 4^+ (black). This time, the effect is qualitatively different. The curves for $t_{trans} = 31.5\,\mu$s lay above the ones for $t_{trans} = 38\,\mu$s, which means that more ions are detected for $t_{trans} = 31.5\,\mu$s for a given retardation potential compared to $t_{trans} = 38\,\mu$s. The slope of the curves for $t_{trans} = 31.5\,\mu$s and $t_{trans} = 38\,\mu$s are very similar. For $t_{trans} = 31.5\,\mu$s the endpoints of the curves are shifted to larger retardation potentials. This is a huge effect. To explain the broadening of the simulated spectra let us regard the following example:

We assume the ions have an initial kinetic energy of $E_{kin} = 5$ eV and a recoil energy of $E_{rec} = 450$ eV. In this energy regime we can calculate the total energy non-relativistically. From this follows:

$$E_{kin} = \frac{1}{2}m \cdot v_{kin}^2 \quad \Rightarrow \quad v_{kin} = \sqrt{\frac{2 \cdot E_{kin}}{m}} = \sqrt{\frac{2 \cdot 5\,\text{eV}}{m}} \tag{3.4.12}$$

$$E_{rec} = \frac{1}{2}m \cdot v_{kin}^2 \quad \Rightarrow \quad v_{kin} = \sqrt{\frac{2 \cdot E_{rec}}{m}} = \sqrt{\frac{2 \cdot 450\,\text{eV}}{m}} \tag{3.4.13}$$

where m is the mass of the ^{35}Ar ion and v_{kin} and v_{rec} the absolute values of the initial kinetic and recoil velocities. We assume that the velocity vectors are parallel: $\vec{v}_{kin} || \vec{v}_{rec}$. In this case the total
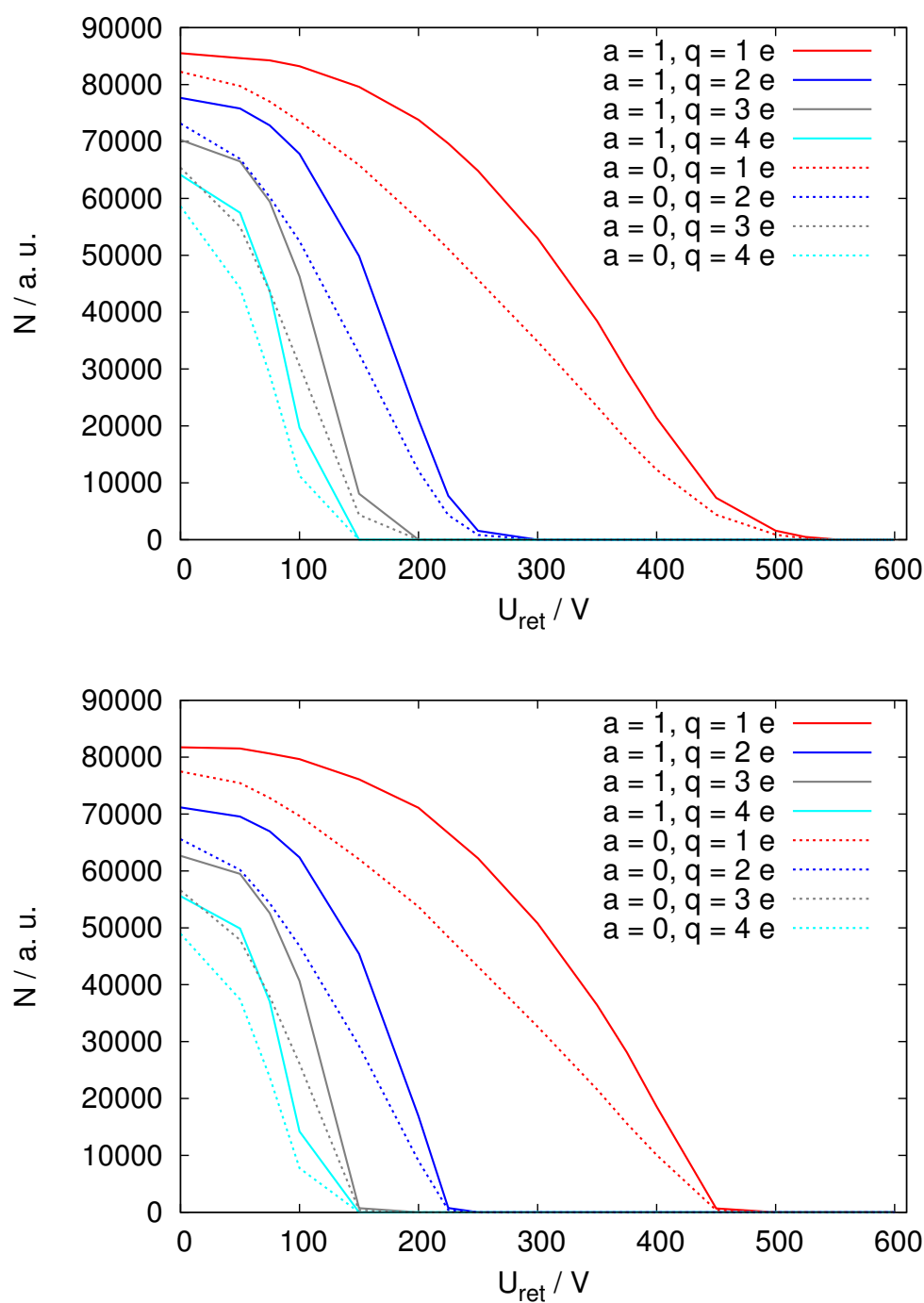
Figure 3.22.: Simulated recoil spectra for the ^{35}Ar decay to ground state ^{35}Cl for the charge states 1^+ (red), 2^+ (blue), 3^+ (grey) and 4^+ (light blue). Sown is a comparison between $t_{trans} = 31.5\,\mu$s (top) and $t_{trans} = 38\,\mu$s (bottom). The dashed lines are for $a = 0$ and the solid ones are for $a = 1$. See text for explanation.

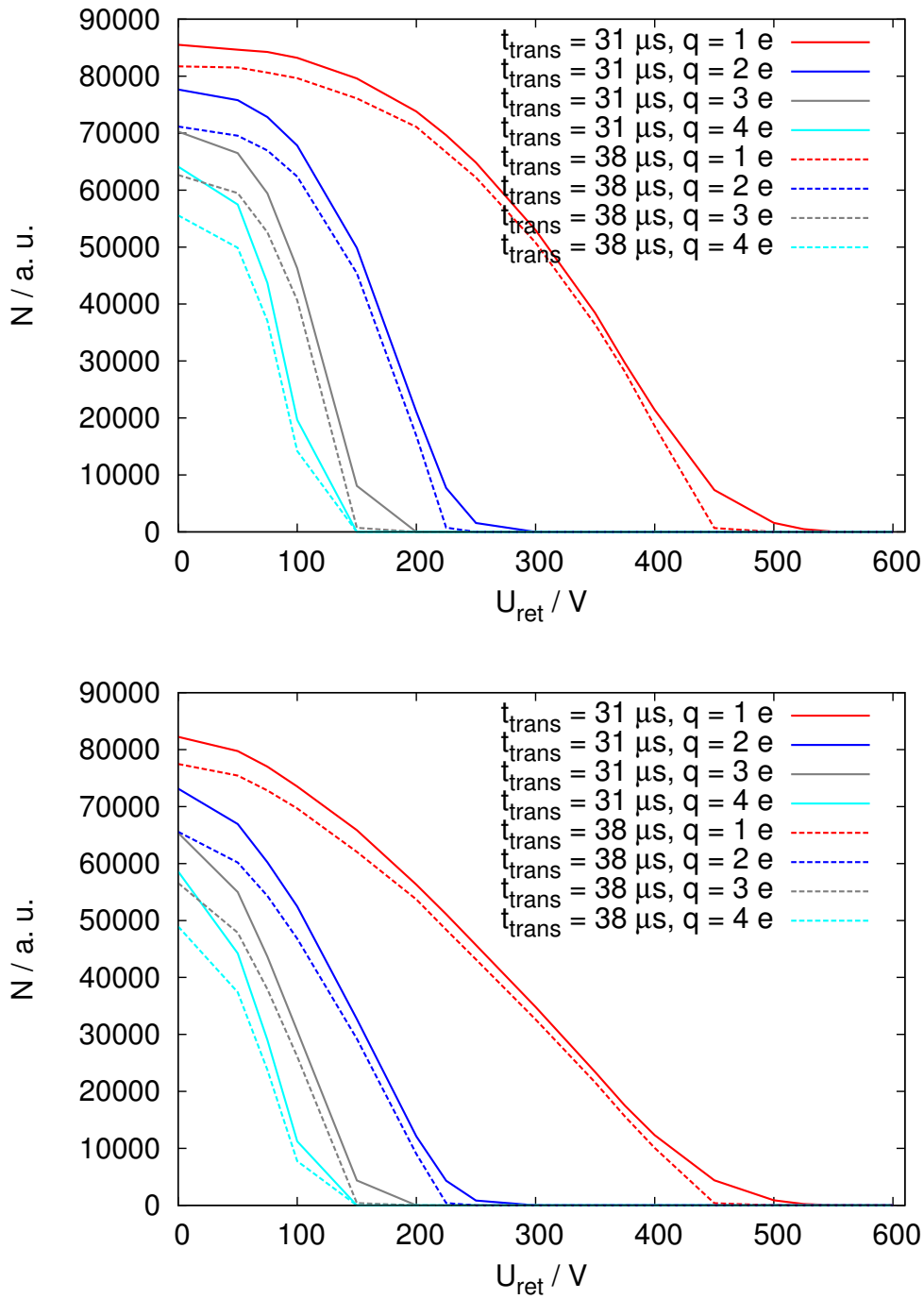**Figure 3.23.:** Simulated recoil spectra for the ^{35}Ar decay to ground state ^{35}Cl for the charge states 1^+ (red), 2^+ (blue), 3^+ (grey) and 4^+ (light blue). Sown is a comparison between $a = 1$ (top) and $a = 0$ (bottom). The dashed lines are for $t_{trans} = 38\,\mu$s and the solid ones are for $t_{trans} = 31.5\,\mu$s . See text for explanation.

kinetic energy can be calculated as:

$$
\begin{aligned}
E_{tot} \quad &= \tfrac{1}{2}m(\vec{v}_{kin} + \vec{v}_{rec})^2 = \tfrac{1}{2}m(v_{kin} + v_{rec})^2 = \tfrac{1}{2}m(v_{kin}^2 + 2\cdot v_{kin}\cdot v_{rec} + v_{rec}^2) \\
&= \tfrac{1}{2}m(\tfrac{2\cdot 450\,\mathrm{eV}}{m} + \sqrt{\tfrac{2\cdot 450\,\mathrm{eV}}{m}\cdot\tfrac{2\cdot 5\,\mathrm{eV}}{m}} + \tfrac{2\cdot 450\,\mathrm{eV}}{m}) = 450\,\mathrm{eV} + 95\,\mathrm{eV} + 5\,\mathrm{eV} = 550\,\mathrm{eV}
\end{aligned}
\tag{3.4.14}
$$

Apart from this we have to consider the field penetration in the analysis plane which reduces the retardation potential from 550 V to about 546 V. All together this explains why we still see detected ions in the simulated spectrum for $t_{trans} = 31.5\,\mu$s at $U_{ret} = 550$ V (compare fig.3.22).

For $t_{trans} = 38\,\mu$s the situation is different. Because of the optimized transfer between the cooler and the decay trap the ions have less initial kinetic energy E_{kin}. This is described in more detail in ref. [Gor12]. This is why the term $2\cdot v_{kin}\cdot v_{rec}$ is smaller as well.

For each of the four charge states 1^+ to 4^+ we have four simulated spectra $N_{sim}(U_{ret}, a, t_{trans}, i\cdot e)$: one for $a = 0$ and $t_{trans} = 31.5\,\mu$s, one for $a = 0$ and $t_{trans} = 38\,\mu$s, one for $a = 1$ and $t_{trans} = 31.5\,\mu$s and one for $a = 1$ and $t_{trans} = 38\,\mu$s which we call $N_{sim}(U_{ret}, 0, 31.5\,\mu\mathrm{s}, i\cdot e), N_{sim}(U_{ret}, 0, 38\,\mu\mathrm{s}, i\cdot e)$, $N_{sim}(U_{ret}, 1, 31.5\,\mu\mathrm{s}, i)$ and $N_{sim}(U_{ret}, 1, 38\,\mu\mathrm{s}, i\cdot e)$. $i\cdot e$ denotes the charge of the ion. These we combined to the following fit function:

$$
\begin{aligned}
F_{fit}(U_{ret}) \quad = \quad & f_{amp}\cdot \sum_{i=1}^{4} c_i \cdot ((1 - f_a)\cdot [f_{trans}\cdot N_{sim}(U_{ret}, 0,\ 31\,\mu\mathrm{s}, i\cdot e) \\
& + (1 - f_{trans})\cdot N_{sim}(U_{ret}, 0,\ 38\,\mu\mathrm{s}, i\cdot e)] \\
& + f_a \cdot [f_{trans}\cdot N_{sim}(U_{ret}, 1,\ 31\,\mu\mathrm{s}, i\cdot e) \\
& + (1 - f_{trans})\cdot N_{sim}(U_{ret}, 1,\ 38\,\mu\mathrm{s}, i\cdot e)]) \\
& + C_{back}
\end{aligned}
\tag{3.4.15}
$$

where c_i are coefficients for the different charge states (e. g. c_1 for 1^+, c_2 for 2^+ and so on), f_{amp} a general scaling factor, f_{trans} a weight factor of the different transfer times ($f_{trans} = 1$ corresponds to $t_{trans} = 31.5\,\mu$s, $f_{trans} = 0$ corresponds to $t_{trans} = 38\,\mu$s), f_a is the factor to weight the simulated spectra for $a = 0$ and $a = 1$ ($f_a = 1$ corresponds to $a = 1$ and $f_a = 0$ to $a = 0$). The $N_{sim}(U_{ret}, a, t_{trans}, i\cdot e)$ are explained above and C_{back} is a constant background. To fit the recoil energy spectrum with a linear combination of $a = 0$ and $a = 1$ is possible since the recoil energy spectrum $N(E_{rec})$ itself is linear in a (compare eq. 1.1.30). This will be shown in the following short example. Simplified, the fit function can be written in the following way:

$$
f_{fit}(a, E_{rec}) \quad = \quad a\cdot f(a = 1, E_{rec}) + (1 - a)\cdot f(a = 0, E_{rec})
$$

where the function $f(a, E_{rec})$ can be written in the form $f(a, E_{rec}) = K(E_{rec}) + a\cdot g(E_{rec})$ where $K(E_{rec})$ and $g(E_{rec})$ are functions of E_{rec} (compare eq. 1.1.30). If we use this, we find:

$$
\begin{aligned}
f_{fit}(a, E_{rec}) \quad &= \quad a\cdot f(a = 1, E_{rec}) + (1 - a)\cdot f(a = 0, E_{rec}) \\
&= \quad a\cdot (K(E_{rec}) + 1\cdot g(E_{rec})) + (1 - a)\cdot (K(E_{rec}) + 0\cdot g(E_{rec})) \\
&= \quad a\cdot (K(E_{rec}) + 1\cdot g(E_{rec})) + (1 - a)\cdot K(E_{rec}) \\
&= \quad K(E_{rec}) + a\cdot g(E_{rec})
\end{aligned}
\tag{3.4.16}
$$

So we see that the fit function does not change the general shape of the spectrum. To be precise with this approach we assume that $N(E_{rec}) \otimes F_{trans}(U_{ret}) \otimes F_{det}(U_{ret})$, where $F_{trans}(U_{ret})$ is the transmission function of the spectrometer and $F_{det}(U_{ret})$ is the response function of the detector, is linear in a. This remains to be shown. To fit the data we use the tool Minuit, release 93.08.
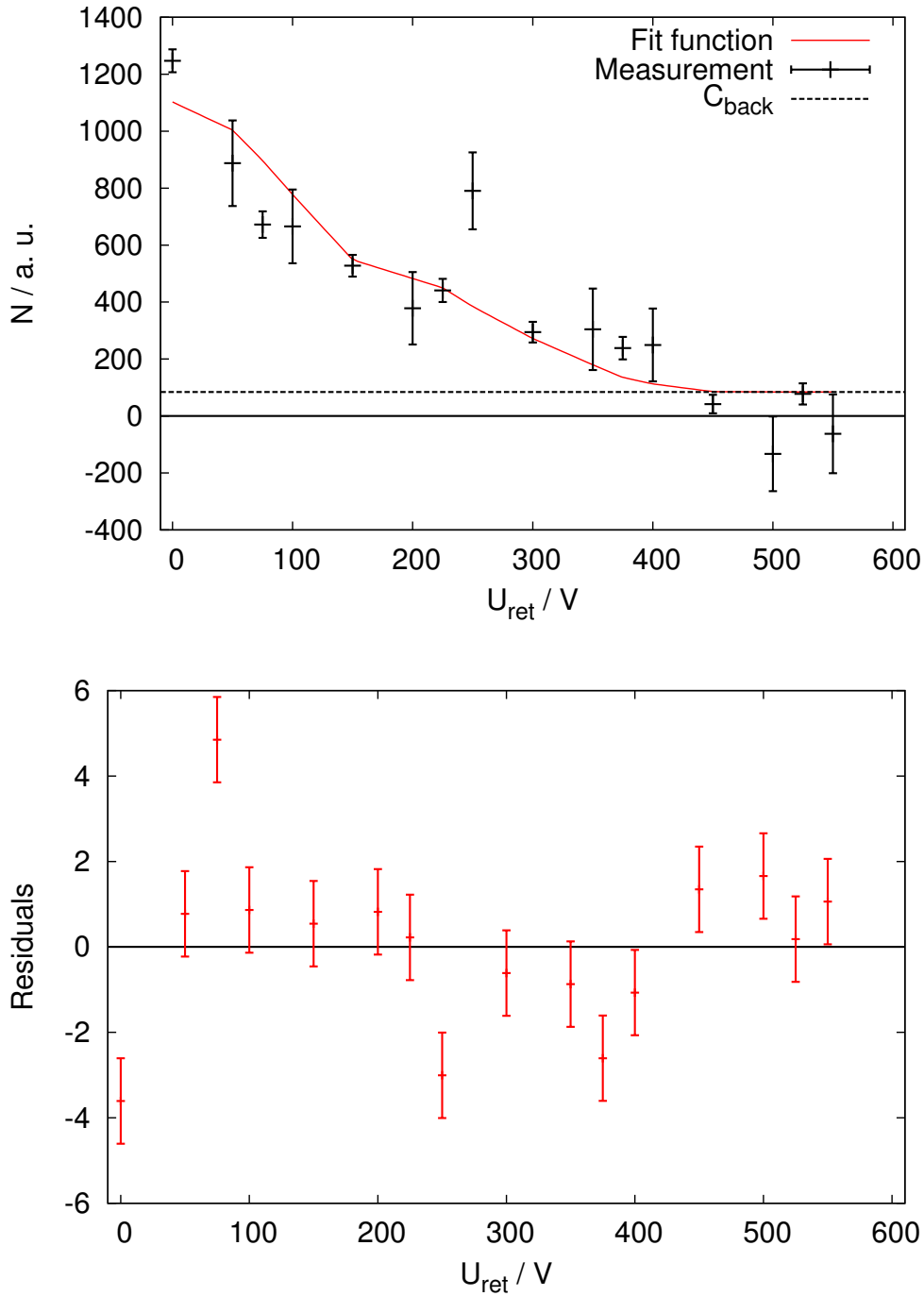
3.4.4.2. Fit results

Figure 3.24.: Fit function with data points (top). The c_i have been fixed to the measured values. The parameter f_{trans} has been limited to the interval [0:1]. The residuals are shown on the bottom. The data points for 0 V and 75 V have the largest residuals.

For the fit we used the spectrum shown in fig. 3.21, but without enlarging the error bars by a factor of $\sqrt{\chi^2/N_{dof}}$ as it is shown in this figure. In a first approach we tried to fit the data while keeping all parameters variable. We assumed reasonable values for the fit parameters like $f_{amp} = 10^{-3}$, $f_a = 1$, $f_{trans} = 0.5$, $c_1 = 1$, $c_2 = 0.1$, $c_3 = 0.1$ and $c_4 = 0$. It was hardly possible to find a minimum. The returned values for the fit parameters were unphysical, e. g. c_5 was orders of magnitudes larger than c_1 and c_2 became even negative.

The first reasonable result we received after fixing the charge state distribution (the c_i in the fit function). For this we used the measured values shown in tab. 3.1, meaning $c_1 = 0.75$, $c_2 = 0.17$, $c_3 = 0.06$ and $c_4 = 0.02$. By this we neglect the uncertainties of these values. Furthermore we limited the factor $f_{trans} \in [0 : 1]$. The fit results in:

$$
\begin{aligned}
f_{amp} &= (1.53 \pm 0.06) \cdot 10^{-2} \\
f_a &= (-0.89 \pm 0.14) \\
C_{back} &= (84 \pm 23)
\end{aligned}
\tag{3.4.17}
$$

with $\frac{\chi^2}{N_{dof}} = \frac{62,76}{12} = 5.23$. f_{trans} was at its upper allowed limit (+ 1.0). The resulting fit function and the residuals are shown in fig. 3.24. The value for 0 V and 75 V show the largest divination. At first glance it seems like the data points at 0 V and 250 V stick out and don't follow the trend of the others. This applies in particular to the 0 V data point, which has a small uncertainty and thus is considered in the fit with a higher weight than the 250 V data point. This is also the reason why the amplitude f_{amp} gets enlarged by the fitting routine as it can be seen in fig. 3.24.

3.4.4.3. Excess count rate for $U_{ret} = 0$ V

In the following we discuss different possibilities for the reason of the increased count rate at $U_{ret} = 0$ V retardation potential.

a) **Detector size**
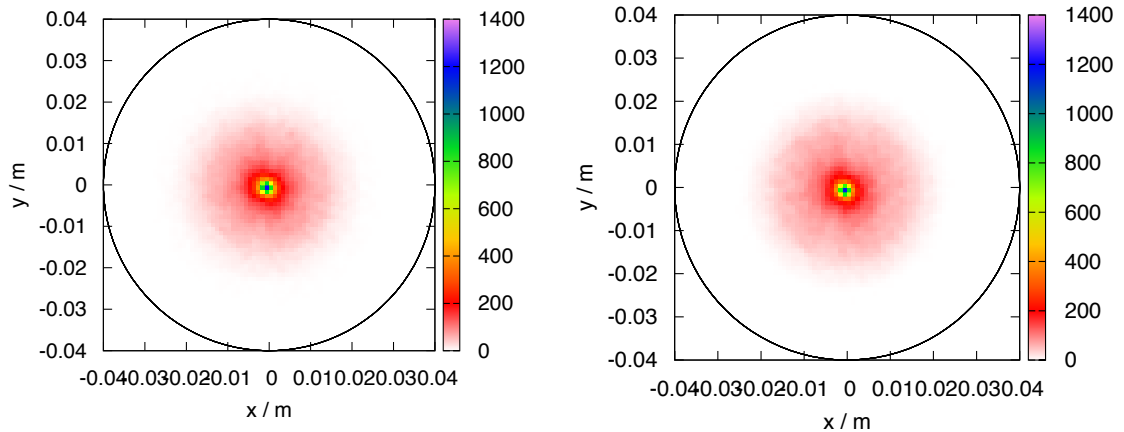
Figure 3.25.: Simulated ion distributions on the detector for $a = 1$, $t_{trans} = 31.5\,\mu s$ and 1^+ charge state. On the left it is shown for 0 V retardation potential, right hand side for 50 V.

First we check if this could be a detector effect. Therefore we have a look on the simulated ion distributions in the detector plane. Fig. 3.25 shows two examples for simulated ion distributions on the detector plane for $a = 1$, $t_{trans} = 31.5\,\mu s$ and 1^+ charge state. On the left

it is shown for 0 V retardation potential, right hand side for 50 V. Obviously they look almost identical. This was checked also for other configurations and charge states, but no significant difference between 0 V and 50 V was found which could explain the behavior of the 0 V data point in our spectrum.

A second example is shown in fig. 3.27 where the simulated count rate normalized to the radius (N/r) as function of the radius is shown for five different retardation potentials 0 V, 50 V, 100 V, 300 V and 450 V. On top it is shown for $a = 1$, $t_{trans} = 31.5\,\mu s$ and 1^+ charge state. At the bottom it is shown for $a = 1$, $t_{trans} = 38\,\mu s$ and 1^+ charge state. We don't see something unexpected because the maximum radius is smaller than the active radius of the detector. The retardation potential has a small effect on the focussing of the ions. The curves for 0 V and 50 V show only small differences that could not be the origin for the behavior of the 0 V datapoint.

Although this cannot cause the increased count rate at $U_{ret} = 0$ V, we could observe the following tendencies:

- For higher charge states, the ions are better focused and the spot size is smaller.

- The retardation potential has a small focussing effect.

- For $t_{trans} = 38\,\mu s$, the ions are better focused than for $t_{trans} = 31.5\,\mu s$.

- All simulated events arrive in the detector plane within a radius of $r < 30$ mm.

b) **Unintentional Penning trap in the spectrometer**
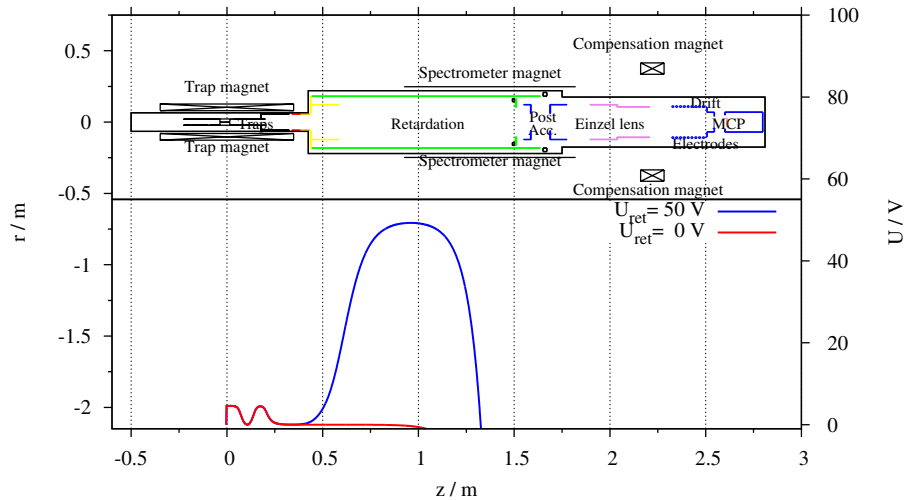
Figure 3.26.: On top a schematic drawing of the electrode and magnet geometry as it is implemented in the simulation program. Below is drawn the simulated electric potential along the symmetry axis for 0 V retardation potential (red) and 50 V retardation potential (blue).

Fig. 3.26 shows on top a schematic drawing of the electrode and magnet geometry as it is implemented in the simulation program. Below is drawn the simulated electric potential along the symmetry axis (z-axis) for 0 V retardation potential (red) and 50 V retardation potential (blue). Between $z = 0.2$ m and $z = 0.5$ m the electric potential along the z-axis shows a local minimum for $U_{ret} = 50$ V. In this area a strong residual magnetic field is present which results from the strong filed of the trap magnet. Altogether this acts as a Penning trap for positively charged ions. Every time the retardation potential is lowered from a value above 0 V – e. g.

179
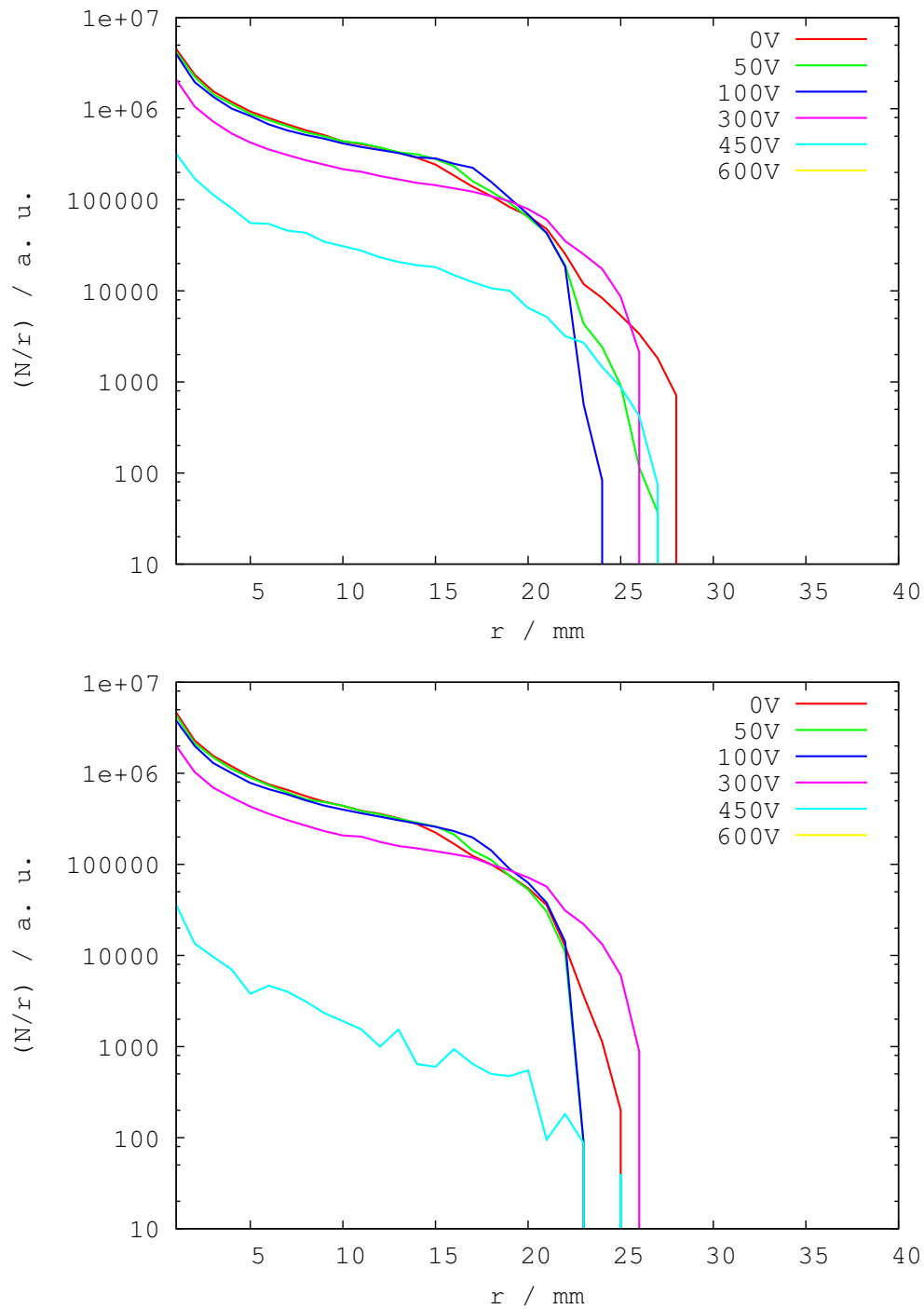
Figure 3.27.: Simulated radial distributions normalized to the radius (N/r) are shown in a logarithmic plot for five different retardation potentials 0V, 50 V, 100 V, 300 V and 450 V. On top it is shown for $a = 1$, $t_{trans} = 31.5 \, \mu$s and 1^+ charge state. At the bottom it is shown for $a = 1$, $t_{trans} = 38 \, \mu$s and charge state 1^+.

50 V – to 0 V the trap is emptied. The typical flight time for a $^{35}Cl^+$ ion from the decay trap to the detector is in the order of $30 - 50\,\mu$s (see sec. 3.3.4.4), while the bin size of the data acquisition is 25 ms. This should result in an increased count rate in the first time bin after a shift to 0 V retardation potential happened. These bins have been sorted out in the data analysis because of the synchronization problem described in sec. 3.4.2 and could not contribute to the excess rate at $U_{ret} = 0$ V.

c) **Recoil ions emitted downwards**
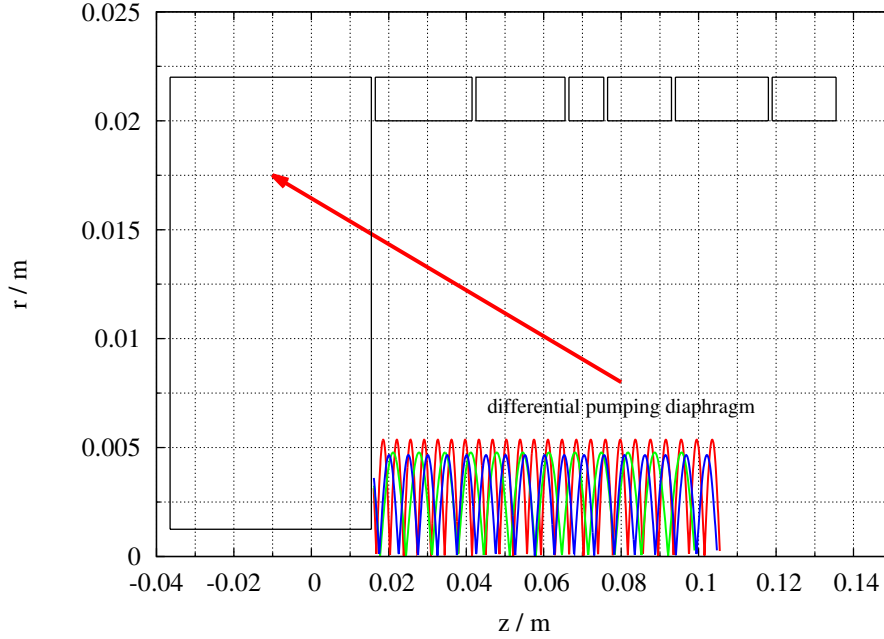
Figure 3.28.: A few exemplary tracks of simulated ^{35}Ar recoil ions that are emitted downwards. The bulk collides with the differential pumping diaphragm. Note that the oscillations are caused by the cyclotron motion of the ions that are emitted from an off-center starting position (initial coordinates x).

Another question is what happens to the ions that are emitted in downward direction, towards the cooler trap? To resolve this question we performed tacking simulations, where the ions have been emitted from the center of the decay trap in direction of the cooler trap. This is achieved by multiplying the z-component of the velocity vector with -1 and adjusting the stopping condition for the reflected ions in the source code of the tracking routine. A few exemplary ions tracks are shown in fig. 3.28. Almost every ions collides with the differential pumping diaphragm and is lost. This is due to their large cyclotron radius. Only $1 - 2\%$ of the ions are able to fly through the hole of the pumping diaphragm. The geometry of the horizontal beam line is not implemented in the tracking simulation, why we cannot for sure determine what happens to the ions that pass the differential pumping diaphragm. Anyway, these $1 - 2\%$ cannot be the reason for the excess rate at $U_{ret} = 0$ V.

d) **Losses of ions from the decay trap**

However, we favor another explanation: The fit of the raw data showed a lifetime of $\tau_1 = (1.91 \pm 0.14)\,$s[17] which is significantly smaller than the ^{35}Ar lifetime, which is $\tau_{dec} = (2.562 \pm$

---

[17]The error of this value was enlarged by a factor of $\sqrt{\chi^2/N_{dof}} = \sqrt{2.95}$ for a better error estimation. See sec. 3.4.3.3.

0.002) s [Che11]. This is an indication that ions are lost from the decay trap during the measurement period. These singly charged ^{35}Ar ions should have low kinetic energies, just above the end cap potential of the decay trap times the charge which is about 5 eV. These ions are blocked by any retardation potential higher than 0 V.

To estimate this effect let us make the following consideration: From the lifetime fit (τ_1, see sec. 3.4.3.3) we can calculate the decay constant of the particles that are released from the decay trap (Γ_s) and from the ^{35}Ar lifetime, which is $\tau_{dec} = (2.562 \pm 0.002)$s [Che11], we calculate the decay constant:

$$\tau_1 = (1.91 \pm 0.08)\,\text{s} \quad \Rightarrow \quad \Gamma_s \approx \frac{1}{\tau_1} = 0.52\,\text{Hz} \tag{3.4.18}$$

$$\tau_{dec} \approx 2.56\,\text{s} \quad \Rightarrow \quad \Gamma_{dec} = \frac{1}{\tau_{dec}} = 0.39\,\text{Hz} \tag{3.4.19}$$

We calculate the rate of recoil ions that leave the trap:

$$\dot{N}_{dec}(t) = \Gamma_{dec} \cdot N(t) \propto \Gamma_{dec} \tag{3.4.20}$$

The rate of recoil plus loss ions is:

$$\dot{N}_s(t) = \Gamma_s \cdot N(t) \propto \Gamma_s \tag{3.4.21}$$

The difference is the amount of loss ions:

$$\dot{N}_{loss}(t) = (\Gamma_s - \Gamma_{dec}) \cdot N(t) = \Gamma_{loss} \cdot N(t) \quad \Rightarrow \quad \Gamma_{loss} = \Gamma_s - \Gamma_{dec} \approx (0.13 \pm 0.04)\,\frac{1}{\text{s}} \tag{3.4.22}$$

Furthermore we have to take into account that a fraction of these ions is absorbed by the anti-ionization wire. To do so, we estimate the probability for recoil ions to be absorbed by the wire P_{wire}. Therefore we have to anticipate the result from sec. 3.5.2. In fig. 3.41 is shown the ratio of ions absorbed by the anti-ionization wire to detected ions for all different combinations of t_{trans} and a and all retardation potentials U_{ret}. For our estimation we only need the value for $U_{ret} = 0$ V. We estimate by eye the probability of absorption for each charge state: $P(1^+) = (0.075 \pm 0.010)$, $P(2^+) = (0.15 \pm 0.01)$, $P(3^+) = (0.21 \pm 0.02)$ and $P(4^+) = (0.26 \pm 0.02)$. Next, we multiply each probability by the measured relative abundance of each charge state (see tab. 3.2) and sum it up to a total probability to hit the wire P_{wire}:

$$P_{wire} = 0.75 \cdot P(1^+) + 0.17 \cdot P(2^+) + 0.06 \cdot P(3^+) + 0.02 \cdot P(4^+) = (0.10 \pm 0.01) \tag{3.4.23}$$

We assume that the loss ions from the decay trap have the same probability to be absorbed by the wire as the recoil ions of charge state 1^+ ($P(1^+)$).

The fraction of ^{35}Cl daughter atoms that undergo electron shake-off after the β^+ decay of ^{35}Ar was measured at the LPC trap experiment in CAEN [Gor12]:

$$P_{shake} = (0.28 \pm 0.10) \tag{3.4.24}$$

At $U_{ret} = 0$ V retardation potential the detector sees this fraction plus the fraction of loss ions times $(1 - P_{wire})$:

$$\begin{aligned} \Gamma_{det1} &= (1 - P(1^+)) \cdot \Gamma_{loss} + P_{shake} \cdot (1 - P_{wire}) \cdot \Gamma_{dec} \\ &= (0.925 \pm 0.015) \cdot (0.13 \pm 0.04)\,\frac{1}{\text{s}} \end{aligned}$$

$$+(0.28 \pm 0.10) \cdot (0.90 \pm 0.01) \cdot (0.39) \cdot \frac{1}{\text{s}}$$

$$= (0.22 \pm 0.05) \cdot \frac{1}{\text{s}} \qquad (3.4.25)$$

At any retardation potential above 0 V the detector only sees the fraction of ^{35}Cl daughter atoms they undergo electron shake-off and become charged:

$$\Gamma_{det2} = P_{shake} \cdot (1 - P_{wire}) \cdot \Gamma_{dec}$$

$$= (0.28 \pm 0.10) \cdot (0.90 \pm 0.01) \cdot (0.39) \cdot \frac{1}{\text{s}}$$

$$= (0.098 \pm 0.034) \cdot \frac{1}{\text{s}} \qquad (3.4.26)$$

To correct for this behavior the data point at 0 V needs to be multiplied with the following correction factor:

$$f_{c,0\,\text{V}} = \frac{\Gamma_{det2}}{\Gamma_{det1}} = \frac{1}{1 + \frac{(1 - P(1^+))}{(1 - P_{wire})} \cdot \frac{\Gamma_{loss}}{\Gamma_{dec}} \cdot \frac{1}{P_{shake}}}$$

$$= \frac{(0.098 \pm 0.034) \cdot \frac{1}{\text{s}}}{(0.22 \pm 0.04) \cdot \frac{1}{\text{s}}}$$

$$= (0.45 \pm 0.18) \qquad (3.4.27)$$

So we repeat the fit with the scaled value for 0 V and this time we fix $f_{trans} = 0$ since this value was at its lower allowed limit. This corresponds to a transfer time of $t_{trans} = 38\,\mu$s and increases the number of degrees of freedom by one. The fit results are:

$$f_{amp} = (8.97 \pm 1.07) \cdot 10^{-3}$$

$$f_a = (0.45^{+0.48}_{-0.39})$$

$$C_{back} = (56 \pm 22) \qquad (3.4.28)$$

with $\frac{\chi^2}{N_{dof}} = \frac{17.2}{13} = 1.32$, which is just within the $\pm 1\,\sigma$ interval around the expected value of the reduced χ^2 distribution[18]. The resulting value for a (which equals to f_a) is in agreement with the Standard Model value of small a obtained from measured ft values [Sev08]. The reduced χ^2 is by a factor 4.5 smaller than in the first fit. The fit function is shown in fig. 3.29 (top) as well as the residuals (bottom). We see that the data point at 250 V shows the largest residuals, which was only present in the 11:15 measurement. In sec. 3.4.3, like for instance in fig. 3.18 and 3.17, we found that the 11:15 data set is in no good agreement with the other data sets 06:40, 08:45 and 12:25. This can have experimental reasons.

The 1 σ errors for f_a are asymmetric (see eq. 3.4.28). The χ^2 as function of the parameter f_a is shown in fig. 3.30. The 1 σ uncertainties are given by the parameter values for which the χ^2 increases by 1 with respect to its minimum. This value is marked with a dashed black line. The χ^2 function is not a perfect parabola why it intersects the dashed line at different distances from its minimum.

---

[18]The expected value of the reduced χ^2 is 1 and its standard divination is $\sqrt{\frac{2}{N_{dof}}} = \sqrt{\frac{2}{13}} = 0.39$
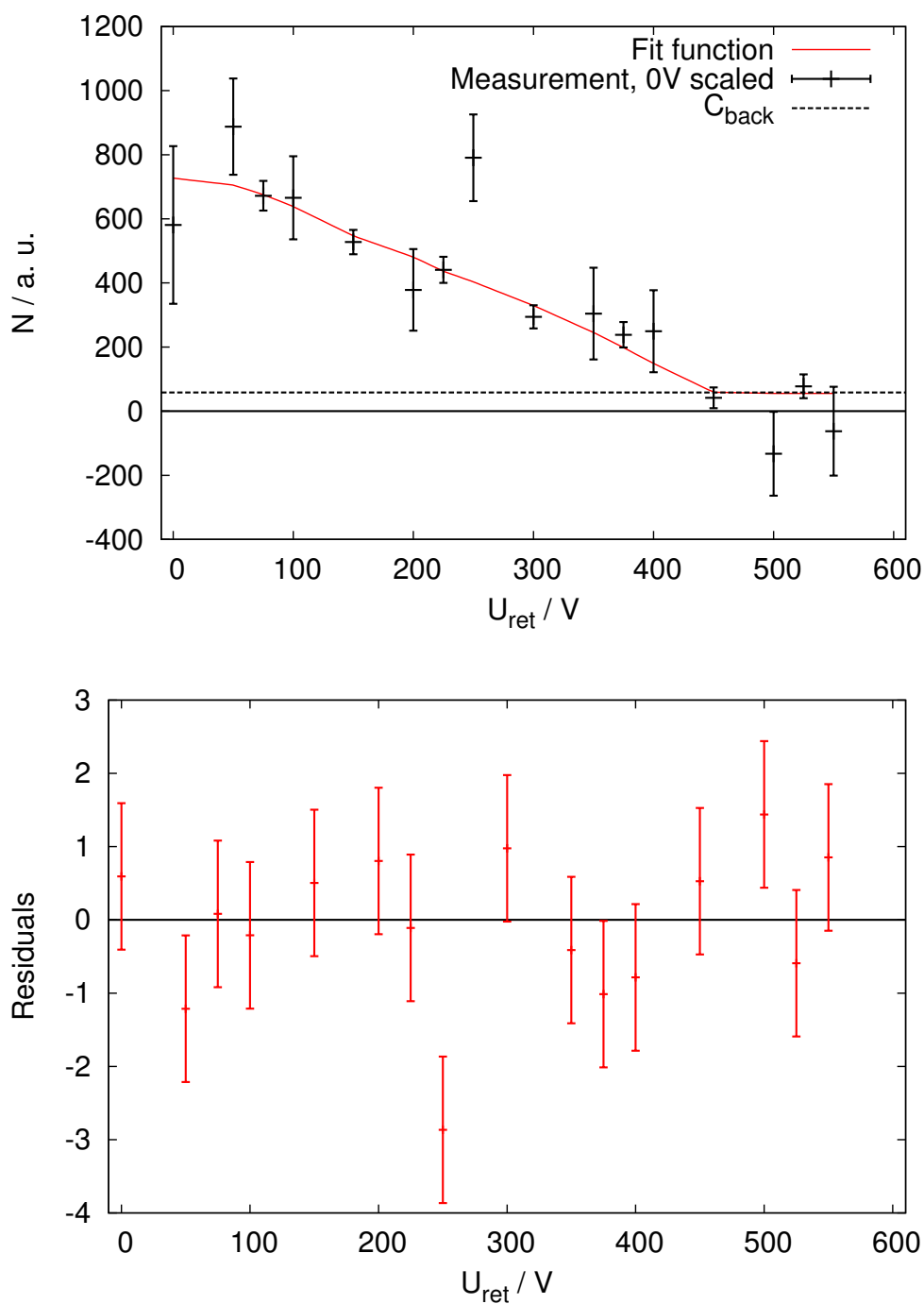
Figure 3.29.: Fit function with data points (on top). For this fit the c_i have been fixed to the measured values. The parameter f_{trans} has been fixed to a value of $t_{trans} = 0$. The data point for 0 V was scaled by the factor $f_{c,\,0\,V} = (0.45 \pm 0.19)$ in this fit. The residuals are shown on the bottom.
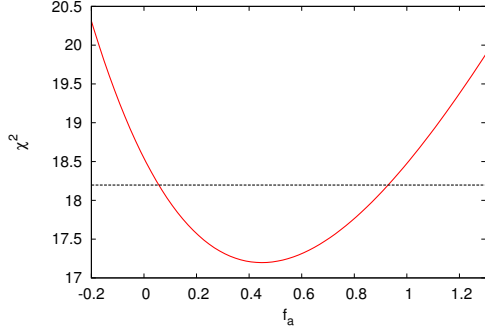
Figure 3.30.: χ^2 as function of the parameter f_a. The $1\,\sigma$ errors for f_a are asymmetric (see eq. 3.4.28). The $1\,\sigma$ uncertainties are given by the parameter values for which the χ^2 increases by 1 with respect to its minimum. This value is marked with a dashed black line. The χ^2 function is not a perfect parabola why it intersects the dashed line at different distances from its minimum.

Finally we repeat the fit without including the 0 V data point to see whether our explanation is accurate and the results consistent. Due to its large uncertainties we don't expect to see a significant difference as the 0 V data point only has a small weight for the fit. If we limit the data points for the fit to $[50\,\mathrm{V}, 550\,\mathrm{V}]$ and repeat the fit we receive the following results:

$$
\begin{aligned}
f_{amp} &= (9.14 \pm 1.10) \cdot 10^{-3} \\
f_a &= (0.39 \pm 0.43) \\
C_{back} &= (56 \pm 23) \quad\quad (3.4.29)
\end{aligned}
$$

with $\frac{\chi^2}{N_{dof}} = \frac{16.8}{12} = 1.4$ with symmetrical errors for f_a this time. This is almost identical to the result before. In fig. 3.31 the resulting fit function (blue curve) together with the fit function which included the 0 V data point (red curve) are shown at the top. Both curves are overlapping almost entirely. On the bottom the residuals of the fit are shown.

3.4.4.4. Estimation of the number of ions in the decay trap

An interesting value is the number of ions that was stored in the defy trap during the October beam time in 2011. This will be a valuable input for Penning trap simulation such as carried out in ref. [Gor12]. The number of ions in the decay trap N_{dt} can be estimated, starting with this equation:

$$
\frac{dN_{MCP}}{dt} = \epsilon_\Omega \cdot \epsilon_{trans} \cdot \epsilon_{tot} \cdot \Gamma_s \cdot N_{dt} \cdot P_{shake} \cdot (1 - P_{wire}) \quad\quad (3.4.30)
$$

with

- $\epsilon_\Omega = 0.5$: The solid angle of the source. The source is designed to have 2π acceptance. The recoil ions that are emitted downwards are lost [Bec11]. They either hit the differential pumping diaphragm or fly through the cooler trap backwards into the vertical beam line where they are lost.

- $\epsilon_{trans} = (0.81 \pm 0.02)$: The transport efficiency from the source through the spectrometer to the detector. This is estimated from the ratio of simulated detected ions to all simulated ions at 0 V. For this we have four simulated values each one for $t_{trans} = 31.5\,\mu s$ and $a = 0$, $t_{trans} = 31.5\,\mu s$ and $a = 1$, $t_{trans} = 38\,\mu s$ and $a = 0$ and $t_{trans} = 38\,\mu s$ and $a = 1$, which are 0.818, 0.844, 0.769 and 0.805. From these we calculate the mean value and the variance.

- $\epsilon_{tot} = (0.30 \pm 0.08)$: The absolute detection efficiency of the MCP detector, which we determined in eq. 2.3.29 from a calibration measurement right before the run.

- $\Gamma_s = \frac{1}{\tau_1} = \frac{1}{(1.88 \pm 0.07)\,\mathrm{s}} = (0.53 \pm 0.02)\,\frac{1}{\mathrm{s}}$ [19]: The decay constant from the decay trap signal (see tab. C.5).

- $P_{shake} = (0.28 \pm 0.10)$ is the probability for the ^{35}Cl daughter atoms to undergo electron shake-off after the beta decay of ^{35}Ar [Gor12].

---

[19]The uncertainty of this value has been enlarged by the factor $\sqrt{\chi^2/N_{dof}}$
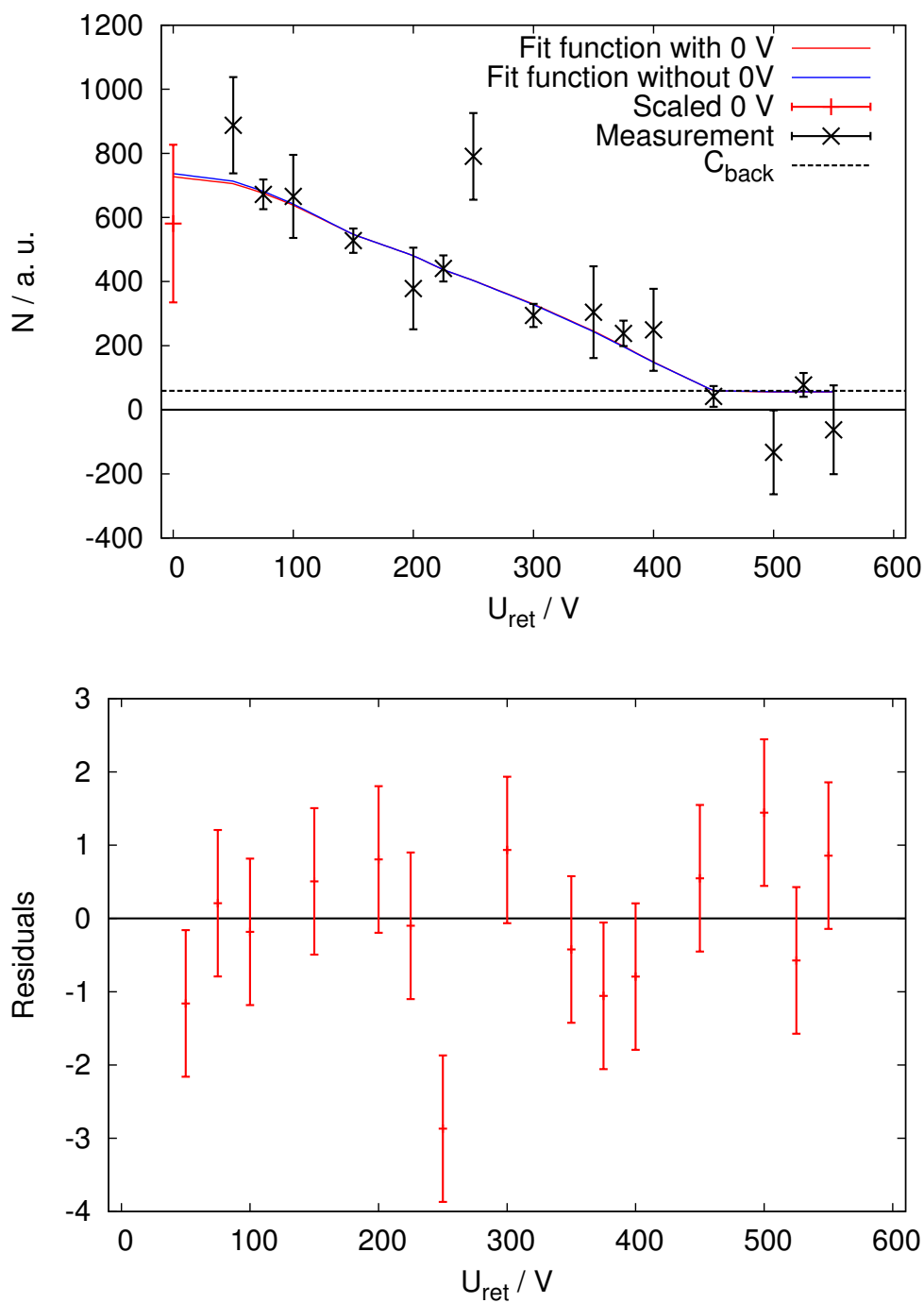
Figure 3.31.: Fit functions with data points (top). The resulting fit function (blue curve) is shown together with the fit function which included the 0 V data point (red curve). The red curve is covered almost entirely by the blue one. The residuals are shown at the bottom.

- $\frac{dN_{MCP}}{dt} = \frac{A_0 \cdot A_k}{\delta t \cdot N_k} \cdot f_{c,0V}$: Where $A_0 = (1.29 \pm 0.07) \cdot 10^3$ is the fitted count rate at 0 V from the combined fit (see tab. C.5), A_k the relative amplitudes for each data set $A_{0640} = 1$ was fixed in the fit, the others were $A_{0845} = (0.55 \pm 0.03)$, $A_{1115} = (0.19 \pm 0.01)$ and $A_{1225} = (0.32 \pm 0.02)$ (see also tab. C.5)[20] and N_k the number of measurements in each data set. These are according to tab. 3.3: $N_{0640} = 999$, $N_{0845} = 999$, $N_{1115} = 499$ and $N_{1225} = 526$. $\delta t = 0.025$ s is the bin size of the histogram which was used for the combined fit. $f_{c,0V} = (0.49 \pm 0.11)$ is the scaling factor for the data point at 0 V retardation potential which takes into account the losses from the decay trap which we see at this retardation voltage (see eq. 3.4.27). With these value we get:

$$
\begin{aligned}
\left(\frac{dN_{MCP}}{dt}\right)_{0640} &= (25.3 \pm 5.8)\frac{1}{\text{s}} \\
\left(\frac{dN_{MCP}}{dt}\right)_{0845} &= (13.9 \pm 3.3)\frac{1}{\text{s}} \\
\left(\frac{dN_{MCP}}{dt}\right)_{1115} &= (9.6 \pm 2.3)\frac{1}{\text{s}} \\
\left(\frac{dN_{MCP}}{dt}\right)_{1225} &= (15.4 \pm 3.6)\frac{1}{\text{s}}
\end{aligned}
\tag{3.4.31}
$$

- $(1 - P_{wire}) = (0.88 \pm 0.01)$, as it has been calculated in eq. 3.4.23.

With these values we can calculate the number of ^{35}Ar ions per trap load in the decay trap by solving eq. 3.4.30 for N_{dt}. This results in:

$$
\begin{aligned}
N_{dt,\,06:40} &= (1590 \pm 800) \\
N_{dt,\,08:45} &= (880 \pm 450) \\
N_{dt,\,11:15} &= (600 \pm 310) \\
N_{dt,\,12:25} &= (970 \pm 490)
\end{aligned}
\tag{3.4.32}
$$

We see that the errors on these values are huge. Within the uncertainties the four different values are in agreement with one another. This is about two orders of magnitude less than what was given in ref. [Bec11] and a factor 2–4 less than what was given in ref. [Gor12]. The value in ref. [Bec11] was determined under totally different conditions from a measurement with ^{122}In ions. The reason for the difference compared to the value from ref. [Gor12], could be that the target has been reused (both measurements used the same target and it was also used for a measurement in 2009).

3.4.4.5. Discussion of the least square fit of the recoil spectrum

With the fit of the recoil spectrum we saw that it was necessary to make certain assumptions to finally get a reasonable result. In particular we have to rely on the measured charge state distribution [Gor12] as well as the tracking simulations. We scaled down the value for $U_{ret} = 0$ V for the reason that its excess is probably caused by low energetic loss ions that escape the decay trap and and only contribute to the count rate at 0 V (see below).The fit revealed two crucial problems:

- **The excess rate at $U_{ret} = 0\,\text{V}$:** This could be explained by the rate of lost ions from the decay trap. This shows the importance of a proper lifetime fit of the signal from the decay trap. This effect could be reduced by the feed of a retardation potential reasonably above the end cap potential of the decay trap.

---

[20]The uncertainties of these values has been enlarged by the factor $\sqrt{\chi^2/N_{dof}}$

- **The unintentional Penning trap between the decay trap and the main retardation electrode in the spectrometer**: Stored particles in this trap could spoil the content of the first time bins after the retardation voltage has been lowered from a higher to 0 V potential. To avoid this Penning trap, a potential equal or above the end cap potential of the decay trap needs to be applied to the first retardation electrode SPRETA01. The following electrodes should successively increase the retardation potential. As a consequence a measurement at 0 V retardation potential is not possible with the current setup.

The resulting value for a can be derived by directly translate the parameter f_a into a value for a:

$$a = f_a = (0.45^{+0.48}_{-0.39}) \tag{3.4.33}$$

This value is in agreement with the value calculated from measured ft values [Sev08] within its uncertainties. The uncertainties of this value are purely statistical.

The estimated number of ions is significantly lower than what was calculated in former runs. Compared to the result from the analysis of the June 2011 data [Gor12], it is about 3–6 times less. In the analysis of the run from 2009 with ^{122}In the calculated ion number was about 2–3 orders of magnitude higher [Bec11]. However, the experimental conditions were different in all three measurements. An explanation for this could be the *worn out* target which was used in two former measurements.

3.5. Systematic effects

For our experiment systematic effects are all energy respectively retardation potential dependent effects that show up in the measurement of the recoil energy spectrum. The simulation tool SimWITCH was used to investigate two important systematic effects of the measurement. These are namely the effect of the ion motion in the decay trap and decay trap potential, as well as the anti-ionization wire in the analysis plane. The effect of the ion motion in the decay trap and decay trap potential, cannot be analyzed separately, since both are coupled, why we discuss them in one subchapter. A discussion of other systematic effects can be found in ref. [Tan11a].

3.5.1. The effect of the ion motion in the decay trap and the decay trap potential

As described the in sec. 3.4.4.1, due to the thermal motion in the decay trap the ions can gain a significant amount of energy which leads to a broadening of the measured recoil spectrum. This could result for the current configuration of the trapping potential, in combination with a detuned transfer time, to a shift of the spectrum's endpoint by about 100 V (see eq. 3.4.14 and its explanation). This is the result of the ion motion in axial direction (in the following we refer to this as the z direction), which they gain from the transfer from the cooler trap [Gor12]. The equation of motion for the z-component for an ion in an ideal Penning trap[21] can be written as [Bro86]:

$$\ddot{z} + \omega_z^2 \cdot z = 0 \quad \text{with} \quad \omega_z = \sqrt{\frac{q \cdot U_0}{m \cdot d^2}} \tag{3.5.1}$$

with $d^2 = \frac{1}{2}(z_0^2 + \frac{\rho_0^2}{2})$ a characteristic geometry parameter, q the charge of the ion, U_0 the potential difference between the central ring electrode and the end cap electrodes, z_0 half the distance between the lower and the upper end cap electrode and ρ_0 the inner radius of the ring electrode. This is the equation of motion of an harmonic oscillator.

The amplitude of this motion is determined by two factors: The transfer time t_{trans} and the depth of the decay trap potential. The maximum energy gain appears to recoil ions which are emitted in the center of the decay trap. This is where the initial kinetic energy of the ions is the highest and in case the momentum vector resulting from the recoil of the ions is parallel to the momentum vector of the axial motion, the total energy can be calculated according to eq. 3.4.14. If the ion decays on an outer position in the decay trap, close to where the electric potential is maximal, the initial kinetic energy of the ions is close to 0. In this case the energy gain is practically identical to the value of the electric potential $U_{trap, end \ cap}$ times the charge of the ions q:

$$\Delta E_{kin, end} = U_{trap, end \ cap} \cdot q \tag{3.5.2}$$

For instance, for a singly charged ion and an end cap potential like it was applied during the October beam time in 2011, which was 4.6 V, the energy gain would be 4.6 eV. These results apply to a transfer time of $t_{trans} = 31.5 \, \mu$s (referred to in ref. [Gor12] as *exp. settings*). What was in ref. [Gor12] referred to as *optimal settings*, respectively $t_{trans} = 38 \, \mu$s, would result in an energy gain that is in fact smaller. In this case the velocity component in axial direction had a value of about $v_z \approx 420$ m/s. This corresponds to a initial kinetic energy of $E_{kin} = 0.032$ eV. According to eq. 3.4.14 we can estimate the maximum energy gain to:

$$\Delta E_{kin, cent} = 2 \cdot \sqrt{E_{rec}} \cdot \sqrt{E_{kin}} + E_{kin} = 7.6 \, \text{eV} \tag{3.5.3}$$

---

[21]An ideal Penning trap has hyperbolically shaped electrodes. Cylindrical Penning traps (like the ones used in WITCH) have additional correction electrodes to correct the deviations from the ideal Penning trap. The advantage of cylindrical Penning traps is that they are easier to fill and empty.

This is about an order of magnitude smaller than the energy gain in eq. (3.4.14). Furthermore we find that the ions are spatially more confined. Here the spatial spread σ_z is 0.4 cm instead of 2.8 cm [Gor12]. This results in a smaller energy gain at the endpoint of the motion. 4 mm in axial direction away from the center, the potential is about 0.03 V higher than in the center, why the potential energy gain for a singly charged ion at this position would be 0.03 eV, which is negligible.
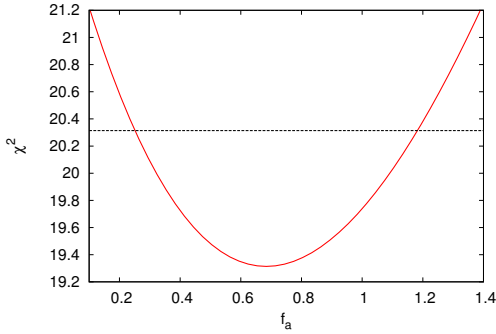

Figure 3.32.: χ^2 as function of the parameter f_a. The 1 σ errors for f_a are asymmetric (see eq. 3.4.28). The 1 σ uncertainties are given by the parameter values for which the χ^2 increases by 1 with respect to its minimum. This value is marked with a dashed black line. The χ^2 function is not a perfect parabola why it intersects the dashed line at different distances from its minimum.

To recapitulate the fit result from the last section: We received a value of $f_a = (0.45^{+0.48}_{-0.39})$ if we fix the parameter f_{trans} to 0 (see eq. 3.4.28). The uncertainty arising from the not precisely known ion distribution in the measurement from the October beam time in 2011 can be estimated by repeating the fit for $f_{trans} = 1$ fixed, which corresponds to $t_{trans} = 31.5\,\mu$s. This results in:

$$
\begin{aligned}
f_{amp} &= (8.11 \pm 0.77) \cdot 10^{-3} \\
f_{a,\,source} &= (0.68^{+0.50}_{-0.43}) \\
C_{back} &= (38 \pm 25)
\end{aligned}
\tag{3.5.4}
$$

with $\frac{\chi^2}{N_{dof}} = \frac{19.3}{13} = 1.48$. In fig 3.33 (top) the resulting fit function with the data points and the residuals (bottom) are shown. The value with the largest deviation is the data point at 250 V. Again the parameter errors are asymmetric, which can be seen from the χ^2 as function of the parameter f_a, which is shown in fig. 3.32. The value of a differs by about:

$$
\Delta a_{source} = |f_a - f_{a,\,source}| = 0.23
\tag{3.5.5}
$$

This is a relative uncertainty of about $\frac{\Delta a}{a} = \frac{0.23}{0.45} = 51\%$. So it is essential to reduce this effect further. Steps towards this could be:

- To successively reduce the potential depth of the decay trap. This is usually limited by experimental conditions.

- Further Penning trap simulations to describe the conditions in the decay Penning trap of our system more precisely are necessary. The effort to simulate the ion cloud evolution in the double Penning trap system of the WITCH experiment, by applying a computer code developed to simulate astrophysical many-body systems improved our understanding of the problem far-ranging but it is still in its initial stage and further investigations should follow.

- The precise determination of the residual gas components in the Penning traps is essential to study the ion cloud behavior in both traps with simulations. Therefore the implementation and test of the scattering on residual gas should be implemented in the tracking simulation routine of SimWITCH.

- Experimental determination of the ion cloud properties by measuring the total and the longitudinal energy distribution of the ion cloud in the decay trap. In combination with tracking simulations a determination of the radial extend of the ion cloud could be performed analogously to the procedure described in ref. [Mad10].
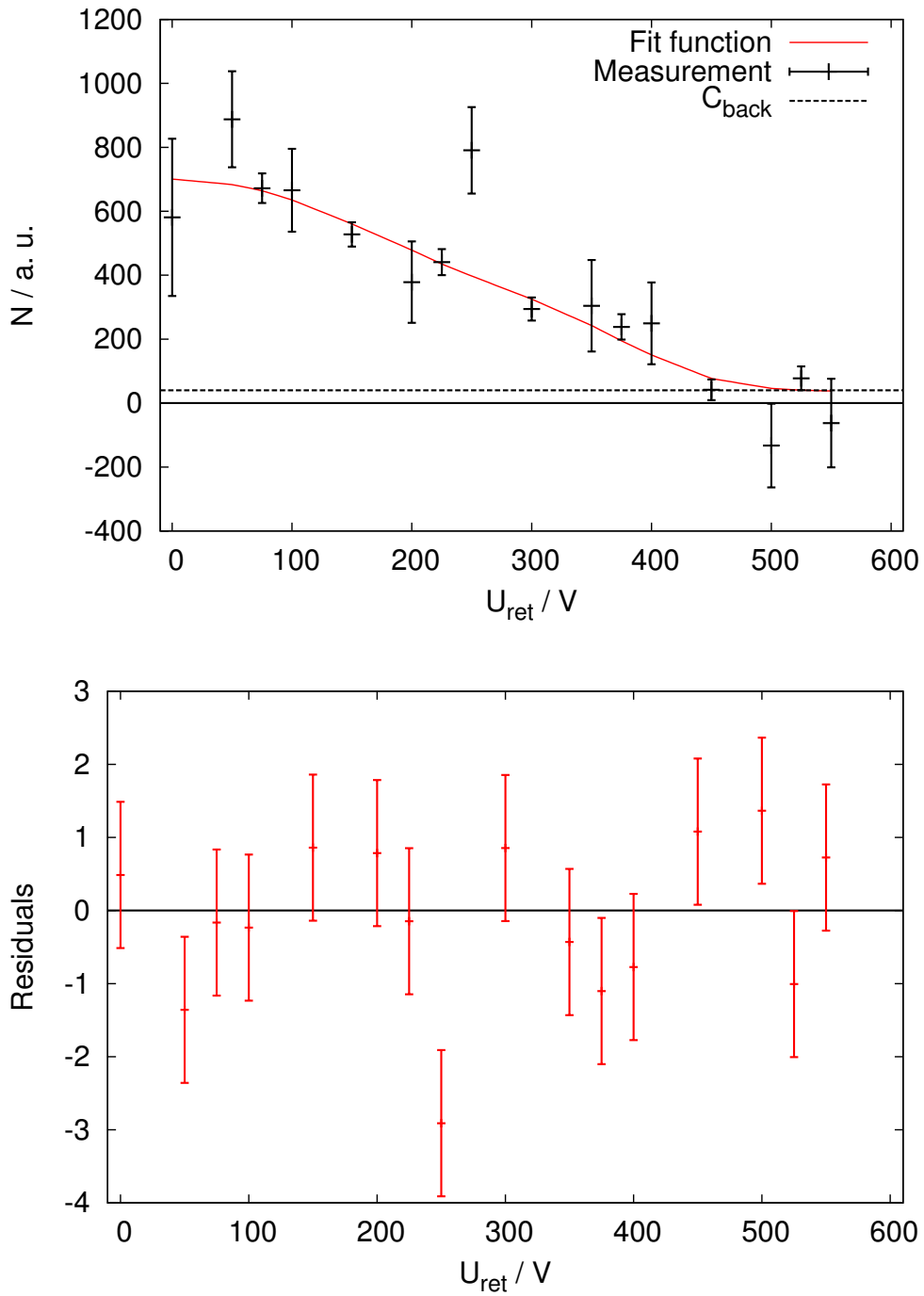
Figure 3.33.: Fit function with data points (top). The c_i have been fixed to the measured values. The parameter $f_{trans} = 1$ was fixed. The data point for 0 V was scaled by the factor $f_{c,0\,V}$. The residuals are shown at the bottom.

3.5.2. The anti-ionization wire in the analysis plane

If a retardation potential above the end cap potential of the decay trap is applied to the spectrometer, due to the more negative potential of the decay trap end cap and the post-acceleration and focussing electrodes a local potential maximum is created. This is shown in fig. 3.34 for a retardation potential of $U_{ret} = 150$ V. The magnetic field lines in this region are almost parallel to the symmetry axis (also labeled as z-axis) of the spectrum meter (see fig. 3.8).
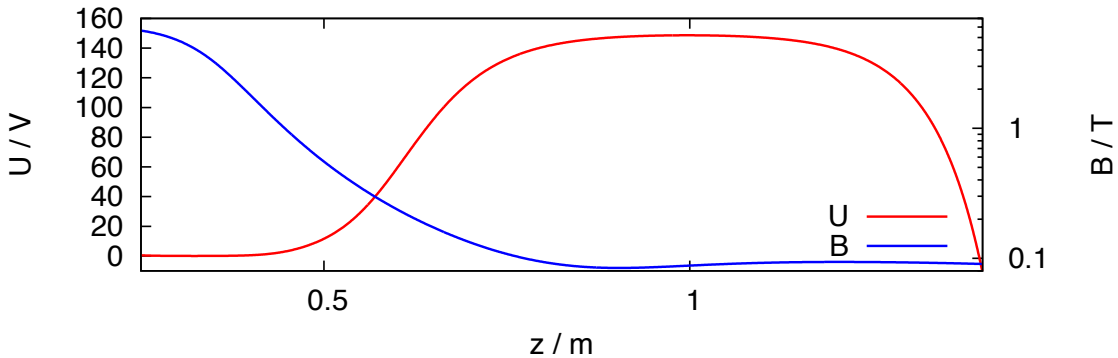
Figure 3.34.: The simulated electric potential and magnetic field along the symmetry axis of the spectrometer from the end of the decay trap to the beginning of the post-acceleration and focussing section for a retardation potential of $U_{ret} = 150$ V.

All together this forms an avoidable Penning trap for electrons, which lead in bygone measurements to a retardation voltage dependent background [Tan11a]. This itself is a serious systematic effect which has to be avoided by any means. Since the magnetic filed in this part of the setup can't be changed, a solution similar to the compensation magnet (see sec. 3.3.2.2) is beyond question. A similar problem in the KATRIN experiment is solved by installing a movable wire scanner, that absorbs the stored particles when it is inserted [Val09, Bec10]. In analogy to this, in the WITCH experiment, a stationary wire was installed right behind the analysis plane, which is meant to empty this Penning trap by absorbing the stored electrons.

The first version of the wire was installed in May 2010 by attaching a solid copper wire with 1.8 mm diameter to the last retardation electrode SPRETA07[22]. This wire hang loose from the top into the spectrometer close to the analysis plane. The distance from the bottom of SPRETA07 to the wire was measured as 58.2 cm on one side and 58.5 cm on the other side. The length was measured as 26.0 cm. In Fig. 3.35(a) the attachment of the wire to SPRETA07 is shown. Fig 3.35(b) shows a view from the top of the spectrometer on the wire.

This first solution showed the correct operation of the wire, that eliminated the retardation dependent background. The problem of this tentative solution was that its positions was not well defined as one could see with the naked eye that the wire off-center by several centimeters (see fig. 3.35(b)). This lead to an improved solution in which the wire is attached to a rigid frame consisting of two metal rods. The anti-ionization wire itself now consist of a 2 mm diameter stainless steel rod located at $z = 0.946$ m (with respect to the center of the trap magnet). The length of the wire is defined by the distance between the two rods which is 328 mm. Pictures of the final version of the anti-ionization wire are shown in fig. 3.36.

---

[22]see fig. 1.6 for electrode labeling
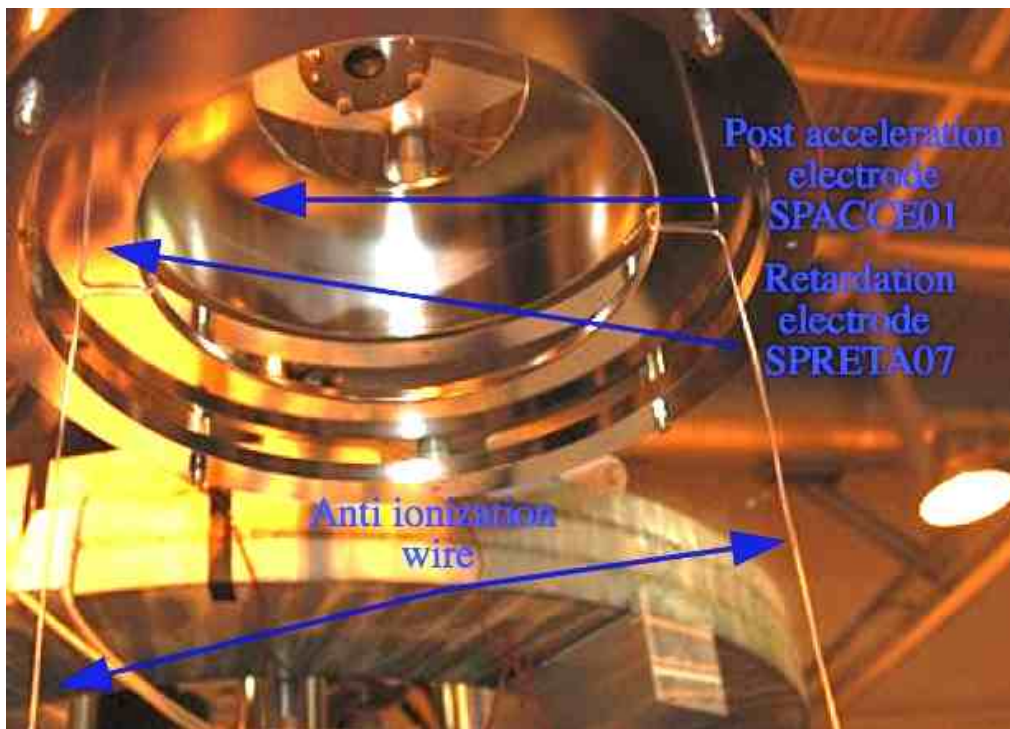
(a) Attachment of the anti-ionization wire to the retardation electrode SPRETA07.
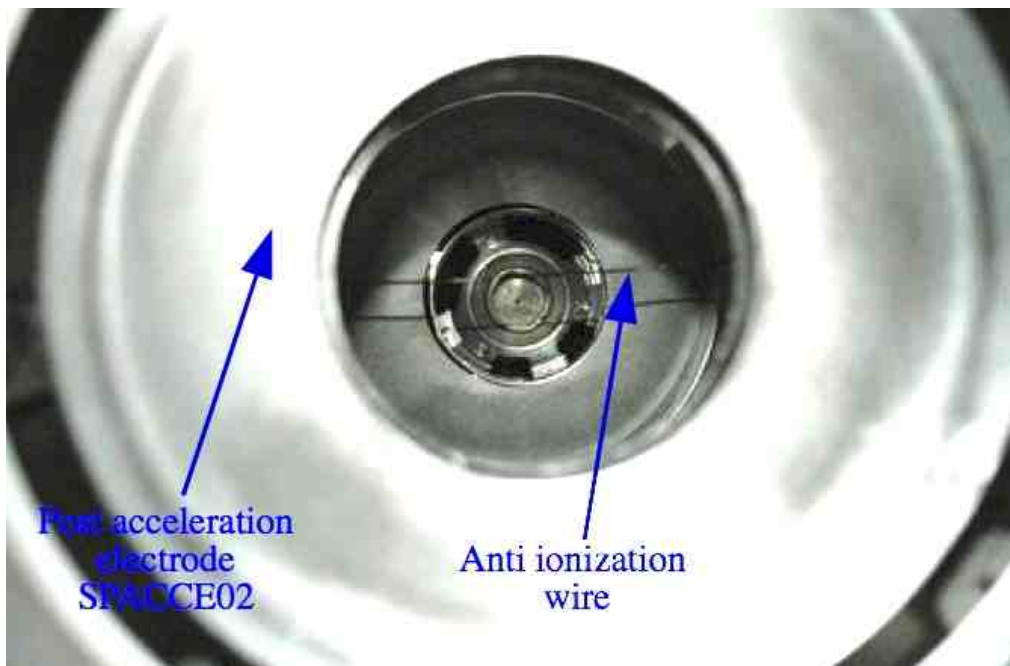
(b) The anti-ionization wire installed in the spectrometer viewed from the top of the cryostat.

Figure 3.35.: (a) A solid stainless steel rod of 2.0 mm diameter hold between two mooting legs which are attached to the retardation electrode SPRETA07 works as an anti-ionization wire in the analysis plane. (b)The final version of the anti-ionization wire mounted between the two mounting legs. Above the two post-acceleration electrodes SPACCE02 and SPACCE01 and the seventh retardation electrode are shown.

(a)   (b)
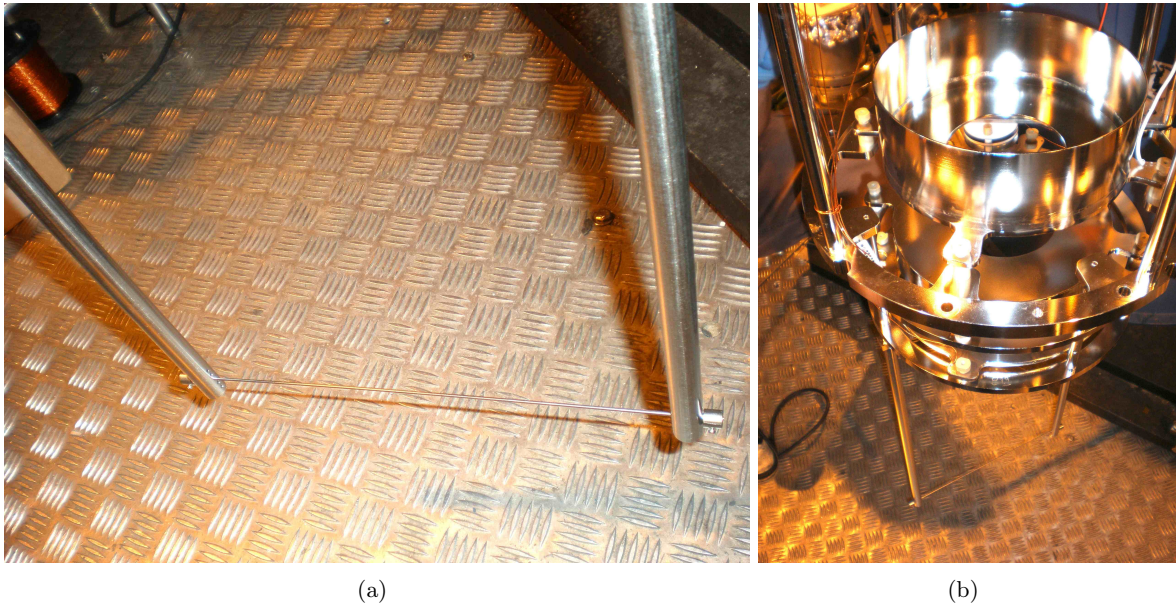
Figure 3.36.: Final solution of the anti-ionization wire. (a) A solid copper wire with 1.8 mm diameter attached to the retardation electrode SPRETA07 works as an anti-ionization wire in the analysis plane. (b) The wire in the spectrometer viewed from the top.
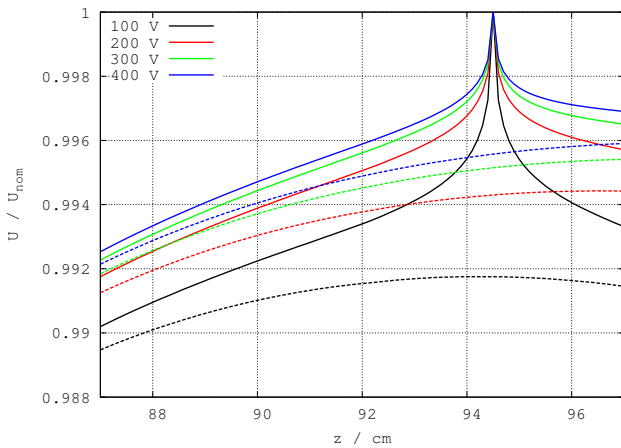
Figure 3.37.: The electric potential U along the z-axis near the analysis plane normalized to its maximum value (U_{nom}) for values of 100 V, 200 V, 300 V and 400 V for U_{nom} from bottom to top.

Since the simulation routine for the calculation of electric fields in the setup is not capable of calculating electric fields of three-dimensional electrode geometries, we use another routine, from the same author, which is called `elcd_3_3`[23][Glu13]. Figure 3.38 shows calculations of the electric potential at the place of the wire for various retardation potential values of (100V, 200 V, 300 V and 400 V). The ripples in the potential close to the edge are caused by the discretization of the geometry. We can see that the difference in the potential between both situations with (left) and without (right)) ranges from less then 1 V to approx. 2 V in the center off center are reduces by a factor of ter. With the wire, the deviations in the electric potential off center are reduces by a factor of roughly 0.5. Also this will also be an advantage.

In fig. 3.37 the ratio of simulated electric potential to the nominal potential along the symmetry axis of the spectrometer in the region of the analysis plane is shown. One can see that with the anti-ionization wire the local maximum of the electric potential is at a well defined position. In the most extreme case of the maximum retardation potential, the difference between simulated potential with anti-ionization wire and without anti-ionization wire, the potentials differ by about 1%. This

---

[23]the routine used in SimWITCH is `elcd2`

194
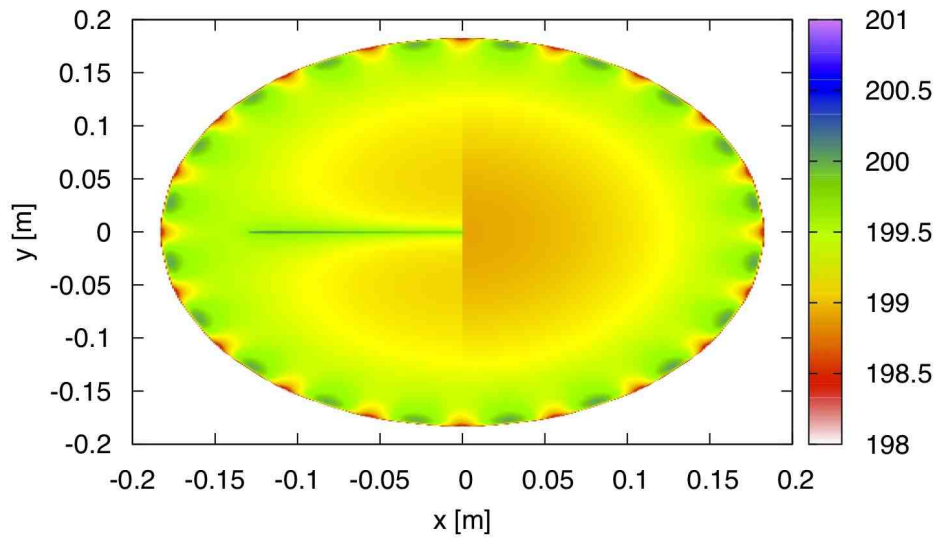
(a) $U_{ret} = 200$ V
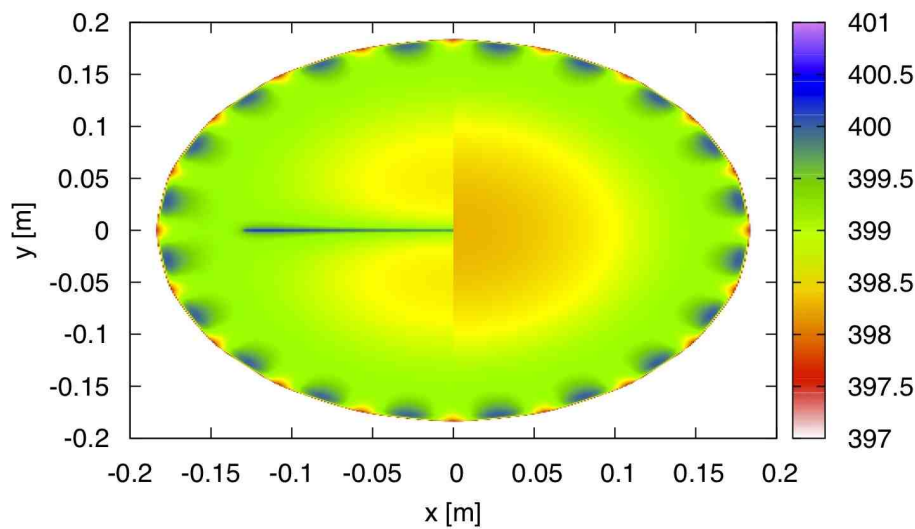
(b) $U_{ret} = 400$ V

Figure 3.38.: The electric potential in the analysis plane with wire (left) and without (right) for 100 V (top) and 200 V (bottom) retardation voltage.

difference is not taken into account by the tracking simulations.

To simulate the effect of the wire on the transmission of the ions, a stopping condition for the particle tracking has been included in the source code. The tracking stops if the following condition, included like this in the source code, is fulfilled:

```
sqrt((x[3]-0.946)*(x[3]-0.946)+x[2]*x[2])<0.001 && sqrt(x[1]*x[1]) < 0.164
```

where `x[1]`,`x[2]` and `x[3]` correspond to the x, y, and z components of the particle position in the tracking routine, 0.946 is the z position of the center of the wire in m, 0.001 the radius of the wire in m and 0.164 is half the length of the wire in m. So the wire engages a cylindrical volume of 328 mm length and 2 mm diameter aligned in direction of the x-axis. Fig. 3.39 shows a few exemplary

ion tracks that collide with the wire (red) and some which fly by (blue).
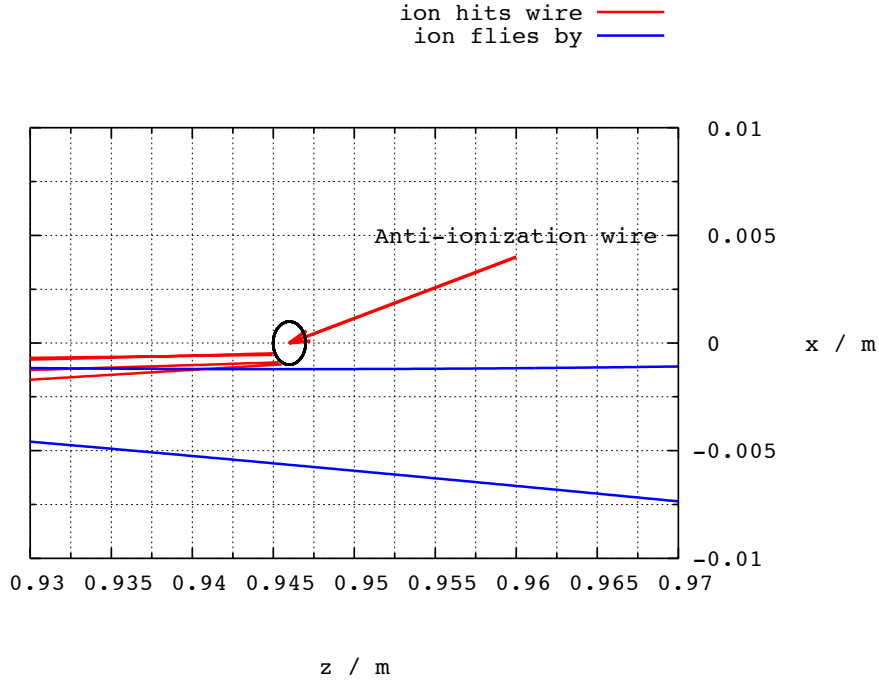
Figure 3.39.: Some exemplary tracks of simulated singly charged ^{35}Cl ions in the spectrometer around the region of the anti-ionization wire. The z- and x-axises are zoomed in so far that no parts of the geometry are in the plotted region anymore. The tracks shown in red are of ions that pass the volume of the anti-ionization wire, track in blue are of ions that fly by.

Fig. 3.40 shows the number of ions absorbed by the anti-ionization wire as function of the applied retardation potential U_{ret} for $t_{trans} = 31.5\,\mu$s (left) and $t_{trans} = 38\,\mu$s (right). The dashed lines correspond to $a = 0$, the solid lines to $a = 1$. Red corresponds to the 1^+ charge state, blue to 2^+, grey to 3^+ and black to 4^+. Each simulation was performed for $N = 100000$ initial events. We see that the amount of absorbed ions strongly depends on the charge of the ions and is rising with higher charge states. This ratio can be about four times higher for the 4^+ charge state compared to the 1^+ charge state at 0 V retardation potential. The amount of absorbed ions drops with higher retardation potentials. This is not unexpected: In fig. 3.13 we see that most of the ions are reflected at $0.5 < z < 0.9$, so the axial position of reflections is actually before the axial position of the wire. This means the anti-ionization wire absorbs ions which would be transmitted if the anti-ionization wire would not be present in the setup.

In fig. 3.41, the ratio of ions absorbed by the anti-ionization wire to detected ions, as function of the applied retardation potential U_{ret}, for $a = 0$ (left) and $a = 1$ (right), is shown. The dashed lines correspond to $t_{trans} = 31.5\,\mu$s, the solid lines to $t_{trans} = 38\,\mu$s. Red corresponds to the 1^+ charge state, blue to 2^+, grey to 3^+ and black to 4^+. We see that this ratio accounts for about 8% for the 1^+ charge state, about 15% for the 2^+ charge state, about 20% for the 3^+ charge state and about 25% for the 4^+ charge state. So it scales almost linearly with the charge of the recoil ion. Moreover we see that the ratio is almost constant for the 1^+ and 2^+ charge states for different retardation potentials. Only at high retardation potentials we can see a sudden increase. If the ratio of ions absorbed by the anti-ionization wire to detected ions stay constant for different retardation voltages it means that the spectral shape of the measured recoil spectrum is changed only marginally. Both
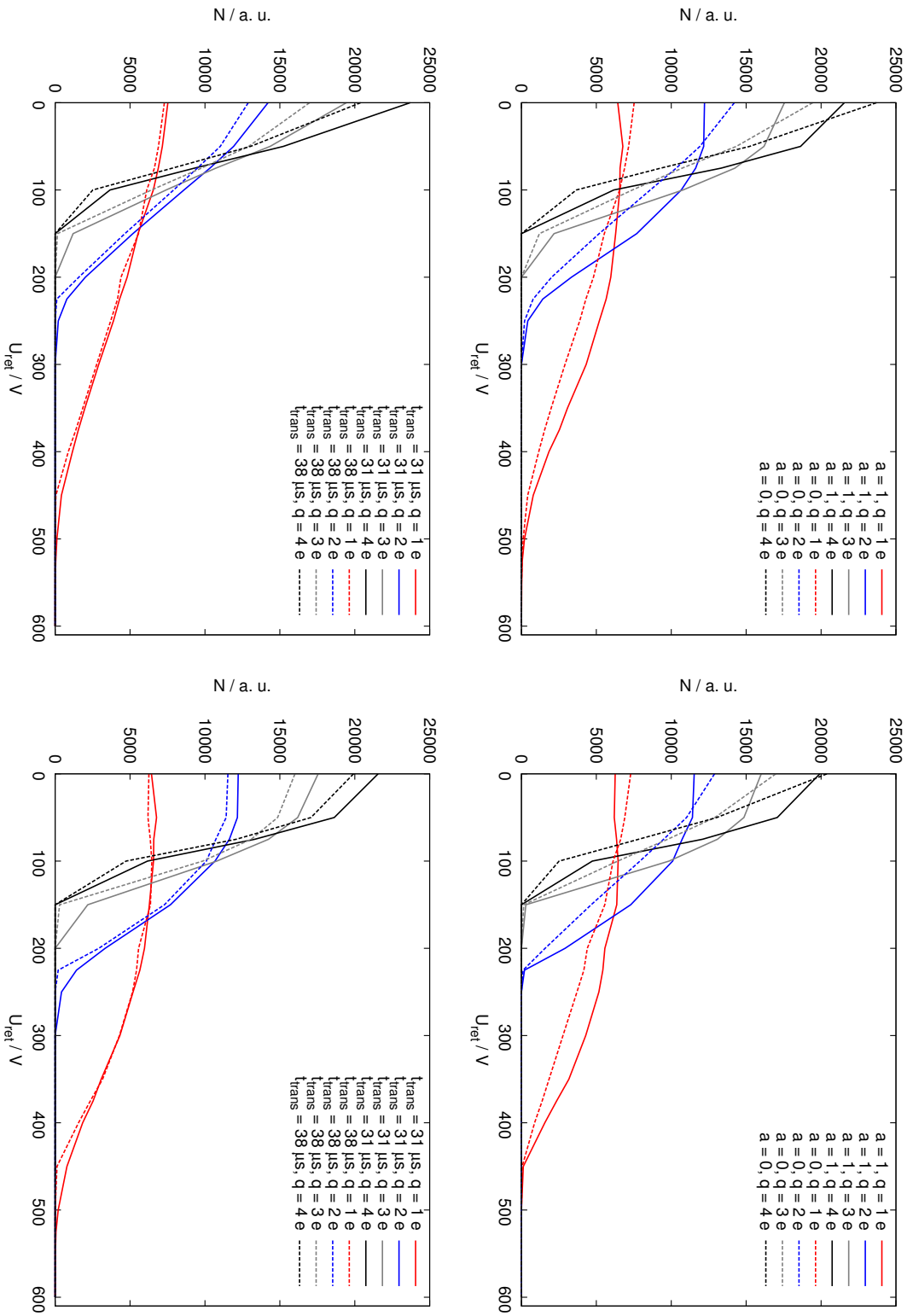
Figure 3.40.: The number of ions absorbed by the anti-ionization wire as function of the applied retardation potential U_{ret} for $t_{trans} = 31.5\,\mu s$ (left) and $t_{trans} = 38\,\mu s$ (right). The dashed lines correspond to $a = 0$, the solid lines to $a = 1$. Red corresponds to the charge state 1^+, blue to 2^+, grey to 3^+ and black to 4^+.
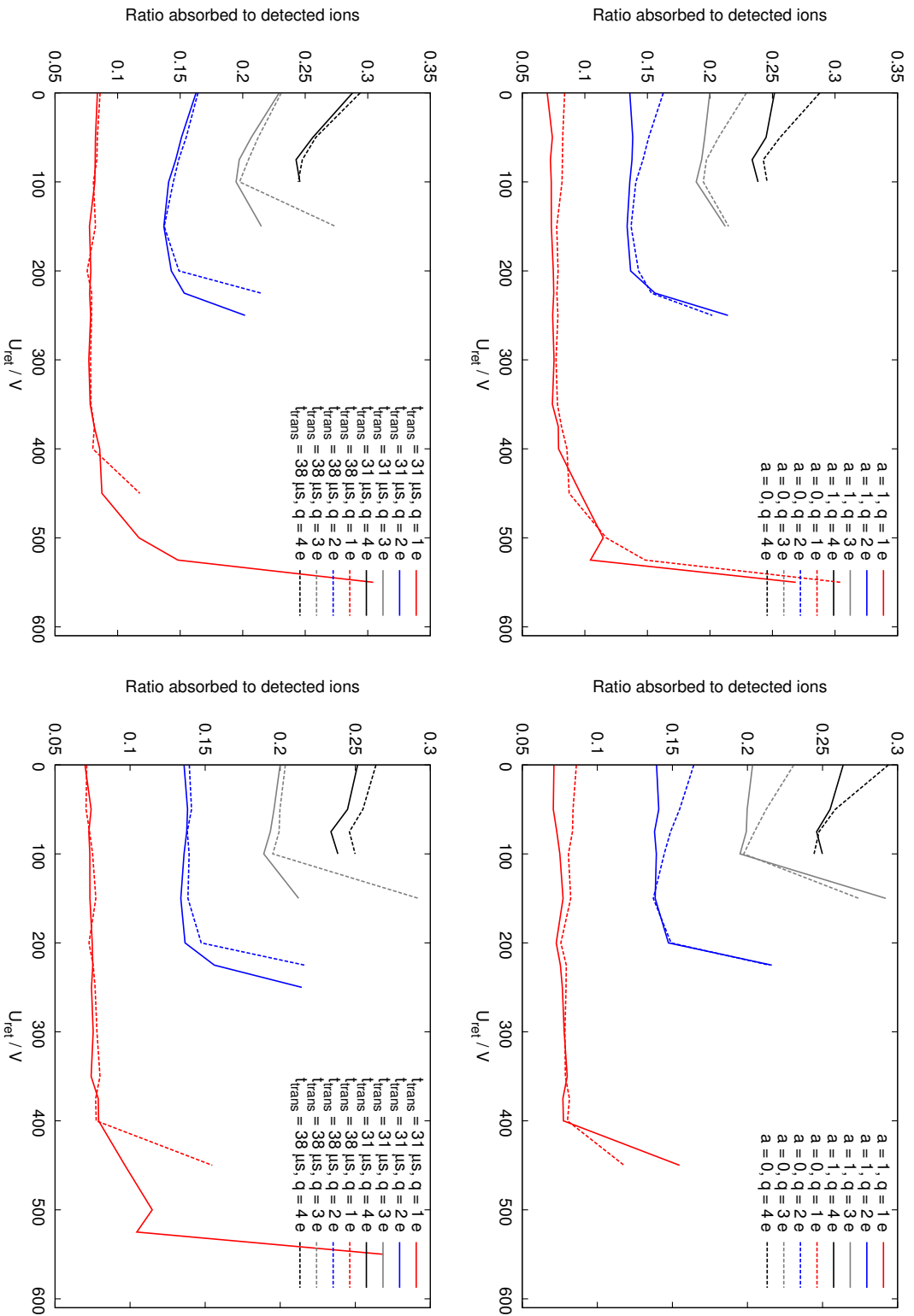
Figure 3.41.: The ratio of ions absorbed by the anti-ionization wire to detected ions as function of the applied retardation potential U_{ret} for $a = 0$ (left) and $a = 1$ (right). The dashed lines correspond to $t_{trans} = 31.5 \, \mu s$, the solid lines to $t_{trans} = 38 \, \mu s$. Red corresponds to the charge state 1^+, blue to 2^+, grey to 3^+ and black to 4^+.

charge states sum up to more than 90% of the recoil ions that undergo electron shake-off after the β decay of ^{35}Ar [Gor12]. For the charge states 3^+ and 4^+, this ratio shows a falling tendency with rising retardation potential U_{ret}. Both charge states 3^+ and 4^+, appear only in the spectrum for retardation potentials $U_{ret} \leq 150$ V. Lets assume the average change in the ratio is about 10%. The relative appearance of the charge states 3^+ and 4^+ sum up to less than 10% [Gor12]. This means the spectral shape will be affected by the presence of the wire by about $10\% \cdot 10\% = 1\%$ between 0 V and 150 V retardation potential.

To estimate the systematic effect of the anti-ionization wire in our measurement we create a new fit function which consists of the number of detected ions plus the ions that were absorbed by the anti-ionization wire instead of the number of detected ions alone. Using this function, we repeat the fit of the recoil spectrum shown in fig. 3.21.

The fit results in:

$$
\begin{aligned}
f_{amp} &= (8.0 \pm 0.9) \cdot 10^{-3} \\
f_{a,wire} &= (0.51^{+0.46}_{-0.38}) \\
C_{back} &= (55 \pm 22) \quad (3.5.6)
\end{aligned}
$$
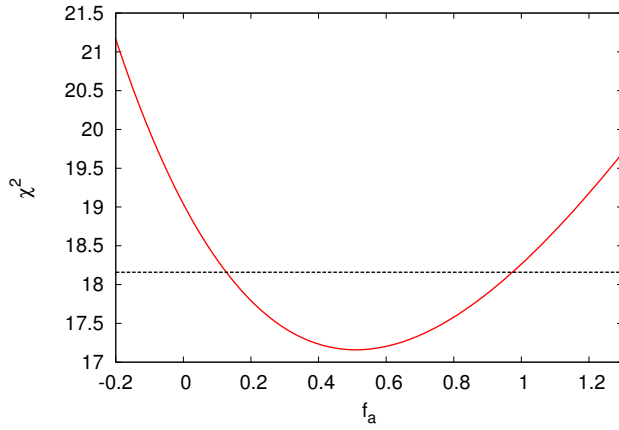
Figure 3.42.: χ^2 as function of the parameter $f_{a,wire}$. The 1σ errors for f_a are asymmetric (see eq. 3.4.28). The 1σ uncertainties are given by the parameter values for which the χ^2 increases by 1 with respect to its minimum. This value is marked with a dashed black line. The χ^2 function is not a perfect parabola why it intersects the dashed line at different distances from its minimum.

with $\frac{\chi^2}{N_{dof}} = \frac{17.2}{13} = 1.32$. In fig 3.43 fit function (top) with the data points and the residuals (bottom) are shown. The value with the largest diviation is again the data point at 250 V. The parameter errors for f_a are again asymmetric (see fig 3.42)

The fit with the original fit function, considering only ions that were detected in the simulations, resulted in $f_a = (0.45^{+0.48}_{-0.39})$ (see eq. 3.4.28). These value of a differs by about:

$$
\Delta a_{wire} = |f_a - f_{a,wire}| = 0.06 \quad (3.5.7)
$$

From this we see that this is also a dominant systematic effect of about $\frac{\Delta a}{a} = \frac{0.06}{0.45} \approx 13\%$. Until now the effect is described by the simulations only partially, by stopping the tracked ions that pass the volume of the anti-ionization wire. The change in the electric potential is at the moment not taken into account in the simulations. This would require a modification of the tracking routine at the cost of computation speed.

Figure 3.43.: Fit function exaggerated by the amount of ions absorbed by the anti-ionization wire with data points (left hand side). For this fit the c_i have been fixed to the measured values. The parameter f_{trans} has been fixed to 0. The data point for 0 V was scaled by the factor $f_{c,0}\,\mathrm{V} = (0.49 \pm 0.19)$ in this fit. The residuals are shown on the right side.

3.6. Summary and conclusion of the data analysis

In this chapter we presented the data analysis of the data obtained from the October beam time in 2011, including a measurement time of about 6 hours of which in the end only about 5 hours have been used to obtain the final result. This analysis provides a correctly averaged recoil spectrum and an extraction of the beta neutrino correlation coefficient a, taking into account several systematic effects of the experiment such as a full description of the source and the spectrometer by using tracking simulations. The main idea of this analysis was not to obtain a competitive value of a. This is not possible due to the lack of statistics and the experimental problems, such as the problems with the proton target and with the WITCH data acquisition system. Our intention was to perform a weak point analysis to optimize the WITCH experiment for a high precision measurement of a by WITCH in the future and to establish a data analysis procedure. This analysis procedure can be divided into three steps:

- **Combined fit of the raw data:** Using factitious time delays, different retardation voltages and data sets are composed to one set of data. This is used to fit all parameters simultaneously to obtain a spectrum of count rate versus retardation potential.

- **Generation of a fit function by using particle tracking simulations:** For each retardation potential that has been applied in the measurement, ^{35}Cl ions with recoil energies drawn from an afore simulated ^{35}Ar recoil spectrum are tracked through the WITCH spectrometer taking into account almost the full systematics of the source and the spectrometer. Repeating each simulation for all charge states from 1^+ up to 4^+ and for values of $a = 0$ and $a = 1$ we compose recoil spectra for all four charge states for $a = 0$ and $a = 1$.

- **Least square fit of the recoil spectrum:** The before compiled fit function is fit to the measured recoil spectrum. Generally speaking it can be possible to to extract a value for a, the charge state distribution of the daughter ions, the signal-to-noise ratio, the lifetime of the signal and the background. To be sure, this necessitates sufficiently good measurement data.

This procedure is not limited to a measurement with a specific isotope (like ^{35}Ar in our case for instance), but can be applied to any kind of recoil spectrum measurement with the WITCH experiment.

The measurement of the November beam time in 2011 showed a systematic effect which is underlying present in the data of the October beam time in 2011, but cannot be seen in the data, which is the following: Contrary to the measurement of the October beam time in 2011, during the November beam time in 2011, the raw data has been recorded with time steps of $\Delta t = 10$ ms instead of $\Delta t = 25$ ms. Fig. 3.44 shows several measurements, obtained in the November beam time in 2011. As one can see the decay curve is superposed by an oscillating signal with a frequency of roughly $\nu \approx 25$ Hz. As the experimental conditions didn't change between the October beam time in 2011 and the November beam time in 2011 this oscillation should have been present in the measurements of the October beam time in 2011 as well, but was probably hidden in the data because of the larger step size of $\Delta t = 25$ ms.

An explanation for this oscillation was found with hindsight. Through a misconstruction in the mounting structure of the double Penning trap system, a crucial component, responsible for highly stacking together the electrodes of the two Penning traps, was loosened in the heating process of the bake-out of the WITCH spectrometer. This resulted in a loosening of the trap electrode stack, followed by a misalignment of the trap system. Since the oscillating frequency in the order of the magnetron frequency of singly charged ^{35}Ar ions, this oscillation is possibly caused by a signal from an ion cloud rotating in an misaligned decay trap. Depending on the position in the decay trap the ions were either able to fully reach the detector or part of it was shielded by the upper trap electrodes [Bre12].
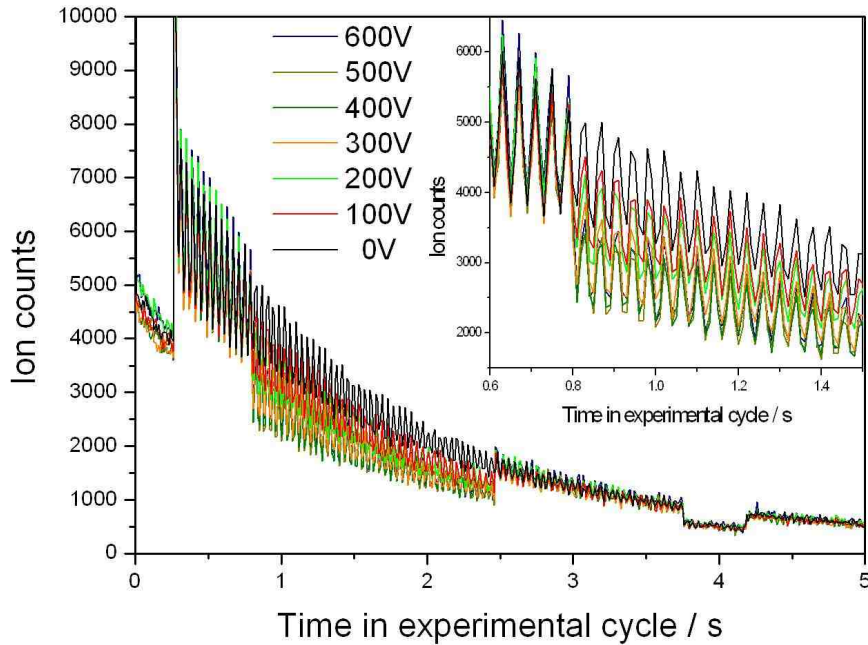
Figure 3.44.: Raw data of several measurements taken during the November beam time in 2011. The artifacts at $t \leq 0.2$ s are caused by the filling of the traps, the preparation of the ion cloud and the transfer from the cooler to the decay trap. The actual measurement starts around 0.2 s. Between 0.8 s and 2.5 s, retardation potentials between 100 V and 600 V have been applied. Between 3.7 s and 4.2 s, $U_{ret} = 600$ V was applied in all measurements. One can observe an oscillating signal with $\nu \approx 25$ Hz. Taken from ref. [Bre11].

Anyway, the problem has been identified and tackled in the preparation for the upcoming measurement [Bre12]. The curial component of the trap mount was redesigned and the bake-out procedure was emulated in a separate test setup which showed no play in the stacking of trap electrodes [Bre12]. The alignment of the trap stack was tested, using the position sensitive MCP detector.

A first analysis of measurements with ^{35}Ar in 2007 and 2009 was shown in ref. [Tan11a], which includes lifetime fits of the decay curve from the decay trap and a roughly extracted retardation spectrum from the measurement in 2009. The data was not used to obtain a value for a or to discuss systematic of that measurement. A first analysis in which an extraction of a a value with the WITCH experiment was presented in ref. [Gor12]. As a part of this analysis Penning trap simulations have been made to determine the ions cloud size properties in the decay trap. These are an important input for the Monte Carlo tracking simulations which are performed with SimWITCH. Since the conditions in the two Penning traps during the October beam time in 2011 were similar to the ones during the June beam time in 2011 we could use these results for our analysis. Anyway, the analysis from ref. [Gor12] did not consider systematic effects or discuss the weak points of the experimental setup.

Since tracking simulations are an essential part of the data analysis procedure, we gave a detailed description of the simulation tool SimWITCH. We also discussed further results that are not directly linked to the data analysis, but important for the characterization of the simulation routine or the experimental setup, in a separate subsection. A limitation of the current SimWITCH routine is its constrain to cylinder symmetric electric and magnetic field geometries. This is a problem in the

correct implementation of the anti-ionization wire. As discussed in sec. 3.5.2 it is an important systematic effect. A possible solution for this problem would be the adoption of the tracking routine KASSIOPEIA which is currently under development for the KATRIN experiment and is capable to simulate tracks of charged particles in fully three-dimensional geometries. The use of this routine will be at the cost of computational speed [Glu12].

Experimental Problems

In addition to the problem with the proton target, the analysis of the data revealed several weak points in this measurement. These will be listed in the following without a particular order:

- **Synchronization:** A proper synchronization of the data acquisition, the trap cycle and the retardation sequence is a must. As it was described in this chapter inaccurate synchronization belittles the confidence of the data and finally results in a reduction of the accumulated data points. It is necessary to test and ensure the proper operation and synchronization of the data acquisition system before upcoming measurements.

- **Measurement of the retardation potential:** The applied retardation potential needs to be measured throughout each measurement. This is the only way to assure the proper operations of the spectrometer. It is essential to rule out malfunctions of the retardation power supply whenever questionable results occur. This also is particularly important to know precisely the rise and fall times when switching the retardation potential.

- **Organization of the stored data:** A good portion of the time spent on the analysis of the data was used to sort and search the relevant information. Different informations - e. g. the information from the slow controls, the configuration of the trap electrode potentials, the timing of the trap cycle, the potentials of the spectrometer, pressures in the beam line system or the acquired data from the two DAQ branches - are stored at different places. This makes the analysis process unnecessarily hard and time consuming.

  It is advantageous if all information, which is related to one measurement is stored at the same place, e. g. a certain subfolder on the DAQ PC. Some of the afore mentioned information is just stored as a setting in the control system software (e. g. the timings and potentials of the trap electrodes) or in the worst case like for the retardation potential as a mere Excel sheet. These crucial informations should be measured rather then to naively trust the correct operation of the corresponding device. In a more advanced state of the experiment the measured informations could be stored in a ROOT TTree, like done at other experiments. This will significantly speed up the analysis process and enhances the durability of the data. It is doubtful that the next generations of collaboration members will be able to find and understand all necessary informations in the data like it is realized currently.

- **Consistency of the DAQ:** The two data acquisition branches used for the recording of this data are inconsistent. As described in sec. 3.2.5 the incredibility of the one branch (the CAMAC system) lead to the decision to discard this data. Things like scalers missing trigger pulses, need to be repaired before the next measurement. Through this circumstance we loose the position information of the detector for our analysis.

- **Dead time measurement:** The before mentioned point brings us to the next one, which is closely connected to it. The dead time of the DAQ system needs to be measured beforehand of a measurement. The random dead time of the CAMAC DAQ, most probably originates from an unsuited LabView code run on a PC with Windows XP as operating system. This

operating system is not suited for fast data acquisitions. Other processes of the running operating system can hinder or slow down the recording the data.

In the recent measurement we assumed that the MCS scaler is dead-time-free. Since the measured rates (see eq. 3.4.31) are below 100 Hz, this assumption should be feasible.

- **Detector calibration:** Although a detector calibration only makes sense with the DAQ ensured to be fully operational, it is important to calibrate the position sensitive MCP detector with ions of comparable mass and energy, like the isotope of interest for the measurement, because the efficiency can depend on the energy and mass of the ion. This point was already mentioned in sec. 2.6.

Many of these have been solved by now. The old DAQ system consisting of a MCS scaler card and a CAMAC system with a multi-channel TDC and scaler has been replaced by system called FASTER with eight channels, four for the delay lines (X1, X2, Y1 and Y2) and one for the main MCP signal (see sec. 2.6 for explanations), one for the REXTRAP trigger, one for to log the retardation voltage and one spare. Each channel is equipped with a CFD, TDC and scaler. The data is stored in ROOT TTrees and an online analysis is possible via a separate PC. The system can handle count rates up to 100 kHz without significant losses and the dead time measurement was determined before the last run. Also a new detector calibration was performed right before the last run.

The measurement cycle

In addition, the analysis laid open multiple shortcomings of the measurement cycle:

- **The 0 V measurement:** As we discussed before a measurement at 0 V retardation potential will be spoiled by the loss ions from the decay trap. Therefore it is not possible to measure at $U_{ret} = 0$ V with the current setup. A retardation voltage slightly above the end cap potential of the decay trap might be suitable instead. If – like in the current measurement – an end cap potential of about 5 V is applied, probably 10 V or 20 V as lowest retardation potential might work. From the fit of the recoil spectrum, obtained from the current data, we know that 50 V did not show an increased count rate.

  The analysis of the November beam time in 2011 data, presented in ref. [Bre11a], could provide a similar spectrum like the one shown in fig. 3.21 but with a larger number of data points, partially measured at different retardation potentials. The spectrum in this reference showed, that most probably a retardation voltage of 10–20 V is sufficient to disable this effect.

- **The retardation sequence:** Potential changes in the retardation sequence should not be made in such fast steps. The power supply needs a certain time to stabilize the applied potential. The data accumulated during this time, cannot be used in the data analysis. When using different retardation sequences, it is important to have several voltages of the same value. This is important for the normalization in the combined fit. Equal potential changes should be in the beginning and at the end of the retardation sequence. The ratio of these can be a measure for the energy distribution of the ions in the decay trap (see sec. 3.6).

- **Avoidance of particle traps in the spectrometer:** The unintentional Penning trap in the spectrometer described and shown in fig. 3.26 must be avoided in future measurements. To do so, it is important that all retardation electrodes and connexions are operational. The first retardation electrode (SPRETA01[24]) should be on the same potential as the end cap electrodes of the decay trap and the following electrodes should successively rais the retardation potential.

---

[24]See fig. 1.6 for electrode labeling.

- **Additional data points:** In the October beam time in 2011, measurements with $\Delta U_{ret} = 75$ V (06:40 and 08:40), $\Delta U_{ret} = 50$ V (11:15) and $\Delta U_{ret} = 150$ V (12:25) were made. To look for systematic effects it is necessary to measure the recoil spectrum with better resolution. We suggest to do two series of measurements each with $\Delta U_{ret} = 20$ V one can e. g. start at $U_{ret} = 50$ V and moving upwards in steps of 20 V until $U_{ret} = 590$ V. With the suggested retardation sequence this means to measure in the first measurement $U_{ret} = 50$ V and $U_{ret} = 70$ V, in the second $U_{ret} = 90$ V and $U_{ret} = 70$ V, in the third measurement $U_{ret} = 90$ and $U_{ret} = 50$ and so on. In the second series we measure the intermediate steps moving downwards. Then the first measurement is $U_{ret} = 580$ V and $U_{ret} = 560$ V, in the second $U_{ret} = 560$ V and $U_{ret} = 540$, in the third $U_{ret} = 540$ V and $U_{ret} = 580$ V and so on. An alternative would be to randomize the applied potentials.

Systematic effects

Through this analysis we were able to estimate two important systematic effects:

- **The ion distribution in the source:** As discussed before, the most crucial input for the tracking simulations is the modeling of the source parameters. Simulations and the data analysis in ref. [Gor12], provided valuable data for tracking simulations that was used throughout the tracking simulations in this chapter. Since the experimental parameters of the source (e. g. the ion distribution corresponding, to the transfer time t_{trans}) are not known precisely we estimated the uncertainty of this systematic effect from the difference between two fits for an upper limit of $t_{trans} = 38\,\mu s$ and an lower limit $t_{trans} = 31.5\,\mu s$. The result is an imprecision of the extracted a value of about $\Delta a_{syst,\,source} = 0.23$. This is a crucial systematic effect for a precision measurement of a.

- **The anti-ionization wire behind the analysis plane:** From tracking simulations we estimated the amount of ions that is absorbed by the anti-ionization wire. Repeating the fit of the recoil spectrum with a modified fit function which was exaggerated by the number of ions that have been absorbed by the anti-ionization wire in the simulation we estimated the effect of this anti-ionization wire for the determination of a. The result is an imprecision of the extracted a value of about $\Delta a_{syst,\,wire} = 0.06$. It is also a crucial systematic effect for a precision measurement of a.

A further systematic effect is the inhomogeneous detection efficiency of the position sensitive MCP detector. The calibration for the October beam time in 2011 and November beam time in 2011 has shown huge fluctuations in the relative efficiency of the detector by a factor of up to 10 (see sec. 2.3.7). Through the effort of the modifications on the detector made in May / June 2012, this problem could be reduced significantly. The latest calibration showed local fluctuations in the detection efficiency by a factor of 2 (see sec 2.5.4). This uneven detection efficiency, if not correctly known and corrected for, can be a problem due to the fact that the retardation voltage has a small effect on the focussing of the ions (see fig. 3.27) and the ion distribution on the detector.

Because of the modest quality of the data and systematic effects of this measurement, the extracted value for a shows large error bars:

$$a = 0.45^{+0.48}_{-0.39}{}_{stat} \pm 0.23_{syst,\,source} \pm 0.06_{syst,\,wire} \tag{3.6.1}$$

This value is in agreement with the value calculated from measured ft values of (0.9004 ± 0.0012) [Sev08]. This result shows that a good deal of work is still to be mastered by the collaboration for

the reduction of the systematic effects. This clearly stands in the way for a precision measurement of a with the intended precision of $\frac{\Delta a}{a} \leq 0.5\%$ [Bec03]. The use of a new target showed an increase in the count rate by about a factor of 30 [Bre11]. In combination with fewer data losses due a corrected synchronization of the DAQ and the retardation power supply, a better efficiency of the main MCP detector (see section 2.6) and a prolonged measurement period (5 days instead of 6 hours), an increase in statistics by a factor 1000 is reachable.

Taking into account the things we learned from this analysis we make suggestion for an upcoming measurement of an ^{35}Ar recoil spectrum, which will be discussed in the following section.

Prospective measurement design

Through the analysis of the data, which we presented in this chapter we learned several things, one should keep in mind for upcoming measurements. As a roundup we'd like to make a suggestion for future measurements which will be presented in the following:

The choice of the sequence of retardation potentials in the measurement is a trade-off between having more retardation potentials included in one measurement and saving measurement time, by not switching so often the voltage. As the retardation power supply always needs a certain time to stabilize after switching to another voltage, every switch of the retardation voltage is accompanied by a loss of the measurement time because the acquired data, during which the switch happens, cannot be use for the analysis, as the retardation voltage is not clearly defined during this time. So these *switching bin* have to be sorted out with hindsight.

For the normalization, the lowest and the highest retardation potential should be present in all measurements. As discussed before, the lowest possible voltage cannot be 0 V, for the reason that this measurement would be spoiled by the losses from the decay trap. Suitable would be a voltage slightly higher than the decay trap potential. From the recent analysis we know that $U_{ret} = 50$ V is in agreement with the other data points of the spectrum and we don't see an artificial increase of the count rate at this retardation voltage. Therefore we suggest to use 50 V as the lowest potential unless other measurements have shown that a smaller voltage is suitable as well. Maybe $U_{ret} = 10$ V if 5 V trapping potential is applied would be enough; experimental checks will have to verify this. Until then, 50 V can serve as a lower limit. For the highest voltage a value of 600 V, like used in the current measurement, is suitable. Simulations have shown that even for a transfer time of $t_{trans} = 31.5\,\mu$s this voltage is sufficient to stop all ions.

Apart from the lowest and highest potentials, two other retardation voltages should be enclosed in each measurement. This way it is easier to include equal retardation potentials in different measurements and we can swap the times when the retardation potentials are applied in the cycle. Secondly, each voltage should be repeated in the measurement at a later time. This will enhance the fit of an exponential decay function.

By keeping the succession of the two potentials we can probe the time evolution of the energy distribution in the decay trap. If we observe losses from the decay trap one would expect that the average energy of the ions in the decay trap is reduced. The cooling process is an evaporative cooling where primarily the ions with high energies are escaping the trap. So, through the course of the measurement cycle the average ion energy should become smaller. Since more high energetic ions are removed from the trap, the average energy will be reduced. If we determine the ratio of count rate, measured at $U_{ret,1}$ to the count rate, measured at $U_{ret,2}$, at different times in the measurement cycle this can be a hint if the energy distribution of the ions stays constant:

$$\frac{\dot{N}(U_{ret\,1})}{\dot{N}(U_{ret\,2})} = const. \tag{3.6.2}$$
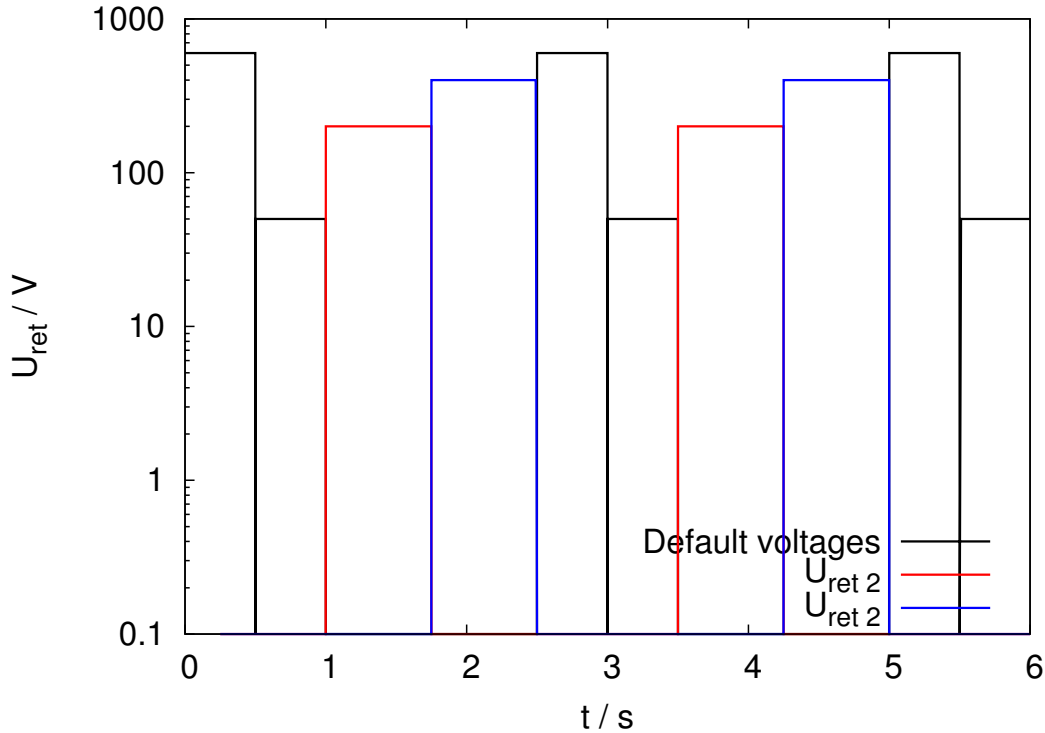
Figure 3.45.: Suggested retardation potential sequence for prospective measurements. In the beginning the overshoot ions from the filling and transfer are partially blocked by applying 600 V retardation potential to go easy on the MCPs. The sequence consists of a lower and an upper retardation potential which is present in all measurements. Here it is shown odor 50 V and 600 V as a lower and an upper voltage. In-between two different retardation potentials, $U_{ret\,1}$ and $U_{ret\,2}$, are applied. Here it is shown for $U_{ret\,1} = 200$ V and $U_{ret\,1} = 400$ V. This series is repeated two times in the measurement cycle.

If for instance $U_{ret\,1} < U_{ret\,2}$, like in our example in fig. 3.45, and the ration in eq. 3.6.2 is not constant but increases, this can be an indication, that the average energy in the trap decreases with time in the measurement cycle. Probably this method is only sensitive if we apply retardation potentials slightly above the end cap potential of the decay trap.

To simplify the data analysis process, it is advantageous to always use similar patterns where only the retardation potentials are varied from one to another measurement. During the analysis of our data we found that one data point (250 V), which was only present in one data set (11:15), did not match the other data points. As a safety cross-check we suggest to have two or better three different measurements with the same retardation potential. To illustrate this with a short example: Assuming we would like to measure at 100 V, 200 V and 300 V. We should at least do three measurements: first w measure 100 V and 200 V, then 200 V and 300 V and finally 300 V and 100 V. The voltages also should appear at different positions in the sequence. If one data point in the measured spectrum would not match, it is easier to tackle the problem.

Through a precise measurement of the count rate of low energies of the recoil spectrum ($U_{ret} < \frac{E_{rec,\,max}}{2}$) a determination of the charge stat distribution of the ^{35}Cl ions after the beta decay of ^{35}Ar is possible. The relative ratios of the charge states have to be included in the fit function, like it was done in eq. 3.4.15 (the c_i). If we keep these variable during the fit of the recoil spectrum this will allow for an alternative method to determine the charge state distribution, like the time-of-flight measurement performed in 2011 at LPC CAEN [Gor12].

By using the higher energies ($U_{ret} > \frac{E_{rec,\,max}}{2}$) one can circumvent the problem of the higher charge states occurring from electron shake-off after the β decay of ^{35}Ar. This part of the spectrum shows a larger gradient and therefore is more sensitive to a divination in the value of a from the expected one.

As a last suggestion, a measurement including 0 V retardation potential could serve as a method to determine the electron shake-off probability of ^{35}Ar after beta decay. To explain this we solve eq. 3.4.27 for P_{shake}:

$$P_{shake} = \left(\frac{1}{\frac{1}{f_{c,\,0V}} - 1} \right) \cdot \left(\frac{(1 - P(1^+))}{(1 - P_{wire})} \right) \cdot \left(\frac{\Gamma_{loss}}{\Gamma_{dec}} \right) \tag{3.6.3}$$

where again P_{shake} is the shake-off probability of ^{35}Ar after beta decay, $P(1^+)$ is the probability for the 1^+ charge state to occur after electron shake-off, P_{wire} is the absorption probability, which has to be determined with simulations, Γ_{loss} the decay rate of the trap losses (see below) and Γ_{dec} the literature decay rate of ^{35}Ar. The method for this determination would be a fit of the measured recoil spectrum, where the measurement at 0 V is scaled with the factor $f_{c,\,0V}$ which is left as a fit parameter. Γ_{loss} will be determined from the fitted signal lifetime τ_1 and the literature value of the ^{35}Ar lifetime τ_{dec} via:

$$\Gamma_{loss} = \Gamma_s - \Gamma_{dec} = \frac{1}{\tau_s} - \frac{1}{\tau_{dec}} \tag{3.6.4}$$

Remark about the current status and the online run in November 2012

The summary of our weak point analysis and the suggestions for future measurements, were made with regard to the online run in November 2012. These were crucial for a successful data taking during that measurement. In the course of the preparation for this run most of the suggestions were implemented. This and the current status of the experiment will be discussed in the next Chapter.

CONCLUSION & OUTLOOK

Form the beginning of weak interaction physics correlation experiments have played a fundamental role. Form today, over 50 year after the formulation of the V–A theory, many of the results remain unsurpassed in this field of physics. Since then, the development of new technologies and techniques – be it the fast evolution in computer technology and algorithms, new data acquisition components and detector technology, data analysis tools and software – advanced tremendously. Altogether this calls for new experiments in this field of research to push the limits further. An interesting candidate is the WITCH experiment. Due to its versatile setup (see sec. 1.3) a multitude of measurements on various nuclei might be possible. Nevertheless the initial goal – the measurement of an ^{35}Ar recoil energy spectrum witch a yet unreached precision of $\frac{\Delta a}{a} < 0.005$ – remains as a challenge.

From its construction and setup [Del05, Bec03], the first commissioning run [Koz05], the improved understanding of the beam line system and the Penning traps [Coe07b], the realization of a particle tracking routine [Fri08, Mad10], the study of systematic effects and installation of a new control system [Tan11a] and the development of many-body simulations in a Penning trap [Gor12], the experiment has made impressive improvements over the last decade. It seems like a precision measurement is approaching steadily. Nevertheless some hurdles need to be overcome.

This work accounts for various important contributions which we will discuss in the following.

The performance of the MCP detector

In this thesis a new 80 mm diameter microchannel plate detector system has been installed using first the feedthroughs and electronics of the former 40 mm diameter microchannel plate detector. This detector setup has been improved significantly. Now, in its present state, the detector works under stable conditions. This was reached through the numerous sanctions, such as moving the signal processing electronics to the outside of the vacuum, protecting the back of the delay line with a metal plate, removing the Penning gauge from the detector flange, assuring the stability of the MCP stack by introducing pintles to the ceramic holders and lowering the high voltage, applied to the detector. We found that a potential of -3.2 kV applied at the front MCP could result in a homogeneous detection efficiency and from simulations we have found a set of voltages which could focus all ^{35}Cl daughter ions from the ^{35}Ar decay from the source to the detector without any losses at electrodes in the setup (see sec. 3.3.4). The latter is particularly important since in the past measurements have been obstructed by discharges when high voltages were applied to the focussing electrodes or the detector. By now we have found a set of voltages where this does not happen.

In sec. 2.5.4 we have shown, that by introducing a shim ring between the two microchannel plates we could achieve a homogeneous detection efficiency over the whole surface of the detector. 84% of the detector surface has 80% or more relative detection efficiency and a total detection

efficiency of $\epsilon_{tot,2012} = (0.40 \pm 0.11)$, which is compatible with the open area ratio of the MCPs, has been determined. The relative position resolution has been measured as $\Delta R = 0.17$ mm with is close to the reference value given by the manufacturer. Altogether, this leaves only little room for improvements. Nevertheless it still needs to be figured out if these results are sufficient for a precision measurement of a.

Meanwhile the most curial part of the detector system has been solved. The two data acquisition systems (namely the MCS and the CAMAC) have been replaced by a new system named FASTER, which was developed at the LPC CAEN, to meet especially the requirements for MCP detectors with delay line position read-out. It disposes of eight channels (one for MCP main, four for the delay lines, one for the REXTRAP trigger one for the retardation voltage and one spare). Each one is equipped with a CFD, a scaler, a TDC and a QDC. The system can handle high count rates up to 10^5 Hz without significant dead time losses, the setting of thresholds is software-based, and online analysis via a software called RHB, implemented in a ROOT framework, is possible via a separate PC.

The calibration procedure

In the context of this work a straightforward calibration procedure has been developed which consists of three measurements in total: two measurements with a radioactive source in a defined position in front of the detector, each one with and without an aperture mask screwed to the MCP stack and a background measurement. Due to its simplicity, the calibration can be performed in a minimum amount of time and provides all necessary information, like relative and absolute detection efficiency and position resolution.

The weakest point of the calibration procedure is the type of source which was used in this process. The commercial ^{241}Am alpha source is not fully comparable to the ^{35}Cl recoil ions we need to detect in our measurement. Their energy is by a factor of about 10^4 higher than the energy of the ^{35}Cl ions and their mass is about an order of magnitude smaller. As already mentioned in sec. 2.6 the application of a commercial ion source with mass and kinetic energy of the ions comparable to the ^{35}Cl daughter ions, is highly recommended.

Weak point analysis and optimization of the measurement cycle

The analysis revealed several experimental deficiencies. The most important results are the following:

- A synchronization problem was identified, which we tackled effectively with a rather uncommon approach (see sec. 3.4.2).

- We could explain the excess count rate at $U_{ret} = 0$ V retardation potential (see sec. 3.4.4.3).

- We identified an unintentional Penning trap between the decay trap and the main retardation electrode at standard electrode settings (see also sec. 3.4.4.3). By adjusting the electrode voltage ratios, the problem can be solved.

- We optimize the measurement cycle (see sec. **??**) and minimized measurement time losses.

These problems have been solved, and as a result of this, the quality of the data taking in the beam time of Nov. 2012 improved.

For our analysis we had to rely on the values set at the power supply and took into account the rise and fall time of the retardation potential. This solution is prone to mistakes. Fluctuations in the applied potential and deviations for the set value of the voltage supply can occur. As this will affect the measurement directly, a cross-check by a measurement of the applied potential is essential

for a precision measurement. With the installation of the new data acquisition system this problem has been solved by recording the applied retardation potential with a separate ADC channel of the new DAQ. The dead time of that system has been checked before and after the last measurement and found to be in a proper regime. The system can handle count rates of about 10^5 Hz without losses.

Additionally, the retardation sequence has been adjusted for less changes in the retardation potential. Only two different retardation potentials, along with two reference voltages – one at a low voltage, one at 600 V, to block all recoil ions – were used in one measurement. This way, the loss of measurement time could be kept at a minimum during the run in Nov. 2012.

The misalignment problem described in sec. 3.6 has been solved by now. The mounting structure for the Penning traps has been rebuild, allowing room for expanding in the heating process. The Penning trap tower was adjusted via a screw on the outside which could tilt the whole structure. By shooting the ion beam from the VBL onto the detector and adjusting the traps from the outside it was possible to find a setting where the ions hit the detector right in the center [Bre12].

Systematic effects of the measurement

The WITCH experiment now approaches a phase where systematic effects play an important role. Through the data analysis describe in part II of this thesis, two important systematic effects have been investigated and their influence has been estimated: the anti-ionization wire in the analysis plane and the radioactive source, respectively the ion cloud in the decay trap. Both have been found to significantly contribute to the systematic uncertainties of the extracted $\beta - \nu$ angular correlation coefficient a.

The systematics due to the unknown ion cloud properties are more difficult to handle. They have a larger impact on the uncertainty on a, with $\Delta a_{source} = 0.23$ (see sec. 3.5.1). In literature, informations concerning large ion numbers in a Penning trap are rare, be it based on measurements or simulations. Eventually for us the most valuable information on the ion cloud properties today, can be found in ref. [Gor12]. These are based on simulations with a tool called Simbuca [Gor11]. These simulations were limited to the 2600 ions in the trap and one given electromagnetic configuration of the Penning trap setup. Because of the Coulomb interactions of the particles, the required CPU time scales with the number of ions squared. Although the use of a modern graphics card can increase the simulation speed drastically, and the technical evolution will probably push the limits further, it is not possible to simulate arbitrary large ion numbers. Although the ion numbers in our measurement are comparable to the numbers in this simulation, the necessary numbers for a high statistics precision measurement are still 1–2 orders of magnitudes larger.

Besides the mere number of simulated particles, it is also necessary to simulate different experimental settings of the electrode configuration of the Penning trap and the magnetic field, to gain a better understanding of the problem. Finally, offline measurements of accessible parameters, like for instance, the total kinetic energy and the longitudinal kinetic energy of the stored ions and the spot size on the main detector, should verify these results.

Anyway, offline measurements with the WITCH setup have not yet been carried out due to manifold technical problems with the setup and time constrains. These reasons are also valid for systematic simulations with many ions in a Penning trap. Although the use of a code like described in ref. [Gor11a], which makes use of a GPU, can speed up these simulation by orders of magnitude compared to the use of a CPU, these simulations have high requirements to the computer hardware and are time consuming, though. For a precision measurement these two tasks remain to be solved.

The systematic uncertainties due to the anti-ionization wire in the analysis plane have been estimated by simulating the amount of ions that were absorbed by the wire. Adding this fraction of ions to the fit function and repeating the fit, changed the vale of a by $\Delta a_{wire} = 0.06$. By this we neglected several things that might contribute to this effect as well: We didn't take into account

a change in the electric field, caused by the anti-ionization wire, we neglect ions that are scattered on the anti-ionization wire and we assume that the anti-ionization wire is perfectly centered in the analysis plane. The first two items can be taken into account by modifying the simulation routine, although it will require lots of work and will cost significantly computation speed. The latter has to be measured in at the setup.

Another important systematic effect is the position dependent detection efficiency. Due to the inconsistency of the two data branches it was not possible to take this into account in our data analysis. Yet, the procedure for this is straightforward: measure the relative detection efficiency of the MCP detector like described in sec. 2.3.7 and 2.5.4 and use this measured efficiency in the data analysis by dividing the actual measurement by the relative efficiency. The calibration of the detector should be carried out before and after a measurement, to see eventual changes in the detection efficiency and be able to account for this in the analysis of the measurement.

Eventually a calibration of the detector could be achieved from measured recoil spectra by comparing the count rate in different detector pixels at different retardation potentials. This way we get rid of the problem of comparing MeV alphas to 100 eV ^{35}Cl recoil ions.

The data analysis procedure

We used a combined fit to extract a recoil energy spectrum from all raw data of the 6 hours successful beam time of the October beam time in 2011 and extracted a value of a from this via a least square fit of the recoil spectrum. By means of this analysis, we could estimate two crucial systematic effects. The final result is (see also eq. 3.4.28):

$$a = 0.45 \, ^{+0.48}_{-0.39} \, _{stat} \pm 0.29_{syst}$$

This value is in agreement with the standard model value of a for the ^{35}Ar decay (see eq. 3.2.4). Due to the moderate quality and limited statistics of the data it was not possible to deduce a more relevant result for a but to identify experimental shortcomings and develop a procedure to analyze the data of upcoming measurements.

For a precision measurement of a, finally new limits on the coupling constants C_S/C_V and C_T/C_A need to be derived from the value of a. Since our current result of a measurement of a is not competitive, this final analysis step has been omitted.

The most important limiting factor for a high precision measurement were the many small problems which have been now identified and now are mostly solved. But apart from this there are several systematic effects to worry about.

A method to measure the relative detection efficiency of the detector has been developed in this thesis. Merely the application of these calibration data on the measurement was omitted because of the inconsistent position information of the measurement. Eventually a new simulation routine could master the problem due to the systematics of the anti-ionization wire. This will be accompanied by higher CPU time recommendations. Finally, most crucial are the systematics of the source. The exact properties of the phase space of the ions are a particularly crucial input for tracking simulations, to obtain the final fit function. A first step to solve this problem has been made by developing a many-body simulation routine for ions in a Penning trap, using graphic cards. Anyway, the so far obtained results are improvable and more simulation should follow soon. These should be accompanied by test measurement, since this is the most crucial systematic effect for a precision measurement of a.

APPENDIX A:
FIGURES AND TABLES FOR THE DETECTOR CALIBRATION

Table A.1.: Expected mean and measured mean of the spots from the mask for the slices along Y = -37 mm (left) and X= -37 mm (right) as returned by the ROOT script.

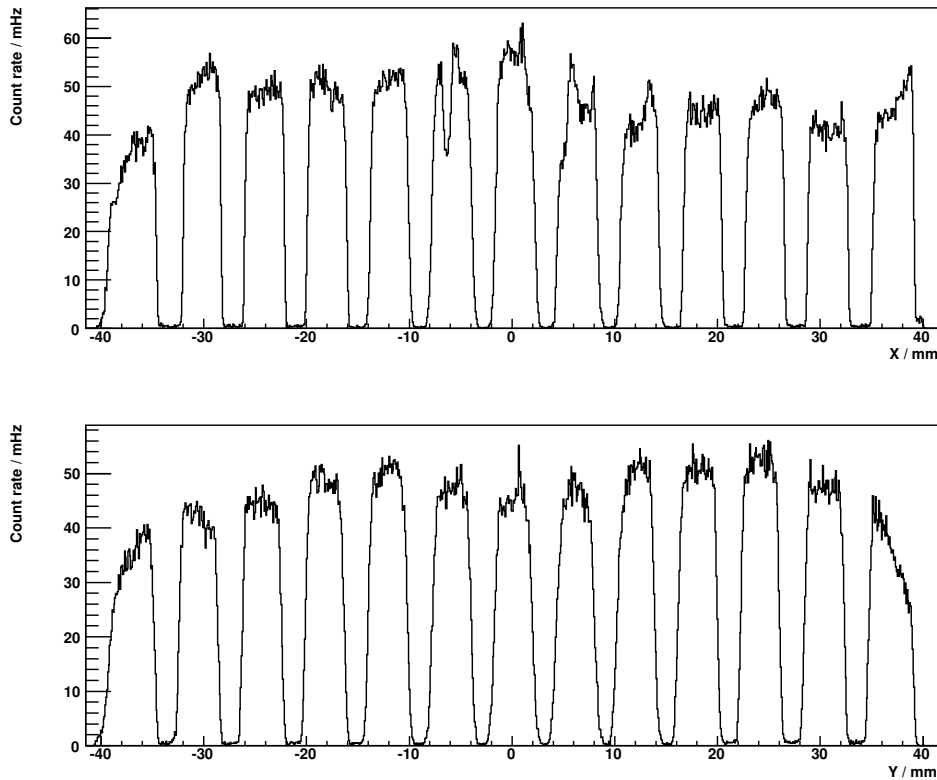| Expected mean	Measured mean	Expected mean	Measured mean
-12.2963	-12.0259	-12.2963	-11.9997
-6.14815	-6.20908	-6.14815	-6.02661
0	-0.217878	0	0.0908781
6.14815	5.92974	6.14815	6.12612
12.2963	11.8844	12.2963	12.3302
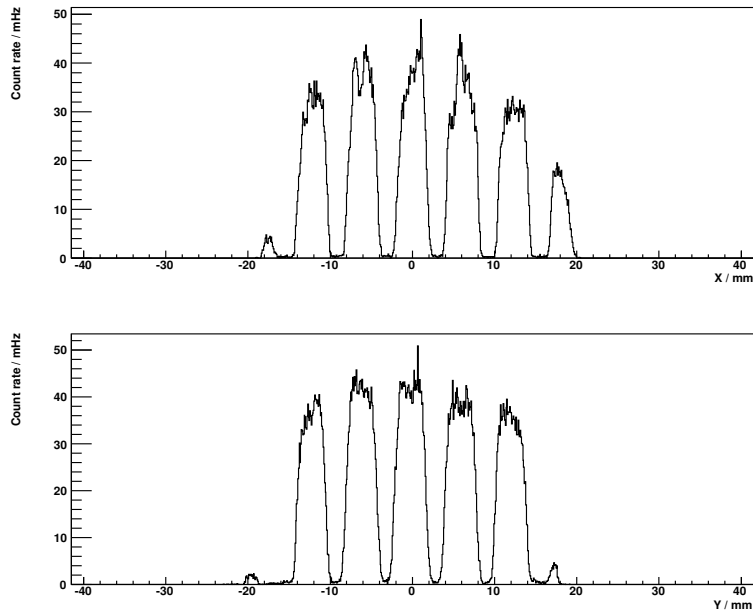
Figure A.1.: Top: 2 mm thick slice of the X-Z plane along Y = -37 mm projected on the X axis. Bottom: 2 mm thick slice of the Y-Z plane along X = -37 mm projected on the Y axis.

Table A.2.: Expected mean measured mean of the spots from the mask for the slices along Y = -31 mm (left) and X= -31 mm (right) as returned by the ROOT script.

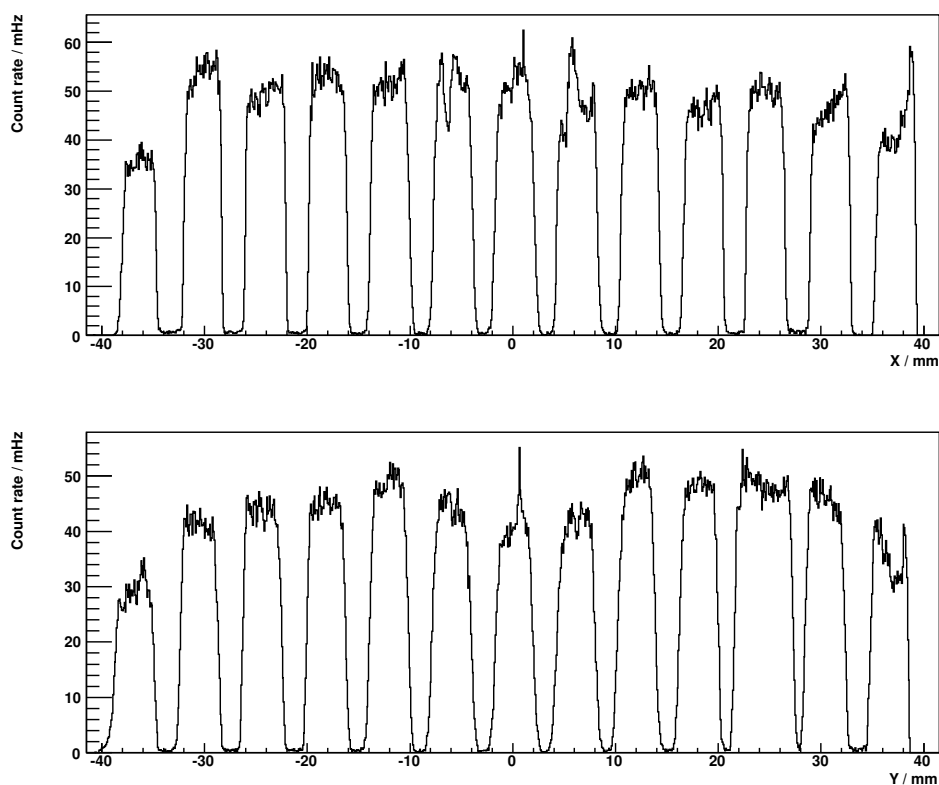| Expected mean	Measured mean	Expected mean	Measured mean
-18.4444	-17.9992	-18.4444	-18.2678
-12.2963	-11.9724	-12.2963	-12.2012
-6.14815	-5.94574	-6.14815	-6.1892
0	0.144385	0	-0.0831038
6.14815	6.26459	6.14815	5.92126
12.2963	12.3211	12.2963	11.9367
18.4444	18.4783	18.4444	18.1001
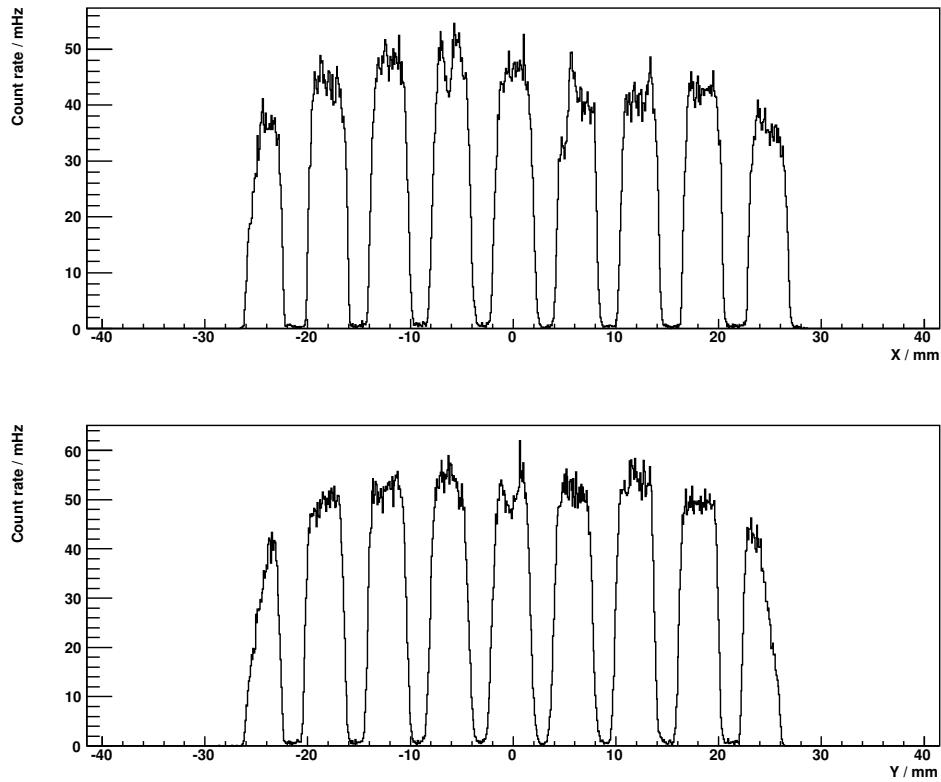
Figure A.2.: Top: 2 mm thick slice of the X-Z plane along Y = -31 mm projected on the X axis. Bottom: 2 mm thick slice of the Y-Z plane along X = -31 mm projected on the Y axis.

Table A.3.: Expected mean and measured mean of the spots from the mask for the slices along Y = -24 mm (left) and X= -24 mm (right) as returned by the ROOT script.

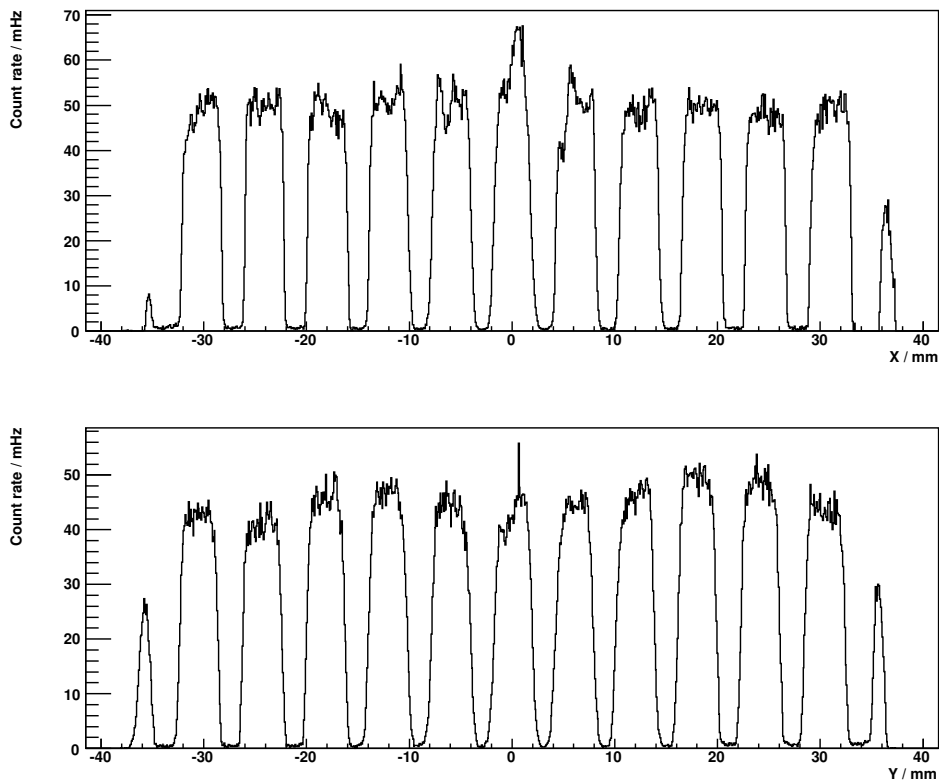| Expected mean	Measured mean	Expected mean	Measured mean
-24.5926	-24.1905	-24.5926	-24.3989
-18.4444	-17.945	-18.4444	-18.1245
-12.2963	-11.9846	-12.2963	-12.0869
-6.14815	-5.92149	-6.14815	-6.16169
0	0.455634	0	-0.109812
6.14815	6.26094	6.14815	5.90723
12.2963	12.3448	12.2963	11.9323
18.4444	18.5503	18.4444	18.0871
24.5926	24.6652	24.5926	24.2032
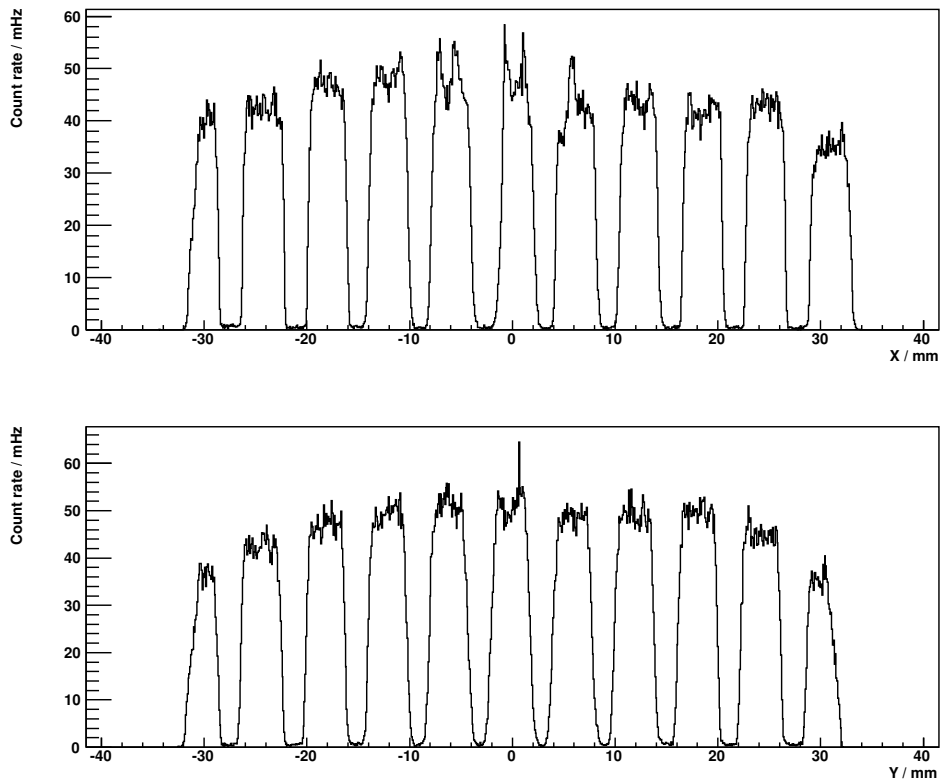
Figure A.3.: Top: 2 mm thick slice of the X-Z plane along Y = -24 mm projected on the X axis. Bottom: 2 mm thick slice of the Y-Z plane along X = -24 mm projected on the Y axis.

Table A.4.: Expected mean and measured mean of the spots from the mask for the slices along Y = -18 mm (top) and X= -18 mm (bottom) as returned by the ROOT script.

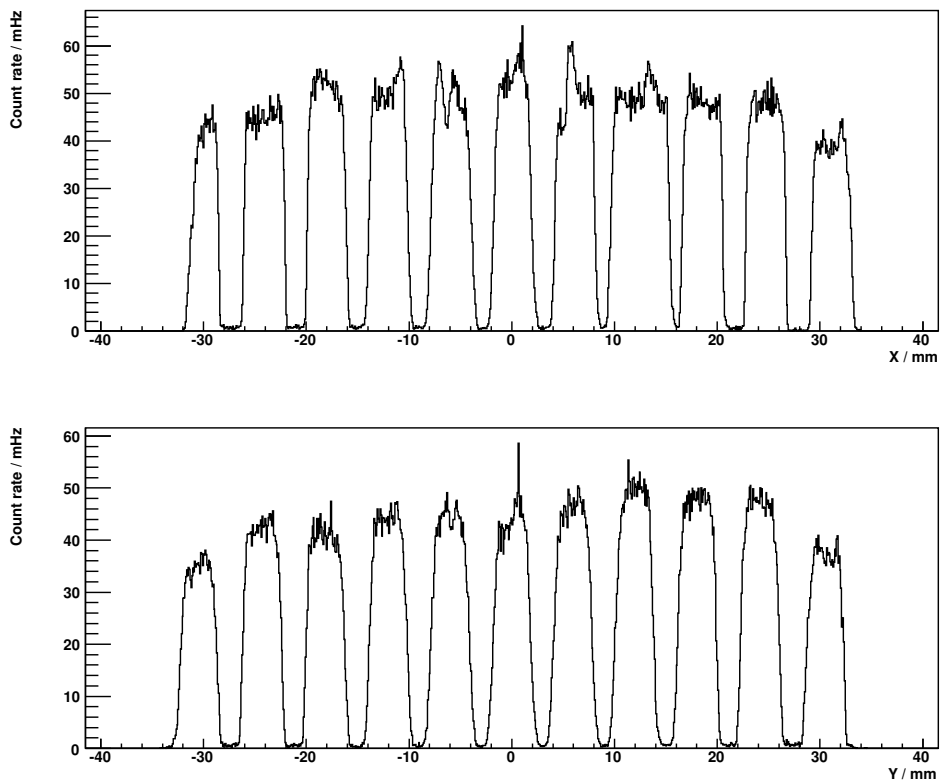| Expected mean	Measured mean	Expected mean	Measured mean
-30.7407	-30.3082	-30.7407	-30.5797
-24.5926	-24.1486	-24.5926	-24.3212
-18.4444	-18.0068	-18.4444	-18.1922
-12.2963	-11.9628	-12.2963	-12.1834
-6.14815	-5.87449	-6.14815	-6.2233
0	0.211268	0	-0.149553
6.14815	6.26787 9	6.14815	5.91044
12.2963	12.4351	12.2963	11.9257
18.4444	18.5465	18.4444	18.0522
24.5926	24.5935	24.5926	24.1649
30.7407	30.9422	30.7407	30.5228
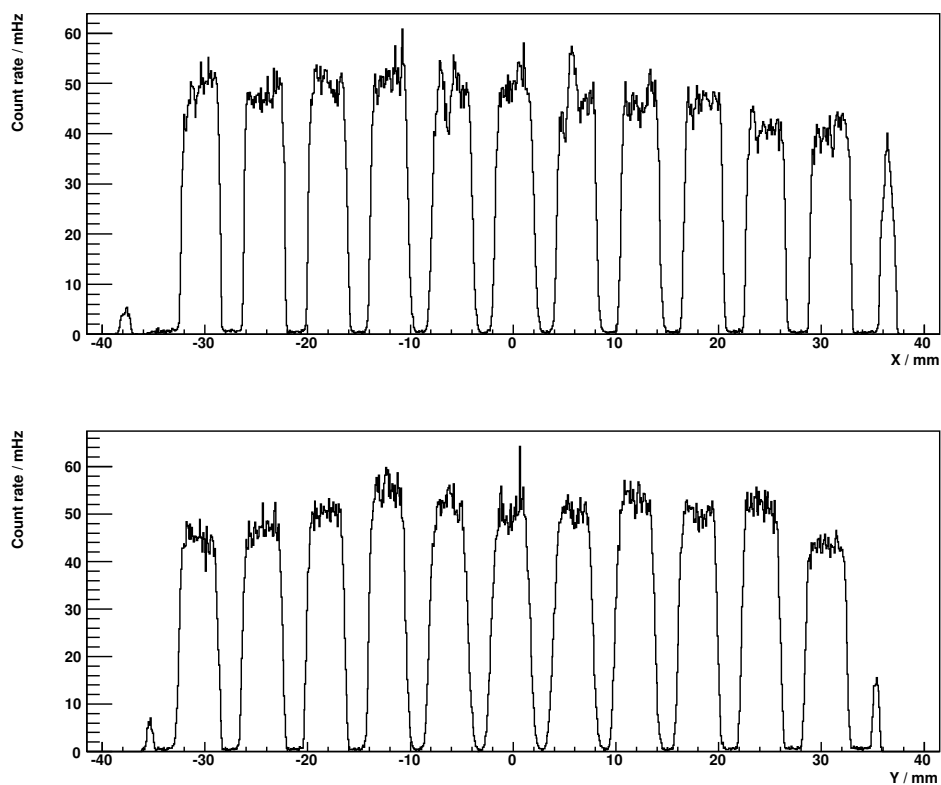
Figure A.4.: Top: 2 mm thick slice of the X-Z plane along Y = -18 mm projected on the X axis. Bottom: 2 mm thick slice of the Y-Z plane along X = -18 mm projected on the Y axis.

Table A.5.: Expected mean and measured mean of the spots from the mask for the slices along Y = -12 mm (left) and X= -12 mm (right) as returned by the ROOT script.

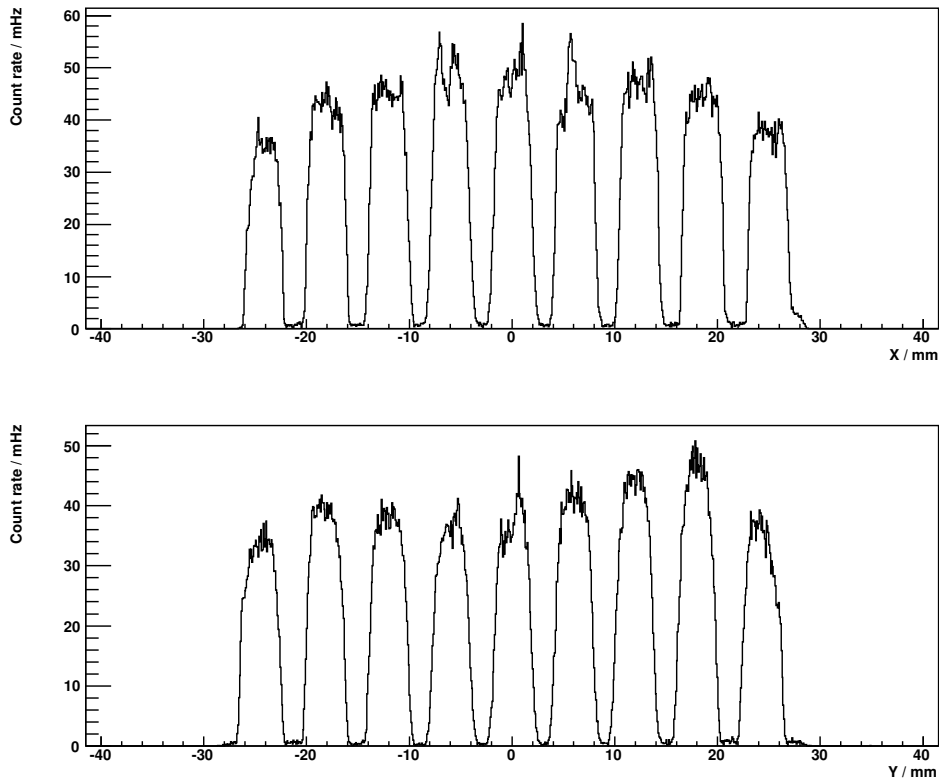| Expected mean	Measured mean	Expected mean	Measured mean
-36.8889	-36.4114	-36.8889	-36.5012
-30.7407	-30.1903	-30.7407	-30.5398
-24.5926	-24.1227	-24.5926	-24.3512
-18.4444	-18.086	-18.4444	-18.1827
-12.2963	-12.0062	-12.2963	-12.1949
-6.14815	-5.86351	-6.14815	-6.08023
0	0.185403	0	-0.00656175
6.14815	6.36309	6.14815	6.00803
12.2963	12.4624	12.2963	11.9943
18.4444	18.5977	18.4444	18.1169
24.5926	24.6481	24.5926	24.2075
30.7407	30.8932	30.7407	30.4271
36.8889	37.3945	36.8889	36.4583
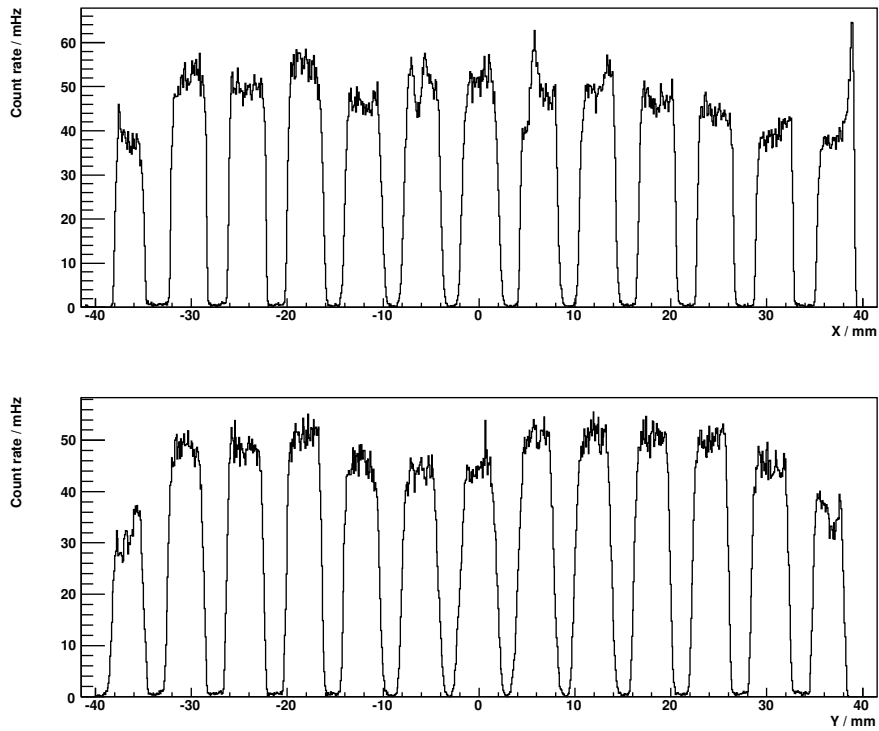
Figure A.5.: Top: 2 mm thick slice of the X-Z plane along Y = -12 mm projected on the X axis. Bottom: 2 mm thick slice of the Y-Z plane along X = -12 mm projected on the Y axis.

Table A.6.: Expected mean and measured mean of the spots from the mask for the slices along Y = -6 mm (left) and X= -6 mm (right) as returned by the ROOT script.

Expected mean	Measured mean	Expected mean	Measured mean
-36.8889	-36.831	-36.8889	-36.9211
-30.7407	-30.1669	-30.7407	-30.4822
-24.5926	-24.1207	-24.5926	-24.3104
-18.4444	-18.0934	-18.4444	-18.1811
-12.2963	-11.9443	-12.2963	-12.1119
-6.14815	-5.82698	-6.14815	-6.00435
0	0.381935	0	0.126302
6.14815	6.39762	6.14815	6.0504
12.2963	12.4694	12.2963	12.064
18.4444	18.6306	18.4444	18.147
24.5926	24.6889	24.5926	24.1595
30.7407	30.8932	30.7407	30.3678
36.8889	37.1919	36.8889	36.7646
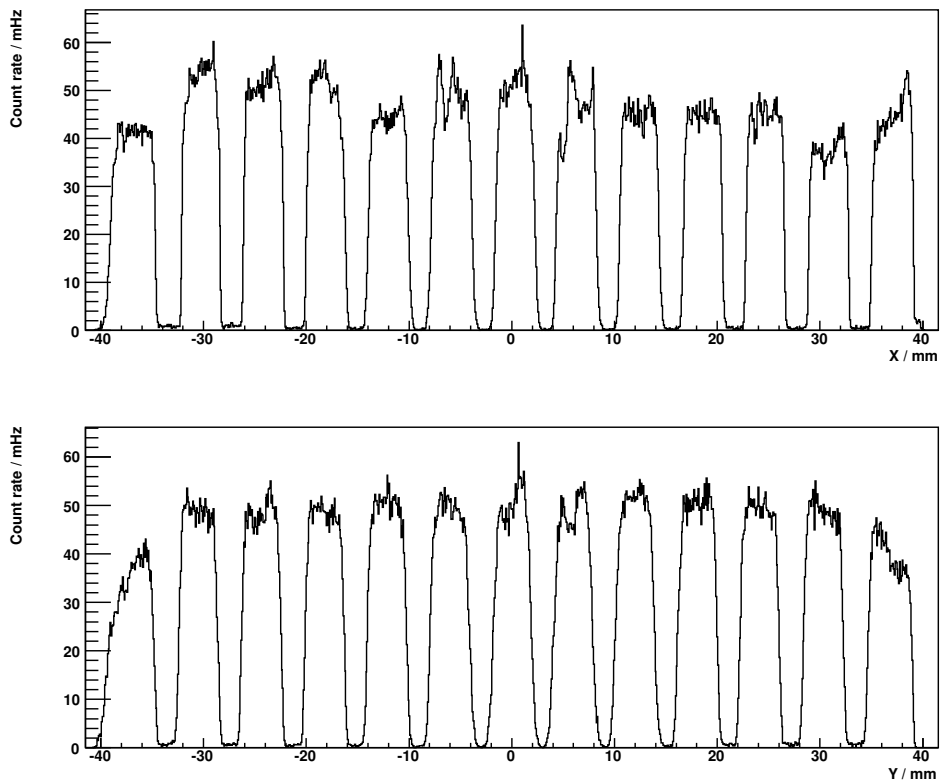
Figure A.6.: Top: 2 mm thick slice of the X-Z plane along Y = -6 mm projected on the X axis. Bottom: 2 mm thick slice of the Y-Z plane along X = -6 mm projected on the Y axis.

Table A.7.: Expected mean and measured mean of the spots from the mask for the slices along Y = 6 mm (let) and X= 6 mm (right) as returned by the ROOT script.

Expected mean	Measured mean	Expected mean	Measured mean
-36.8889	-36.7726	-36.8889	-36.8633
-30.7407	-30.0495	-30.7407	-30.499
-24.5926	-24.0101	-24.5926	-24.2955
-18.4444	-17.9969	-18.4444	-18.194
-12.2963	-11.865	-12.2963	-12.0423
-6.14815	-5.78975	-6.14815	-5.83375
0	0.311884	0	0.173845
6.14815	6.49965	6.14815	6.22296
12.2963	12.5434	12.2963	12.1418
18.4444	18.5883	18.4444	18.1418
24.5926	24.6648	24.5926	24.2036
30.7407	30.7669	30.7407	30.4434
36.8889	37.2496	36.8889	36.7385

Figure A.7.: Top: 2 mm thick slice of the X-Z plane along Y = 6 mm projected on the X axis. Bottom: 2 mm thick slice of the Y-Z plane along X = 6 mm projected on the Y axis.

Table A.8.: Expected mean and measured mean of the spots from the mask for the slices along Y = 12 mm (left) and X= 12 mm (right) as returned by the ROOT script.

Expected mean	Measured mean	Expected mean	Measured mean
-36.8889	-36.2896	-36.8889	-36.7905
-30.7407	-30.0653	-30.7407	-30.4893
-24.5926	-23.9932	-24.5926	-24.3439
-18.4444	-17.9612	-18.4444	-18.1124
-12.2963	-11.8947	-12.2963	-12.0005
-6.14815	-5.76865	-6.14815	-5.93991
0	0.250214	0	0.210763
6.14815	6.33955	6.14815	6.22545
12.2963	12.4479	12.2963	12.1333
18.4444	18.5922	18.4444	18.1685
24.5926	24.6325	24.5926	24.2801
30.7407	30.9598	30.7407	30.1302
36.8889	37.4307	36.8889	36.6359

Figure A.8.: Top: 2 mm thick slice of the X-Z plane along Y = 12 mm projected on the X axis. Bottom: 2 mm thick slice of the Y-Z plane along X = 12 mm projected on the Y axis.

Table A.9.: Expected mean and measured mean of the spots from the mask for the slices along Y = 18 mm (left) and X= 18 mm (right) as returned by the ROOT script.

Expected mean	Measured mean	Expected mean	Measured mean
-30.7407	-30.0945	-30.7407	-30.4473
-24.5926	-24.054	-24.5926	-24.2406
-18.4444	-17.9558	-18.4444	-18.0763
-12.2963	-11.9273	-12.2963	-12.0539
-6.14815	-5.83389	-6.14815	-5.93453
0	0.144078	0	0.182212
6.14815	6.31576	6.14815	6.13305
12.2963	12.4454	12.2963	12.0921
18.4444	18.523	18.4444	18.0727
24.5926	24.6826	24.5926	24.2128
30.7407	31.0558	30.7407	30.488

Figure A.9.: Top: 2 mm thick slice of the X-Z plane along Y = 18 mm projected on the X axis. Bottom: 2 mm thick slice of the Y-Z plane along X = 18 mm projected on the Y axis.

Table A.10.: Expected mean and measured mean of the spots from the mask for the slices along Y = 24 mm (left) and X= 24 mm (right) as returned by the ROOT script.

Expected mean	Measured mean	Expected mean	Measured mean
-30.7407	-29.8018	-30.7407	-30.4354
-24.5926	-24.0198	-24.5926	-24.2435
-18.4444	-17.984	-18.4444	-18.1159
-12.2963	-11.9297	-12.2963	-11.9803
-6.14815	-5.89471	-6.14815	-5.97207
0	0.155134	0	0.0844906
6.14815	6.22318	6.14815	6.00631
12.2963	12.3313	12.2963	12.009
18.4444	18.221	18.4444	18.102
24.5926	24.7397	24.5926	24.196
30.7407	31.1558	30.7407	30.5483

Figure A.10.: Top: 2 mm thick slice of the X-Z plane along Y = 24 mm projected on the X axis. Bottom: 2 mm thick slice of the Y-Z plane along X = 24 mm projected on the Y axis.

Table A.11.: Expected mean and measured mean of the spots from the mask for the slices along Y = 31 mm (left) and X= 31 mm (right) as returned by the ROOT script.

Expected mean	Measured mean	Expected mean	Measured mean
-24.5926	-23.6427	-24.5926	-24.356
-18.4444	-18.0378	-18.4444	-18.1548
-12.2963	-11.9638	-12.2963	-11.9709
-6.14815	-5.99189	-6.14815	-5.88602
0	0.106303	0	0.173591
6.14815	6.22699	6.14815	6.0897
12.2963	12.3958	12.2963	11.9622
18.4444	18.5678	18.4444	18.0268
24.5926	24.7218	24.5926	24.2472

Figure A.11.: Top: 2 mm thick slice of the X-Z plane along Y = 31 mm projected on the X axis. Bottom: 2 mm thick slice of the Y-Z plane along X = 31 mm projected on the Y axis.

Table A.12.: Expected mean and measured mean of the spots from the mask for the slices along Y = 37 mm (left) and X= 37 mm (right) as returned by the ROOT script.

Expected mean	Measured mean	Expected mean	Measured mean
-12.2963	-12.1714	-12.2963	-12.1303
-6.14815	-6.09897	-6.14815	-6.12058
0	0.0593549	0	-0.145552
6.14815	6.30687	6.14815	5.84972
12.2963	12.5269	12.2963	11.8074
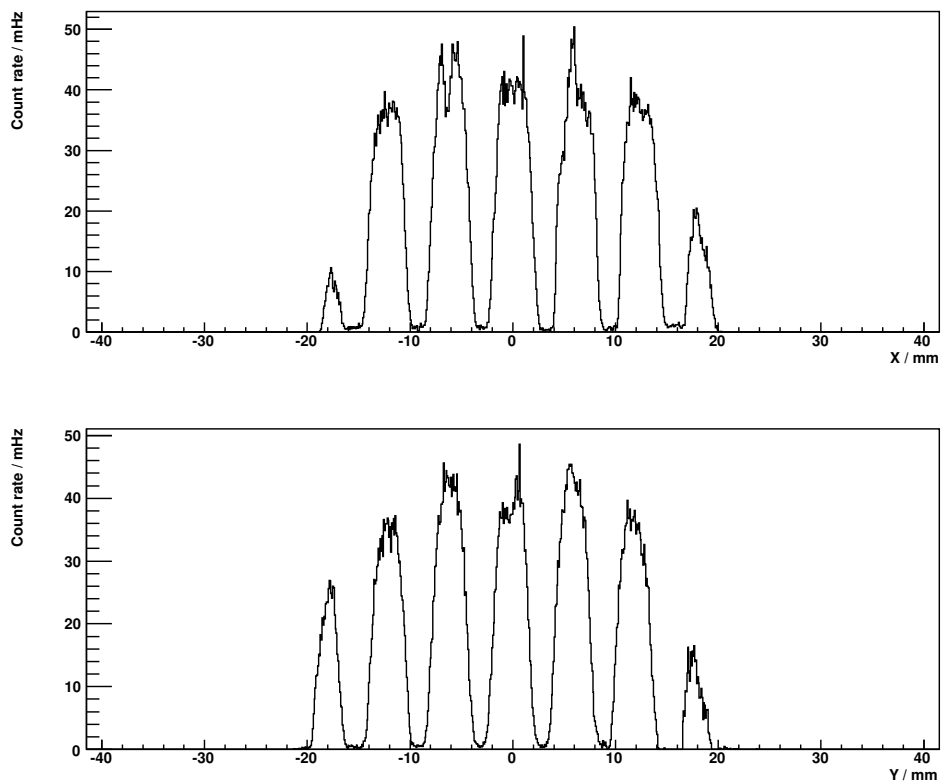
Figure A.12.: Top: 2 mm thick slice of the X-Z plane along Y = 36 mm projected on the X axis. Bottom: 2 mm thick slice of the Y-Z plane along X = 37 mm projected on the Y axis.

PHYSICAL CHARACTERISTICS   **SPECIFICATIONS**

Outside Diameter:	86.61mm (3.410") $\pm$ 0.08mm
Quality Diameter:	75.00mm (2.953") Minimum
Border Width:	N/A (Rimless)
Thickness:	1.50mm (.059") $\pm$ 0.03mm
Material Type:	Long-Life™ MCP-10
Center-to-Center Spacing:	32µm Nominal
Pore Size:	25µm Nominal
Bias Angle:	8° $\pm$ 1°
Open Area Ratio:	45% Minimum
Electrode Material:	Nichrome (80/20)
Electrode Bias Identification:	Input Side
Electrode Diameter:	Input: 85.22mm (3.355") $\pm$ 0.13mm
	Output: 85.60mm (3.370") $\pm$ 0.13mm
Electrode Sheet Resistance:	Input: 100 Ohms Maximum
	Output: 100 Ohms Maximum
Electrode Penetration:	Input: 0.5-1.0 Channel Diameters
	Output: 0.5-1.0 Channel Diameters

ELECTRICAL CHARACTERISTICS   **SPECIFICATIONS**

Gain @ 900 Volts:	400 Minimum
Gain @ 1200 Volts:	10,000 Minimum
Bias Current Range @ 1200 Volts:	20-199 Microamps
Resistance (For Reference Only):	6-60 Megohms
Maximum Specified Operating Voltage:	1200 Volts
Test/Inspection Level:	Detection Quality

Figure A.13.: Specification sheet of the MCPs provided by the manufacturer. Remark: Burle Industries was bought out by Photonis in 2005.
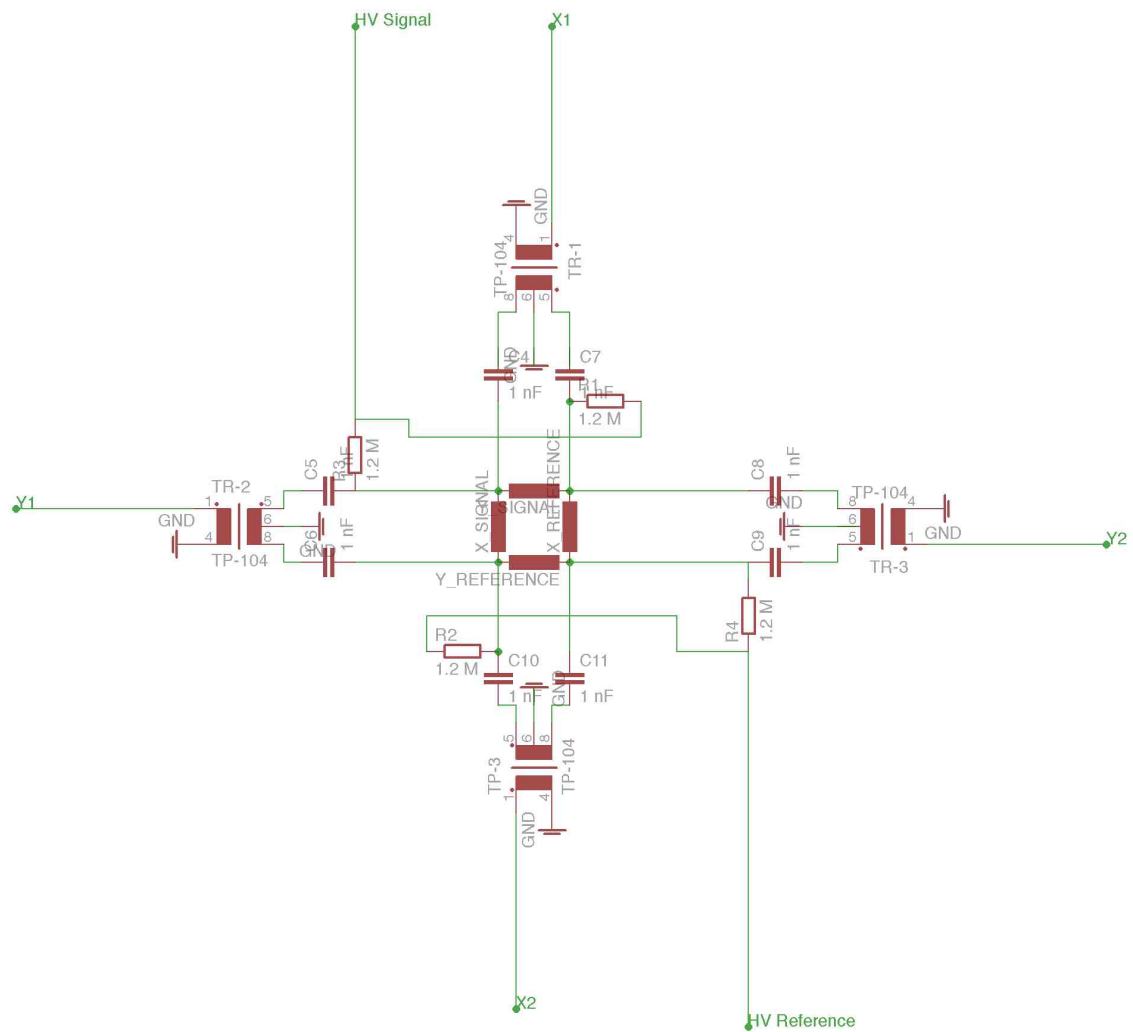
Figure A.14.: Electric scheme of the signal processing how it was accomplished for the old WITCH detector. First all signals are decoupled from the high voltage with 1.2 nF capacitors. The *Reference* and *Signal* signals from each end for the delay lines are later subtracted from each outer for noise reduction by using pulse transformers (TP-104).

Figure A.15.: Full ^{241}Am decay scheme, taken from [Bas06].

Appendix B:
Figures of the raw data and tables of the switching files
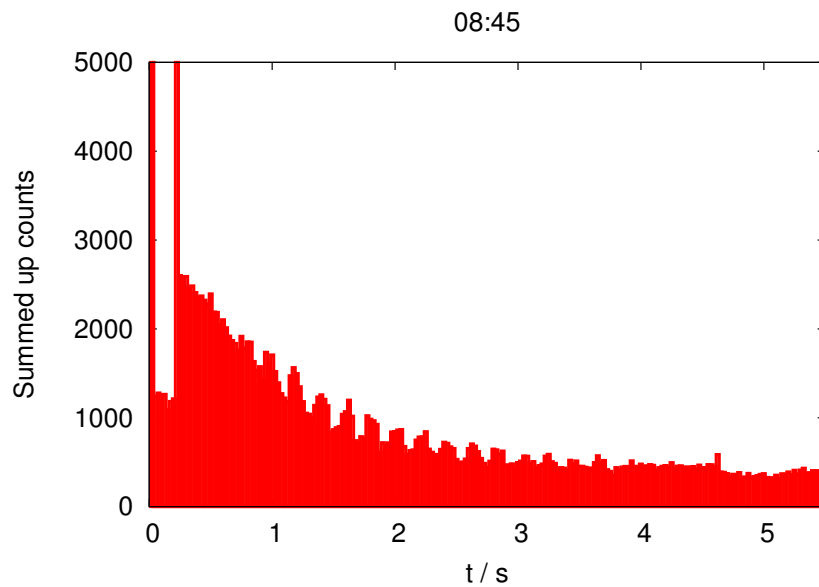
Figure B.1.: Raw data of the 08:45 measurement. The 999 individual measurements are summed up to one histogram. The first peak around $t = 0$ originates from ions that are injected into the cooler trap with too much kinetic energy to be stopped by the electric potential of the upper end caps of the cooler trap. These ions are shot through the trap system and reach the main detector. Th second peak around $t = 0.25$ originates from the transfer of the ion cloud from the cooler into the decay trap. At $0.25\,\text{s} < t \leq 5.5\,\text{s}$ the ions are stored in the decay trap while part of them decay.
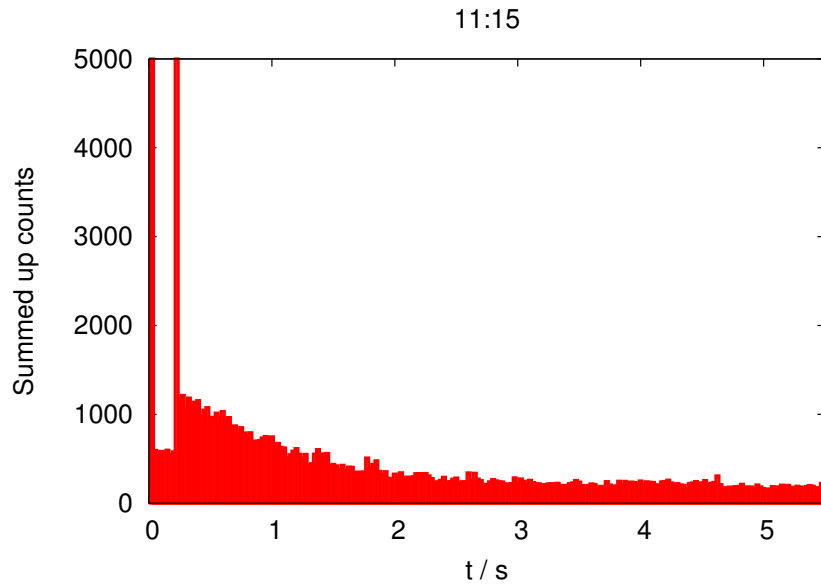
Figure B.2.: Raw data of the 11:15 measurement. The 499 individual measurements are summed up to one histogram. The first peak around $t = 0$ originates from ions that are injected into the cooler trap with too much kinetic energy to be stopped by the electric potential of the upper end caps of the cooler trap. These ions are shot through the trap system and reach the main detector. Th second peak around $t = 0.25$ originates from the transfer of the ion cloud from the cooler into the decay trap. At $0.25\,\text{s} < t \leq 5.5\,\text{s}$ the ions are stored in the decay trap while part of them decay.
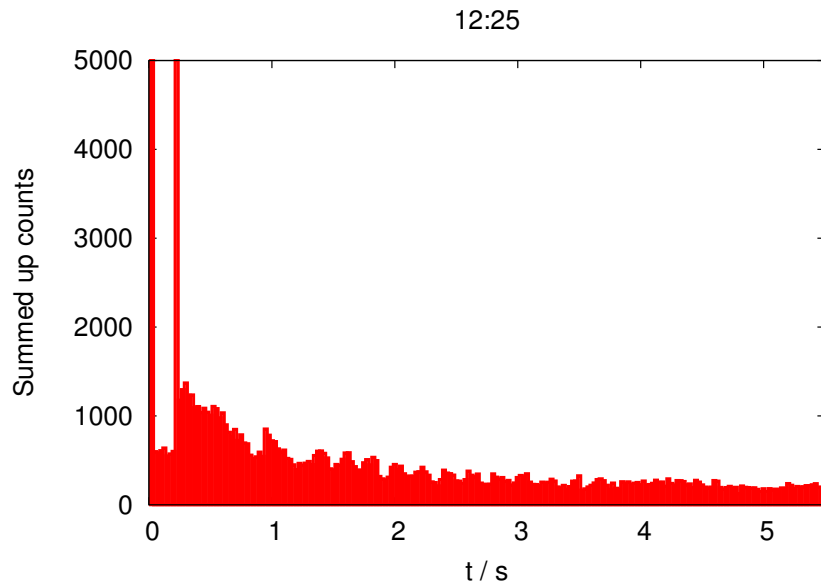
Figure B.3.: Raw data of the 12:25 measurement. The 526individual measurements are summed up to one histogram. The first peak around $t = 0$ originates from ions that are injected into the cooler trap with too much kinetic energy to be stopped by the electric potential of the upper end caps of the cooler trap. These ions are shot through the trap system and reach the main detector. Th second peak around $t = 0.25$ originates from the transfer of the ion cloud from the cooler into the decay trap. At $0.25\,\text{s} < t \leq 5.5\,\text{s}$ the ions are stored in the decay trap while part of them decay.

Table B.1.: Default retardation sequences for the measurement cycles recorded 01/11/12 at 06:04, 08:45, 11:15 and 12:25.

Switching time / s	U_{ret} / V, 06:40	U_{ret} / V, 08:45	U_{ret} / V, 11:15	U_{ret} / V, 12:25
0	0	0	0	0
0.025	0	0	0	0
0.05	0	0	0	0
0.075	0	0	0	0
0.1	0	0	0	0
0.125	0	0	0	0
0.15	0	0	0	0
0.175	0	0	0	0
0.2	0	0	0	0
0.225	0	0	0	0
0.25	0	0	0	0
0.275	0	0	0	0
0.3	0	0	0	0
0.325	0	0	0	0
0.35	0	0	0	0
0.375	0	0	0	0
0.4	0	0	0	0
0.425	0	0	0	0
0.45	0	0	0	0
0.475	0	0	0	0
0.5	0	0	0	0
0.525	0	0	0	0
0.55	0	0	0	0
0.575	0	0	0	0
0.6	600	75	50	150
0.625	600	75	50	150
0.65	600	75	50	150
0.675	600	75	50	150
0.7	0	0	100	300
0.725	0	0	100	300
0.75	0	0	100	300
0.775	0	0	100	300
0.8	525	150	150	450
0.825	525	150	150	450
0.85	525	150	150	450
0.875	525	150	150	450
0.9	0	0	0	0
0.925	0	0	0	0
0.95	0	0	0	0
0.975	0	0	0	0
1	450	225	200	150

Switching time / s	U_{ret} / V, 06:40	U_{ret} / V, 08:45	U_{ret} / V, 11:15	U_{ret} / V, 12:25
1.025	450	225	200	150
1.05	450	225	200	150
1.075	450	225	200	150
1.1	0	0	250	450
1.125	0	0	250	450
1.15	0	0	250	450
1.175	0	0	250	450
1.2	375	300	300	300
1.225	375	300	300	300
1.25	375	300	300	300
1.275	375	300	300	300
1.3	0	0	0	0
1.325	0	0	0	0
1.35	0	0	0	0
1.375	0	0	0	0
1.4	300	375	350	300
1.425	300	375	350	300
1.45	300	375	350	300
1.475	300	375	350	300
1.5	0	0	400	0
1.525	0	0	400	0
1.55	0	0	400	0
1.575	0	0	400	0
1.6	225	450	450	150
1.625	225	450	450	150
1.65	225	450	450	150
1.675	225	450	450	150
1.7	0	0	0	0
1.725	0	0	0	0
1.75	0	0	0	0
1.775	0	0	0	0
1.8	150	525	500	450
1.825	150	525	500	450
1.85	150	525	500	450
1.875	150	525	500	450
1.9	0	0	550	0
1.925	0	0	550	0
1.95	0	0	550	0
1.975	0	0	550	0
2	75	600	600	300
2.025	75	600	600	300
2.05	75	600	600	300
2.075	75	600	600	300
2.1	0	0	0	0
2.125	0	0	0	0
2.15	0	0	0	0
2.175	0	0	0	0
2.2	75	600	600	450

Switching time / s	U_{ret} / V, 06:40	U_{ret} / V, 08:45	U_{ret} / V, 11:15	U_{ret} / V, 12:25
2.225	75	600	600	450
2.25	75	600	600	450
2.275	75	600	600	450
2.3	0	0	550	0
2.325	0	0	550	0
2.35	0	0	550	0
2.375	0	0	550	0
2.4	150	525	500	150
2.425	150	525	500	150
2.45	150	525	500	150
2.475	150	525	500	150
2.5	0	0	0	0
2.525	0	0	0	0
2.55	0	0	0	0
2.575	0	0	0	0
2.6	225	450	450	450
2.625	225	450	450	450
2.65	225	450	450	450
2.675	225	450	450	450
2.7	0	0	400	0
2.725	0	0	400	0
2.75	0	0	400	0
2.775	0	0	400	0
2.8	300	375	350	150
2.825	300	375	350	150
2.85	300	375	350	150
2.875	300	375	350	150
2.9	0	0	0	0
2.925	0	0	0	0
2.95	0	0	0	0
2.975	0	0	0	0
3	375	300	300	300
3.025	375	300	300	300
3.05	375	300	300	300
3.075	375	300	300	300
3.1	0	0	250	0
3.125	0	0	250	0
3.15	0	0	250	0
3.175	0	0	250	0
3.2	450	225	200	450
3.225	450	225	200	450
3.25	450	225	200	450
3.275	450	225	200	450
3.3	0	0	0	0
3.325	0	0	0	0
3.35	0	0	0	0
3.375	0	0	0	0
3.4	525	150	150	300

Switching time / s	U_{ret} / V, 06:40	U_{ret} / V, 08:45	U_{ret} / V, 11:15	U_{ret} / V, 12:25
3.426	525	150	150	300
3.45	525	150	150	300
3.475	525	150	150	300
3.5	0	0	100	0
3.525	0	0	100	0
3.55	0	0	100	0
3.575	0	0	100	0
3.6	600	75	50	150
3.625	600	75	50	150
3.65	600	75	50	150
3.675	600	75	50	150
3.7	0	0	0	0
3.725	0	0	0	0
3.75	0	0	0	0
3.775	0	0	0	0
3.8	0	0	0	0
3.825	0	0	0	0
3.85	0	0	0	0
3.875	0	0	0	0
3.9	0	0	0	0
3.925	0	0	0	0
3.95	0	0	0	0
3.975	0	0	0	0
4	0	0	0	0
4.025	0	0	0	0
4.05	0	0	0	0
4.075	0	0	0	0
4.1	0	0	0	0
4.125	0	0	0	0
4.15	0	0	0	0
4.175	0	0	0	0
4.2	0	0	0	0
4.225	0	0	0	0
4.25	0	0	0	0
4.275	0	0	0	0
4.3	0	0	0	0
4.325	0	0	0	0
4.35	0	0	0	0
4.375	0	0	0	0
4.4	0	0	0	0
4.425	0	0	0	0
4.45	0	0	0	0
4.475	0	0	0	0
4.5	600	600	600	600
4.525	600	600	600	600
4.55	600	600	600	600
4.575	600	600	600	600
4.6	600	600	600	600

Switching time / s	U_{ret} / V, 06:40	U_{ret} / V, 08:45	U_{ret} / V, 11:15	U_{ret} / V, 12:25
4.625	600	600	600	600
4.65	600	600	600	600
4.675	600	600	600	600
4.7	600	600	600	600
4.725	600	600	600	600
4.75	600	600	600	600
4.775	600	600	600	600
4.8	600	600	600	600
4.825	600	600	600	600
4.85	600	600	600	600
4.875	600	600	600	600
4.9	600	600	600	600
4.925	600	600	600	600
4.95	600	600	600	600
4.975	600	600	600	600
5	0	0	0	0
5.025	0	0	0	0
5.05	0	0	0	0
5.075	0	0	0	0
5.1	0	0	0	0
5.125	0	0	0	0
5.15	0	0	0	0
5.175	0	0	0	0
5.2	0	0	0	0
5.225	0	0	0	0
5.25	0	0	0	0
5.275	0	0	0	0
5.3	0	0	0	0
5.325	0	0	0	0
5.35	0	0	0	0
5.375	0	0	0	0
5.4	0	0	0	0
5.425	0	0	0	0
5.45	0	0	0	0
5.475	0	0	0	0
5.5	0	0	0	0

Table B.2.: Number of counts and switching files for the measurements 06:40 and 08:45 recorded 01/11/11

Time / s	Counts, 06:40	Switching, 06:40	Counts 08:45	Switching 08:45
0.025	9731	0	12858	0
0.05	1455	0	1244	0
0.075	1428	0	1279	0
0.1	1302	0	1261	0
0.125	1314	0	1264	0
0.15	1318	0	1092	0
0.175	1459	0	1184	0
0.2	1329	0	1214	0
0.225	195198	0	219122	0
0.25	3215	0	2601	0
0.275	3180	0	2536	0
0.3	3075	0	2590	0
0.325	2954	0	2475	0
0.35	2925	0	2485	0
0.375	2861	0	2409	0
0.4	2796	0	2362	0
0.425	2847	0	2372	0
0.45	2760	0	2324	0
0.475	2662	0	2283	0
0.5	2654	0	2394	0
0.525	2730	0	2190	0
0.55	2619	0	2186	0
0.575	2594	0	2051	0
0.6	2455	0	2104	0
0.625	2125	0.5	2014	0.5
0.65	1452	1	1920	1
0.675	1421	1	1870	1
0.7	1583	1	1837	1
0.725	1503	1	1762	1
0.75	2254	0	1917	0
0.775	2304	0	1787	0
0.8	2271	0	1855	0
0.825	1982	0.5	1852	0
0.85	1407	1	1634	1
0.875	1321	1	1535	1
0.9	1274	1	1576	1
0.925	1241	1	1438	1
0.95	1945	0	1738	0
0.975	1878	0	1616	0
1	1958	0	1707	0

Time / s	Counts, 06:40	Switching, 06:40	Counts 08:45	Switching 08:45
1.025	1830	0	1521	0
1.05	1277	1	1394	1
1.075	1147	1	1272	1
1.1	1150	1	1223	1
1.125	1056	1	1182	1
1.15	1587	0	1473	0
1.175	1561	0	1564	0
1.2	1706	0	1498	0
1.225	1661	0	1349	0.5
1.25	1365	0.5	1182	1
1.275	1040	1	1052	1
1.3	1077	1	1041	1
1.325	1024	1	1000	1
1.35	1237	1	1140	0
1.375	1443	0	1234	0
1.4	1530	0	1258	0
1.425	1458	0	1208	0
1.45	1283	0.5	1136	0.5
1.475	1034	1	840	1
1.5	1012	1	866	1
1.525	1053	1	889	1
1.55	1068	1	902	1
1.575	1237	0	1039	0
1.6	1252	0	1070	0
1.625	1310	0	1198	0
1.65	1269	0	1018	0
1.675	913	1	743	1
1.7	945	1	722	1
1.725	888	1	788	1
1.75	900	1	771	1
1.775	1190	0	1023	0
1.8	1068	0	983	0
1.825	1055	0	967	0
1.85	1095	0	926	0
1.875	1007	0	613	1
1.9	835	1	720	1
1.925	834	1	701	1
1.95	828	1	719	1
1.975	922	1	841	0
2	995	0	845	0
2.025	975	0	862	0
2.05	948	0	868	0
2.075	867	0	677	1
2.1	791	1	588	1
2.125	797	1	631	1
2.15	726	1	640	1
2.175	866	1	750	0
2.2	908	0	784	0

Time / s	Counts, 06:40	Switching, 06:40	Counts 08:45	Switching 08:45
2.225	926	0	785	0
2.25	878	0	844	0
2.275	819	0.5	647	1
2.3	733	1	612	1
2.325	750	1	588	1
2.35	730	1	587	1
2.375	746	1	645	0.5
2.4	839	0	725	0
2.425	828	0	713	0
2.45	931	0	674	0
2.475	752	0.5	654	0
2.5	594	1	532	1
2.525	607	1	498	1
2.55	595	1	502	1
2.575	608	1	536	1
2.6	789	1	654	0
2.625	929	0	706	0
2.65	715	0	681	0
2.675	788	0	621	0.5
2.7	573	1	543	1
2.725	544	1	487	1
2.75	539	1	441	1
2.775	549	1	512	0.5
2.8	629	0	648	0
2.825	665	0	639	0
2.85	675	0	592	0
2.875	695	0	626	0
2.9	487	1	468	1
2.925	503	1	469	1
2.95	480	1	481	1
2.975	479	1	430	1
3	549	0.5	496	0.5
3.025	656	0	513	0
3.05	685	0	570	0
3.075	648	0	567	0
3.1	498	1	485	1
3.125	411	1	508	1
3.15	463	1	441	1
3.175	441	1	463	1
3.2	496	0.5	480	0.5
3.225	605	0	569	0
3.25	569	0	589	0
3.275	637	0	506	0
3.3	522	0.5	487	0
3.325	411	1	375	1
3.35	418	1	439	1
3.375	429	1	434	1
3.4	456	1	408	1

Time / s	Counts, 06:40	Switching, 06:40	Counts 08:45	Switching 08:45
3.425	559	0	523	0
3.45	608	0	482	0
3.475	544	0	514	0
3.5	537	0	453	0.5
3.525	334	1	455	1
3.55	375	1	444	1
3.575	327	1	432	1
3.6	342	1	434	1
3.625	606	0	497	0
3.65	508	0	573	0
3.675	538	0	495	0
3.7	499	0	520	0
3.725	422	1	417	1
3.75	338	1	397	1
3.775	396	1	355	1
3.8	366	1	439	0.5
3.825	450	0	416	0
3.85	499	0	446	0
3.875	495	0	453	0
3.9	468	0	449	0
3.925	522	0	516	0
3.95	505	0	454	0
3.975	519	0	446	0
4	530	0	479	0
4.025	506	0	451	0
4.05	499	0	460	0
4.075	559	0	473	0
4.1	498	0	465	0
4.125	490	0	412	0
4.15	490	0	439	0
4.175	482	0	454	0
4.2	477	0	463	0
4.225	438	0	445	0
4.25	543	0	495	0
4.275	463	0	436	0
4.3	476	0	456	0
4.325	501	0	460	0
4.35	449	0	442	0
4.375	475	0	448	0
4.4	466	0	413	0
4.425	459	0	452	0
4.45	479	0	425	0
4.475	435	0	468	0
4.5	493	0	439	0
4.525	428	0	438	0
4.55	445	0	473	0
4.575	454	0	472	0
4.6	448	0	451	0

Time / s	Counts, 06:40	Switching, 06:40	Counts 08:45	Switching 08:45
4.625	486	0	587	0
4.65	377	0.5	391	1
4.675	296	1	386	1
4.7	345	1	373	1
4.725	320	1	334	1
4.75	296	1	365	1
4.775	366	1	359	1
4.8	306	1	384	1
4.825	342	1	331	1
4.85	337	1	334	1
4.875	312	1	374	1
4.9	335	1	332	1
4.925	360	1	340	1
4.95	314	1	350	1
4.975	344	1	363	1
5	366	1	371	1
5.025	323	1	329	1
5.05	258	1	316	1
5.075	332	1	326	1
5.1	334	1	354	1
5.125	290	1	317	1
5.15	374	0.5	370	0.5
5.175	470	0	364	0
5.2	438	0	391	0
5.225	397	0	360	0
5.25	415	0	410	0
5.275	413	0	368	0
5.3	378	0	412	0
5.325	421	0	432	0
5.35	446	0	376	0
5.375	386	0	382	0
5.4	438	0	406	0
5.425	386	0	406	0
5.45	396	0	364	0
5.475	402	0	320	0
5.5	408	0	415	0

Table B.3.: Number of counts and switching files for the measurements 11:15 and 12:25 recorded 01/11/11

Time / s	Counts, 11:15	Switching, 11:15	Counts 12:25	Switching 12:25
0.025	7357	0	6670	0
0.05	595	0	599	0
0.075	579	0	587	0
0.1	584	0	610	0
0.125	573	0	639	0
0.15	597	0	551	0
0.175	546	0	573	0
0.2	578	0	601	0
0.225	128633	0	122595	0
0.25	1198	0	1178	0
0.275	1214	0	1296	0
0.3	1058	0	1372	0
0.325	1183	0	1233	0
0.35	1087	0	1237	0
0.375	1137	0	1092	0
0.4	1155	0	1106	0
0.425	988	0	1038	0
0.45	1048	0	1087	0
0.475	1076	0	1042	0
0.5	966	0	1009	0
0.525	965	0	1107	0
0.55	1014	0	1083	0
0.575	968	0	980	0
0.6	1033	0	1035	0
0.625	943	1	900	0.5
0.65	965	1	816	1
0.675	858	1	769	1
0.7	871	1	849	1
0.725	788	1	725	1
0.75	851	1	788	1
0.775	791	1	696	1
0.8	768	1	687	1
0.825	793	1	559	1
0.85	692	1	522	1
0.875	700	1	540	1
0.9	704	1	593	1
0.925	735	0.5	546	1
0.95	751	0	853	0
0.975	733	0	783	0
1	747	0	721	0

Time / s	Counts, 11:15	Switching, 11:15	Counts 12:25	Switching 12:25
1.025	672	0.5	712	0
1.05	673	1	630	1
1.075	630	1	597	1
1.1	622	1	617	1
1.125	512	1	522	1
1.15	545	1	511	1
1.175	587	1	451	1
1.2	615	1	397	1
1.225	553	1	466	1
1.25	505	1	447	1
1.275	550	1	469	1
1.3	429	1	489	1
1.325	445	1	453	1
1.35	553	0	555	0.5
1.375	604	0	604	0
1.4	542	0	607	0
1.425	555	0	579	0.5
1.45	561	0	528	1
1.475	425	1	406	1
1.5	437	1	394	1
1.525	421	1	454	1
1.55	379	1	446	0.5
1.575	427	1	513	0
1.6	373	1	583	0
1.625	407	1	587	0
1.65	404	1	486	0.5
1.675	342	1	430	1
1.7	351	1	391	1
1.725	344	1	390	1
1.75	354	1	473	0.5
1.775	509	0	509	0
1.8	389	0	451	0
1.825	438	0	535	0
1.85	477	0	498	0.5
1.875	358	1	320	1
1.9	323	1	292	1
1.925	355	1	282	1
1.95	281	1	311	0.5
1.975	265	1	423	0
2	328	1	454	0
2.025	293	1	398	0
2.05	343	1	435	0
2.075	282	1	349	1
2.1	294	1	315	1
2.125	286	1	325	1
2.15	298	0.5	321	1
2.175	333	0	368	0
2.2	334	0	373	0

Time / s	Counts, 11:15	Switching, 11:15	Counts 12:25	Switching 12:25
2.225	334	0	423	0
2.25	335	0	372	0.5
2.275	308	1	333	1
2.3	277	1	259	1
2.325	237	1	251	1
2.35	241	1	214	1
2.375	258	1	284	0.5
2.4	292	1	391	0
2.425	223	1	358	0
2.45	244	1	351	0
2.475	271	1	335	0.5
2.5	284	1	270	1
2.525	232	1	267	1
2.55	242	1	241	1
2.575	241	1	285	0.5
2.6	342	0	380	0
2.625	258	0	334	0
2.65	337	0	317	0
2.675	272	0.5	347	0
2.7	254	1	245	1
2.725	207	1	232	1
2.75	212	1	200	1
2.775	241	1	234	1
2.8	267	1	348	0
2.825	252	1	311	0
2.85	241	1	291	0
2.875	239	1	308	0
2.9	218	1	264	1
2.925	213	1	275	1
2.95	220	1	225	1
2.975	286	0.5	246	0.5
3	229	0	308	0
3.025	274	0	331	0
3.05	248	0	316	0
3.075	211	1	350	0
3.1	258	1	256	1
3.125	233	1	230	1
3.15	220	1	228	1
3.175	218	1	218	1
3.2	203	1	256	0
3.225	210	1	247	0
3.25	218	1	255	0
3.275	220	1	288	0
3.3	218	1	268	0.5
3.325	224	1	202	1
3.35	201	1	192	1
3.375	199	1	219	1
3.4	201	1	176	1

Time / s	Counts, 11:15	Switching, 11:15	Counts 12:25	Switching 12:25
3.425	221	0	206	0.5
3.45	228	0	266	0
3.475	256	0	268	0
3.5	238	0	327	0
3.525	200	1	166	1
3.55	182	1	179	1
3.575	200	1	201	1
3.6	218	1	220	0.5
3.625	211	1	246	0
3.65	166	1	285	0
3.675	191	1	292	0
3.7	167	1	272	0
3.725	244	1	220	0.5
3.75	206	1	174	1
3.775	188	1	245	1
3.8	196	1	186	1
3.825	248	0	176	1
3.85	208	0	260	0
3.875	246	0	244	0
3.9	234	0	258	0
3.925	238	0	232	0
3.95	232	0	244	0
3.975	216	0	252	0
4	250	0	227	0
4.025	214	0	268	0
4.05	241	0	224	0
4.075	236	0	228	0
4.1	234	0	242	0
4.125	206	0	277	0
4.15	206	0	252	0
4.175	241	0	257	0
4.2	244	0	210	0
4.225	260	0	292	0
4.25	229	0	241	0
4.275	209	0	224	0
4.3	220	0	273	0
4.325	206	0	272	0
4.35	201	0	263	0
4.375	160	0	226	0
4.4	220	0	236	0
4.425	229	0	194	0
4.45	244	0	276	0
4.475	224	0	256	0
4.5	228	0	224	0
4.525	256	0	200	0
4.55	209	0	190	0
4.575	224	0	200	0
4.6	234	0	273	0

Time / s	Counts, 11:15	Switching, 11:15	Counts 12:25	Switching 12:25
4.625	307	0	266	0
4.65	209	0.5	196	1
4.675	174	1	180	1
4.7	170	1	194	1
4.725	182	1	208	1
4.75	171	1	190	1
4.775	188	1	197	1
4.8	189	1	126	1
4.825	214	1	212	1
4.85	181	1	197	1
4.875	182	1	195	1
4.9	182	1	186	1
4.925	162	1	192	1
4.95	206	1	174	1
4.975	184	1	150	1
5	164	1	181	1
5.025	148	1	150	1
5.05	160	1	182	1
5.075	188	1	170	1
5.1	158	1	177	1
5.125	184	1	170	1
5.15	204	0	190	0.5
5.175	188	0	184	0
5.2	202	0	240	0
5.225	180	0	220	0
5.25	172	0	186	0
5.275	192	0	207	0
5.3	182	0	198	0
5.325	172	0	204	0
5.35	188	0	217	0
5.375	198	0	217	0
5.4	192	0	226	0
5.425	176	0	238	0
5.45	172	0	200	0
5.475	224	0	196	0
5.5	222	0	232	0

APPENDIX C:
TABLES OF FIT RESULTS, FIT FUNCTIONS AND RESIDUALS

Table C.1.: Fit results of the individual fit of the 06:40 data, as returned by the fit routine Minuit.

Fit variable	Value returned by Minuit	Error calculated by Minuit
τ_1	+1.99899607E+00	5.13287701E-02
C	+3.13877184E+02	3.55700752E+00
A_0	+1.14068655E+03	4.35838473E+01
A_{75}	+6.25583401E+02	5.12377866E+01
A_{150}	+4.92892282E+02	4.71824653E+01
A_{225}	+4.45373621E+02	4.65923256E+01
A_{300}	+3.96620665E+02	4.88680907E+01
A_{375}	+2.22419963E+02	4.54723449E+01
A_{450}	+1.05186093E+02	4.27659534E+01
A_{525}	-1.05246631E+01	4.19659435E+01
B	+2.49055021E+03	5.06336956E+01
τ_2	+9.35879477E-01	1.85656747E-02

Table C.2.: Fit results of the individual fit of the 08:45 data, as returned by the fit routine Minuit.

Fit variable	Value returned by Minuit	Error calculated by Minuit
τ_1	+2.45782390E+00	+1.89491354E-01
C	+3.25112675E+02	+4.04811249E+00
A_0	+4.52632778E+02	+4.93439672E+01
A_{75}	+2.06237766E+02	+5.42483786E+01
A_{150}	+1.84288651E+02	+4.81059281E+01
A_{225}	+4.67085341E+01	+4.23763916E+01
A_{300}	+1.70386770E+00	+4.22027050E+01
A_{375}	-3.95322270E+01	+4.00125778E+01
A_{450}	-3.00304345E+01	+3.56225837E+01
A_{525}	-3.06076924E+01	+3.48257264E+01
B	+2.52661465E+03	+5.89135158E+01
τ_2	+1.02620632E+00	+1.58929214E-02

Table C.3.: Fit results of the individual fit of the 11:15 data, as returned by the fit routine Minuit.

Fit variable	Value returned by Minuit	Error calculated by Minuit
τ_1	4.24498357E+00	+1.98833530E-01
C	+1.62470267E+02	+1.26754432E+00
A_0	+1.11183589E+02	+4.25538614E+00
A_{50}	+5.43160787E+01	+1.53340260E+01
A_{100}	+2.22221251E+01	+1.32696347E+01
A_{150}	+4.39336536E+01	+1.34156401E+01
A_{200}	+1.82581698E+01	+1.27855973E+01
A_{250}	+6.56229842E+01	+1.43118142E+01
A_{300}	-1.90299115E+00	+1.34565082E+01
A_{350}	+2.75216210E+01	+1.35293991E+01
A_{400}	+2.27372970E+01	+1.21683866E+01
A_{450}	+9.30427164E-01	+6.04415707E-03
A_{500}	−1.51130278E+01	+1.14631174E+01
A_{550}	-9.46424506E+00	+5.17125797E+01
B	+1.30009257E+03	+9.90618995E+00
τ_2	+8.20351804E-01	+3.88811130E-01

Table C.4.: Fit results of the individual fit of the 12:25 data, as returned by the fit routine Minuit.

Fit variable	Value returned by Minuit	Error calculated by Minuit
τ_1	+2.51551356E+00	+1.64470552E-01
C	+1.71614652E+02	+2.78537081E+00
A_0	+2.95266341E+02	+3.53063747E+01
A_{150}	+2.95266341E+02	+3.53063747E+01
A_{300}	+2.82991346E+01	+2.98593959E+01
A_{450}	-5.97539631E+01	+2.74275620E+01
B	+1.10050543E+03	+3.19925421E+01
τ_2	+9.52574311E-01	+3.53167982E-02

Table C.5.: Fit results of the combined fit of all four data sets, as returned by the fit routine Minuit.

Fit variable	Value returned by Minuit	Error calculated by Minuit
A_0	+1.24713837E+03	+4.00850163E+01
A_{50}	+8.87657550E+02	+1.50256430E+02
A_{75}	+6.72064391E+02	+4.63637927E+01
A_{100}	+6.65670344E+02	+1.29516221E+02
A_{150}	+5.27713162E+02	+3.80593385E+01
A_{200}	+3.78274028E+02	+1.27304410E+02
A_{225}	+4.41058435E+02	+4.06816417E+01
A_{250}	+7.90650254E+02	+1.35142756E+02
A_{300}	+2.94347021E+02	+3.61906668E+01
A_{350}	+3.04382171E+02	+1.43130552E+02
A_{375}	+2.38370437E+02	+3.95460340E+01
A_{400}	+2.49296682E+02	+1.27864524E+02
A_{450}	+4.18026541E+01	+3.24105358E+01
A_{500}	-1.32914505E+02	+1.30919423E+02
A_{525}	+7.75795485E+01	+3.72262977E+01
A_{550}	-6.25627612E+01	+1.38525047E+02
C	+1.47518614E-01	+2.33120631E-03
A_{0640}	+1.00000000E+00	+0.00000000E+00
A_{0845}	+5.50279400E-01	+1.68360867E-02
A_{1115}	+1.89381669E-01	+1.21793413E-02
A_{1225}	+3.19002028E-01	+1.16363673E-02
B_{0640}	+2.21642737E+03	+3.56319471E+01
B_{0845}	+2.32634797E+03	+3.51635955E+01
B_{1115}	+1.13382382E+03	+1.89813621E+01
B_{1225}	+1.07899276E+03	+1.47718746E+01
τ_s	+1.90908506E+00	+3.80396882E-02
τ_b	+9.68137441E-01	+9.89960362E-03
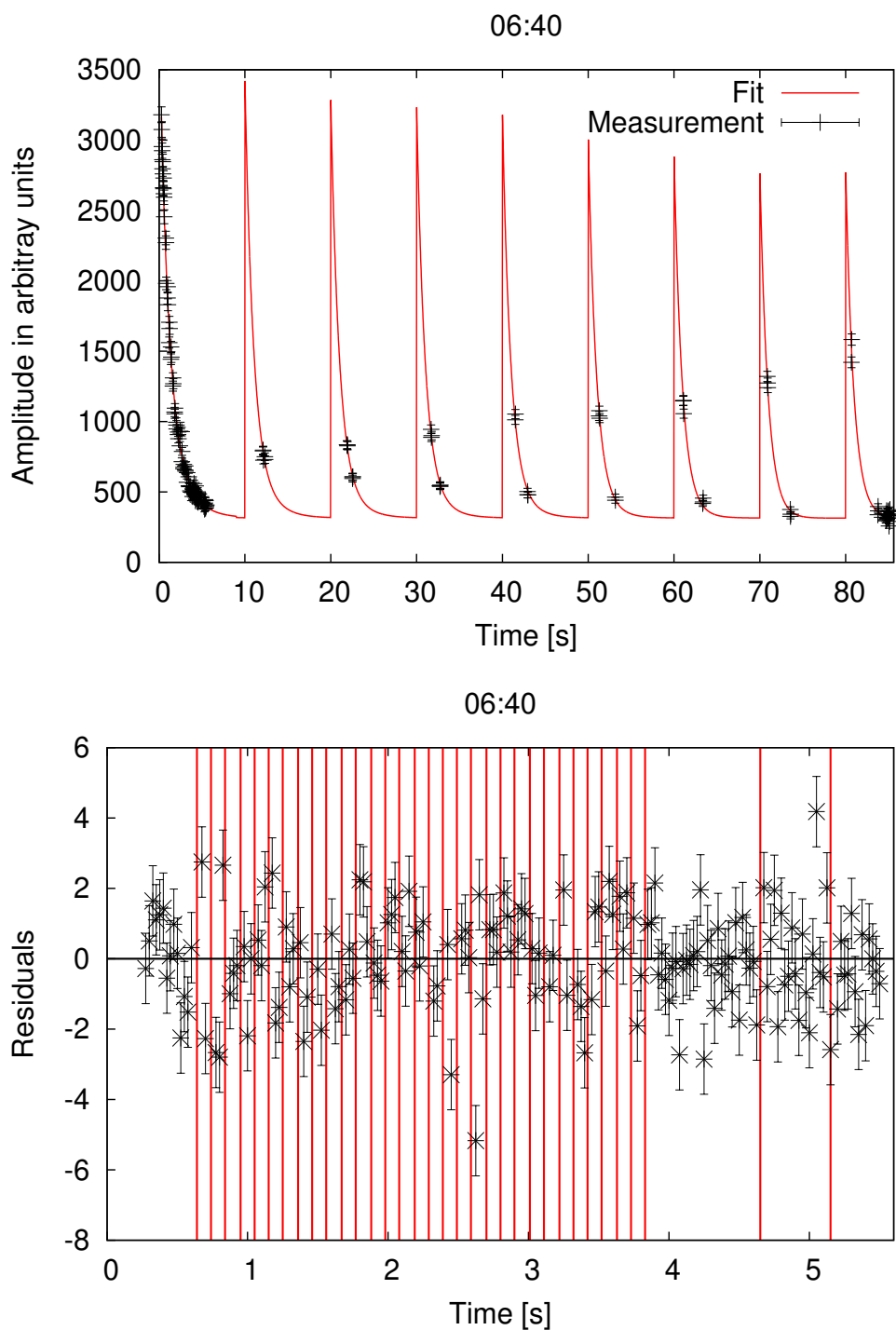
Figure C.1.: Data of the 06:40 measurement with time delays of 10 s for each retardation step. The fit function is drawn with a red line. The graph on the bottom shows the residuals without the delay times for the different retardation voltages. The times of the voltage switching are marked with vertical red lines.
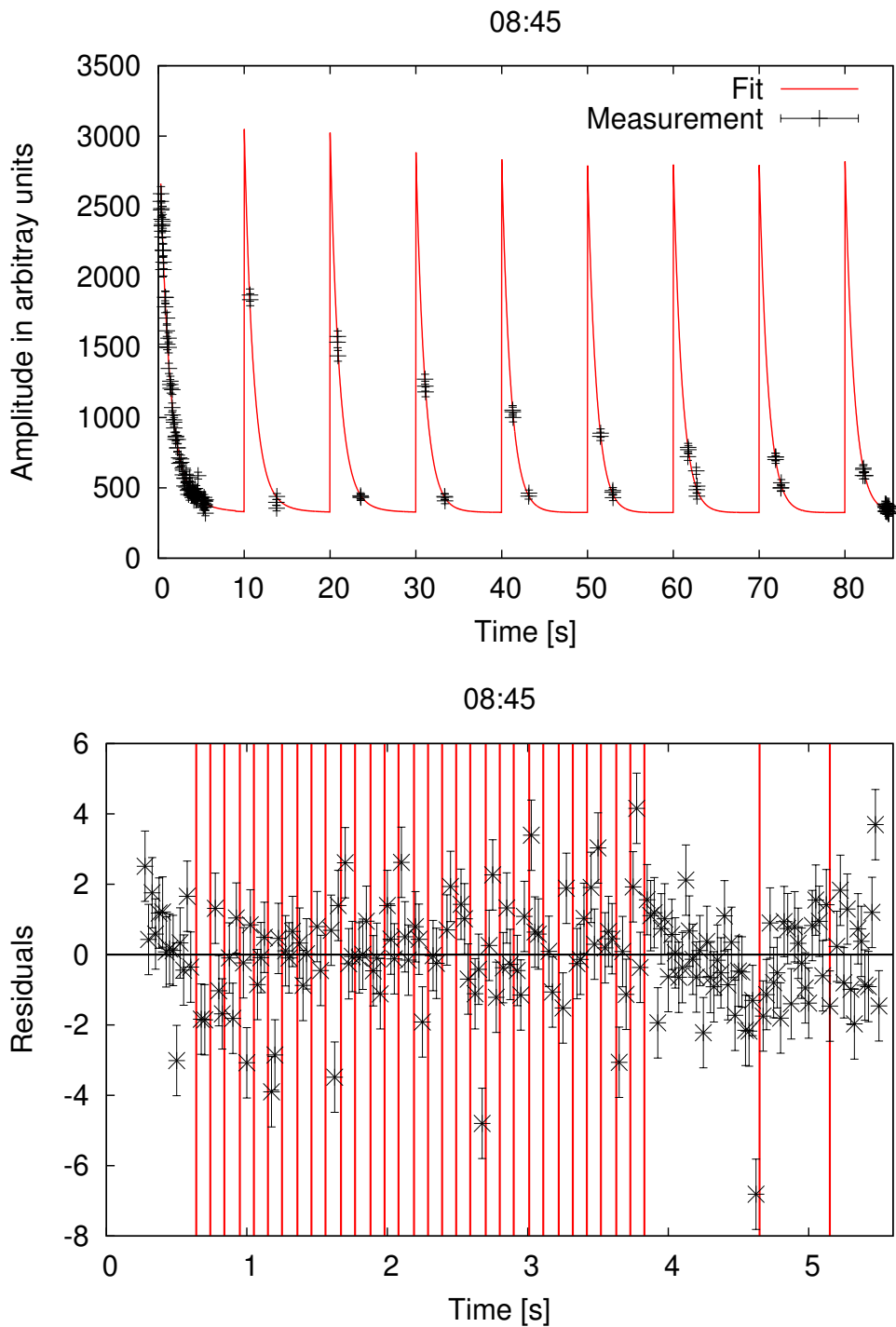
Figure C.2.: Data of the 08:45 measurement with time delays of 10 s for each retardation step. The fit function is drawn with a red line. The decrease in the target's performance already becomes visible in the smaller amplitude. The graph on the bottom shows the residuals without the delay times for the different retardation voltages. The times of the voltage switching are marked with vertical red lines.
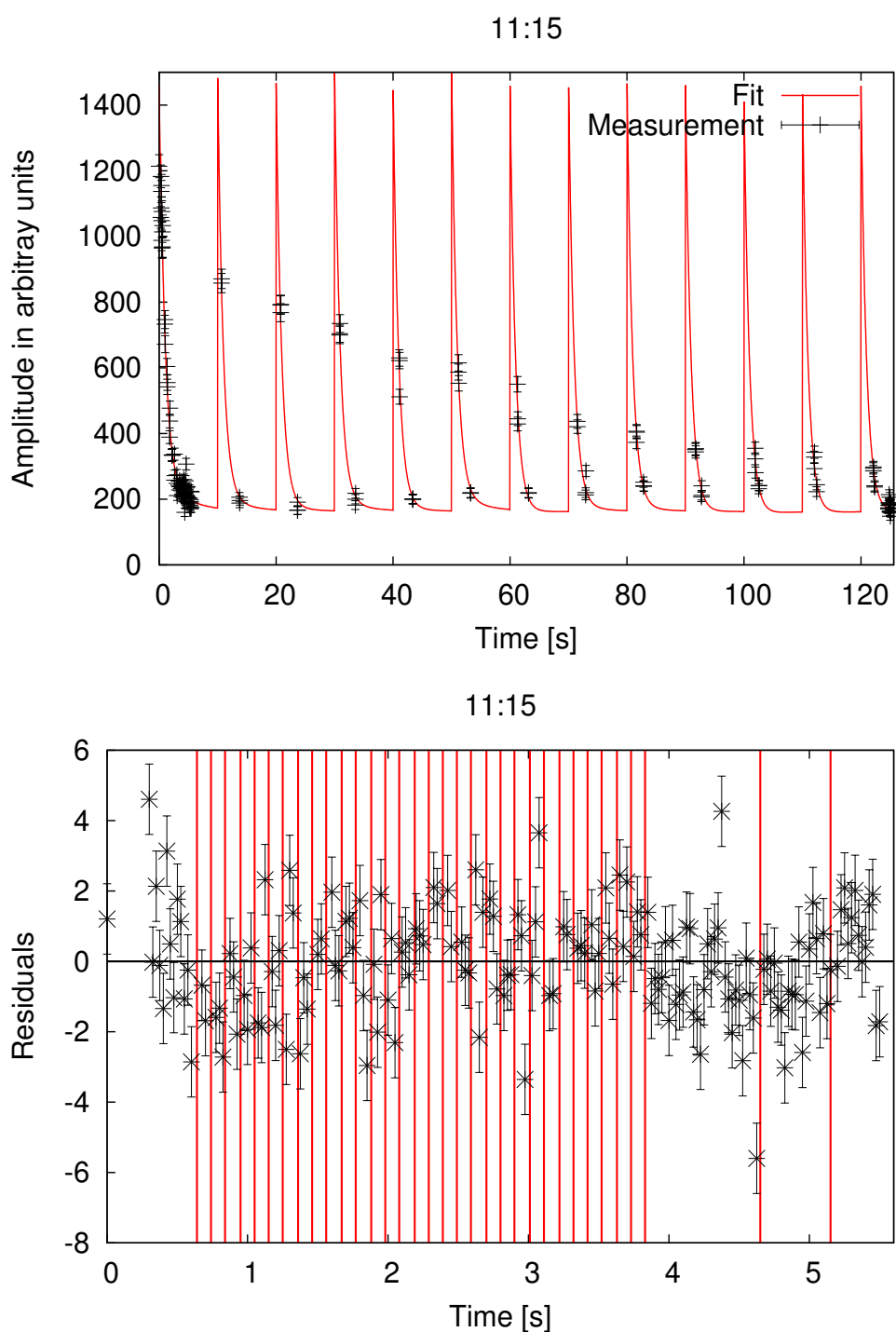
Figure C.3.: Data of the 11:15 measurement with time delays of 10 s for each retardation step. The fit function is drawn with a red line. Further decrease in the target's performance becomes obvious regarding the smaller amplitude. The graph on the bottom shows the residuals without the delay times for the different retardation voltages. The times of the voltage switching are marked with vertical red lines.
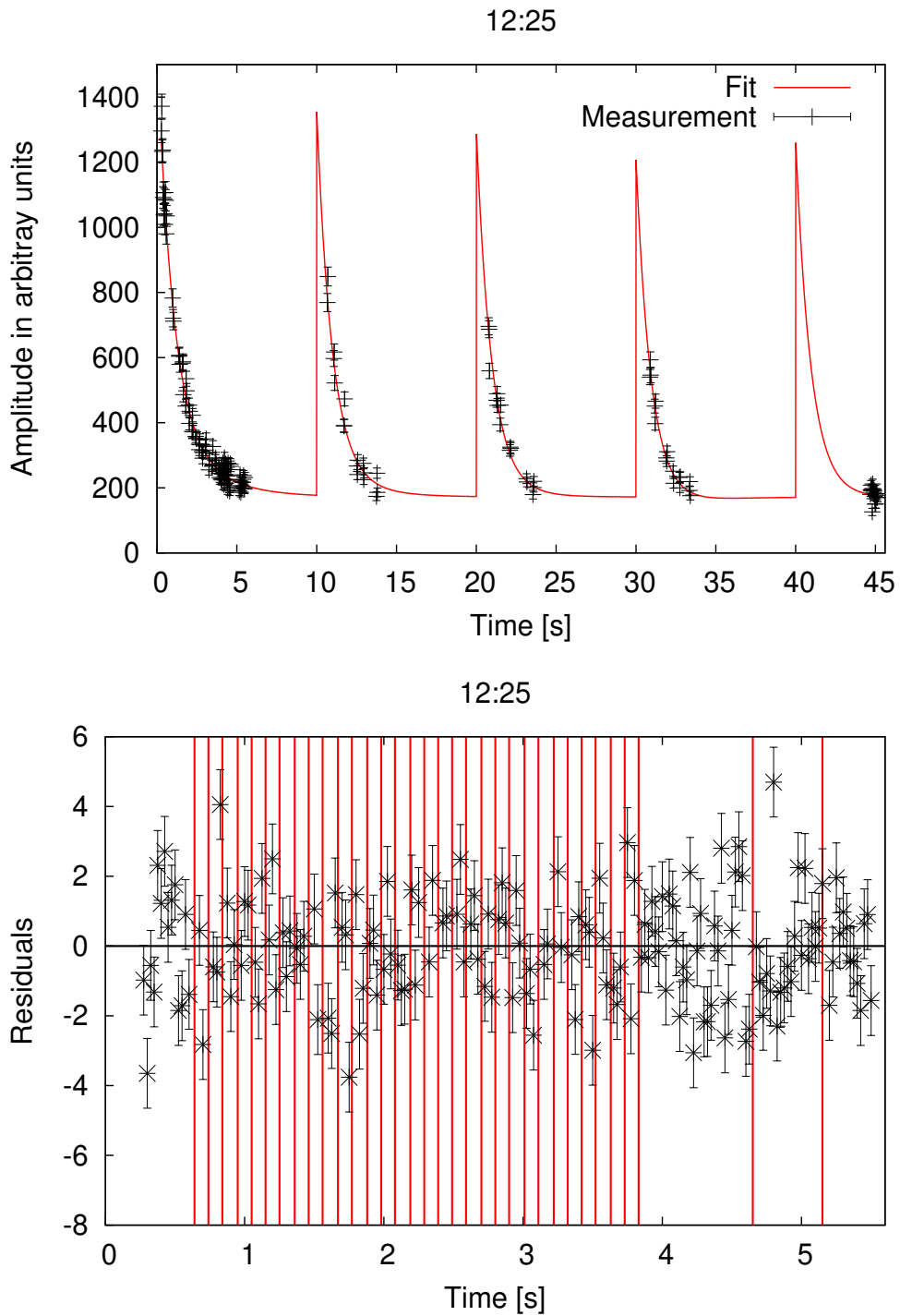
Figure C.4.: Data of the 12:25 measurement with time delays of 10 s for each retardation step. The fit function is drawn with a red line. The graph on the bottom shows the residuals without the delay times for the different retardation voltages. The times of the voltage switching are marked with vertical red lines.
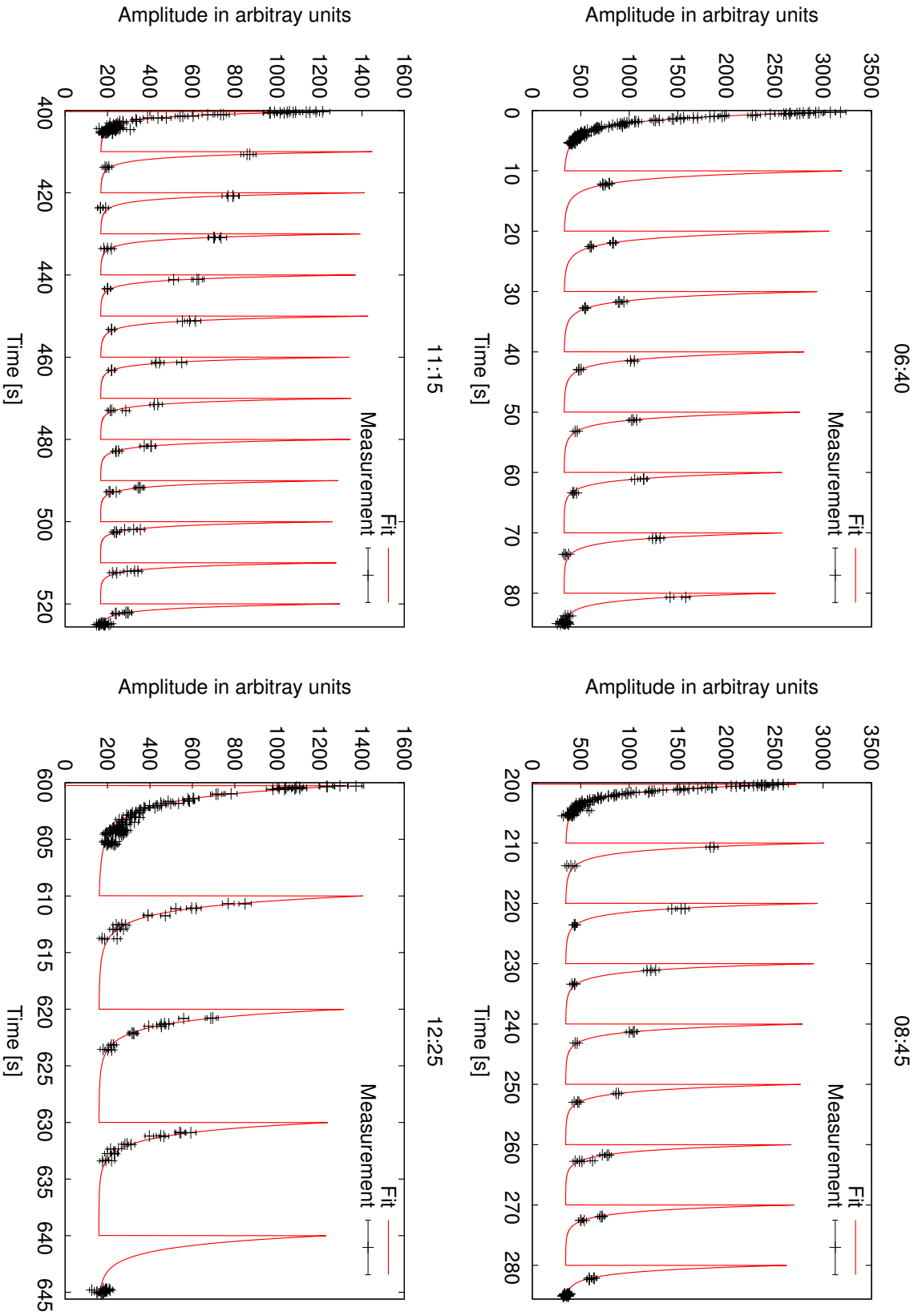
Figure C.5.: Zooms on the fit function and the data of the combined fit of each data set, 06:40 and 08:45 on top, 11:15 and 12:25 on the bottom. Uncertainties are multiplied by a factor of $\sqrt{(\chi^2)} = 1.72$.
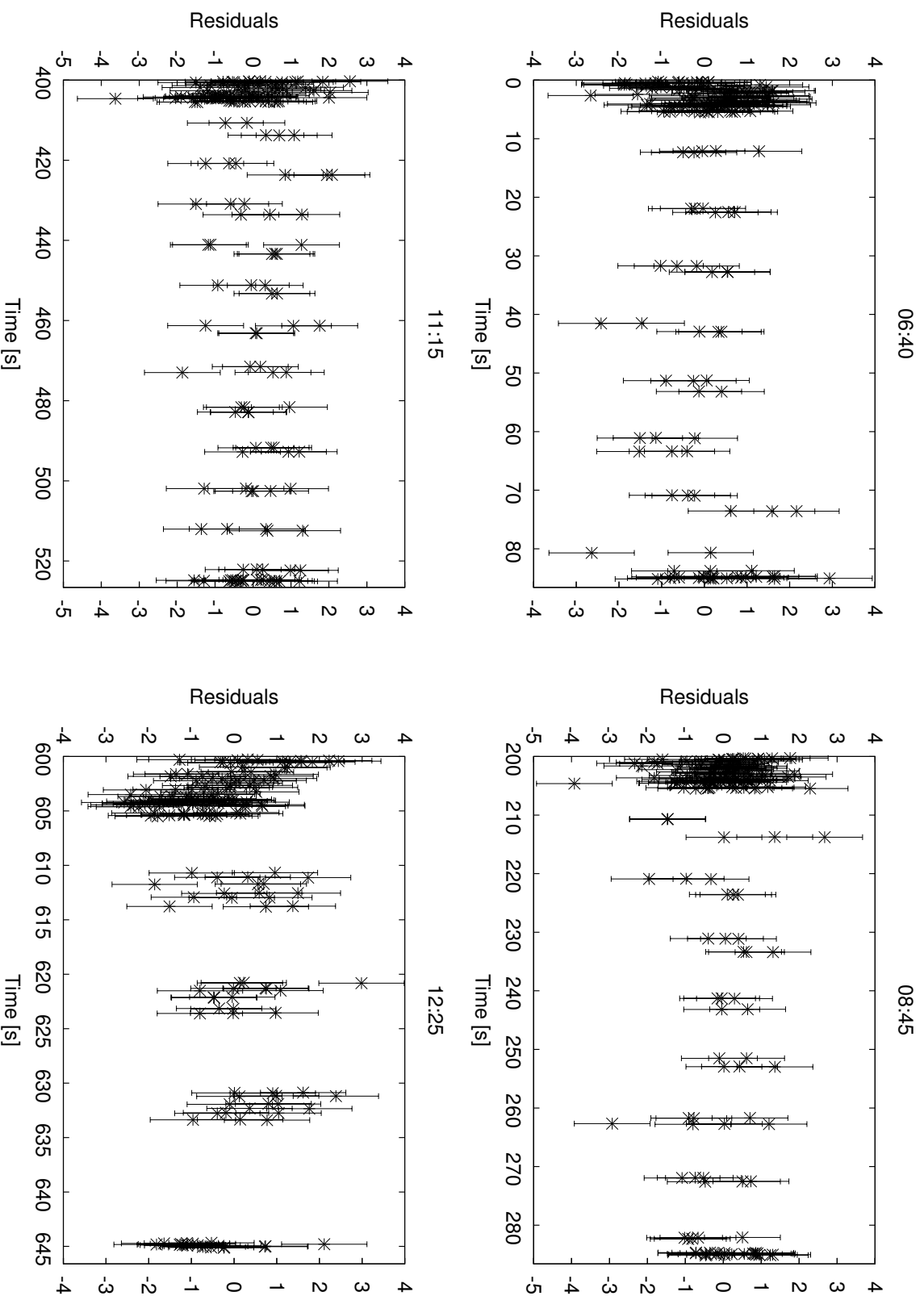
Figure C.6.: Zooms on the residuals of the combined fit of each data set, 06:40 and 08:45 on top, 11:15 and 12:25 on the bottom. Uncertainties are multiplied by a factor of $\sqrt{(\chi^2)} = 1.72$).

List of figures

List of tables

References

[Ade99]   E. G. Adelberger et al., *Positron-neutrino correlation in the* $0^+ \rightarrow 0^+$ *decay of* ^{32}Ar, Phys. Rev. Lett. 83 (1999) 1299.

[Alv37]   L. W. Alvarez, *Nuclear K Electron Capture*, Phys. Rev. 52 (1937) 134–135.

[Ame05]   F. Ames et al., *Cooling of radioactive ions with the Penning trap REXTRAP*, Nuclear Instrumentations and Methods in Physical ResearchA 538 (2005), 17–32.

[And57]   H. L. Anderson & C. M. G. Lattes, *Search for the Electronic Eecay of the Positive Pion*, Il Novo Cimento VI 6 (1957) 3216–3241.

[Aud95]   G. Audi and A. H. Wapstra, *The 1995 update to the atomic mass evaluation*, Nuclear Physics A595 vol. 4 (1995) 409–480.

[Avi12]   O. Aviv, *Beta decay measurements from* ^6He *using an electrostatic ion beam trap*, J. Phys.: Conf. Ser. 337 (2012) 012020.

[Azu77]   G. Azuelos et al., *Half-lives and branching ratios of some T=1/2 nuclei*, Phys. Rev. C 15 (1977) 1847–1851.

[Bar12]   J. Barnstedt, *Fortgeschrittenen-Praktikum – Versuch MCP-Detektoren*, Versuchsanleitung, Institut für Astronomie und Astrophysik, Abteilung Astronomie, Eberhard Karls Universität Tübingen, (2012). *http://astro.uni-tuebingen.de/seminars/praktikum/VersuchsAnleitungMCP.pdf*

[Bas06]   M. S. Basunia, Nuclear Data Sheets 107, 3323 (2006).

[Bae08]   S. Baeßler et al., *First measurements with the neutron decay spectrometer aSPECT*, Eur. Phys. J. A 38 (1) (2008) 17–26.

[Bea11]   O. von Beayer, O. Hahn & L. Meitner, *Über die β-Strahlen des aktiven Niederschlags des Thoriums*, Phys. Z. 12 (1911) 273–279.

[Bak11]   A. Bakenecker, *An offline ion source for* ^{40}Ar *ions for the WITCH experiment*, Bachelor thesis, WWU Münster (2011).

[Bec96]   H. Becquerel, *On the rays emitted by phosphorescence*, Comptes Rendus 122 (1896) 420–421.

[Bec96a] H. Becquerel, *On the invisible rays emitted by phosphorescent bodies*, Comptes Rendus 122 (1896) 501–503.

[Bec03]   M. Beck et al., *WITCH: a recoil spectrometer for β-decay*, Nuclear Instruments and Methods in Physics Research B204 (2003) 521–525.

[Bec10]   M. Beck, K. Valerius et al., *Effect of a sweeping conductive wire on electrons stored in a Penning-like trap between the KATRIN spectrometers*, Eur. Phys. J. A 44 (2010) 499–51.

References

[Bec11] M. Beck et al., *First detection and energy measurement of recoil ions following beta decay in a Penning trap with the WITCH experiment*, European Physics Journal A (2011) 47–45.

[Bec12] M. Beck, private communication.

[Beg77] M. A. B. Beg et al., *Manifest Left-Right Symmetry and its Experimental Consequences*, Phys. Rev. Lett. 38 (1977) 1252.

[Ber12] J. Beringer et al., Particle Data Group, PR D86, 010001 (2012). URL: *http://pdg.lbl.gov*

[Bla52] J. M. Blatt &V. F. Weisskopf, *Theoretical Nuclear Physics*, J. Wiley & Sons(1952) 682.

[Bla03] K. Blaum et al., *Masses of ^{32}Ar and ^{33}Ar for Fundamental Tests*, Phys. Rev. Lett. 91 26 (2003) 260801.

[Bla06] K. Blaum, *High-accuracy mass spectrometry with stored ions*, Phys. Rep. 425 (2006) 1–78.

[Bre11] M. Breitenfeldt, *First high-quality data with ^{35}Ar: the search for scalar weak currents with WITCH*, presentation, AP seminar, GSI, Feb. (2011).

[Bre11a] M. Breitenfeldt, *Analysis of the MCS On-Off-measurements as taken in November 2011*, WITCH internal report (2012).

[Bre12] M. Breitenfeldt, private communication (2010, 2011,2012).

[Bre13] M. Breitenfeldt, in preparation.

[Bro86] L. S. Brown & G. Gabrielse, *Geonum theory: Physics of a single electron or ion in a Penning trap*, Rev. Mod. Phys. 58 (1) (1986) 233.

[Bur05] Burle Industries, INC. Procedures and Specifications of MCP 75/32/8 D 60:1, (2005)[1]

[Cer11] CERN radiation protection service, source group, data sheet of source No. 4263RP.

[Cer12] CERN radiation protection service, source group, private communication.

[Che11] J. Chen, J. Cameron, B. Singh, Nuclear Data Sheets 112,2715 (2011).

[Coe07] S. Coeck et al., *A pulsed drift cavity to capture 30 keV ion bunches at ground potential*, Nuclear Instruments and Methods in Physics Research A 572 (2007) 585–595.

[Coe07a] S. Coeck et al., *Ab initio simulations on the behavior of small ion clouds in the WITCH Penning trap system*, Nucl. Instr. Meth. A 574 (2007) 370-384.

[Coe07b] S. Coeck, *Search for non Standard Model physics in nuclear β-decay with the WITCH experiment*, PhD thesis, K U Leuven (2007).

[Cor09] T. J. Corona, *Tools for Electromagnetic Field Simulation in the KATRIN Experiment*, master thesis, MIT (2009).

[Del05] B. Delauré, *Development of a Penning Trap based Set-up for Precision Tests of the Standard Model*, PhD thesis, K. U. Leuven (2005).

[Ebe79] E. H. Eberhardt, *Gain model for microchannel plates*, J. for Applied Optics, 18(9) (1979) 1–6.

---

[1]Burle Industries was bought out by Photonis in 2005.

[Egg05] F. Eggert, *Standardfrei Elektronenstrahl-Mikroanalyse*, Books On Demand GmbH Norder-stedt (2005).

[End90] P. M. Endt, *Energy levels of A = 21-44 nuclei (VII)*, Nuclear Physics A521, 1 (1990).

[Est11] ESTAR homepage, *http://physics.nist.gov/PhysRefData/Star/Text/ESTAR.html.* (2011).

[Fer34] E. Fermi, *Versuch einer Theorie der β-Strahlen. I*, Z. Phys. 88 (1934) 161–177.

[Fer11] S. Fernandez et al., *Microstructure evolution of nanostructured and submicrometric porous refractory ceramics induced by a continuous high-energy proton beam*, J. of Nuclear Materials IV 416(1-2) (2011) 99–110.

[Fey58] R. P. Feynman & M. Gell-Mann, *Theory of the Fermi Interaction*, Phys. Rev. 109 (1958) 193–198.

[Fir37] M. Fierz, *Zur Fermischen Theorie des β-Zerfalls*, Z. Phys. 104 (1937) 553–565.

[Fle11] X. Fléchard et al., *Measurement of the $\beta - \nu$ correlation coefficient $a_{\beta\nu}$ in the β decay of trapped $^6He^+$ ions*, Journal of Physics G: Nuclear and Particle Physics, 38(5) (2011) 055101.

[Fle11a] X. Fléchard, private communication (2011).

[Fra11] H. Franberg et al., *Off-line commissioning of the ISOLDE cooler*, Nucl. Instr. Meth. B 266 19-20 (2008) 4502–4504.

[Fri08] P. Friedag, *Bahnverfolgungssimulationen für das WITCH-Experiment*, Diploma thesis, WWU Münster (2008).

[Fri12] P. Friedag, *Setup and callibration of the position sensitive micro channel plate detector of the WITCH experiment*, WITCH internal report (2012).

[Gam36] G. Gamow & E. Teller, *Selection Rules for the β-Disintegration*, Phys. Rev. 49 (1936) 895–899.

[Gar51] M. W. Garrett, *Thick Cylindrical Coil Systems for Strong Magnetic Fields with Field or Gradient Homogeneities of the 6th to 20th Order* J. Appl. Phys., 22 (1951) 1091.

[Glu93] F. Glück, *Measurable distributions of unpolarized neutron decay*, Phys. Rev. D 47 (1993) 2840–2848.

[Glu95] F. Glück, I. Jo, J. Last, *Measurable parameters of neutron decay*, Nucl. Phys. A 593 (1995) 125–150.

[Glu98] F. Glück, *Order-α radiative correction to ^6He and ^{32}Ar β decay recoil spectra*, Nuclear Physics A 628 (1998) 493–502.

[Glu05] F. Glück et al., *The neutron decay retardation spectrometer aSPECT: Electromagnetic design and systematic effects*, Eur. Phys. J. A 23 (2005) 135.

[Glu11] F. Glück, *Axisymmetric electric field calculation with zonal harmonic expansion*, Progress In Electromagnetics Research B 32 (2011) 319.

[Glu11a] F. Glück, *Axisymmetric magnetic field calculation with zonal harmonic expansion*, Progress In Electromagnetics Research B 32 (2011) 351.

[Glu12]   F. Glück, private communication (2012).

[Glu13]   F. Glück, to be published (2013).

[Gol57]   M. goldhaber et al., *Helicity of Neutrinos*, Phys. Rev. 109 (1957) 1015–1018.

[Gor05]   A. Gorelov et al., *Scalar interaction limits from the $\beta - \nu$ correlation of trapped radioactive atoms*, Phys. Rev. Lett., 94 (2005) 142501.

[Gor11]   S. van Gorp et al., *Simbuca, using a graphics card to simulate Coulomb interactions in a penning trap*, Nucl. Instr. Meth. **A** 638 (1) (2011) 192–200.

[Gor11a] S. van Gorp, private communication (2011).

[Gor12]   S. van Gorp, *Search for physics beyond the standard electroweak model with the WITCH experiment*, S. van Gorp, PhD thesis, K U Leuven, (2012).

[Ham58]   W. B. Herrmansfeldt et. al., *Determination of the Gamow-Teller beta decay interaction from the decay of Helium-6*, Phys. Rev. Lett. 1 (1958) 61.

[Har09]   J. C. Hardy & I. Towner, *Superallowed $0^+ \rightarrow 0^+$ nuclear β decays: A new survey with precision tests of the conserved vector current hypothesis and the standard model*, Phys. Rev. C 79 (2009) 055502.

[Her01]   P. Herczeg, *Beta Decay Beyond the Standard Model*, Prog. Part. Nucl. Phys. 46 (2001) 413-457.

[Imp58]   G. Impeduglia et. al., *β Decay of the Pion*, Phys. Rev. Lett. 1 (1958) 249–251.

[Iso12]   ISOLDE homepage, *http://isolde.web.cern.ch/ISOLDE/* (2012).

[Iac06]   V. E. Iacob et al., *Precise half-life measurements for the superallowed β^+ emitters ^{34}Ar and ^{34}Cl*, Phys. Rev. C 74, 055502 (2006).

[Jac57]   J. Jackson, S. Treiman & H. Wyld, *Possible Tests of Time Reversal Invariance in Beta Decay*, Phys. Rev. 106(3) (1957) 517–521.

[Jac57a] J. Jackson, S. Treiman & H. Wyld, *Coulomb Corrections in allowed beta transitions*, Nucl. Phys. 4 (1957) 206.

[Jan60]   J. Janecke, *The Half Lives of Some Positron Emitters with Superpermitted Transitions*, Z. Naturforsch. 15a (1960) 593.

[Joh63]   C. S. Johnson et al., *Precision Measurement of the Recoil Energy Spectrum from the Decay of ^6He*, Phys. Rev. 132 (1963) 1149–1165.

[Jol34]   F. & I. Joliot-Curie, *Artificial Production of a New Kind of Radio-Element*, Nature 133 (1934) 201–202.

[Kno10]   G. F. Knoll, *Radiation detection and measurement*, 4$^{\text{th}}$ ed., Wiley (2010).

[Koe56]   O. Koefed-Hansen, *Theoretical angular correlations in allowed beta decay*, Dan. MAt. Fys. Medd. 28 (1956).

[Kon10]   G. Konrad et al., *Impact of neutrondecy experiments on non-Standard Model physics*, World Scientific, *Physics Beyond the Standard Models of Particles, Cosmology and Astrophysics, Proceedings of the Fifth International Conference - Beyond 2010* (2010) 660-672.

[Koz05] V. Y. Kozlov, *WITCH, a Penning trap for weak interaction studies*, Ph. D. thesis, KU Leuven (2005).

[Kug00] E. Kugler, *The ISOLDE facility*, Hyperfine Interactions, 129 (2000) 23–42.

[Lan149] L. M. Langer & H. C. Price Jr., *Beta-Spectra of Forbidden Transitions*, Phys. Rev. 1949 76 (5) (1949) 641–646.

[Lee56] T. D. Lee & C. N. Young, *Question of Parity Conservation in Weak Interactions*, Phys. Rev. 104 (1) (1956) 254-258.

[Lie05] E. Liénard, et al., *Performance of a micro-channel plates position sensitive detector*, Nuclear Instruments and Methods in Physics Research A 551 (2005) 375–386.

[Lie11] E. Liénard, private communication (2011).

[Lob85] V. M. Lobashev & P. E. Spivak, *A method for measuring the electron antineutrino rest mass*, Nucl. Inst. and Meas. A 240 (1985) 305–310.

[Mad10] J. Mader, *Untersuchung von Eigenschaften und systematischen Effekten am WITCH Experiment*, Diploma thesis, WWU Münster (2010).

[Moh75] R. N. Mohapatra & J. C. Pati, *Left-right gauge symmetry and an isoconjugate model of CP violation*, Phys. Rev. D 11 (1975) 566.

[Moh75a] R. N. Mohapatra & J. C. Pati, *'Natural' left-right symmetry*, Phys. Rev. D 11 (1975) 2558.

[Nak10] K. Nakamura et al. (Particle Data Group), *2010 and 2011 partial update for the 2012 edition*, J. Phys. G 37 (2011) 075021.

[Ndt12] NDT Recourse Center homepage, *http://www.ndt-ed.org, Transmitted Intensity and Linear Attenuation Coefficient, http://www.ndt-ed.org/EducationResources/CommunityCollege/Radiography/Physics/attenuationCoef.htm* (2012).

[Nis12] NIST hompage, *X-Ray Mass Attenuation Coefficients, http://physics.nist.gov/PhysRefData/XrayMassCoef/tab1.html* (2012).

[Nis12a] NIST homepage, *Palladium Z = 46, http://physics.nist.gov/PhysRefData/XrayMassCoef/ ElemTab/z46.html* (2012).

[Nor11] Fachhochschule Nordhause, physikalisch-technisches Messpraktikum: Versuchsanleitung *Versuch K1: Grundversuche zur Kernphysik I (Statistik, α- und β-Strahlung, Abstandsgesetz) http://www.fh-nordhausen.de/uploads/media/Versuch_K1_R0_02.pdf* (2011).

[Nud12] NuDat 2.6 homepage, *http://www.nndc.bnl.gov/nudat2/chartNuc.jsp* (2012).

[Oxf02] Oxford Instruments, *Operators's Handbook for superconducting magnet system*, supplied to N. Severijns, project nr. 6195, (2002).

[Oxf11] Oxford Instruments, private communication (2011).

[Pak09] S. Pakvasa, *50 Years of V-A (Living Dangerously)*, J. of Phys. Conf. Ser. 196 (2009) 012005.

[Pat74] J. C. Pati, A. Salam, *Lepton number as the fourth 'color'*, Phys. Rev. D 10 (1974) 275.

[Pau30]   W. Pauli, *Liebe radioaktive Damen und Herren*, open letter, 1930.

[Pau33]   W. Pauli, *Über die Formulierung der Naturgesetze mit fünf homogenen Koordinaten - Teil I : Klassische Theorie*, Annalen Phys. 18 **5**5 (1933) 305–336.

[Pau33a]   W. Pauli, *Über die Formulierung der Naturgesetze mit fünf homogenen Koordinaten - Teil II : Die Diracschen Gleichungen für die Materiewellen*,Annalen Phys. 18 5 5 (1933) 337–372.

[Pen10]   L. Penscu et al., *Development of high efficiency Versatile Arc Discharge Ion Source at CERN ISOLDE*, Rev. Sci. Instrum. A 81 2 (2010) 906–910.

[Pho11]   Photonis, USA, private communication (2011).

[Pic92]   A. Picard et al., *A solenoid retarding spectrometer with high resolution and transmission for keV electrons* Nucl. Inst. and Meas. B 63 (1992) 345–358.

[Pre92]   W. H. Press, S. A. Teukolsky, W. T. Vettering and B. P. Flannery, *Numerical Recipes in C*, Cambridge University Press, Second Edition (1992).

[Pri81]   P. J. Prince and J. R. Dormand, *High order embedded Runge-Kutta formulae*, J. Comput. and Appl. Math., 7 (1981) 67–75.

[Qua13]   Quadrant Engineering Plastic Products homepage, *www.quadrantplastics.com*, KETRON PEEK-1000 data sheet, *http://www.quadrantplastics.com/fileadmin/quadrant/documents/QEPP/EU/Product_ Data_Sheets_PDF/AEP/KetronPEEK_1000_D_PDS_0808.pdf* (2013).

[Ram11]   J. P. Ramos, *Effect of calcium oxide microstrucuture on the diffusion of isotopes*, Masterthesis, University of Aveiro (2012).

[Rei56]   F. Reines & C. L. Cowan, *The Neutrino*, Nature 178 (1956) 446–449.

[Rod06]   D. Rodriguez et al., *The LPCTrap facility: A novel transparent Paul trap for high-precision experiments*, Nucl. Inst. and Meth. in Phys. Res. A 565 (2) (2006) 876–889.

[Roe11]   RoentDek Handels GmbH, *MCP Delay Line Detector Manual*, *http://www.roentdek.com/manuals/ MCP Delay Line manual(9.22.1003.1).pdf* (2011).

[Roe11a]   RoentDek Handels GmbH, *DLD 40 and DLD 80 assembly movie*, *http://www.roentdek.com/info/movies/dld_40_80_assembl.htm* (2011).

[Roe11b]   RoentDek Handels GmbH, *Storage, handling and operation of microchannel plates*, *http://www.roentdek.com/manuals/handling_channel_v20040309.pdf*.

[Roe11c]   RoentDek Handels GmbH, *The FAMP8 and FAMP1+ Manual*, *http://www.roentdek.com/manuals/The FAMPManual (6.2.90.x).pdf* (2011).

[Roe11d]   RoentDek Handels GmbH, *The RoentDek Constant Fraction Discriminators CFD8b, CFD4b and CFD1b*, *http://www.roentdek.com/manuals/CFD Manual (9.1.904.1).pdf* (2011).

[Roe12]   RoentDek Handels GmbH, private communication (2010, 2011 & 2012).

[Ros55]   M. E. Rose, *Beta- and Gamma-Ray Spectroscopy*, Interscience Publishers, Inc., New York (1955) 271–291.

[Rus53]   B. M. Rustad & S. L. Ruby, *Correlition between Electron and Recoil Nucleus in ^6He Decay*, Phys. Rev. 89 (4) (1953) 880–881.

[Rus55]   B. M. Rustad & S. L. Ruby, *Gamow-Teller Interaction in the Decay of ^6He*, Phys. Rev. 97 (1955) 991–1002.

[Sal64]   A. Salam, and J. C. Ward, Phys. Lett. 13 (1964) 168–171.

[Sch74]   P. Schagen, Advances in image pick-up and display, vol. 1, Academic Press, New York (1974) 1.

[Sci04]   N. D. Scielzo et al., *Measurement of the $\beta - \nu$ Correlation using Magneto-optically Trapped ^{24}Na*, Phys. Rev. Lett. 93 (2004) 102501.

[Sci12]   N. D. Scielzo et al., *The β-decay Paul trap: A radiofrequency-quadrupole ion trap for precision β-decay studies*, Nucl. Inst. and Meth. in Phys. Res. A 681 (2012) 94–100.

[Sev08]   N. Severijns et al., *Ft values of the $T = 1/2$ mirror β transitions*, Phys. Rev. C 78, 055501 (2008).

[Sev06]   N. Severijns, M. Beck & O. Naviliat-Cuncic, *Tests of the standard electroweak model in beta decay*, Rev. Mod. Phys. 78(3) (2006) 991–1042.

[Sud57]   E. C. G. Sudarshan & R. E. Marshak, *The Nature of the Four-Fermion Interaction*, Proc. Conf. on Mesons and Newly Discovered Particles, Padua-Venice (Conference held in Sept 1957) 508–515.

[Sud58]   E. C. G. Sudarshan & R. E. Marshak, *Chirality Invariance and the Universal Fermi Interaction*, Phys. Rev. 109 (5) (1958) 1860–1862.

[Tan11]   M. Tandecki et al., *Computer controls for the WITCH experiment*, Nuclear Instruments and Methods in Physics Research A 629 (2011) 396–405.

[Tan11a]   M. Tandecki, *Progress at the WITCH Expriment towards Weak Interaction Studies*, PhD thesis, KU Leuven (2011).

[Tra11]   E. Traykov et al., *A compact radio frequency quadrupole for ion bunching in the WITCH experiment*, Nucl. Instr. Meth. A 648 1 (2011) 1–14.

[Val09]   K. Valerius, *Spectrometer-related background processes and their suppression in the KATRIN experiment*, PhD thesis, WWU Münster (2009).

[Ver78]   J. H. Verner, *Explicit Runge-Kutta methods with estimates of the local truncation error*, SIAM J. Numer. Anal., 15 (1978) 772.

[Vet11]   P. Vetter et al. *Search for Oscillation of the Electron-Capture Decay Probability of Pm-142*. Lawrence Berkeley National Laboratory: Lawrence Berkeley National Laboratory. Retrieved from: *http://escholarship.org/uc/item/5tb254wb*.

[Wei67]   S. Weinberg, Phys. Rev. Lett. 19 (1967) 1264–1266.

[Wic66]   G. L. Wick et al., *A new measurement of the ft value for the mirror decay $^{35}Ar(\beta^+)^{35}Cl$ and a calculation of the vector coupling constant*, Nucl. Phys. A 138 (1969) 209–230.

[Wik12]   Wikipedia homepage, Entry for Moiré Pattern, *http://en.wikipedia.org/wiki/Moire_pattern* (2012).

[Wit09]   F. E. Wietfield, *aCORN: An experiment to measure the electron-antineutrino correlation in neutron decay*, Nuclear Instruments and Methods in Physics Research A 611 (2009) 207–210.

[Wiz09]   J. L. Wiza, *Microchannel Plate Detectors*, Nucl. Instr. and Meth. in Phys. Res. A 162 (1979) 587–601.

[Wu79]   C. S. Wu et al., *Experimental Test of Parity Conservation in Beta Decay*, Phys. Rev. 105 (1957) 1413–1414.

[Yer04]   B. Yerozolimsky, *New Approaches to Investigations of the Angular Correlations in Neutron Decay*, arXiv:nucl-ex/0401014 (2004).

[Zak121]   D. Zákǒucký, private communication (2011).

[Zbo12]   M. Zbǒril, private communication (2012).

Acknowledgements

272

Lebenslauf

Persönliche Daten

Name	Peter Friedag
Geburtsdatum	20.04.1981
Geburtsort	Nordhorn
Eltern	Gisela Friedag, geb. Hoffmann am 26.03.1944 in Grunau, Rs /Gb, technische Zeichnerin
	Manfred Friedag, geb. am 20.12.1942 in Münster, staatlich geprüfter Augenoptikermeister
Geschwister	Dagmar Friedag-Silder, geb. am 23.02.1968 in Berlin
	Andrea Friedag, geb. am 14.10.1972 in Nordhorn
Staatsangehörigkeit	deutsch
Familienstand	ledig

Schulausbildung und Studium

09/1987 – 07/1991	Grundschule Stadtflur in Nordhorn
09/1991 – 07/1993	Orientierungsstufe Deegfeld in Nordhorn
09/1993 – 07/2000	Gymnasium am Stadtring in Nordhorn
06/2000	Allgemeine Hochschulreife
10/2001 – 10/2002	Studium der Chemie an der Westfälischen Wilhelms-Universität Münster
10/2002 – 02/2008	Studium der Physik an der Westfälischen Wilhelms-Universität Münster
02/2008	Fertigstellung der Diplomarbeit in der Arbeitsgruppe Weinheimer mit dem Thema *Bahnverfolgungssimulationen für das WITCH-Experiment*
03/2008	Beginn der Dissertation am Institut für Kernphysik der Westfälische Wilhelms-Universität Münster unter Betreuung von Prof. Dr. Christian Weinheimer

Berufliche Tätigkeit

10/2000 – 08/2001	Zivildienst in der Drogenberatungsstelle Nordhorn
10/2006 – 01/2007, 04/2007 – 08/2007, 09/2007 – 11/2007	Studentische Hilfskraft an der Westfälischen Wilhelms-Universität Münster
03/2008 – heute	Wissenschaftlicher Mitarbeiter am Institut für Kernphysik an der Westfälischen Wilhelms-Universität Münster